UCLA
UCLA Electronic Theses and Dissertations

Title
Developments in Mesoscale Correlative Multimodal X-ray Microscopy

Permalink
https://escholarship.org/uc/item/3f13f8rk

Author
Lo, Yuan Hung

Publication Date
2019

Peer reviewed|Thesis/dissertation

eScholarship.org Powered by the California Digital Library
University of California

UNIVERSITY OF CALIFORNIA
Los Angeles

Developments in Mesoscale Correlative Multimodal X-ray Microscopy

A dissertation submitted in partial satisfaction
of the requirements for the degree
Doctor of Philosophy in Bioengineering

by

Yuan Hung Lo

2019

© Copyright by
Yuan Hung Lo
2019

Abstract of the Dissertation

Developments in Mesoscale Correlative Multimodal X-ray Microscopy

by

Yuan Hung Lo
Doctor of Philosophy in Bioengineering
University of California, Los Angeles, 2019
Professor Jianwei Miao, Co-chair
Professor Gerard Chee Lai Wong, Co-chair

X-ray and electron microscopy are crucial tools that are widely used in basic and translational sciences to detect, understand, and treat diseases. Operating at length scales between molecular machineries and individual cells, those mesoscale imaging techniques enable studies into macromolecular assembly, biomechanics, biomaterials, and cellular engineering, among many others. As X-ray and electron techniques become more advanced, however, we have reached a point at which single modal imaging is asymptotically approaching its usefulness for solving challenging scientific and engineering problems.

Since most natural systems comprise hierarchical organizations with heterogeneous compositions, individual imaging methods do not have the scope to understand the comprehensive set of rules governing a system's mesoscale self-organization and to make predictions of its macroscopic behaviors. This necessitates the development of a hybrid imaging approach that integrates X-ray and electron microscopy, and presents an opportunity to leverage both modalities in a complementary fashion. The four studies presented in this dissertation demonstrates the use of intra- or intermodal X-ray and electron microscopy to study a variety of organic and inorganic samples with heterogeneous compositions and mesoscale morphologies. This hybrid microscopy approach reveals multidimensional and multiscale insights into the structural, chemical, and dynamic properties of the samples.

Study 1 integrates X-ray fluorescence microscopy and ptychography for 3D imaging of frozen hydrated green algae; it highlights the potential of such an intramodal method for non-destructive correlative imaging with nanometer spatial resolution and elemental specificity. Study 2 combines X-ray and electron microscopy in 2D and 3D to study highly heterogeneous meteoric grains with elemental and chemical identification; it is used to reveal the meteorite's mineralogical properties, and at the same time showcases the power of multimodal X-ray and electron imaging.

Study 3 leverages linearly polarized X-rays and electron scanning nanodiffraction to reveal crystal orientations in dichroic coral particles. This demonstration suggests the possibility of combining X-ray and electron methods to study optically anisotropic materials across multiple length scales. Finally, Study 4 presents a novel lensless in situ coherent diffractive imaging technique for generating high spatiotemporal resolution movies of ultrafast dynamics. This technique may be integrated into existing X-ray diffractive imaging microscopes to add a temporal dimension to the multimodal imaging paradigm.

Taken together, this dissertation promotes multidisciplinary thinking in hybrid X-ray and electron imaging—one that seeks to integrate the strengths of each microscopy technique into a comprehensive correlative imaging paradigm that can help solve today's most challenging problems.

The dissertation of Yuan Hung Lo is approved.

Dan Ruan

Louis-Serge Bouchard

Gerard Chee Lai Wong, Committee Co-chair

Jianwei Miao, Committee Co-chair

University of California, Los Angeles
2019

To my parents…

for their tireless dedication to my education.

And to my lovely wife Iris…

for her unconditional love and support.

Table of Contents

List of Figures

LIST OF TABLES

ACKNOWLEDGMENTS

I would like to sincerely thank my advisor, Professor Jianwei (John) Miao, for his mentorship and support over the past five years, and for showing me the value of passion and persistence. I am forever grateful for the opportunity he provided me to grow and discover myself in a nurturing setting. I would also like to thank all members of the Coherent Imaging Group for their guidance throughout this journey, for without them this journey would have been much less enjoyable. Finally, I would like to thank my committee for their support and consideration of this thesis.

Chapter 3 is an adapted version of the article "Correlative 3D x-ray fluorescence and ptychographic tomography of frozen-hydrated green algae." Reprinted from Deng et al., *Sci. Adv.* 2018; **4**:eaau4548. © The Authors, some rights reserved; exclusive licensee American Association for the Advancement of Science. Distributed under a Creative Commons Attribution NonCommercial License 4.0 (CC BY-NC, http://creativecommons.org/licenses/by-nc/4.0/). I thank and acknowledge the contributions from the coauthors, Junjing Deng, Marcus Gallagher-Jones, Si Chen, Alan Pryor Jr., Qiaoling Jin, Young Pyo Hong, Youssef S. G. Nashed, Stefan Vogt, Jianwei Miao, and Chris Jacobsen.

Chapter 4 is an adapted version of the article "Multimodal x-ray and electron microscopy of the Allende meteorite." Reprinted from Lo et al., *Sci. Adv.* 2019; **5**:eaax3009. © The Authors, some rights reserved; exclusive licensee American Association for the Advancement of Science. Distributed under a Creative Commons Attribution NonCommercial License 4.0 (CC BY-NC, http://creativecommons.org/licenses/by-nc/4.0/). I thank and acknowledge the contributions from the coauthors, Chen-Ting Liao, Jihan Zhou, Arjun Rana, Charles S. Bevis, Guan Gui, Bjoern Enders, Kevin M. Cannon, Young-SangYu, Richard Celestre, Kasra Nowrouzi, David Shapiro, Henry Kapteyn, Roger Falcone, Chris Bennett, Margaret Murnane, and Jianwei Miao.

Chapter 5 is an adapted version of the article "X-ray linear dichroic ptychography reveals mis-orientations within coral skeleton single crystals." Reprinted from Lo et al., 2019 (*Submitted*). I thank and acknowledge the contributions from the coauthors, Jihan Zhou, Arjun Rana, Drew Morrill, Christian Gentry, Bjoern Enders, Young-Sang Yu, Chang-Yu Sun, David Shapiro, Roger Falcone, Henry Kapteyn, Margaret Murnane, Pupa U. P. A. Gilbert, and Jianwei Miao.

Chapter 6 is an adapted version of the article "In situ coherent diffractive imaging." Reprinted from Lo et al., *Nat. Comm.* 2018; **9**:1826. © The Authors, some rights reserved. Distributed under a Creative Commons Attribution NonCommercial License 4.0 (CC BY-NC, http://creativecommons.org/licenses/by-nc/4.0/). I thank and acknowledge the contributions from the coauthors, Lingrong Zhao, Marcus Gallagher-Jones, Arjun Rana, Jared J. Lodico, Weikun Xiao, B.C. Regan, and Jianwei Miao.

Appendix B is an adapted version of the article "Correlative cellular ptychography with functionalized nanoparticles at the Fe L-edge." Reprinted from Gallagher-Jones et al., *Sci. Rep.* 2017; **7**:4757. © The Authors, some rights reserved. Distributed under a Creative Commons Attribution NonCommercial License 4.0 (CC BY-NC, http://creativecommons.org/licenses/by-nc/4.0/). I thank and acknowledge the contributions from the coauthors, Marcus Gallagher-Jones, Carlos Sato Baraldi Dias, Alan Pryor Jr., Karim Bouchmella, Lingrong Zhao, Mateus Borba Cardoso, David Shapiro, Jose Rodriguez, and Jianwei Miao.

Lastly, I acknowledge support by STROBE: A National Science Foundation Science and Technology Center under Grant No. DMR 1548924 and the Office of Basic Energy Sciences of the US DOE (DE-SC0010378).

Vita

2014-2019	Graduate Student Researcher Department of Physics and Astronomy University of California, Los Angeles Los Angeles, CA
2014-2017	Graduate Teaching Assistant University of California, Los Angeles Los Angeles, CA
2014-2015	Technology Fellow UCLA Office of Intellectual Properties Los Angeles, CA
2011	B.S. Biophysics Department of Physics University of California, San Diego

Publications

M. Gallagher-Jones*, C. S. B. Dias*, A. Pryor Jr.*, K. Bouchmella, L. Zhao, **Y. H. Lo**, M. B. Cardoso, D. Shapiro, J. A. Rodriguez and J. Miao. Correlative cellular ptychography with functionalized nanoparticles at the Fe L-edge. *Scientific Reports* **7**, 4757 (2017).

A. Pryor Jr., Y. Yang, A. Rana, M. Gallagher-Jones, J. Zhou, **Y. H. Lo**, G. Melinte, W. Chiu, J. A. Rodriguez, J. Miao. GENFIRE: A generalized Fourier iterative reconstruction algorithm for high-resolution 3D imaging. *Scientific Reports* **7**, 10409 (2017).

Y. H. Lo, L. Zhao, M. Gallagher-Jones, A. Rana, J. Lodico, W. Xiao, B.C. Regan, J. Miao. In situ coherent diffractive imaging. *Nature communications* **9**, 1826 (2018).

J. Deng*, **Y. H. Lo***, M. Gallagher-Jones, S. Chen, A. Pryor Jr., Q. Jin, Y. P. Hong, Y. S. G. Nashed, S. Vogt, J. Miao, C. Jacobsen. Correlative 3D x-ray fluorescence and ptychographic tomography of frozen-hydrated green algae. *Science Advances* **4**, eaau4548 (2018).

Y. H. Lo, C.-T. Liao, J. Zhou, A. Rana, C. S. Bevis, G. Gui, B. Enders, K. M. Cannon, Y.-S.Yu, R. Celestre, K. Nowrouzi, D. Shapiro, H. Kapteyn, R. Falcone, C. Bennett, M. Murnane, J. Miao. Multimodal x-ray and electron microscopy of the Allende meteorite. *Science Advances* **5**, eaax3009 (2019).

Y. H. Lo, J. Zhou, A. Rana, D. Morrill, C. Gentry, B. Enders, Y.-S. Yu, C.-Y. Sun, D. Shapiro, R. Falcone, H. Kapteyn, M. Murnane, P. U. P. A. Gilbert, J. Miao. X-ray linear dichroic ptychography reveals mis-orientations within coral skeleton single crystals. *Submitted* (2019).

A. Rana, J. Zhang, M. Pham, A. Yuan, **Y. H. Lo**, H. Jiang, S. Osher, J. Miao. Ptychographic coherent diffractive imaging for attosecond pulses. *Submitted* (2019).

**denotes equal contribution*

CHAPTER 1

Introduction

1.1 Background and motivation

Throughout human history, the ability to visualize the natural world microscopically has always been integral to humanity's great leaps in scientific discovery and technological innovations. The light microscope allowed mankind to see cells and bacteria for the first time, and to learn about the basic units of living organisms. The fluorescent microscope provided precise localization of individual molecules in living cells with great specificity, allowing scientists to understand how complex systems of molecules and cells interact to maintain life's fine balance. The electron microscope helped decipher biomolecular structures and inorganic materials at their most fundamental level, and has significantly advanced our understanding of how structure relates to function at the sub-atomic and molecular level. As evidenced by these achievements, the act of observing the micro- and nanoscopic world is often enough to gain invaluable insights into the ways in which complex living systems grow and interact with their surroundings.

In addition to the aforementioned methods, lens-based X-ray microscopy also recently experiened major developments in instrumentation and software. New synchrotron light sources paved the way to brighter X-ray microscopes, enabling applications in environmental science, geo- and cosmo-chemistry, polymer science, biology, magnetism, energy, materials and surface science [6–9]. Concurrently, X-ray flourescence, transmission full-field and scanning X-ray microscopy also advanced toward capturing mesoscale biology that ranges from molecular machines to single cells, and helping to discover the rules and guiding principles of mesoscale self-organization. X-ray microscopy occupies a unique niche between electron and optical microscopy by offering a nice balance between sample penetration depths and short wavelengths.

Then, in 1999, lensless coherent diffractive imaging (CDI) [10] was experimentally demonstrated for the first time. The microscopy technique offered a robust solution to the long sought-after phase problem in diffraction imaging, in which the recorded diffraction intensities are insufficient to reconstruct real space images due to the phase not being recorded by the detector. By computationally solve for the phase, CDI opened up X-ray microscopy to the realistic possibility of imaging non-crystalline specimens in a truly diffraction and dose-limited manner. After its inception, a myriad of CDI-inspired imaging techniques ensued, with demonstrations on a wide variety of samples [11, 12]. Furthermore, continuous development in instrumentation has pushed spatial resolution better than 10 nm [13]. As coherent diffractive X-ray microscopy enters the mainstream, it is now a still-growing yet proven technique.

Altogether, in the past few decades advances in the different aforementioned microscopy techniques have individually driven incredible advances in material science, biology, engineering and medicine. They have pushed the boundaries of how small and detailed we can see into the natural world, and have fundamentally transformed the way we understand the world. Even now, those areas of imaging are still developing at an accelerated rate.

However, despite the rapid growth within each imaging disciplines, no single microscopy technique can adequately address the grand challenge underlying much of science and technology in the 21st century: How do nano- to microscopic structures and interactions manifest into macroscopic properties and functions in inorganic materials and biological systems? In the mesoscale spatial regime, small building blocks self-organize to form large, functional structures. A comprehensive set of rules governing mesoscale self-organization has not been established, making the prediction of macroscopic behaviors extremely difficult. Microscopy is poised to answer this question, but imaging researchers are oftentimes too focused on perfecting their own techniques that they neglect to understand how their methods fit into the larger context of microscopy as a practical tool.

While current imaging methods may individually probe some parts of the length scale continuum, no single method can effectively image across all length scales. Each imaging technique operates best in fairly narrow regimes, confined by parameters such as specimen size and maximum spatial resolution. For instance, transmission electron microscopy (TEM) methods, such as single-particle analysis (SPA) and cryo-electron tomography (cryo-ET), play important roles in structural cell biology and provide unprecedented insight into the macromolecular organization of cellular environments at nanometer to angstrom resolution [14]. Unfortunately, electron microscopy faces a trade-off between spatial resolution, imaging contrast, and specimen thickness. In general, the thicker the specimen, the lower the achievable resolution, with the optimal biological specimens thickness being less than 500 nm [15,16]. In contrast, soft X-ray microscopy can penetrate deep into intact cells, permitting two dimensional and (2D) three dimensional (3D) characterization of bulk biological specimen in their near-native environments [6, 17], and hard X-ray microscopy has non-destructively imaged millimeter sized objects in 3D with $\sim$15 nm resolution [18]. Nonetheless, X-ray microscopy as a whole still trails behind TEM in terms of achievable spatial resolution due to light source brilliance and limitations in instrumentation.

Additionally, just as most natural systems comprise complex, multifaceted properties, so too the imaging system used to study them should be able to adequately collect those multidimensional information. The reality is that, oftentimes, new discoveries are made in isolation as we currently lack a paradigm to analyze and correlate all of that big data to gain insights into a material's functionality. In other words, current optical, X-ray and electron microscopies are still too isolated and slow to provide a comprehensive understanding of functional systems in real time, and this severely holds back progress in science and innovation.

One way to approach such shortcomings is to leverage the strengths of each techniques correlatively and integrate them into a new imaging platform. Microscopy of the 21st century should go beyond advancing each imaging modality's capabilities and promote horizontal integration across disciplines to develop a hybrid multiscale, multidimensional imaging paradigm. Such a paradigm should enable studies of specimens across the atomic, molecular, and cellular levels, and provide multifaceted structural, elemental and chemical mappings.

Similar correlative approaches are being explored in other disciplines. In the medical imaging community, functional data generated by functional magnetic resonance imaging (fMRI) and positron emission tomography (PET) have been correlated with anatomical information from computed tomography (CT) to provide comprehensive screening and diagnosis of diseases [19–21]. In the electron microscopy community, cryo-correlative light and electron microscopy (cryoCLEM) combines the power of fluorescence microscopy (FM) with that of electron microscopy (EM) to study the same sample [22, 23] across multiple length scales. Cryogenic FM labels and identifies specific proteins, and also captures their dynamics in fixed or living cells. Then EM provides the full environmental context in high-resolution, with which the fluorescence data can correlate with to reveal connections between structure and interactions [14]. Even within the X-ray microscopy community, correlative cryogenic light and lens-based X-ray microscopy has been developed to study a common frozen hydrated specimens [7, 24, 25]. As improvements in synchrotron-based coherent X-ray flux is only starting to pay scientific dividend recently, such multi-modal integration is just beginning in the

X-ray diffractive imaging community.

1.2 Specific contributions

To that end, the main objective of this dissertation is to explore ways in which X-ray CDI can be used cooperatively with electron and optical microscopy to establish a hybrid mesoscale imaging paradigm. In this endeavor, I leverage X-ray polarization, spectromicroscopy and X-ray fluorescence to simultaneously collect multidimensional data from a single sample. I then explore how the information obtained from X-ray microscopy can augment data from electron and optical microscopy to establish a more complete picture of the sample. A second objective is to develop and demonstrate a proof-of-concept for a new CDI technique that can capture ultrafast dynamic phenomena in situ, with spatial resolution that is theoretically diffraction-limited. The hope is that such a time-resolved CDI technique can add an additional temporal dimension to the multi-modal imaging paradigm.

This dissertation is organized into two overarching aims. First aim contains three chapters, with an additional chapter in the appendix, and the second aim contains one chapter. In the following paragraphs I will describe those aims and summarize the 4 studies that address them.

Aim 1: To combine X-ray, electron and optical microscopy and collect multidimensional data for correlating different properties of a common sample

Project 1A: Integrating hard X-ray fluorescence and ptychography to simultaneously image a common sample

Chapter 3: Correlative 3D X-ray fluorescence and ptychographic tomography of frozen-hydrated green algae

Accurate knowledge of elemental distributions within biological organisms is critical for understanding their cellular roles. The ability to couple this knowledge with overall cellular architecture in three dimensions deepens our understanding of cellular chemistry. Using a whole, frozen-hydrated *Chlamydomonas reinhardtii* cell as an example, in this chapter we report the development of 3D correlative microscopy through a combination of simultaneous cryogenic X-ray ptychography and X-ray fluorescence microscopy. By taking advantage of a recently developed tomographic reconstruction algorithm, termed GENeralized Fourier Iterative REconstruction (GENFIRE), we produce high-quality 3D maps of the unlabeled algas cellular ultrastructure and elemental distributions within the cell. We demonstrate GENFIREs ability to outperform conventional tomography algorithms and to further improve the reconstruction quality by refining the experimentally intended tomographic angles. As this method continues to advance with brighter coherent light sources and more efficient data handling, we expect correlative 3D X-ray fluorescence and ptychographic tomography to be a powerful tool for probing a wide range of frozen-hydrated biological specimens, ranging from small prokaryotes such as bacteria, algae, and parasites to large eukaryotes such as mammalian cells, with applications that include understanding cellular responses to environmental stimuli and cell-to-cell interactions.

Project 1B: Integrating soft X-ray ptychography, spectromicroscopy, energy dispersive spectroscopy and electron tomography to image a common sample

Chapter 4: Multimodal X-ray and electron microscopy of the Allende meteorite

Multimodal microscopy that combines complementary nanoscale imaging techniques is critical for extracting comprehensive chemical, structural, and functional information, particularly for heterogeneous samples. X-ray microscopy can achieve high-resolution imaging of bulk materials with chemical, magnetic, electronic, and bond orientation contrast, while electron microscopy provides atomic-scale spatial resolution with quantitative elemental composition. In this chapter, we combine X-ray ptychography and scanning transmission X-ray (STXM) spectromicroscopy with three-dimensional energy-dispersive spectroscopy (EDS) and scanning transmission electron (STEM) tomography to perform structural and chemical mapping of an Allende meteorite particle with 15 nm spatial resolution. We use textural and quantitative elemental information to infer the mineral composition and discuss potential processes that occurred before or after accretion. We anticipate that correlative X-ray and electron microscopy can overcome the limitations of individual imaging modalities and opens up a route to future multiscale nondestructive microscopies of complex functional materials and biological systems.

Project 1C: Using linearly polarized X-rays and electron diffraction to probe crystal orientations in biominerals

Chapter 5: X-ray linear dichroic ptychography reveals mis-orientations within coral skeleton ‘single crystals’

Biominerals such as sea shells, corals, bone and tooth enamels are optically anisotropic materials with unique nanoscale organization that translates into exceptional macroscopic mechanical and thermal properties, providing the inspirations needed to engineer new and superior biomimetic structural composites. In this chapter, we use fragments of *Seriatopora aculeata* coral skeleton as a model and demonstrate, for the first time, X-ray linear dichroic ptychography. We map the crystal c-axis orientations in the coral skeleton with 35 nm spatial resolution. Linear phase dichroic imaging at the O K-edge energy shows strong polarization-dependent contrast and reveals the presence of both narrow ($< 20°$) and wide

($> 35°$) c-axis angular spread in the sub-micrometer coral fragments. These X-ray ptychography results were corroborated using 4D scanning transmission electron nano-diffraction. Evidence of co-oriented but disconnected corallite sub-domains indicates a much more diverse nanoscale crystalline architecture than previously appreciated, suggesting the need for a new model to elucidate coral skeleton formation. Looking forward, we anticipate that X-ray linear dichroic ptychography can be applied to study nano-crystallites, interfaces, nucleation, and mineral growth of optically anisotropic materials with sub-ten nanometers spatial resolution over a wide field of view.

Aim 2: To develop novel coherent diffractive imaging reconstruction algorithm for high spatiotemporal resolution in situ imaging

Project 2A: Investigating time-invariant real space redundancies as robust algorithm constraints for phase retrieval

Chapter 6: In situ coherent diffractive imaging

Coherent diffractive imaging (CDI) has been widely applied in the physical and biological sciences using synchrotron radiation, X-ray free-electron laser, high harmonic generation, electrons, and optical lasers. One of CDIs important applications is to probe dynamic phenomena with high spatiotemporal resolution. In this chapter, we report the development of a general in situ CDI method for real-time imaging of dynamic processes in solution. By introducing a time-invariant overlapping region as real-space constraint, we simultaneously reconstructed a time series of complex exit wave of dynamic processes with robust and fast convergence. We validated this method using optical laser experiments and numerical simulations with coherent X-rays. Our numerical simulations further indicated that in situ CDI can potentially reduce radiation dose by more than an order of magnitude relative to conventional CDI. With further development, we envision that in situ CDI could be applied to probe a range of dynamic phenomena in the future.

1.3 Summary of dissertation

In summary, the four studies comprising this dissertation combine CDI with X-ray fluorescence, spectromicroscopy, electron microscopy, fluorescence microscopy, and tomography to advance toward an adaptive imaging paradigm for multiscale and multidimensional sample characterizations. In terms of experiments, this collection of work explores intramodal (different measurements from a single light source that simultaneously provide multidimensional information) and intermodal (different measurements from multiple light sources that sequentially provide multidimensional information) techniques and examines ways to acquire data efficiently by maintaining samples in a consolidated environment. In terms of data analysis, the work compares and contrasts data obtained from different modalities and explores ways to synthesize the assortment of information to gain in-depth understanding of the sample. The far-reaching goal of this work is to formulate a hybrid imaging paradigm that can non-destructively probe structures and functions at length scales between single molecules and whole cells. Hopefully such a microscopy platform can accelerate research in basic sciences and engineering and enable imaging to address grand challenges in science and technology.

CHAPTER 2

Technical background

This chapter gives an overview of the underlying principles of two imaging techniques commonly used throughout this thesis. Namely, X-ray coherent diffractive imaging and tomography. This chapter is meant to only provide a general grasp of the techniques to understand the main studies in the rest of this dissertation. For a more comprehensive overview of each topic, please see the suggested articles cited at the end of each section for more details.

2.1 Coherent diffractive imaging

In a traditional visible light microscope, a refractive lens system is used to Fourier transform the light scattered from a sample to form images on a detector. However, since X-ray interacts weakly with matter (refractive indices are extremely close to 1), refractive lenses similar to those in visible light microscopy do not work for X-ray imaging. Hence, diffractive optics must be used instead, in spite of their severe limitations. For instance, Fresnel zone plate X-ray lenses, which are commonly used in X-ray microscopy, are limited in spatial resolution by the size of the finest detail in the width of the outermost zone. Increasing the resolution thus depends heavily on advancing the nanofabrication processes used to manufacture such lenses. Additional challenge is posed by the need to keep the diffraction efficiencies within an acceptable range (typically above 10%), thereby implying that a certain zone plate thickness must be achieved. Consequently, lens-based X-ray microscopy typically only achieve ∼25 nm spatial resolution, which is nowhere near the wavelength limit.

Coherent diffractive imaging (CDI) is a lensless X-ray imaging technique that illuminates an object with a coherent laser-like beam and collects the scattered light intensities on a detector, then computationally recovers the image in post-processing, effectively using algorithms as virtual lenses. CDI uses the fact that the measured detector intensity patterns in the far-field Fraunhofer diffraction plane also contain information about large scattering vectors, and therefore offer in principle wavelength-limited resolution approaching the nanometer scale. This translates to an increase in the numerical aperture, but without the difficult need for fabricating X-ray lenses. The key challenge in CDI, however, is to solve the phase problem, as only intensities are recorded in the detector. In 1999, Miao et al [10] demonstrated that the phase problem can indeed be solved by oversampling the measured diffraction pattern in Fourier space. In practice, this means that the detector must have a pixel size that is inversely proportional to the size of the object, and that the sample needs to be isolated.

2.1.1 Coherent diffractive imaging principles

Once the oversampling requirement is met, the image of the object can be recovered with an advanced phase retrieval algorithm by taking advantage of the fact that the diffracted wave is proportional to the Fourier transform of the object. Over the years, many algorithms have been developed to retrieve the phase of images, such as error-reduction (ER), hybrid input-output (HIO) [26], guided HIO [27], Difference Map [28], and Oversampling Smoothness [29], but the basic approach remains the same: the algorithm seeks to reconstruct $f(x, y)$, a real or complex-valued object function, from $|F_{\mathrm{m}}(u, v)|$, the modulus of its Fourier transform, or the diffraction pattern measured on the detector.

To illustrate this point, let's use HIO as an example. In the first iteration

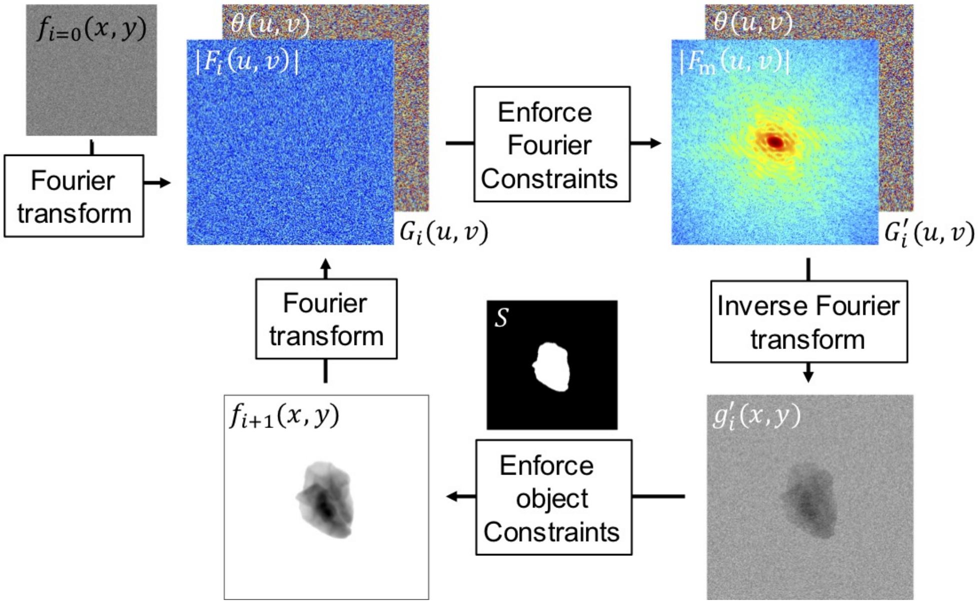

Figure 2.1: CDI phase retrieval algorithm for recovering the image from the modulus of diffraction intensity.

$(i = 0)$, HIO starts with initial guesses of the phase, $\phi(x, y)$, and the magnitude, $|f_{i=0}(x, y)|$, to formulate an object guess in real space. They typically comprise of random numbers. In the i^{th} iteration, the object guess is

$$g_i(x, y) = |f_i(x, y)|e^{i\phi(x,y)}. \tag{2.1}$$

The algorithm then Fourier transforms the object guess to obtain the Fourier guess,

$$G_i(u, v) = |F_i(u, v)|e^{i\theta(u,v)}, \tag{2.2}$$

and the Fourier constraint is enforced by replacing the modulus term $(|F_i(u, v)|)$ with the measured diffraction intensity $(|F_{\text{m}}(u, v)|)$ while keeping the calculated phase. This returns the update Fourier guess

$$G_i'(u, v) = |F_{\text{m}}(u, v)|e^{i\theta(u,v)}. \tag{2.3}$$

Next, the Fourier guess is inverse Fourier transformed back into real space to obtain the updated object guess,

$$g_i'(x, y) = |g_i'(x, y)|e^{\phi'(x,y)}. \tag{2.4}$$

At this point, object constraint is enforced by applying a known support on the object. This returns the final updated object estimate of the current iteration,

$$f_{i+1}(x,y) = \begin{cases} g_i'(x,y), & (x,y) \in S \\ g_i(x,y) - \beta g_i'(x,y), & (x,y) \notin S. \end{cases} \tag{2.5}$$

where β is a constant usually chosen to be anywhere between 0.5 and 1.0 that facilitates feedback between current and previous iterations. Additional constraints can be applied to the object guess if prior information is known, such as enforcing realness if the object is known to be a weakly phased object, and enforcing positivity in the pixel values since electron density of the object cannot be negative. The convergence of the algorithm is measured by the R-factor (R_F), or the normalized root-mean-squared error between the modulus of measured and calculated diffraction intensities.

$$R_F = \frac{\Sigma||F_{\mathrm{m}}(u,v)| - |G'(u,v)||}{\Sigma|F_{\mathrm{m}}(u,v)|}. \tag{2.6}$$

These steps are repeated for a set number of iterations, or until the algorithm reaches below a predefined R_F threshold. See [11] for a more comprehensive review of CDI, and see [8] for review on current state of synchrotron-based, hard X-ray nanoscale microscopy techniques.

2.1.2 Ptychography principles

Ptychography is a scanning CDI method that combines the utility of CDI with scanning transmission X-ray microscopy (STXM), which raster scans a sample with focused X-ray beam at the focal plane and records transmitted X-ray intensity as a function of the sample position. Ptychography overcomes major disadvantages in both techniques: in STXM it is the limited achievable resolution due to difficulty of fabricating high quality X-ray optics, and in CDI it is the limited applicability to isolated objects for the use of support.

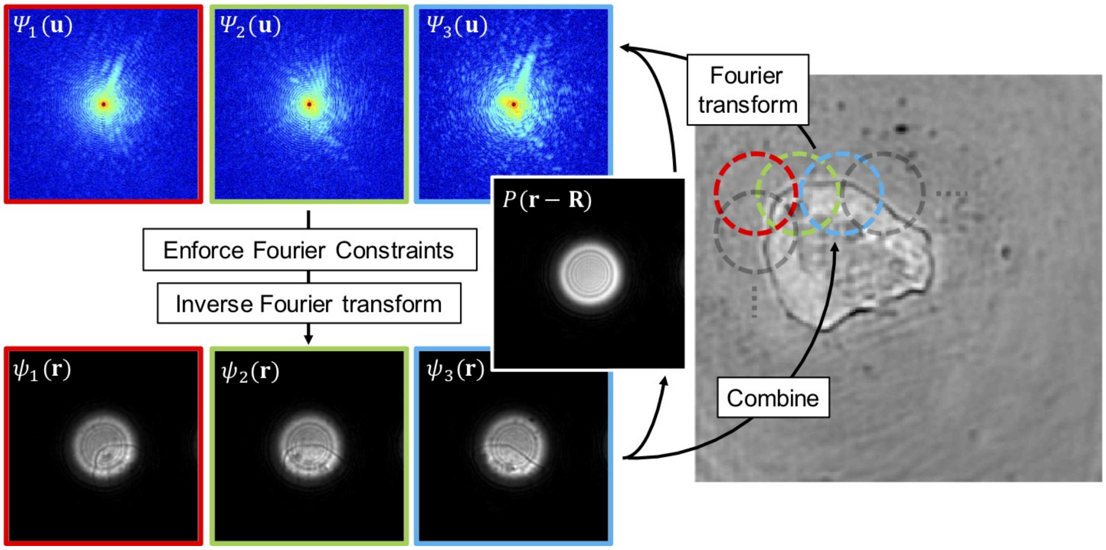

Figure 2.2: Iterative ptychography phase retrieval algorithm.

In ptychography, multiple diffraction patterns are recorded by scanning a confined X-ray illumination — localized with focusing optics or aperture — over an extended specimen. The spatial overlap between adjacent probe positions provides sufficient over-determination of information on the scanned areas. The dataset with redundancy can then be fed into iterative phase retrieval algorithms to quickly and robustly solve for the amplitude and phase of the object, as well as the complex probe function of the system.

In its simplest form, which assumes that the probe function is perfectly known, the basic ptychographic phase-retrieval problem is to find the complex-valued object transmission function at each scan position that best matches adjacent overlapping areas in real space, and also matches the measured diffraction pattern in Fourier space. To illustrate this further, consider one of the popular ptychographic phase retrieval algorithms, named extended ptychographic iterative engine (ePIE) [30]. The algorithm works as follows.

Initiate an estimated complex-valued object transmission function at j^{th} scan position, $\psi_j(\mathbf{r})$, by multiplying object estimate, $O_j(\mathbf{r})$, by the shifting probe estimate, $P(\mathbf{r}-\mathbf{R}_j)$, giving

$$\psi_j(\mathbf{r}) = O_j(\mathbf{r})P_j(\mathbf{r}-\mathbf{R}_j). \tag{2.7}$$

Fourier transform $\psi_j(\mathbf{r})$ to obtain the Fourier space estimate of the object transmission function, then enforce the Fourier constraint by replacing the modulus with the square-root of the measured diffraction intensity, $I_j(\mathbf{u})$,

$$\Psi_j(\mathbf{u}) = \sqrt{I_j(\mathbf{u})}\frac{F[\psi_j(\mathbf{r})]}{|F[\psi_j(\mathbf{r})]|}. \tag{2.8}$$

Update the transmission function estimate by inverse Fourier transform,

$$\psi'_j(\mathbf{r}) = F^{-1}[\Psi_j(\mathbf{u})], \tag{2.9}$$

and combining current estimate with previous estimates of the object,

$$O_{j+1}(\mathbf{r}) = O_j(\mathbf{r}) + \alpha\frac{P^*_j(\mathbf{r}-\mathbf{R}_j)}{|P_j(\mathbf{r}-\mathbf{R}_j)|^2_{\max}}(\psi'_j(\mathbf{r})-\psi_j(\mathbf{r})), \tag{2.10}$$

and probe,

$$P_{j+1}(\mathbf{r}) = P_j(\mathbf{r}) + \beta\frac{O^*_j(\mathbf{r}+\mathbf{R}_j)}{|O_j(\mathbf{r}+\mathbf{R}_j)|^2_{\max}}(\psi'_j(\mathbf{r})-\psi_j(\mathbf{r})), \tag{2.11}$$

where α and β can be thought of as the step-size of the updates, with larger value providing a faster update, and vice versa. The process will repeat for each diffraction pattern at positions j, and an iteration is complete when all diffraction patterns are used to update the object and probe guesses. See [12] for a more comprehensive review of X-ray ptychography.

2.2 Tomography

Tomography, originally developed for medical imaging, has found wide applications in basic biological and material sciences over the past few decades. The Greek word tomos means a section, a slice, or a cut. So tomography is the process of imaging a cross section of an object. Simply put, the goal of tomography is to

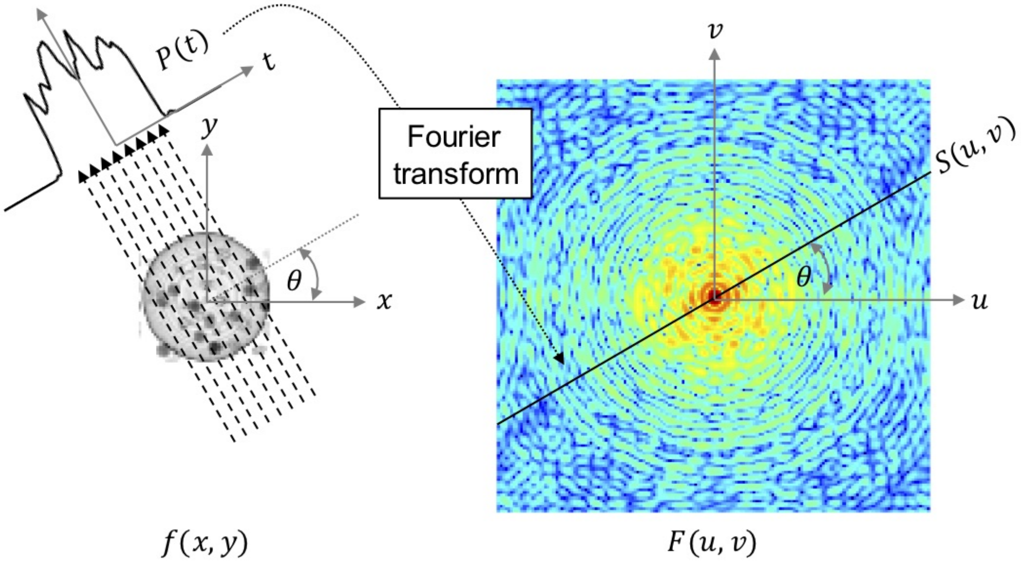

Figure 2.3: Projection slice theorem.

recover a 3D object from a limited set of 2D linear projection images of the object at different angles. The foundation of tomography is described by the projection slice theorem, also known as central slice theorem and Fourier slice theorem.

2.2.1 Projection slice theorem

Considering a two-dimensional (2D) object, the projection slice theorem states that the one-dimensional (1D) Fourier transform of a parallel projection of the object viewed from any angle (i.e. a 1D profile perpendicular to the viewing direction) is equal to a slice (or a line in the 1D case) of the 2D Fourier transform of the original object at the corresponding angle. It follows that with sufficient parallel projections measured at various angles around the object, it should then be possible to estimate the object — with all its internal features — by simply performing a 2D inverse Fourier transform. Mathematically, for a simple 2D case, the Fourier transform of an object, $f(x, y)$, is

$$F(u, v) = \int_{-\infty}^{\infty} \int_{-\infty}^{\infty} f(x, y) e^{-i2\pi(ux+vy)} dx dy. \tag{2.12}$$

A defined 1D projection at angle θ, $P_\theta(t)$, and its Fourier transform is

$$S_\theta(w) = \int_{-\infty}^{\infty} P_\theta(t) e^{-i2\pi wt} dt. \tag{2.13}$$

Consider the Fourier transform along the line in the frequency domain where $v = 0$, the integral becomes

$$F(u, 0) = \int_{-\infty}^{\infty} \int_{-\infty}^{\infty} f(x, y) e^{-i2\pi(ux)} dx dy. \tag{2.14}$$

Since the phase factor no longer depends on y, we can split the integral into two,

$$F(u, 0) = \int_{-\infty}^{\infty} \left[\int_{-\infty}^{\infty} f(x, y) dy \right] e^{-i2\pi ux} dx. \tag{2.15}$$

The term in brackets represent the projection along the line of constant x, i.e.

$$P_{\theta=0}(x) = \int_{-\infty}^{\infty} f(x, y) dy. \tag{2.16}$$

Replacing the bracketed term by $P_{\theta=0}(x)$ gives

$$F(u, 0) = \int_{-\infty}^{\infty} P_{\theta=0}(x) e^{-i2\pi ux} dx. \tag{2.17}$$

Thus, we have the following relationship between the 1D vertical projection and the 2D Fourier transform of the object:

$$F(u, 0) = S_{\theta=0}(u). \tag{2.18}$$

This is the simplest form of the projection slice theorem. Note that this result is independent of the orientation between the object and the coordinate system. In summary, the Fourier transform of a 1D parallel projection at angle θ, $P_\theta(x)$, taken from a 2D object, $f(x, y)$, gives a slice of the 2D Fourier transform, $F(u, v)$, traversing along an angle θ. The extension of projection slice theorem to three dimensions (3D) is valid and straightforward, and the 3D version of the projection slice theorem underlies much of the tomography results presented in this dissertation.

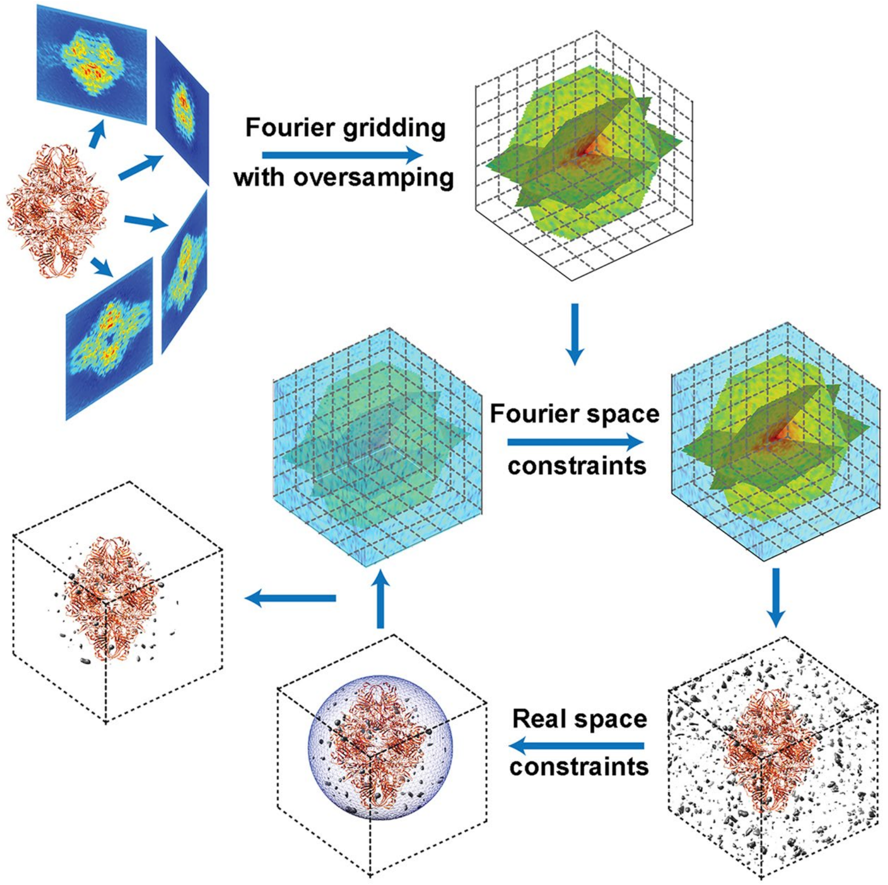

Figure 2.4: GENFIRE algorithm (*Figure reprinted from* [1]).

2.2.2 GENFIRE

In most X-ray and electron tomography experiments, the specimen is anchored on a substrate such as a TEM grid with dimensions that is typically much larger than that of the specimen. The large substrate prohibits the imaging system from sampling high tilt angles (typically angles higher than ±65°) during tomography data acquisition, effectively preventing the collection of one third of the information in Fourier space. This issue, termed the missing wedge problem, adversely affects reconstruction quality and poses a serious problem in tomography experiments.

GENFIRE, or GENeralized Fourier Iterative REconstruction algorithm, is a Fourier-based tomographic reconstruction algorithm that alleviates the missing wedge effect by using Fourier transform's global representation of the measurements to fill in the missing information. GENFIRE first assembles a 3D Fourier grid by oversampling the 2D projections (padding zeros then Fourier transforming the projection), then estimate the 3D object by iterating between real and Fourier space to search for a global solution that is concurrently consistent with the measurements and general physical constraints.

The algorithm works as follows. In the first iteration (i=0), the initial guess of the 3D object being reconstructed is initialized as the Fourier transform of a volume of random values ($\Psi_i(\mathbf{k})$). In the i^{th} iteration, apply the inverse Fourier transform to obtain real space estimate,

$$\rho_i(\mathbf{r}) = F^{-1}[\Psi_i(\mathbf{k})]. \tag{2.19}$$

Then in object space, apply the support (S) constraint to the estimate, which sets non-zero voxels outside the support and negative-valued voxels inside the support to zero, while keeping other voxels the same,

$$\rho_i'(\mathbf{r}) = \begin{cases} 0, & \text{if } (\mathbf{r} \notin S) \cup (\rho_i(\mathbf{r}) < 0) \\ \rho_i(\mathbf{r}), & \text{otherwise.} \end{cases} \tag{2.20}$$

Next, Fourier transform the updated real space estimate, $\rho_i'(\mathbf{r})$, to obtain the modified Fourier space estimate, $\Psi_i'(\mathbf{k})$,

$$\Psi_i'(\mathbf{k}) = F[\rho_i'(\mathbf{r})]. \tag{2.21}$$

Update the Fourier space estimate (i.e. $(i+1)^{\text{th}}$ iteration estimate) by enforcing measured Fourier voxels,

$$\Psi_{i+1}(\mathbf{k}) = \begin{cases} \Psi_{\text{obs}}(\mathbf{k}), & \text{if voxel is measured} \\ \Psi_i'(\mathbf{k}), & \text{if voxel is not measured} \end{cases} \tag{2.22}$$

Above steps constitute a single iteration. Progress of reconstruction is monitored by the R-factor ($R_{\mathbf{k}}$), which compares estimated Fourier voxels with measured

Fourier voxels ($\mathbf{k}_{known}$),

$$R_{\mathbf{k}} = \frac{\Sigma_{\mathbf{k}_{\text{known}}} |\, \Psi_{\text{obs}}(\mathbf{k}) - \Psi_{i+1}(\mathbf{k})|}{\Sigma_{\mathbf{k}_{\text{known}}} |\, \Psi_{\text{obs}}(\mathbf{k})|}. \tag{2.23}$$

The algorithm can run for a predefined number of iterations, or until the R-factor drops below a certain threshold. See [1] for a comprehensive introduction to GENFIRE.

CHAPTER 3

Correlative 3D X-ray fluorescence and ptychographic tomography of frozen-hydrated green algae

3.1 Introduction

Imaging biological material in a native or near-native state is central to modern high-resolution microscopy. Recent developments in optical fluorescence microscopy allow for real-time imaging of cellular processes at subwavelength resolution [31]. On the other hand, cryo-electron tomography in combination with focused ion beam milling now offers exquisite views inside cells, resolving organelles, and even individual protein complexes, without the need for additional staining [32, 33]. However, these techniques are not without their limitations: The need for fluorescent labels allows for only a preselected subset of cells components to be imaged in light microscopy, and the low penetration depth of electrons through soft matter limits cryo-electron tomography to either small, non-eukaryotic cells or thin sections. Therefore, there is a need for additional complementary techniques that can image thick specimens under a near-native state, without the need for sectioning, and can also provide imaging contrast by means of variable X-ray absorption, fluorescence, and phase shift from endogenous composition to avoid the need for dehydrating or chemically staining specimens.

X-ray microscopy is one such technique, as it provides sufficient penetrating power to image whole cells with high spatial resolution, high contrast, and in three dimensions (3D) [34, 35]. Similar to other methods, it is also compatible with cryogenic imaging of frozenhydrated samples for minimal chemical and structural modification of the specimen. Moreover, X-ray fluorescence microscopy (XFM) allows one to measure intrinsic trace element distributions with partsper- million sensitivity in cells without the need to add or genetically encode specific fluorescence labels [36–39]. However, the resolution of existing cryo X-ray microscopes is limited by the optics used, to about 30-nm resolution in 2D [40] and about 60 nm in 3D [35].

Coherent diffractive imaging (CDI) offers a means to surpass the aforementioned limitations. CDI collects scattered X-rays from noncrystalline samples or nanocrystals using bright coherent X-rays [10,11]. When these diffraction patterns are collected over a large scattering angle and are sufficiently oversampled [41], they can be computationally inverted to produce high-resolution images using iterative phase retrieval algorithms [42, 43]. In CDI, the effective numerical aperture of the imaging system can be increased, resulting in higher resolution images than conventional X-ray microscopy. Moreover, by properly selecting the X-ray wavelength, CDI permits imaging of thick biological samples without chemical labeling or sectioning due to X-rays large penetration depth and natural contrast arising from internal electron density [44–53]. However, phase retrieval in CDI requires isolated objects or finite illumination due to the algorithmic constraint. Ptychography, a scanning CDI method [12], has proven to be a powerful method to overcome this constraint for imaging extended objects such as whole cells [5,54,55] and biological materials [56, 57] in 2D and 3D. Furthermore, ptychography can be combined with XFM to simultaneously image the internal structures and trace elements distributions within cells.

Previous X-ray tomography studies have imaged *Chlamydomonas reinhardtii* using soft X-ray microscopy [34, 58] and X-ray ptychography [59], with organelle segmentations performed via thresholding based on estimated mass density, but without clear elemental identification. Moreover, while simultaneous ptychography and XFM have been applied to simultaneously image a dehydrated diatom [60] and frozen-hydrated algae [55, 61] in 2D, its extension to 3D has not been realized because of the limited number of tomographic projections obtained and the challenges of projection alignment.

Here, we report the implementation of a correlative tomography technique, combining simultaneously acquired ptychography and XFM images with a new tomography algorithm, GENeralized Fourier Iterative REconstruction (GENFIRE), to obtain tomograms of an intact, cryogenically preserved *C. reinhardtii* cell. GENFIRE iterates between real and reciprocal space to search for the best-possible 3D reconstruction that is concurrently consistent with the measured images and general physical constraints such as the sample boundary and positivity [1,62]. From the GENFIRE reconstructions, we map out the 3D cellular locations of key algal organelles and confirm their identities with 3D XFM elemental maps.

3.2 Methods

C. reinhardtii sample preparation and cryogenic preservation

C. reinhardtii cells, approximately 10 µm in diameter, were grown to the early exponential phase in tris-acetate-phosphate medium at 296 K on a rotary shaker (100 rpm). Five microliters of cell suspensions was dropped onto a plasma-treated Si_3N_4 window (200 nm thick, 1.5 mm by 1.5 mm membrane area). The window was then mounted onto a Vitrobot Mark IV plunge freezer (FEI), where the temperature and humidity were set and equilibrated at 22°C and 100%, respectively. The window was blotted for 2 s with a blot force of 0 and then immediately plunged into a liquid ethane bath cooled by liquid nitrogen (LN_2). Cells were embedded in an ice layer with a thickness of 1.2±0.2 mm. The cryogenically prepared samples were observed using a cryogenic light microscope and then stored in LN_2 until they were retrieved for use in the X-ray microscope.

Ptychography and XFM data acquisition Our experiment was carried out at the Bionanoprobe beamline, a hard X-ray nanoprobe with cryogenic sample environment and transfer capabilities, located at the Advanced Photon Source (APS) in Argonne National Laboratory [63]. Before data collection, a Si_3N_4 membrane supporting frozen-hydrated cells was mounted on a sample cartridge and then loaded into a LN_2-cooled transfer chamber in a cryogenic workstation. The transfer chamber was connected to the Bionanoprobe and delivered the shuttle to the main high-vacuum (10^{-7} torr) chamber. A sample exchange robot was used to grip the sample cartridge from the shuttle and deliver it to the sample stage that was cooled conductively from a LN_2 reservoir. During data collection, a cryogenic sample environment was maintained by a Cu cold finger and the LN_2 reservoir inside the vacuum chamber. The sample was maintained at 110 K by conductive cooling. Furthermore, a cold shield made of Al was used around the sample to minimize radiation heat loss. More details about the setup and thermal condition characterization can be found elsewhere [63]. For X-ray measurements, a monochromatic X-ray beam at 5.5 keV of energy was spectrally filtered using a Si $\langle 111 \rangle$ double-crystal monochromator (DCM). Details of the experimental setup are shown in Fig. 3.1. A Fresnel zone plate with an outermost zone width of 70 nm was used to focus the coherent X-ray beam down to a spot size of approximately 90 nm, with a depth of focus of approximately 102 µm. The cryogenically preserved sample was placed at the focus position and was scanned in fly-scan mode for data collection [61, 64–66]. In this fly-scan mode, the fast scan was set along the horizontal (x) direction, where a piezo-scanning stage was set to move across a scan line at a constant velocity by a Delta Tau Turbo PMAC2 Ultralite VME motion control system. The control system used feedback provided by a laser interferometer system reading piezoscanning stage positions to match the

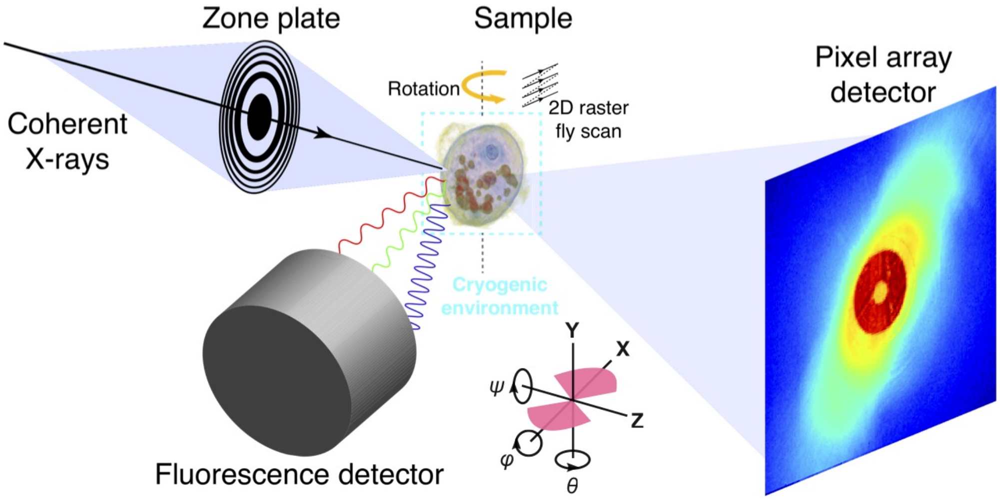

Figure 3.1: Experimental schematics for simultaneous X-ray fluorescence and ptychography measurements. A coherent monochromatic X-ray beam was focused by a Fresnel zone plate into a spot of ∼90 nm on a sample. The sample, preserved in the cryogenic environment, was raster fly-scanned in the x-y plane. During the scan, fluorescent signals and diffraction patterns were simultaneously recorded by a fluorescence detector and a pixel array detector, respectively. After finishing a 2D scan, the sample was rotated to a new angle until completing the whole 3D scan. Bottom schematic shows the orientation of 3D reconstructions with respect to experimental setup, where pink regions contain measured projection data between −6° and 56°. (*Figure reprinted from* [2])

desired position and send triggers to detectors.

As the sample was scanned, a collimated four-element (four independent detection areas) silicon drift detector (Hitachi Vortex- ME4, mounted at 90° to the incident X-ray beam) and a Dectris Pilatus 100K hybrid pixel array detector (2 m downstream of the sample) were simultaneously triggered for every 50 nm sample motion to record both the fluorescence spectra (each element of the detector records a fluorescence spectrum that consists of 2048 energy channels) and ptychographic diffraction patterns, respectively. The corresponding pixel time for each acquisition was 65 ms, including 4 ms data readout time between triggers in the Pilatus detector. A single projection scan covered a 10 µm by 10 µm field of view and took about 48 min to collect $\sim 40,000$ data points. For tomography, the sample was rotated in 2° angular spacings, so that a total of 63 projections at different angles were acquired in an angular range of $-68°$ to $56°$ over a period of 3 days, including experimental interruptions.

The X-ray flux of the focused coherent beam was of the order of 3×10^8 photons/s. For each projection, the estimated radiation dose deposited to the sample with 65-ms exposure time per 50 nm^2 pixel was about 2.1×10^7 gray (Gy). In the tomography scan consisting of 63 projections, there was 1.3×10^9 Gy in total imparted dose to the sample, except for one specific region which will be discussed below. A 1.3×10^9 Gy is above the 4.3×10^7 Gy dose at which the diffraction quality for atom-to-atom spatial correlation starts to degrade, as observed in X-ray macromolecular crystallography (42), but well below the dose $\sim 3 \times 10^{13}$ Gy, which was estimated for single metal atom detection in electron microscopy [67]. Although chemical bonds are broken, no notable mass loss or redistribution has been observed at 30- to 100-nm length scales when studying frozen-hydrated specimens at cryogenic temperatures with a dose of $\sim 10^9$ Gy [40, 68].

3D GENFIRE reconstructions of the XFM data

2D fluorescence maps (P, S, Cl, K, and Ca) were compiled from the recorded fluorescence spectra using MAPS software [69], where the spectrum from each scan pixel was fitted with modified Gaussians. For XFM tomography, the best 53 of the 63 XFM projections (10 projections were excluded due to their obvious image distortion) were manually selected from each of the five fluorescence channels (figs. S1 to S5). Hot pixels in the fluorescence images caused by readout errors were removed. Background subtraction was performed on each projection as follows. First, the image was smoothed with a Gaussian kernel, and a threshold was applied to define a region outside of the cell. This region was used to calculate a mean background, which was subsequently subtracted from each image. Since the isolated spherical features in the P channel had the highest signal-to-noise ratio, we used the center of mass method to align the P images to a common tilt axis [70]. Masks created by thresholding smoothed projection images were applied to further isolate XFM signals from the surrounding. After alignment and masking of the P channel data, we used the same parameters to align the K, Ca, S, and Cl projections to the common axis, as all XFM data were acquired simultaneously and thus shared the same set of orientation parameters.

For the P channel XFM dataset, GENFIRE reconstruction was performed using positivity and support constraints and with an oversampling ratio of 2 over 100 iterations, which constituted one GENFIRE macro iteration. After each macro iteration, one angular refinement macro iteration was performed to optimize tilt angles. In each angular refinement macro iteration, an angular search range between $-2°$ and $2°$ with $0.5°$ increments was used to optimize all three Euler angles as the reconstructed volume was back projected at different angles and compared with measured projections by cross-correlation. A total of five GENFIRE macro iterations followed by angular refinements were performed to obtain the final reconstructed 3D volume. The refined angles obtained from P XFM were then used to reconstruct the K, Ca, Cl, and S XFM and ptychography datasets using the same reconstruction parameters. The convergence of the reconstruction process was monitored by an error function, defined as the difference between the back-projected images from the reconstruction and the measured XFM projections. For more details on the implementation of GENFIRE and angular refinement, see [1].

3D GENFIRE reconstruction of the ptychography data

2D ptychographic projections were reconstructed using 200 iterations of the extended ptychographic iterative engine algorithm [30] implemented in a custom software package developed for fly-scan ptychography [64]. This algorithm used graphical processing units to speed up data processing [71]. For reconstruction, the central 256×256 pixels of each diffraction pattern were used, resulting in an image pixel of 10.2 nm. Because the X-ray monochromator was not stable at the beginning of the experiment, the reconstruction quality of the first few scans was poor. After excluding these scans and other low-quality projections, the best 47 ptychographic phase projections were used for tomographic reconstruction (fig. S6). The spatial resolution of 2D phase images was about 30 nm, estimated by Fourier shell correlation (49) on two identical scans at 0° (fig. S7). Note that since the magnitude image of each ptychographic projection was very weak due to the use of hard X-rays, we applied the phase images for the tomographic reconstruction.

The 47 phase projections were background-subtracted, aligned by the center of mass method [70], and masked and binned by two before GENFIRE reconstruction. GENFIRE was run using positivity and support constraints, with an oversampling ratio of 2 over 50 iterations, and using initial input angles obtained via angular refinement of P XFM data. Because the specimen was thinner than the depth of focus associated with both the ptychography and fluorescence images, we were able to use ptychography to produce linear, 2D projection maps of the specimens net phase shift (proportional to projected mass, as used in other demonstrations of ptychographic tomography [56]) and fluorescence to produce linear, 2D projection maps of elemental content. Thus, both imaging methods provide linear 2D projections at each rotation angle, as required for standard tomography. The GENFIRE technique then provides an improved approach to assemble and align these projection images and modalities in the Fourier domain to yield a 3D image by inverse Fourier transform. Five macro iterations of GENFIRE and angular refinement were performed to obtain the final reconstructed 3D volume. The convergence of GENFIRE was monitored by the same metric as the XFM reconstructions.

3.3 Results

3D XFM and ptychography reconstructions

Figure 3.2 (A to D) shows GENFIRE 3D XFM and ptychography phase-contrast reconstructions, respectively. The tomographic reconstructions of the elemental XFM densities indicate that P and Ca are particularly enriched within circular structures that are mainly distributed within the cytoplasm and in close proximity to the cell wall. These structures are determined to be acidocalcisomes, also known as polyphosphate bodies [72–74]. They are electron-dense organelles, with sizes ranging from 0.2 to 1 mm, that are rich in Ca and P (Fig. 3.2B). They have proton and calcium pumps and exhibit enzymatic activities in their limiting membranes [72]. North of the acidocalcisomes, S XFM volume shows the location of the pyrenoid, which is situated at the inner side of the cup-shaped chloroplast visible in the ptychography reconstruction. The pyrenoid is electron-dense and contains relatively higher S concentration than its surrounding, presumably due to the predominant composition of S-rich RuBisCO enzymes required for photosynthesis. The low S density halo surrounding the pyrenoid is indicative of the starch sheath.

The 3D Cl XFM distribution shows most Cl localized in the periphery of the alga. This extracellular Cl distribution most likely reflects that the cell was in good hydrated condition at the time of the experiment, as the cell was still surrounded by a layer of trisacetate-phosphate cell medium immediately before plunge freezing. The 3D K distribution is homogeneous throughout the entire cell, further suggesting that the cell is reasonably preserved with most K ions present in native sites. The ∼1-mm cutouts of the ptychography phase-contrast reconstruction show the pyrenoid and numerous electron-dense bodies inside the cell (Fig. 3.2C and D). Mass density calculation follows the procedures outlined

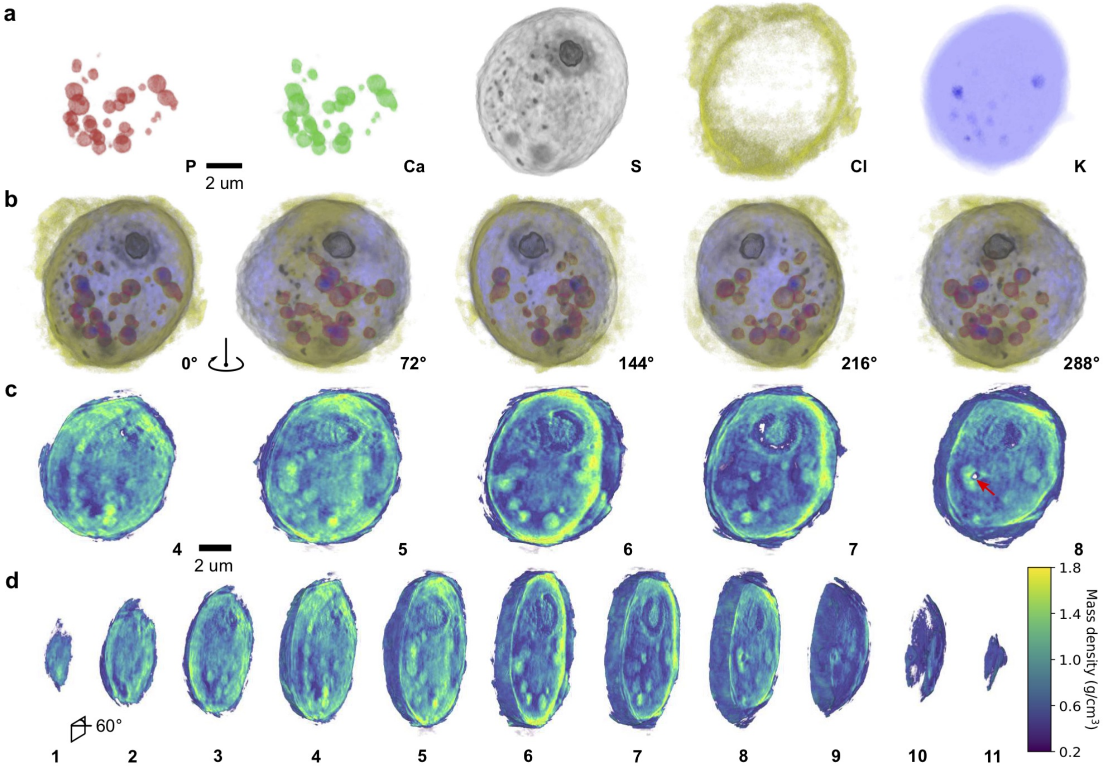

Figure 3.2: GENFIRE X-ray fluorescence and ptychographic tomography reconstructions. (**A**) 0° projection view of reconstructed 3D volumes of P (red), Ca (green), S (black), Cl (yellow), and K (blue) channels. (**B**) Projected views of the composite reconstructed XFM volume, rotated in 72° increments, showing clear localization of pyrenoid (S channel) near the top and acidocalcisomes near the bottom (P and Ca channels). (**C**) Select ∼1-µm slabs of the reconstructed ptychography volume, cut into the volume at 60° experimental projection angle, showing the pyrenoid, chloroplast, various electron-dense spherical organelles, and a damaged spot in slab 8 due to X-ray overexposure (red arrow). (**D**) Complete set of cutouts from the same ptychography volume, viewed at 60° angle. Numbers correspond to those in (**C**). The color bar is for (**C**) and (**D**). (*Figure reprinted from* [2])

in [59] and is obtained using calculated electron density derived from the phase tomography result.

During data acquisition, the focused X-ray beam dwelled on one spot of the cell for an extended amount of time at the 0° position as the shutter was unintentionally left open. This resulted in a region with abnormally high radiation exposure and consequent mass loss. This region can be seen in the eighth cutout in Fig. 3.2C (red arrow) as a $\sim$0.6 mm wide and $\sim$2.2 mm long void near the polyphosphate bodies on the left side of the cell.

Figure 3.3A shows 2-mm-thick slabs of the superimposed XFM and ptychography volumes and highlights colocalization of various organelles inside the cell. The addition of ultrastructure information from ptychography to XFM provides structural context for the fluorescent signals and helps confirm the identities and locations of acidocalcisomes and pyrenoid inside the algae. The correlated volumes also provide clues into the possible location of the nucleus in the low-density region near the center of the cell, as there is little to no fluorescent signal in that area. The high density and the absence of strong fluorescent signal near the cell edge also suggest the location of cup-shaped chloroplast.

Correlative S XFM and ptychography information helps define the cell boundary, and the two dense, dark S clusters near the bottom of the cell suggest the location of contractile vacuoles, which are known to play a role in osmoregulation and contain S-rich ion channels. Moreover, there are several small bodies, about 250 to 400 nm in diameter, with relatively high concentrations of S (see also S channel in Fig. 3.2A) that are localized to one edge of the cell. Together, they suggest the location of mitochondria, which plays a role in FeS biogenesis [75]. Figure 3.3B displays the same 2-mm-thick slabs at 60° to provide another view of the correlated volume.

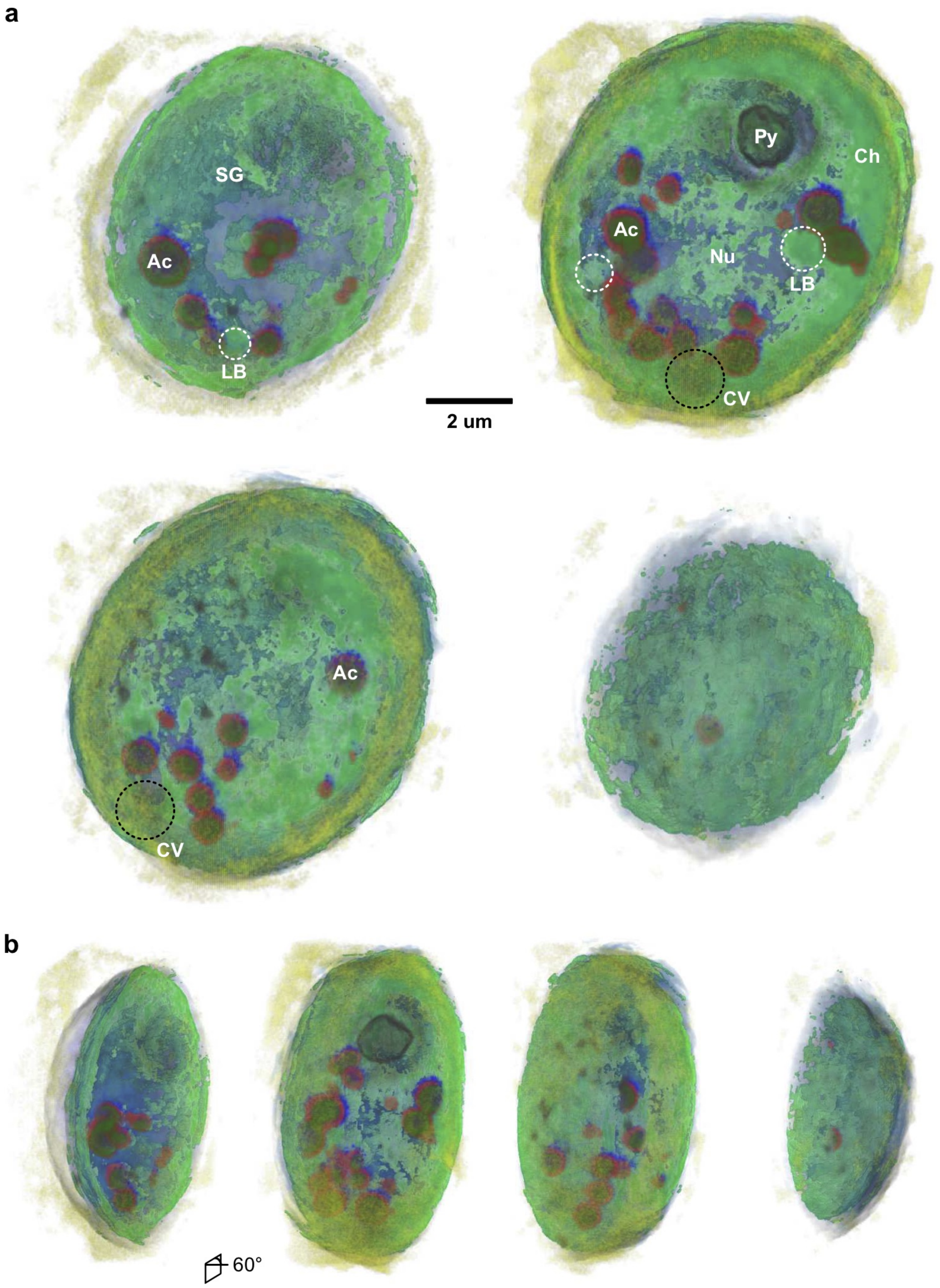
a
SG
Ac
LB
Py
Ch
Ac
Nu
LB
CV
2 um
Ac
CV
b
60°

Comparison results between GENFIRE and filtered back projection

When the number of projections is limited, due to experimental and radiation dose-related constraints, this gives rise to incomplete sampling; the missing wedge problem. Under these circumstances, GENFIRE [1, 62] produces better 3D reconstructions than other tomographic methods such as filtered back projection (FBP), equal slope tomography [76], and simultaneous iterative reconstruction technique. Figure 3.4 (A to E) shows the projections of FBP reconstruction along the missing wedge direction for ptychography, P, S, Ca, and K distributions, respectively. The corresponding GENFIRE reconstructions are shown in Fig. 3.4 (F to J). GENFIREs Fourier-based iterative approach provides a better recovery of missing data and more detailed information on cellular ultrastructure in all cases.

3D reconstruction improvement with angular refinement

Before alignment, unprocessed projection images showed noticeable out-of-plane rotation and drift from tilt axis due to the imperfect motor stage movement. Inaccuracies in projection alignment in any direction will result in lower reconstruction

---

Figure 3.3 *(preceding page)*: Superimposed X-ray fluorescence and ptychography volumes. (**A**) Two-micrometer-thick cutouts through the superimposed volumes showing spatial correlation between X-ray fluorescent signals and electron-dense organelles. P-rich (dark green) and Ca-rich (red) acidocalcisomes (Ac) can be seen, as well as starch granules (SG), pyrenoid (Py), and chloroplast (Ch). The void in the center of the cell suggests the location of low contrast nucleus (Nu). Two dark spots in the S volume (black) near the bottom of the cell (black dashed circles) suggest the locations of contractile vacuoles (CVs). Some ∼1-µm-diameter electron-dense organelles suggest the presence of lipid bodies (white dashed circles). Scale bar, 2 µm. (**B**) Same cutouts as (**A**), but displayed at 60°.

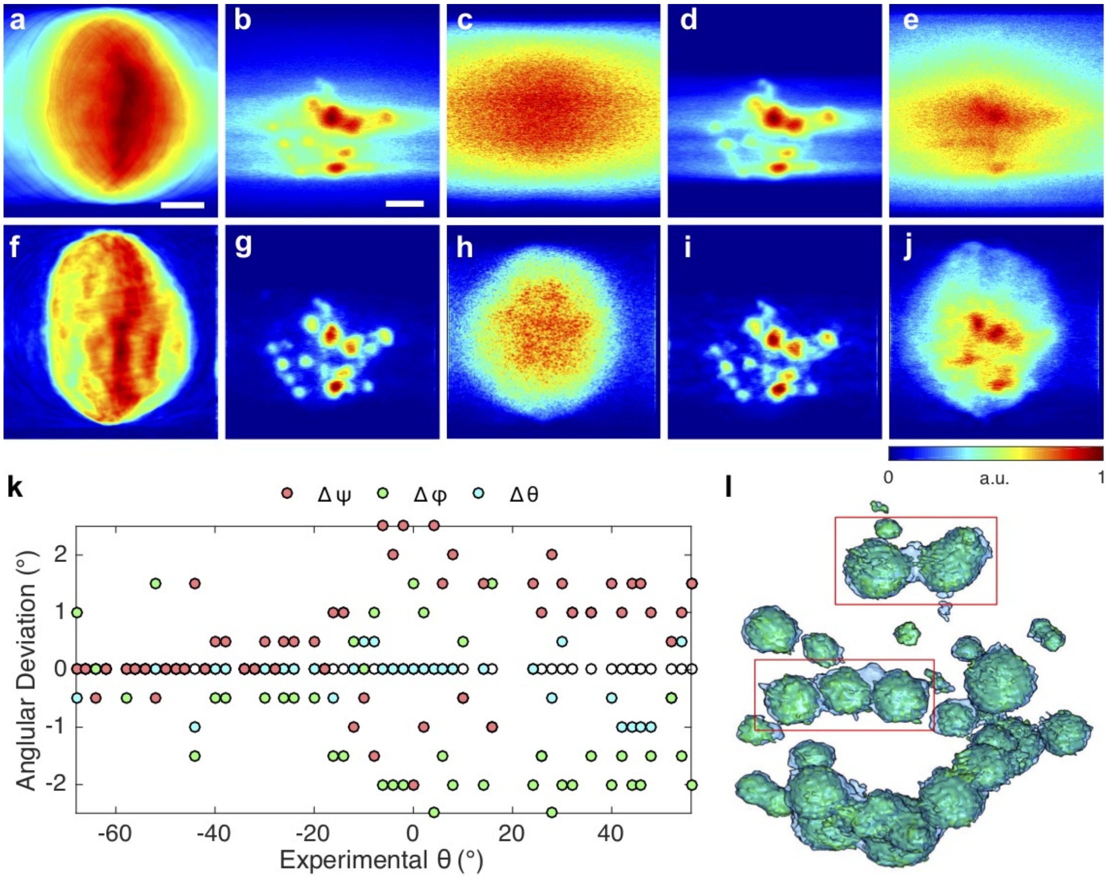

Figure 3.4: GENFIRE and FBP reconstruction comparison and angular refinement. (**A**-**E**) FBP reconstructions for ptychography phase contrast, P, S, Ca, and K channels, respectively, projected from the missing wedge direction (i.e., x direction). (**F**-**J**) GENFIRE reconstructions of the corresponding volumes shown in (**A**-**E**), projected from the same missing wedge direction, showing a much better recovery of missing information. Scale bars, 2 µm. a.u., arbitrary units. (**K**) P channel angular refinement results revealing angular deviations from the recorded tilt axes [ϕ deviation (green), $\mathit{\Psi}$ deviation (red), and θ deviation (cyan)]. To see angular orientation with respect to experimental setup, see Fig.1. (**L**) Improvements in the P channel 3D reconstruction as a result of angular refinement. Light blue and light green volumes are before and after angular refinement, respectively. Red boxes highlight volumes where angular refinement helped resolve individual acidocalcisomes better. (*Figure reprinted from* [2])

resolution. At worst, this may lead to misinterpretation of reconstruction artifacts in the cell as true cellular features. To algorithmically correct this experimental error in projection tilt angles, an angular refinement procedure was incorporated into the GENFIRE tomographic reconstruction workflow [1]. Because X-ray fluorescence and ptychography data were acquired simultaneously in this experiment, we used the P channel projections for initial angular refinement because they had the best signal-to-noise ratio and used the resulting updated angles for all other reconstructions. We found angular deviations to be between ±2° in ϕ and ψ (i.e., out-of-plane rotation) and ±1.5° along the rotation axis Fig. 3.4K. Figure 3.4L shows noticeable improvement in reconstruction quality after angular refinement. The blue and green solid volumes represent the reconstructions before and after the angular refinement, respectively. Individual polyphosphate bodies in close proximity are better differentiated and isolated after the refinement.

3D resolution estimation

We quantify the 3D resolution of the reconstructions by plotting the density variations across cellular features in three axial directions (Fig. 3.5A and C) and with 3D power spectrum analysis (Fig. 3.5B and D). Both analyses indicate a resolution of ∼125 nm along the x and y axes and ∼140 nm along the z direction for the 3D fluorescence reconstruction. The spatial resolution of fluorescence microscopy cannot exceed the Rayleigh resolution corresponding to the beam spot size (∼90 nm). The final 3D reconstruction resolution would degrade due to a low signal-to-noise ratio of the images, a limited number of projections, the missing wedge, and the tilt angle misalignment. The angular refinement feature and iterative reconstruction in GENFIRE allow us to alleviate these issues and achieve a final 3D resolution that approaches (but does not exceed) the Rayleigh resolution. The 3D ptychography reconstruction achieves a resolution of ∼45 nm along the x and y axes and ∼55 nm along the z direction, thus taking advantage of the well-known

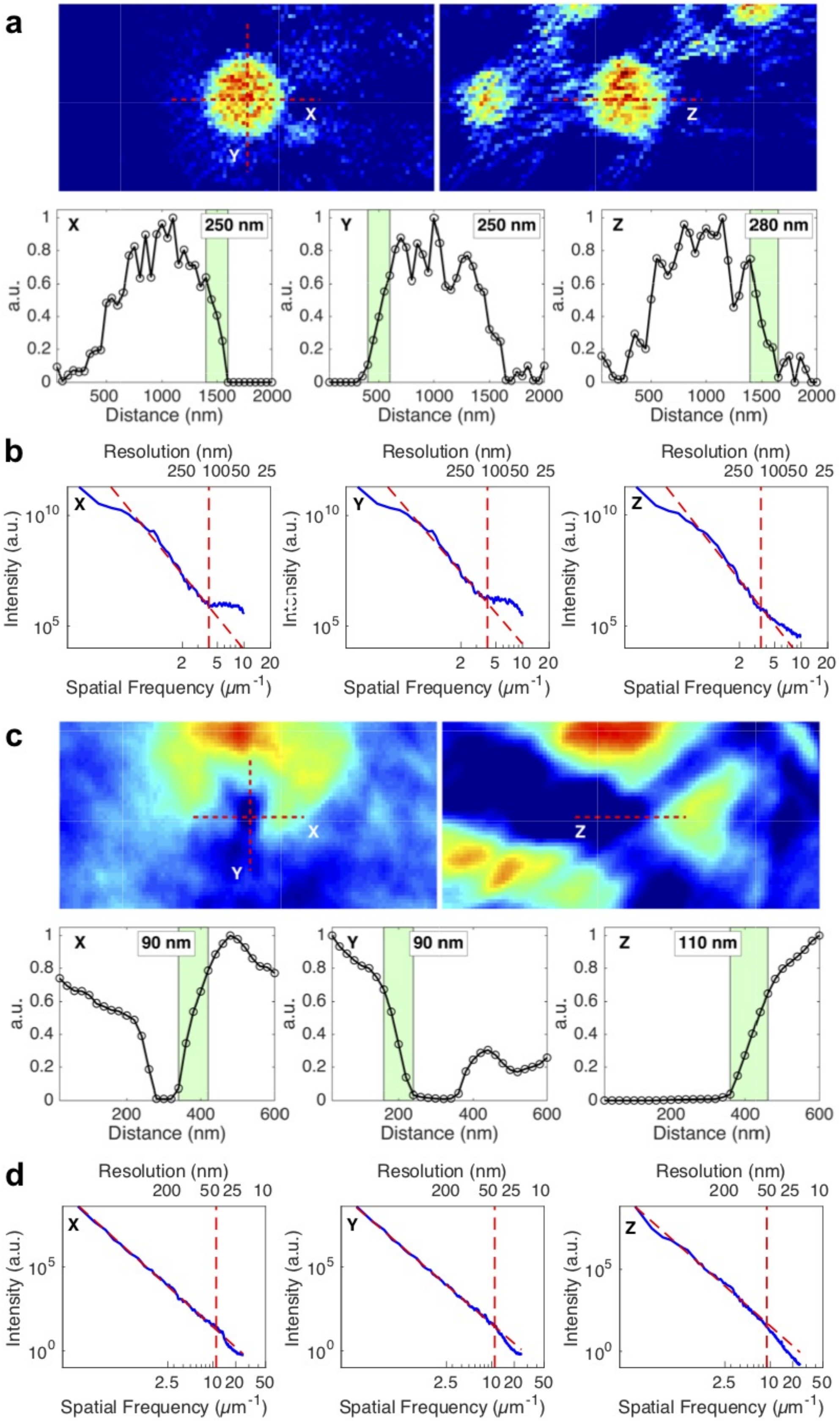
a
X
Y
Z
X
250 nm
Y
250 nm
Z
280 nm
a.u.
Distance (nm)
b
Resolution (nm)
250 100 50 25
Intensity (a.u.)
10^{10}
10^{5}
Spatial Frequency (μm^{-1})
2 5 10 20
c
X
Y
Z
X
90 nm
Y
90 nm
Z
110 nm
a.u.
Distance (nm)
d
Resolution (nm)
200 50 25 10
Intensity (a.u.)
10^{5}
10^{0}
Spatial Frequency (μm^{-1})
2.5 10 20 50

gain in resolution beyond the illumination spot size that ptychography provides. The decrease in resolution along the z direction is expected due to the limited number and angular range of projections.

3.4 Discussion

Revealing 3D cellular ultrastructure via correlative imaging without chemical labeling

Simultaneous tomography using XFM and ptychography provides complimentary information about *C. reinhardtii*. GENFIRE 3D XFM reconstructions localize and confirm the identity of various organelles based on the distribution of trace elements (Fig. 3.2A and B). In a complementary fashion, GENFIRE reconstruction of X-ray ptychography phase images produces a high-resolution 3D map of alga ultrastructure with contrast dictated by components electron densities. The

---

Figure 3.5 *(preceding page)*: Quantification of 3D reconstruction resolution. (**A**) One-pixel-thick layer of a reconstructed acidocalcisome in the P channel XFM volume along x and y (top left) and z directions (top right). Line scan profiles along the dashed lines shown in the top images gives a resolution of ∼125, ∼125, and ∼140 nm along x, y, and z directions, respectively (bottom). (**B**) 3D power spectrum analysis of XFM along three axial directions, with cutoff spatial frequency at azimuthally averaged signal deviating from the power-law relationship, showing good agreement in the resolution estimation. (**C**) One-pixel layer through the burnt hole in ptychography reconstruction in x and y (top left) and z (top right). Line scan indicates a resolution of ∼45 nm along x and y directions and ∼55 nm along the z direction. (**D**) 3D power spectrum analysis of ptychography reconstruction along three axial directions. To see angular orientation with respect to the experimental setup, see Fig. 3.1. (*Figure reprinted from* [2])

3D location of the pyrenoid, chloroplast, and various isolated dense bodies can be identified (Fig. 3.2C and D). In addition, the 3D reconstruction even localizes a small cellular volume that is affected by beam-induced radiation damage (Fig. 3.2C, red arrow). All this mapping and identification is realized without the requirement of sectioning or labeling that may compromise cell integrity and introduce unwanted artifacts into cellular structures.

When both ptychography and XFM 3D volumes are overlaid, many interesting observations can be made. First, some of the electron-dense bodies found in the ptychography volume correlate well with P and Ca XFM signals and can be confidently identified as acidocalcisomes (Fig. 3.3A); in the past, this identification usually involved different experiments using tools such as electron microscopy and X-ray microanalysis to get the structural and elemental information [72, 77]. In this work, however, both types of correlative information are acquired simultaneously.

Second, in addition to occupying the cell interior, K XFM volume also exhibits higher concentrations in some distinct regions that correlate well with acidocalcisomes in the cytosol (Fig. 3.3A). This suggests that each acidocalcisome may be in a different biochemical state and that surface ionic pumps could be undergoing K exchange with the cytosolic environment. As the resolution of this correlative 3D imaging technique continues to improve in the future, it will be able to provide even finer detailed elemental and chemical analysis into the complex biochemical activities of individual organelles in their native cellular states.

Third, S XFM volume not only delineates the cell boundary but also labels the location of the pyrenoid. In addition, some small S clusters suggest potential locations of mitochondria, and two faint S clusters near the bottom of the cell point to the possible locations of the contractile vacuoles, which contain S-rich H+-pyrophosphatase and vacuolar adenosine triphosphatase enzymes [78] and are involved in osmoregulation. Ultrastructure information from contractile vacuoles may not show up in ptychography due to their relatively homogeneous density compare to their surroundings; however, through S X-ray fluorescence, the locations of those organelles with respect to the cell can be visualized. This important complementary advantage between ptychography and XFM will provide researchers with even more insights into complex structural biology than either method can do alone.

Last, the white dashed circles in Fig. 3.3A highlights some regions of the ptychography volume that appears to be electron-dense bodies but do not contain Ca or P, suggesting that they are different organelles. This unexpected finding, along with the organelles size, location, and visibility in ptychography volume, led us to believe that at least some of those bodies are algal lipid bodies. The size of those dense bodies ranges from 0.5 to 1 mm in diameter and are localized near the chloroplast [79], which agree well with the properties of lipid bodies in literature. Also, since lipid bodies are known to have good contrast in X-ray [24,34,80,81], they are expected to be visible in ptychography volume. This ability to confirm the identities of individual organelles in 3D ptychography using XFM rather than relying on mass density thresholding, as demonstrated in previous X-ray 3D imaging works on *C. reinhardtii* [58, 59], highlights the power of this correlative microscopy tool for studying complex biological structures.

Optimizing 3D reconstruction with GENFIRE angular refinement

The GENFIRE algorithm was used to produce high-quality 3D XFM and ptychography reconstructions from a limited number of 2D projections. GENFIREs angular refinement feature allows us to overcome errors in the recorded rotation angles due to imperfections in the rotation stage, resulting in higher quality reconstructions. Angular refinement can be thought of as a way to provide information on the experimental setups overall stability. Our angular refinement result shows small q deviations from recorded angles in the negative rotational angles (Fig.

3.4K), which increased noticeably as the stage tilted into the positive angular range. This suggests that the stage stability differed between the positive and negative angles during the 3-day data acquisition period. This type of diagnostic information could help devise better tomographic data collection schemes in the future to ensure that the highest quality data can be obtained.

Simultaneous data collection streamlines data processing

In addition to considerably shortening the data collection time, the correlative microscopy method demonstrated here can also shorten postprocessing workflow and prevent additional sources of reconstruction errors. Since all data are acquired simultaneously, the computational projection image alignment procedure performed on one dataset can be applied to the rest. This is helpful for aligning XFM datasets, where object boundary in some channels is not always defined. Likewise, image segmentation parameters obtained from separating the object from background in one dataset can be shared with all others. Efficient post-processing workflow, such as those mentioned above, is especially important for correlative tomography reconstructions, where multiple tomograms with different information content need to be processed efficiently and consistently to obtain results in a timely manner.

In this work, we demonstrate an application of 3D correlative microscopy by combining GENFIRE with X-ray ptychography and XFM tomography to image a whole frozen-hydrated *C. reinhardtii* in 3D. XFM provides trace element distributions of various organelles within the alga, and they are coupled with ptychography to reveal complex ultrastructure information. This simultaneous data acquisition process streamlines the experiment and saves researchers considerable amount of time in sample transfer between different instruments and in searching for the exact specimen on the sample substrate to do correlative imaging. It reduces the total radiation dose accumulated on the sample from the sequential imaging approach and alleviates damage from exposing the sample to different imaging conditions. Furthermore, we also demonstrate GENFIREs superior 3D reconstruction capability when dealing with limited number of projections. This presents yet another avenue to reduce the amount of tomographic data necessary to achieve high-quality 3D reconstructions and can further minimize radiation damage imparted on the sample.

One of the limitations of this initial demonstration is the very long time period used to collect the data. There are a number of speedups that we plan on using in the future. First, scan trajectories with better photon utilization will be used. The fly-scan scheme used in this experiment only implemented continuous motion along one scan axis, while the other axis was still in step-scan mode. By applying continuous motion throughout the whole projection scan [82] or even the whole 3D scan (e.g., spiral tomography [83]), the scan time can be reduced by avoiding the overhead between scan lines. For instance, in this experiment, the overhead was about 5 min for one 2D projection scan. Second, a double-multilayer monochromator with a spectral bandwidth of 10^{-2} delivers $\sim$20 times more flux than the DCM source used in the present measurement, which can speed up this correlative 3D measurement. This improvement will be significant as the APS is upgraded, which will provide at least 100 times more coherent flux. Last, using the dose fractionation theorem [84], the total photons for a 3D measurement can be divided into many tilt angles, so each 2D projection will be acquired rapidly with high-throughput detectors. This means that more angular projections can be obtained to achieve higher quality 3D reconstruction while reducing the missing wedge effect.

Another limitation of this method concerns imaging large specimens such as thick whole mammalian cells, which may introduce depth of focus problems when acquiring tomography projection data. To scale up and generalize the range of applications achievable by ptychography, additional techniques have been developed, such as multislice ptychography [85, 86], which allows ptychography to go beyond the depth of focus limits and image thick biological specimens with high resolution in 3D [87, 88]. A detailed discussion of the thickness limits of X-ray microscopy and its relationship to electron microscopy of biological specimens is available [89]. Moreover, ongoing efforts in synchrotron source upgrades and faster and larger data handling will decrease data acquisition time and allow scientists to scale up the type and size of biological specimen they can image using ptychography.

With the improvements described above, we believe that the combination of X-ray ptychography for structural information, X-ray fluorescence for trace element information, and GENFIRE for synthesizing 2D data into 3D will become an important microscopy tool in structural biology. By combining with new developments in dosereduced imaging, this technique will allow researchers to image whole, unsectioned eukaryotic cells and elucidate each components elemental compositions, all the while preserving structural integrity. As this tool continues to develop, we envision that it can find a nice niche between fluorescence light microscopy, where selective intracellular components and macroscopic intercellular phenomena are imaged in lower resolution, and cryo-electron microscopy, where fine internal ultrastructure of thinned subregions is imaged in higher resolution. This will open the door to study a myriad of biological problems where high-resolution elemental identification and complex internal structure information are required in 3D.

CHAPTER 4

Multimodal X-ray and electron microscopy of the Allende meteorite

4.1 Introduction

X-ray and electron microscopies visualize structure and function in organic and inorganic systems over spatial scales that range from tens of micrometers all the way down to the atomic scale. Recent advances in X-ray ptychography [11, 12, 90, 91], which is a powerful coherent diffractive imaging (CDI) method [10], have extended soft X-ray imaging toward 5-nm spatial resolution [92, 93]. Ptychographic X-ray CDI has also demonstrated the ability to image extended integrated circuits [94, 95] and biological structures [5, 54–56, 61] in two dimensions (2D) and three dimensions (3D), with sub20-nm spatial resolution. Scanning transmission X-ray microscopy (STXM) with X-ray absorption spectroscopy (XAS) can map bulk specimens with 20-nm resolution; when performed in the soft X-ray regime, STXM can simultaneously extract chemical-specific maps of carbon, nitrogen, oxygen, and transition metals such as iron, manganese, and nickel [96] for materials and biochemically relevant samples.

Exciting developments in electron microscopy, such as the introduction of cryogenic preservation of biological specimens at near-native conditions in thin amorphous ice films, as well as the introduction of aberration-corrected electron microscopes, have ushered in a new era of cryoelectron microscopy [97, 98] and atomic electron tomography [62, 70, 99, 100], thus enabling unprecedented imaging of materials and the associated structure-function relationships at a fundamental level.

Despite all the advancements, to date, no single imaging technique can provide a full comprehensive map of a samplethe limitations of each method dictate specific sample requirements, sizes, and the type of information that can be extracted. For instance, while electron microscopy offers unmatched atomic resolution, so far this method is only applicable to very thin samples owing to multiple scattering effects [97, 99]. In contrast, because of the high penetration ability of short wavelengths, X-ray microscopy can probe samples that are tens to hundreds of micrometers thick and, in addition, has substantially less stringent sample requirements than electron microscopy [11, 101]. However, the spatial resolution of 3D X-ray microscopy is currently below its theoretical limit due to technical challenges in achieving high coherent X-ray flux at synchrotron radiation facilities. Therefore, correlated electron and X-ray microscopies that take advantage of different contrast mechanisms can provide more comprehensive maps of a sample to solve challenging scientific problems.

Multimodal imaging has been implemented very successfully by the light microscopy [102, 103] and medical imaging communities [104–106]. In the case of X-ray and electron microscopies, multimodal imaging offers complementary advantages: high spatial resolution across multiple length scales, with ensemble elemental abundances and local atomic and chemical information. Combining these methods also offers potential strategies for alleviating sample radiation damageX-rays have a higher sample damage threshold than electrons in inelastic scattering experiments,while electrons are more dose efficient than X-rays in elastic scattering experiments [107]. Correlative imaging can also provide multifaceted experimental maps to guide computational modeling, thereby promoting rapid discovery and deployment of new materials to tackle scientific questions that would otherwise be too difficult to address [108]. These challenges strongly motivate a new paradigm shift toward multimodal imaging that combines advanced X-ray and electron microscopies for studying the same specimen and take advantage of recent advances in sample preparation, imaging instrumentation, and synchrotron coherent radiation flux.

In this work, we investigate an Allende meteorite grain using X-ray ptychography and STXM in 2D, combined with energy-dispersive spectroscopy (EDS) and high-angle annular dark-field (HAADF) imaging in 3D. The Allende meteorite is a CV3 carbonaceous chondrite that was an observed fall in Mexico on 8 February 1969. Allende was well studied at the time because of laboratory facilities being prepared to receive lunar samples from the Apollo program. Allende consists of larger chondrules and calcium-aluminumrich inclusions set in a fine-grained matrix of micrometer- to submicrometer-sized silicates, oxides, sulfides, and metals. The highly heterogeneous phase assemblage and various nanoscale petrographical characteristics are ideal for demonstrating the advantages of multimodal X-ray and electron microscopy techniques.

As tomography is rapidly being adopted by the planetary science community, previous works have demonstrated 3D microscopy on Allende [109, 110]. In this study, we significantly enhance the spatial resolution achieved thus far [111] to infer the mineral composition and discuss potential processes that occurred before or after accretion. Our imaging results reveal many small internal textures and channels that strongly suggest shock veins and melt aggregates, while our spectroscopic measurements constrain the classifications of major meteoric components to silicates, sulfides, and oxides. This multidimensional study of the Allende meteorite provides possible hints into the origins and transport of refractory phases within the early solar nebula and highlights the potential of combined X-ray and electron imaging for studying heterogeneous materials.

4.2 Methods

Sample preparation

Unsorted Allende meteorite fragments were placed in an agate mortar and immersed in ethanol and then gently pounded by an agate pestle into small grains of submicrometer thickness so that both soft X-rays and electrons can penetrate the sample. The resulting ethanol suspension was sonicated for 2 min for further dispersion. The supernatant solution was dropped using a pipette onto a carbon film on 200 mesh copper transmission electron microscopy (TEM) grids and air-dried on the grids for 24 hours before data acquisition.

STXM and ptychography data acquisition

STXM and X-ray ptychography data were recorded at beamline 7.0.1 in the Advanced Light Source (ALS) [92, 93] — the Coherent Scattering and Microscopy (COSMIC) beamline — at the Lawrence Berkeley National Laboratory (LBNL). COSMIC provides monochromatic soft X-rays with energies ranging from 250 to 2500 eV, spanning the carbon and sulfur K-edges, and is optimized for spectromicroscopy of elements commonly found in mineral samples, including Fe, Ni, Mg, and Al. X-rays were focused using a Fresnel zone plate with a 45-nm outer zone width to give a total coherent flux of approximately 10^9 photons/s at the sample position. The sample substrate TEM grid was mounted onto a standard FEI CompuStage sample manipulator derived from an FEI CM200 series TEM and secured with a Hummingbird 3-mm half-grid tip. The use of a TEM-compatible sample holder was a crucial enabling technology that permitted seamless sample transfer between the X-ray and electron microscopes. Other commercially available TEM sample holders designed for tomography, cryo-tomography, and in situ experiments can also fit into the chamber environment.Once mounted, the sample chamber was pumped down to 1×10^{-6} torr. Diffraction data were recorded with a fast charge-coupled device camera developed by LBNL with the following specifications: 50 frames/s, 15-bit dynamic range with a 12-bit analog-to-digital converter, and 1 megapixel. Images were acquired without a beamstop.

STXM data were recorded with 10-ms dwell time using an 80 ×80 square scan grid that proceeded with 40-nm steps to cover a 3.2×3.2-mm field of view. XAS data can be collected using either point spectra at a single location, a line scan along a direction, or an image stack over a sequence of photon energies. We first performed a line energy scan to determine the correct absorption edge for the elements and then collected image stacks with energies varying across the absorption edge. Complete STXM-XAS image stacks using the above parameters were recorded at the Fe L_3-edge (707 eV), Ni $L_{2/3}$-edge (865/848 eV), Mg K-edge (1302 eV), and Al K-edge (1551 eV). Energy scan steps increased with 1-eV steps from 15 eV below the edge, then changed to 0.25-eV steps within ±5 eV of absorption resonance, followed by 1-eV steps to 15 eV above the edge. STXM energy stacks of each element took 30 to 60 min to record.

Ptychography data were recorded using double-exposure mode with 15/150-ms dwell times to enhance dynamic range and scanned in an 80×80 square grid with 35-nm steps to cover a 2.8×2.8-mm field of view. The resulting pixel size was 8 nm/pixel. Each ptychography image comprised 6400 diffraction patterns of 128×128 pixels. The total dose (D_p) deposited on the meteorite grain was estimated as $D_p = \left(\frac{P_t}{A}\right)\left(\frac{\mu}{\rho}\right)E$, where the fluence ($P_t/A$) for 100-ms exposure is 6.46×10^{10} photons/mm^2, μ is the linear absorption coefficient, ρ is the average density of minerals, and μ/ρ was estimated to be 10 cm^2 g^{-1} with the average photon energy (E) at 1100 eV. The dose per projection was estimated to be 1.1×10^7 gray, which was within the tolerable dose for imaging at the resolution presented in this work [112]. To compare absorption contrast differences for each element, ptychography images at both 5 eV below and directly on resonance were collected at the Fe L_3-edge, Ni $L_{2/3}$-edge, Mg K-edge, and Al K-edge. Phase retrieval of complex images was initially performed at COSMIC using the distributed graphics processing unit (GPU) based ptychographic solver SHARP [113]. To further improve reconstruction quality and to remove artifacts due to the rectilinear scanning grid, final ptychographic images presented in our results were refined using a parallel ptychography reconstruction algorithm [114, 115], with an update condition derived from the hybrid projection-reflection algorithm [116–119]. Each reconstruction ran for 5000 iterations, where the probe was updated continuously after the fifth iteration.

HAADF and EDS data acquisition

Electron tomography data were collected at the National Center for Electron Microscopy. For TEM experiments, a Titan 60-300 equipped with a HAADF detector (Gatan, Pleasanton,CA) and four windowless silicon drift EDS detectors (FEI Super-X) were used with a solid angle of 0.7 srad. The microscope operated in scanning transmission electron microscopy (STEM) mode at 200 kV with an electron beam current of ∼550 pA for STEM-EDS maps and ∼40 pA for HAADF-STEM imaging. A typical total dose for the complete tomography series was ∼1300 $e^-/Å^2$, and a typical total dose for an EDS map was ∼1100 $e^-/Å^2$. EDS data were collected as a tilt series of scanned spectrum images, which measured emitted X-rays from regions probed by the electron beam. The images were drift-corrected over ∼120 s, assuming a time-dependent linear drift model at different tilt angles.

HAADF-STEM scans and probes local structural information by collecting electrons scattered onto the HAADF detector. All tilt series of projection images were typically acquired between −64° and 72°,with a linear tilt step of 2°. The tilt range was limited by the shadowing of the sample holder (Hummingbird, Lacey, WA). HAADF-STEM images were acquired with a convergence semi-angle of 10 mrad at a detector inner semi-angle of 63 mrad and outer semi-angle of 305 mrad.

Image size was 1024×1024 pixels with a pixel size of 4.67 nm. Each projection image was binned by 3 to have a pixel size of 14.01 nm. We carefully checked the integrity of the samples before and after taking tomographic tilt series using zero-degree projections and before and after EDS mapping. We observed no visible sample damage.

HAADF, EDS, and XAS data analysis

Tomography reconstruction was performed using the GENeralized Fourier Iterative REconstruction (GENFIRE) algorithm [1]. Before reconstruction, elemental tilt series of C, O, Mg, Al, Si, S, Cr, Fe, and Ni were extracted from the EDS spectra using Pythons HyperSpy package [120] for multidimensional data analysis. HAADF and EDS projections were aligned to a common tilt axis using the center of mass and common line methods [70]. The background was subtracted from each projection by removing the average value in an empty region of the sample, and the process was optimized by minimizing the differences between common lines. Next, projections were normalized to have the same total sum, as the integrated 3D density of the sample should be constant. Each GENFIRE reconstruction ran for 100 iterations, using an oversampling ratio of 2 and a 0.7-pixel interpolation distance, and with positivity and support constraints enforced.

Elemental abundances in the meteorite grain were estimated from the zero-degree EDS image using HyperSpy. The spectral data were a 3D array, where x and y axes corresponded to probe positions and the z axis corresponded to the energy of detected X-rays. Non-negative matrix factorization was used to decompose data dimensionality and segment regions based on spectral similarities. Net X-ray intensities were obtained in HyperSpy by sampling and integrating the background-subtracted spectrum peaks at the elements of interest. To obtain quantitative elemental compositions at subregions of the grain, mass fractions were quantified using the Cliff-Lorimer equation [121], $\frac{I_1}{I_2} = k^*_{12}\frac{C_1}{C_2}$, where

I_i and C_i are the integrated peak intensities and mass fractions of the ith element, respectively, and k^*_{12} is the thickness-corrected Cliff-Lorimer sensitivity factor (k-factor) between elements 1 and 2. For more than two species, the formula becomes $\Sigma_{i=1,2,3...} C_i = 1$. The default k-factors were provided by EDS system manufacturer Bruker software and account for detector sensitivity to different elements dispersed X-rays. Thickness correction was applied to the vendor-supplied k-factors to obtain k^*_{12} [122], which accounts for non-negligible absorption and fluorescence effects in the thick sample, and was calculated using the average grain thicknesses estimated from EDS tomography results.

Local chemical information in the meteorite was provided by STXM-XAS analysis using the MANTiS software [123]. A series of STXM transmission images recorded at different incident X-ray energies spanning different atomic resonances were first converted to optical densities using fully transmitting regions in the specimen. Hot pixels were replaced by the average value in the surrounding pixels, and the background was subtracted. The image stack was then aligned iteratively using the center of mass and common line alignment methods. Next, spectra in the 3D image stack were decomposed using principal components analysis (PCA) and k-means clustering to group spectra with similar spectral signatures. Last, singular value decomposition without reference spectra was used to produce chemical maps and their corresponding absorption spectra.

Ptychography data analysis with SQUARREL

To derive quantitative elemental information from the complex (amplitude and phase) ptychography images, here, we introduced a new semi-quantitative analysis method in X-ray ptychography, named Scattering QUotient Analysis to REtrieve the Ratio of ELements (SQUARREL). In this method, the complex ptychographic images are used to calculate the scattering quotient map (f_q) [124–126], which is defined as

$$f_q \equiv \frac{\ln(|T(x,y;E)|)}{\phi(x,y;E)} = \frac{\Sigma_i N_i(x,y;E)\beta_i(E)}{\Sigma_i N_i(x,y;E)\delta_i(E)} = \frac{\Sigma_i N_i(x,y;E) f_{Ii}(E)}{\Sigma_i N_i(x,y;E) f_{Ri}(E)} \cdot |T(x,y;E)| \tag{4.1}$$

and $\phi(x,y;E)$ are the transmission magnitude image $(0 \leq |T| \leq 1)$ and the phase retardation image $(\phi \leq 0)$ of the complex transmission function, or $T(x,y;E) = |T(x,y;E)|\exp[i\phi(x,y;E)]$, that was acquired by ptychography at an X-ray photon energy (E). N_i is the atomic number density of the ith element in the sample. β and δ are the imaginary and real part of the complex refractive index (n) decrement, respectively. f_{Ii} and f_{Ri} are the imaginary and real part of complex atomic scattering factors, respectively, where $n = 1 - \delta + i\beta \propto (1 - f_{Ri} + if_{Ii})$. Note that the complex atomic scattering factors are averaged values along the projection through the sample and $f_q \leq 0$.

The scattering quotient is, in principle, independent of sample thickness variation since the thickness has been canceled out in the quotient [126, 127]. As a result, the scattering quotient is especially suitable for studying inhomogeneous specimens where conventional analysis methods cannot distinguish thickness variations from changes in refractive indices of different compositions, since both thickness and composition variations contribute to changes in light absorption and phase retardation. The scattering quotient map images have been used as a previously unidentified contrast mechanism in materials [128–130] and as an image segmentation and classification method for biological samples [126, 127]. The key idea to SQUARREL is to convert a scattering quotient map to a two-element ratio map, $R_a = R_a(f_q; E)$, given a fixed amount of a third element as a priori knowledge. The two-element ratio conversion function (R_a) is derived by a direct comparison to a theoretical calculation, which is based on the tabulated complex refractive indices from The Center for X-Ray Optics (CXRO) or National Institute of Standards and Technology (NIST) Standard Reference Database [131] of the mixture in atomic %.

For example, given a priori knowledge of a possible compound or a mixture $Z(Z = X_pY_qV_r)$ with X, Y, V elements and with p, q, r atoms, the conversion function can be calculated to provide a two-element ratio, e.g. a q-to-p ratio at a given r. The mixtures atomic number density reads $N_Z = N_{AV}(p\rho_X + q\rho_Y + r\rho_V)/(pM_X + qM_Y + rM_V)$, where N_{AV} is the Avogadro constant, $\rho_{X,Y,V}$ are the individual constituents mass number density, and $M_{X,Y,V}$ are the individual constituents atomic mass number.We can then get the individual constituents atomic number density, $N_X = pN_Z$, $N_Y = qN_Z$, $N_V = rN_Z$, to finish the theoretical scattering quotient calculation of the mixture Z. After choosing an appropriate X-ray photon energy (E), i.e., a horizontal line out from fig. S15, the two-element conversion function, $R_a(E)$, behaves as a smooth and monotonic function, which correlates f_q and R_a. Therefore, we can convert scattering quotient maps into two-element ratio maps.

4.3 Results

HAADF and EDS tomography

Figure 4.1 shows the schematics of the multimodal electron and X-ray spectral imaging setup, where HAADF and EDS tomography were performed on the same Allende meteorite grain deposited on a carbon-coated TEM grid and then later transported to the COSMIC beamline for X-ray imaging. Slices through the GENFIRE HAADF reconstruction of the grain showed various internal morphologies that revealed different phase assemblages (Fig. 4.2A and fig. S1). The reconstruction spatial resolution was estimated to be approximately 15 nm using the 10 to 90% knife edge method (fig. S13A). In the larger meteorite matrix, we observed long internal channels, 20 to 50 nm in diameter, that were suggestive of shock veins (Fig. 4.2A, green arrow). Adjacent to the matrix were two high-intensity spherical granules that are representative of melt pockets (Fig. 4.2A, red and teal

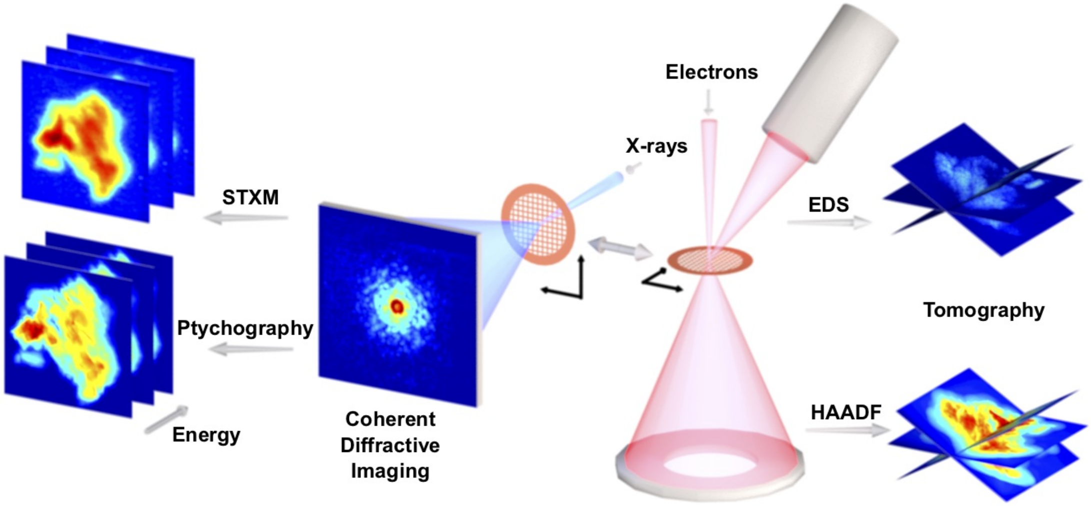

Figure 4.1: Multimodal X-ray and electron nanoscopic spectral imaging scheme. Allende meteorite grains deposited on a TEM grid were transferred between a Titan60-300 electron microscope and the COSMIC soft X-ray beamline for tomographic, ptychographic, and spectromicroscopic imaging. COSMICs TEM-compatible sample holder enabled the same meteorite grain to be imaged using both imaging modalities to extract multidimensional datasets, providing chemical, structural, and functional insights with high spatial resolution. (*Figure reprinted from* [3])

arrows).

Next, we determined the grains elemental compositions using EDS tomography to understand the textural differences between various regions. EDS signal indicated the presence of C, O, Mg, Al, Si, S, Cr, Fe, and Ni in the grain (Fig. 4.2B and figs. S2 to S10 and S14). The superimposed EDS and HAADF GENFIRE reconstructions revealed three main mineral domains: (i) iron-magnesium silicate (Fig. 4.2B, purple and teal), (ii) aluminum-chromium iron oxide (Fig. 4.2B, yellow), and (iii) iron-nickel sulfide (Fig. 4.2B, red). Note that the gradual transition between Fe and Mg contents at different depths in the iron-magnesium silicate can be seen in 3D.

To quantify elemental abundances, we applied the Cliff-Lorimer ratio method [122] on the integrated peak intensities to obtain the elements relative concentrations (Methods; fig. S14). On average, the iron-magnesium silicate was 13% Fe, 18% Mg, 49% O, and 20% Si; the aluminum-chromium iron oxide was 25% Al, 29% C, 5% Cr, 4% Fe, and 37% O; and the iron-nickel sulfide was 28% Fe, 22% Ni, and 50% S. Note that the buildup of C contamination on the sample during data acquisition contributed to the high C composition in the analysis, which should normally be approximately 1%. The elevated C composition could also be attributed to the large variation in absorption as the sample tilts relative to the EDS detector, which could be especially pronounced for elements with large mass absorption coefficients such as C. As the sample was tilted to different angles, the heterogeneity in the sample might cause huge point-to-point variations in absorption,which could artificially elevate the apparent C abundance.

On the basis of elemental quantification, the large mass of iron-magnesium silicate is likely olivine, pyroxene, or serpentines, all of which are high temperature primitive nebular condensates commonly found in carbonaceous chondrites and interplanetary dust particles. The oxides and metal sulfides adjacent to the host rock typically condense over a similar range of temperatures. Together with the sil-

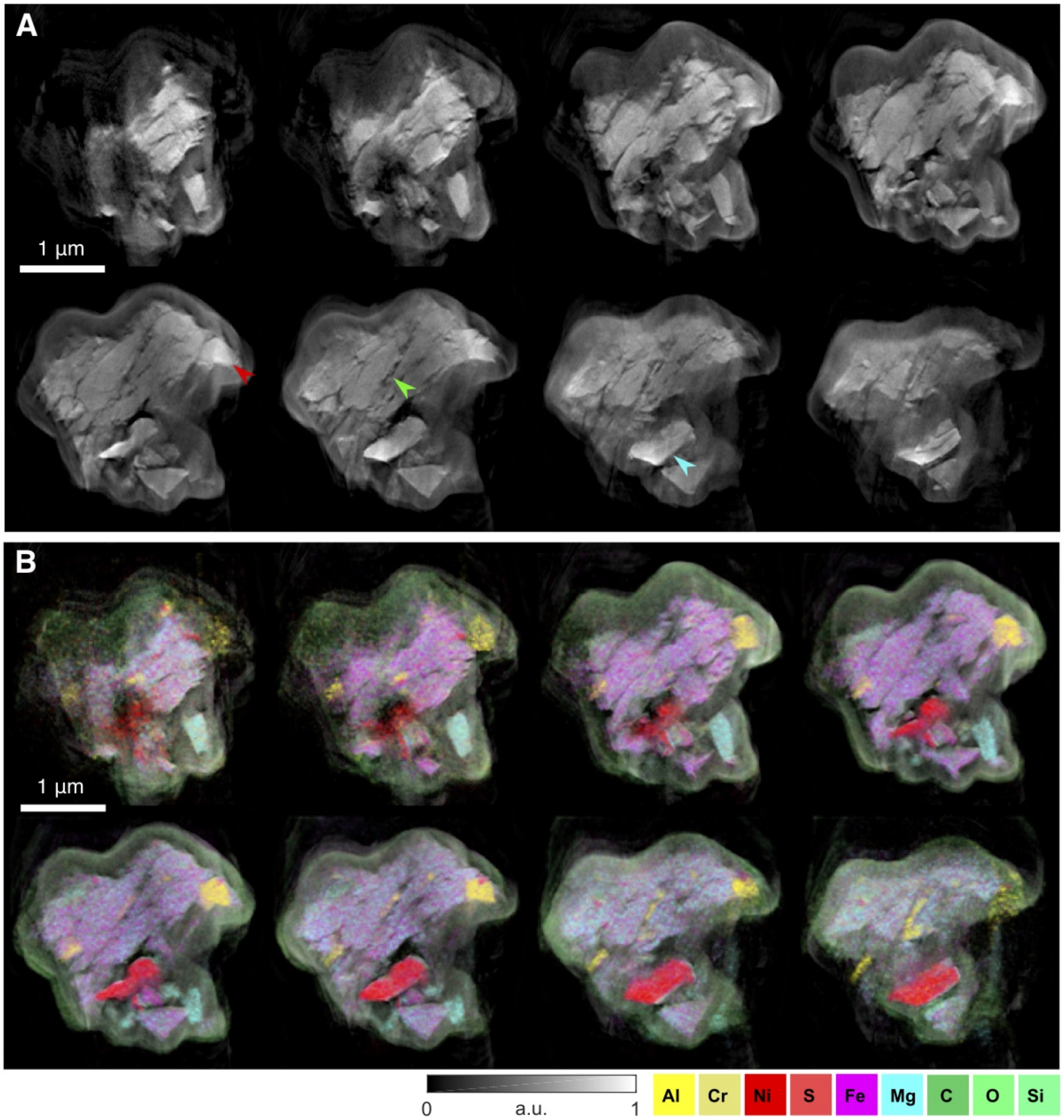

Figure 4.2: HAADF and EDS GENFIRE tomography reconstructions. Representative 14-nm-thick layers in the reconstructed 3D HAADF (**A**) and EDS (**B**) volumes of the Allende meteorite grain. The red arrow points to melt pockets, and the green arrow points to shock veins that were embedded, which suggest that the sample had at some point experienced impact-induced heating, cracking, and melting. The traces of aluminum and chromium in the veins that are visible in the EDS reconstructions reveal that the veins were filled with metallic recrystallization. a.u., arbitrary units. (*Figure reprinted from* [3])

icates, the proximity of these three mineral phases confirms the high-temperature nebular environment of the grains accreted components [132].

Ptychography and STXM-XAS

To complement the electron microscopy results, we used differential X-ray absorption contrast to study elemental locations and abundances in more detail. We collected 2D ptychography images of the grain on and below the core level absorption resonance energies for Al, Fe, Mg, and Ni, the four major elements in the grain (fig. S11). The spatial resolution was estimated to be approximately 20 nm using the 10 to 90% knife edge method (fig. S13B). By dividing the on-edge and pre-edge absorption images of each element, we can pinpoint the locations of each element with high contrast and spatial resolution (Fig. 4.3A to D).

In general, the spatial distributions of the four elements agreed well with those observed in the EDS data. However, upon closer inspection, we observed regions with higher Fe concentration in the silicate that coincided with the Al melt pockets and veins (Fig. 4.3A and B, red arrows). While the Al melts were visible in EDS tomography, the colocation of Fe in the same melts was difficult to detect in EDS. This is because the overall Fe contrast in the melts was lowered by being embedded in the large iron silicate. Although EDS did not have sufficient contrast or resolution to discern the presence of Fe in the vein, X-ray absorption at the Fe L-edge was able to provide enough sensitivity to detect these fine chemical differences. The Mg absorption difference image did not show the presence of Mg in the same melts (Fig. 4.3C, red arrows), as evidenced by the large gaps where the melts should be, which suggests that Mg might not have melted under high temperature.

In addition to providing sensitive chemical localization in the grain, complex ptychography images can also be used to quantitatively estimate elemental compositions by our newly developed SQUARREL method. As a proof-of-principle demonstration, we quantified the Ni and Fe content in the iron-nickel sulfide region, consistent with pentlandite $[(\mathrm{Fe_Ni})_9\mathrm{S}_8]$ [133]. The empirical compound formula of the sulfide is $\mathrm{Fe_pNi_qS_{0.89}}$, where $p+q=1$.We first calculated scattering quotients of the logarithmic transmission magnitude and the phase retardation images from the ptychographic images as shown in fig. S11. To apply SQUARREL, we then calculated the theoretical complex refractive indices of the iron-nickel sulfide.

The calculated sum $(\Sigma_i N_i \delta_i)$ of the atomic number density (N_i) and real decrement part (δ_i) of the complex refractive indices of $\mathrm{Fe_pNi\ L_qS_{0.89}}$ are shown in fig. S15A. Similarly, the calculated sum $(\Sigma_i N_i \beta_i)$ of the atomic number density and imaginary decrement part (β_i) of the complex refractive indices are shown in fig. S15B. Both sums are normalized to N_{AV} for convenience. The calculated scattering quotient f_q (fig. S15C) is simply the quotient of fig. S15 (A and B). We can then convert a scattering quotient to a two-element, q-to-p, ratio, which is the key of SQUARREL. In principle, any horizontal line out from fig. S15C can be used as a conversion function. However, practically speaking, a monotonic and smooth function far from resonance, i.e., elemental absorption edges, works much better since it is less prone to noise or other uncertainties. As such, one should avoid choosing an X-ray spectral range adjacent to an elemental absorption energy; i.e., no resonant absorption is needed in the SQUARREL method. Furthermore, choosing a range with a monotonic function assures that the conversion is unique.

Figure 4.3 shows two scattering quotient maps for Mg pre-edge (Fig. 4.3E) and Al pre-edge (Fig. 4.3F) images. This region of interest is shown in Fig. 4.3B (dashed red rectangle). The maps present different and novel image contrast compared to conventional XAS images or phase-contrast images. Complete scattering quotient maps derived from all ptychographic images (fig. S11) are shown in fig. S16. Figure 4.3 shows the Fe-to-Ni ratio maps derived from Mg pre-edge (Fig.

4.3G) and Al pre-edge (Fig. 4.3H) images, where 100% implies a pure nickel sulfide mixture without iron. In general, the converted ratio maps from both pre-edges agree well with each other, despite small differences that could be attributed to uncertainties that will be discussed later. On the basis of the Ni-Fe ratio maps extracted from SQUARREL, the Ni:Fe in the region of interest of our sample is around 1:1 and is consistent with the nominal Ni:Fe in pentlandite, which further supports our assumption of the iron-nickel sulfide as pentlandite.

Besides ptychography, XAS can act as a fingerprint to understand the meteorites phase assemblages and redox states. We collected STXM-XAS images across the Fe L_3-edge, Ni $L_{2/3}$-edge, Mg K-edge, and Al K-edge and analyzed them for unique spectral characteristics (fig. S12). PCA generated representative absorption spectra of the four major elements in the grain: Al, Fe, Mg, and Ni (Fig. 4.3I-L). The Al K-edge spectrum agreed well with the spectrum of Al_2O_3 published elsewhere [134]. The Ni $L_{2/3}$-edge spectrum is similar to that of synthetic nickel sulfide and pure nickel [135,136], while the overall Mg K-edge spectral signature was consistent with those of magnesium silicates [137].

PCA returned two unique Fe spectra (Fig. 4.3J), whose spectral signatures closely match published reference spectra [138] of iron silicate (Fig. 4.3J, solid purple line) and iron sulfide (Fig. 4.3J, dashed yellow line). Moreover, the regions represented by the two spectra precisely match the iron-magnesium silicate and iron-nickel sulfide previously identified in EDS and ptychography, further substantiating the presence of different Fe chemical states in the grain. In the case of iron silicate, the relative Fe L_{3a} and L_{3b} peaks are anticorrelated and dependent on the Fe redox state, where the L_{3a} peak increases linearly relative to the L_{3b} peak as $Fe^{3+}/\Sigma Fe$ ratios decrease [139]. Since L_{3b} has a higher peak intensity than L_{3a}, we concluded that the Fe in the iron silicate was mostly in its reduced Fe^{2+} form. This ability to distinguish different mineral polymorphs is a strong advantage of the XAS over EDS and highlights the complementary nature of X-ray and electron microscopy.

4.4 Discussion

The combination of X-ray and electron microscopy for studying the Allende meteorite yields complementary information about the structural and chemical states of this heterogeneous sample. In combination, this information can help identify the possible mineral phases present in the meteoric grain with nanometer spatial resolution. Figure 4.4 shows the ternary phase diagrams derived from the Cliff-Lorimer ratios calculated using the EDS data. They plot the compositions of major elements in iron-nickel sulfide, iron-magnesium silicate, and aluminum-chromium iron oxide regions of the grain. Some other mineral types with similar elemental makeup are included for reference.

Comparisons between these compositions suggest that the sulfide is likely a pentlandite [$(\mathrm{Fe,Ni})_9\mathrm{S}_8$] and that the oxide belongs to the chromite-hercynite spinel series [$\mathrm{Fe(Cr,Al)_2O_4}$]. XAS results for Al, Mg, and Ni all show spectral fingerprints that are consistent with their respective mineral phases as found in the literature. As for the silicate, analysis of Fe X-ray absorption spectra shows the Fe with a predominantly +2 oxidation state, which narrows down possible mineral candidates to ferrosilite [$(\mathrm{Fe^{2+},Mg})_2\mathrm{Si_2O_6}$], wadsleyite [$(\mathrm{Mg,Fe^{2+}})_2\mathrm{SiO_4}$], or more likely olivine [$(\mathrm{Mg,Fe^{2+}})_2\mathrm{SiO_4}$] [140, 141], and excludes candidates such as majorite [$\mathrm{Mg_3(Fe^{3+},Al,Si)_2(SiO_4)_3}$]. Together, analyses from both X-ray and electron microscopy data helped narrow down the identities of the various phase assemblages and provided a detailed nanoscopic petrographical picture of the meteorite grain.

Moreover, using the SQUARREL method from X-ray images, we quantified the Ni and Fe composition in the iron-nickel sulfide region and reaffirmed the identity of pentlandite that was predicted by EDS analysis. Theoretically, both

Mg pre-edge and Al pre-edge scattering quotient maps should provide the sameor at least very similar nickel-to-iron ratio maps. However, several possible sources of uncertainties and errors can affect the results accuracy. The conversion functions based on Mg and Al pre-edge energies are offset by the same constant to account for systematic errors or uncertainties and to ensure that the ratio is within 0 to 100%. Given uncertainties in the X-ray energies used in our experiments, we also calculated the variation of the conversion function based on different X-ray photon energies, namely, shifted horizontal line outs from fig. S15C.When the X-ray energy varied ±5 eV around Mg pre-edge energy (E=1295 eV), the resulting conversion function, $R_a = R_a(f_q; E)$, returned ∼5% change in the q-to-p ratio. To test the robustness of this conversion, we also calculated the mixture with a slightly different amount of sulfur. When the amount of sulfur was varied from 0.85 to 0.95, the resulting q-to-p ratio changes ∼10%.

To further test the robustness of SQUARREL, we also included a fourth element in the mixture so that the mixture now becomes $\mathrm{Fe_pNi_qS_{0.89}W_l}$, where the fourth element W could be Al, Mg, Si, C, or O. The inclusion of these potential elements was based on our EDS analysis. From this calculation, we found that including additional elements did not have large effects (∼5%) on the q-to-p ratio. Assuming uncorrelated sources of uncertainties or errors, we calculated the statistical variation based on the product of independent variables. This provides the SD of the uncertainty on the order of 12% (i.e., $\sqrt{5\%^2 + 10\%^2 + 5\%^2}$), accounting for the SQUARREL methods total uncertainty. Last, we note that the SQUARREL method relies on tabulated data from the CXRO database, which might introduce additional unaccounted uncertainties. According to [142, 143], the estimated uncertainties of the current CXRO tabulation could be off by 3 to 10% at X-ray energies ranging from 500 to 1000 eV and could be off by as much as 20 to 30% near X-ray elemental absorption edges. Note that in the future, these sources of error can be reduced with additional calibration measurements.

Regardless of those uncertainties, SQUARREL analysis of ptychography data provides semiquantitative two-element ratio compositions with spatial specificity, and it confirms the elemental distributions observed in EDS. Extracting an accurate nickel-to-iron ratio is very important for identifying different mineral phases [144, 145], and SQUARREL could serve as a general and complementary nondestructive analysis tool with EDS to quantify compositions in thickness-varying and heterogeneous samples. Last, we note that because we implemented correlative electron and X-ray imaging, the main scientific findings regarding the Allende meteorite do not rely on SQUARREL. Instead, the mineral phase identification is done using the well-established STEM EDS, with complementary information from STXM absorption spectromicroscopy. The SQUARREL method is presented here as a proof-of-concept demonstration to introduce a new complementary method that can be used for future nondestructive elemental composition identification, particularly of rare samples.

An extension of SQUARREL to include more elements without a priori knowledge of a third element is also possible and is worth exploring in future work. This extension could extend to a general multi-element ratio quantification method for X-ray and even extreme ultraviolet ptychography [117–119]. The combined usage of scattering quotient and quantitative phase images from ptychography created a new analysis method that can be used to derive semiquantitative composition information [146].

Besides identifying possible mineral types, HAADF tomography and X-ray ptychography provide high-resolution textural information to explain possible processes that affected the Allende parent body during and after accretion. In general, shock melting causes a series of changes in meteorites, starting with the generation of localized shock veins and pockets, followed by the transformation of minerals to high-pressure polymorphs and the formation of diaplectic glass, and then end with the recrystallization of highly deformed minerals [147, 148]. High-resolution views of the minerals internal morphologies in Figs. 2B and 3B show the silicate filled with nanoscopic Fe, Al, and Cr veins, which provide strong evidence of melts resulting from impact shocks and heat-induced metamorphism [149, 150]. Moreover, the absence of Mg in the same veins shown in the ptychography difference maps (Fig. 4.3C) indicates no Mg in the veins or that no melting of Mg-bearing phases occurred.

In summary, the evidence gathered from the two imaging modalities agrees well with previous 2D studies of Allende [151, 152] at a coarser resolution, but the nanoscale resolution provides the ability to study fine-grained matrix material in greater detail and the observed melt channels provide insight into processes that cannot be seen at larger scales. The different phases identified are high-temperature refractory nebular condensates [132], some of which may have formed in the hotter inner parts of the solar nebula and were later transported out to the cooler carbonaceous chondrite region of the protoplanetary disk [153]. In this particular sample studied, there are no obvious chondrules, and the assemblage represents the agglomeration of primitive fine-grained silicate dust in the nebula. Allende is classified as shock stage S1 or unshocked, but its parent body had to have experienced large-scale impact events during accretion and at a later time to dislodge meteorites. The nanoscale melt channels seen in this work may provide evidence of these impacts, and further study could constrain the pressures and timing (pre-accretion versus post-accretion) of the melting events.

In addition to the meteorite samples discussed in this work, many other interesting materials with heterogeneous compositions, domains, phases, and defects can benefit from this multimodal microscopy approach. Studies of complicated samples require both macroscopic and microscopic investigations to provide multidimensional morphological and chemical information.

Here, we also suggest a potential strategy for improving this multimodal approach. First, one could use X-ray ptychography to probe bulk samples that are tens of micrometers in size to understand aggregate chemical and structural properties with few-nanometer spatial resolution. Next, atomic electron tomography [62] can be used to probe select regions on the sample surface that are a few nanometers thick to create 3D atomic models of boundary morphologies. This atomic information can correlate with bulk X-ray observations to provide a comprehensive, multiplelength scale investigation into a single specimen. Unlike other nanocrystallographic approaches that may rely on the use of a focused ion beam to destructively section bulk specimens for STEMelectron energy-loss spectroscopy or electron diffraction, the nondestructive multimodal imaging paradigm proposed here is especially suitable for probing scarce extraterrestrial samples (e.g., from Stardust, Hyabusa, or OSIRIS-REx missions), which are extremely rare and should therefore not be destroyed after a single measurement.

In addition, correlative measurements of the same sample recorded with different modalities can be used synergistically to reduce overall data requirement. For instance, ptychography reconstructions are known to benefit from having accurate input probe or object initializations, which may be provided by HAADF-STEM. Accurate prior knowledge can help ptychography algorithm converge faster and may also reduce data redundancy necessary to achieve good results. In the future, similar strategies can be explored with other modalities to formulate a dose-efficient data acquisition scheme for 2D and 3D correlative imaging.

Other than methodology development, several improvements in X-ray microscopy will enhance the applicability of this multimodal method. Currently, synchrotron-based ptychography is still flux-limited, with each acquisition taking on the order of tens of minutes to hours. As such, ptychographic spectromicroscopy is still not practical for most experiments. Nonetheless, the upcoming ALS Upgrade will offer at least 100 times brighter soft X-rays than what is currently available, which will markedly reduce data acquisition time and push toward new resolution limits. As for dealing with sample radiation damage,more

X-ray microscopy beamlines are currently implementing cryogenic capabilities, which will allow radiation-sensitive samples to be probed repeatedly with minimum damage. Moreover, efforts to develop advanced inter-instrument sample transfer mechanisms as well as data collection and processing workflows are currently underway. In the future, a fully consolidated sample environment will allow seamless sample transfer between X-ray and electron microscopes for sequential imaging and will enable studies of delicate samples or samples in situ.

In this work, we demonstrated a new multimodal imaging approach by combining HAADF and EDS tomography with X-ray ptychography and STXM absorption spectromicroscopy to study a small subsection of the Allende CV3 carbonaceous chondrite meteorite. We also introduced a new semiquantitative ptychography analysis method, named SQUARREL, for determining elemental compositions in a mixed material. The synergistic relationship between electron and X-ray imaging and their complementary advantages are highlighted. The multidimensional data provided quantitative chemical and textural information on the diverse phase assemblage in the meteorite grain. Quantifying relative elemental abundances in the phase assemblage suggests the classifications of rock-forming silicates as pyroxenes or olivine, sulfide as pentlandite, and oxide as chromium spinel. This assemblage is consistent with previous studies of Allende that reveal a fine-grained matrix consisting of refractory nebular condensates. Morphological studies of the assemblage reveal nanoscopic metallic shock veins and pockets filled with Al, Fe, and Cr. The observation of shock veins suggests that the Allende parent body or accreted components experienced impact-induced melting at some stage. As this multimodal imaging approach continues to develop beyond this initial demonstration and toward intramodal integration, we expect it to be useful for probing complicated heterogeneous systems and gaining new insights across multiple length scales.

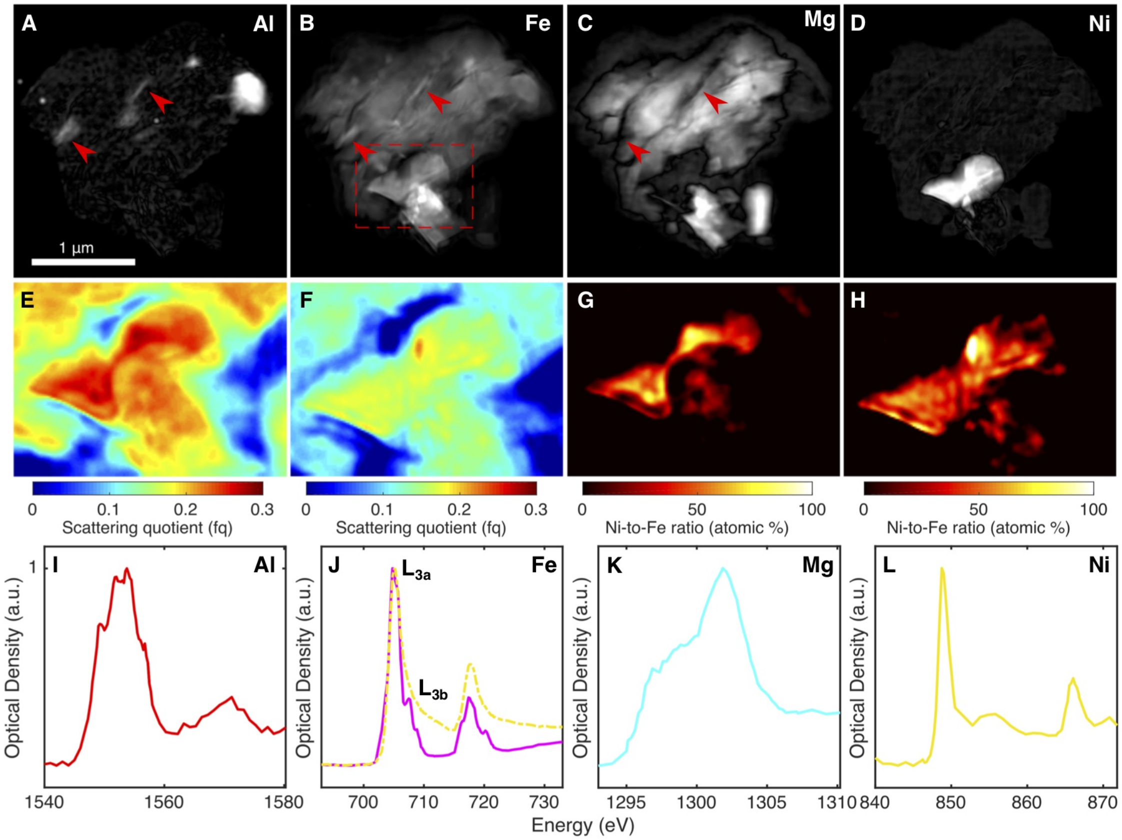
A
Al
1 µm
B
Fe
C
Mg
D
Ni
E
F
G
H
0
0.1
0.2
0.3
Scattering quotient (fq)
0
0.1
0.2
0.3
Scattering quotient (fq)
0
50
100
Ni-to-Fe ratio (atomic %)
0
50
100
Ni-to-Fe ratio (atomic %)
I
Al
1
Optical Density (a.u.)
1540
1560
1580
J
Fe
L_{3a}
L_{3b}
Optical Density (a.u.)
700
710
720
730
K
Mg
Optical Density (a.u.)
1295
1300
1305
1310
L
Ni
Optical Density (a.u.)
840
850
860
870
Energy (eV)

Figure 4.3 *(preceding page)*: X-ray ptychography and STXM absorption spectromicroscopy. (**A-D**) Localization of major elements in the meteorite revealed by dividing pre-edge and on-edge ptychography images at the absorption edges for Al, Fe, Mg, and Ni. The absorption quotient maps, displayed in logarithmic scale, show the presence of Fe in the shock veins of the silicate that is barely observable in EDS images (red arrows). (**E**,**F**) Scattering quotient (f_q) maps derived from ptychographic Mg pre-edge and Al pre-edge images, respectively. This region of interest is a zoomed-in view from the dashed red rectangle shown in (**B**). (**G**,**H**) Ni-Fe ratio maps from Mg pre-edge and Al pre-edge scattering quotient maps, respectively. These ratio maps are converted using the SQUARREL method, given a fixed amount of sulfur. The color bar indicates the Ni-Fe ratio and 100% implies a pure nickel sulfide region. (**I-L**) Absorption spectra generated from STXM energy scans across the four absorption edges, revealing unique spectral fingerprints for each respective element and also showing pronounced spectral differences in the different iron-containing regions. Relative peak intensities between Fe L_{3a} and L_{3b} also reveal the presence of predominant Fe^{2+} species. Colors of the solid lines match colors of mineral regions in Fig. 4.2B. (*Figure reprinted from* [3])

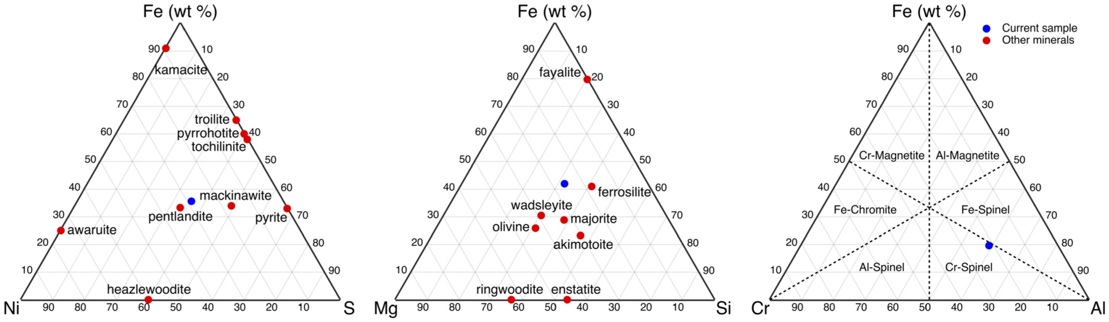

Figure 4.4: Possible grain composition based on EDS quantification of elemental abundances. Ternary plots of major elements as quantified by the Cliff-Lorimer method for three different mineral types in the meteoric grain. Quantitative compositional information narrows down the possible mineral types and suggests that the sulfide is similar to pentlandite (**A**), the silicate is similar to ferrosilite (**B**), and the oxide is a chromium spinel or chromite (**C**). wt %, weight %. (*Figure reprinted from* [3])

CHAPTER 5

X-ray linear dichroic ptychography reveals mis-orientations within coral skeleton 'single crystals'

5.1 Introduction

Humans have been using biologically-created materials as technologies since the dawn of humanity. Biominerals such as seashells, mollusks, corals, and bone exhibit remarkable mechanical properties with complex hierarchical organizations [154]. Due to their unique characteristics, biominerals often outperform their artificially-synthesized inorganic counterparts, thus attracting significant interest in understanding the mechanisms of the biologically-controlled mineralization processes for modern nanotechnology [155]. Careful understanding of the three-dimensional arrangement of biominerals has important engineering implications, and has led to bioinspired materials that outperform their synthetic analogs [156].

One of the most common natural biomineralizations exists in the form of calcium carbonate ($CaCO_3$), which occurs in bacteria, algae, marine organisms and humans [157]. $CaCO_3$ absorb light anisotropically, such that the π-bonded p orbitals of O and C atoms parallel to the crystal c-axis exhibit maximum absorption when aligned parallel to linearly polarized light. The absorption intensity changes with a cos^2 law with respect to the azimuthal orientation, and reflects the average lateral orientation of the carbonate group in the crystal. This information can infer various structural and mechanical properties in the biomineral [158]. Despite its widespread occurrence, much of the basic mechanisms underlying $CaCO_3$ mineral formation remain unknown.

The optical anisotropy in $CaCO_3$ has been leveraged in polarized visible light microscopy to study macroscopic biomineral structure and formation mechanisms [159, 160], and with imaging polarimetry to study crystal orientation uniformity [161, 162]. In the shorter wavelength regime, X-ray absorption near-edge structure spectroscopy (XANES) has been used to study average orientations of various polymorphs of calcium carbonates [163, 164], and polarization-dependent imaging contrast (PIC) mapping using X-ray photoemission electron microscopy (X-PEEM) has been demonstrated to quantitatively map crystal orientations in $CaCO_3$ [165, 166]. Currently PIC mapping mostly use X-PEEM in reflection geometry to achieve tens of nanometer resolution. However, their surface-only sensitivity and limited achievable resolution does not allow direct visualization of subdomain crystal boundaries that are crucial to understanding the nucleation process and the overall crystal growth mechanism. While scanning transmission X-ray microscopy (STXM) has taken advantage of dichroic contrast to study polymer fibers [167] to resolve 30 nm features, the technique is limited in achievable spatial resolution by the focusing optics, which have impractical efficiency and working distance at high spatial resolution.

Although macroscopic morphologies in biominerals have been studied extensively, their nanoscopic structures are still not studied routinely in a quantitative fashion, mostly due to the lack of a proper transmission microscope that offers bulk-sensitive information beyond 5 nm of depth, with spatial resolution better than a few tens of nm. But with the development of high brilliance synchrotron radiation facilities worldwide, advancements in high-resolution imaging techniques, and the increasing availability of insertion device X-ray sources providing polarization control, such as elliptically polarizing undulators (EPU), new synchrotron-based tools are now becoming available for probing nanoscale crystal orientation anisotropy in $CaCO_3$.

Ptychography [114, 168] is one such promising tool for high resolution studies of biominerals. It is an emergent scanning coherent diffractive imaging technique [10, 11] that has demonstrated 5 nm resolution [169] and is attracting significant attention for its general applicability. Ptychography uses spatially overlapping far-field diffraction intensities from the sample with phase retrieval algorithms to iteratively recover the aperture and complex exit wave of the object. This non-invasive technique offers few tens of nm spatial resolution imaging of sponge glass fiber [170], dentine [57], bone [56] and frozen-hydrated cells [2] in two dimensions (2D) and three dimensions (3D). Vectorial version of ptychography for studying anisotropic materials has been demonstrated with visible light to study biominerals [171], and with X-rays to probe magnetic materials [172]. Synchrotron-based X-ray dichroic ptychography should not only be able to probe materials with the same orientational sensitivity as conventional techniques such as X-PEEM, but can do so with higher spatial resolution, bulk sensitivity, and with both absorption and phase information.

In this work, we present the first X-ray linear dichroic ptychography of biominerals using coral species *Seriatopora aculeata* as an example. We imaged several coral particles below and on the π^* peak of the O K-edge and observed significant contrast differences between absorption and phase images. We then performed PIC mapping on the linear dichroic ptychography absorption images to quantitatively determine crystal *c*-axis orientations in the coral with 35 nm spatial resolution. We also qualitatively validated our ptychography results by correlating the PIC maps with 4D-STEM [173], a scanning nano-electron diffraction technique for probing crystal orientations in crystalline materials. Our results reveal that at the nanoscale, crystallites orientations can be narrowly spread in a co-oriented fashion that is characteristic of spherulitic crystals, but also randomly distributed in sprinkle-like fragments. Moreover, we verified, for the first time, linear dichroic phase contrast in the biominerals at a pre-edge energy before absorption resonance. The use of such phase contrast may lead to new dose-efficient dichroic imaging techniques for studying optically anisotropic biominerals, and has important implications for understanding nanoscale organization of general classes of biominerals.

5.2 Methods

Seriatopora aculeata **skeleton preparation**

The *S. aculeata* sample used in this study is a pencil-thick, short and tapered branch termed nubbin. An entire *S. aculeata* coral skeleton, $\sim 10\times10\times10$ cm^3 in size, was purchased from (Tropical Fish World, El Cerrito, CA) (fig. S1). A ∼1 cm long nubbin was broken off from the rest of the coral skeleton, placed in an agate mortar and immersed in 100% ethanol, then gently fractured by an agate pestle into micrometer-sized grains. The resulting ethanol suspension was sonicated for 2 minutes for further dispersion, and the supernatant solution was transferred by pipette onto a 200 mesh copper transmission electron microscopy (TEM) grid coated with carbon film and air-dried for 24 hours before data acquisition.

X-ray linear dichroic ptychography

Soft X-ray ptychographic microscopy measurements were performed at the imaging branch of the undulator beamline (7.0.1) — COherent Scattering and MICroscopy (COSMIC) — at the Advanced Light Source (ALS), Lawrence Berkeley National Laboratory (LBNL), Berkeley, CA (USA) [92, 93]. COSMIC provides monochromatic soft X-rays with energies ranging from 250 to 2500 eV, spanning the carbon and sulfur K-edges. Coherent and monochromatic X-rays were focused onto the sample using a Fresnel zone plate with 45 nm outer zone width and had a total coherent flux of approximately 10^9 photons/s at the sample position. The TEM grid containing the sample was secured using a Hummingbird 3 mm half-grid tip, then mounted onto a standard FEI CompuStage sample manipulator derived from an FEI CM200 series TEM. Diffraction data were recorded with a fast charge-coupled device (CCD) camera developed by LBNL [174] that is capable of 50 frames/sec, 15-bits dynamic range with a 12-bit analog-to-digital converter and with a 1 megapixel detector. Diffraction patterns were acquired without a beamstop and were automatically pre-processed onsite.

Ptychographic measurements consisted of single diffraction patterns recorded at each scan point with 200 or 300 ms dwell time and scanned in a square grid with 40 nm steps to cover an approximately 1.5×1.5 µm field of view, with a reconstruction pixel size of 10.1 nm/pixel. Linear dichroic ptychography data were collected at 0°, 45°, 90° and 135° linear polarizations. The 0° and 90° data were collected with the EPU tuned to horizontal and vertical polarizations, respectively. Since, at the time of these measurements, only linear horizontal and vertical polarizations were under remote computer control, the TEM grid was physically rotated clockwise in-plane by $\sim$135° with respect to the upstream beam, and then the 45° and 135° data were collected using the horizontal and vertical polarizations again.

The same linear dichroic data with 4 polarizations was collected at two X-ray energies around O K-edge π^* peak: one at pre-edge (534.5 eV, or 1.5 eV before the π^* peak) and another at on-edge (536.5 eV, or 0.5 eV after the π^* peak). The pre-edge energy used was estimated to be near the negative phase peak and thus have the most negative phase shift relative to vacuum, to achieve optimal phase contrast. The on-edge energy was chosen to be slightly off the absorption peak at 536 eV to reduce beam attenuation caused by specimen thickness. The resonant energy at the O edge rather than the C edge was used in this study because the 3:1 ratio of O to C in $CaCO_3$ means imaging at O resonance gives significantly greater signal-to-noise ratio, contrast, and hence resolution in addition to allowing for greater material penetration. After all data were acquired, ptychography reconstructions were performed using regularized ptychographic iterative engine (rPIE) [175] with 300 iterations, with $\beta_{obj} = 0.7$ and $\beta_{probe} = 0.7$, and updating the initial probe only after the 100^{th} iteration.

X-ray absorption spectroscopy

Scanning transmission X-ray microscopy (STXM) with X-ray absorption spectroscopy (XAS) was measured at ALS beamline 7.0.1.2. The spectromicroscopy data were recorded with 5 ms dwell time and proceeded with 60nm steps in a square grid scan, with energies spanning the entire O K-edge from 525 to 555 eV. Energy scan steps proceeded with 0.5 eV steps from 525 to 530 eV, then 0.2 eV from 530 to 542 eV, and finally with 0.5 eV steps from 542 to 555 eV. The same energy scan parameters were repeated for X-ray linear polarizations at 0°, 45°, 90°, and 135°. All spectra are normalized via subtraction of the average image from non-resonant energies from 525 to 530 eV.

X-ray absorption spectra were generated using the MANTiS software [123]. STXM-XAS images at each linear polarization were first converted to optical densities (OD) using fully transmitting regions in the specimen, then aligned using cross correlation. Principal component analysis (PCA) was used to reduce the dimensionality of spectral information in the images to obtain absorption signatures of the coral (fig. S2). The first principal component spectrum at each polarization, which represents the average absorption present in the coral, was shown in this work.

Polarization-dependent Imaging Contrast mapping

Crystallographic c-axis orientations in coral particles were calculated using PIC mapping [165], a method that uses linear dichroism effects to quantitatively determine the angular orientation of micro- and nanocrystals. We used the closed-form expression to compute the in-plane angle, χ, and out-of-plane angle, γ, of the crystal c-axis with respect to the linear polarization vector. Here, in-plane is defined as the TEM grid plane that is perpendicular to the X-ray beam. Given 3 EPU polarization angles 0°, 90° and 45°, the electric field vectors at each polarization is $\vec{E}_1 = E_0\hat{x}$, $\vec{E}_2 = E_0\hat{y}$, and $\vec{E}_3 = (\vec{E}_1+\vec{E}_2)/\sqrt{2}$, where $\hat{x}$ and $\hat{y}$ are unit vectors. The unit vector describing c-axis the orientation is $\hat{c} = \hat{x}\mathrm{sin}\chi\mathrm{cos}\gamma + \hat{y}\mathrm{sin}\chi\mathrm{sin}\gamma + \hat{z}\mathrm{cos}\chi$. For the ith polarization, the signal intensity is $I_i = I_A + I_B(\vec{E}_i\cdot\vec{c})$, where I_A and I_B are positive fitting parameters. Algebraic manipulations of the three components yield

$$\mathrm{cos}^2\gamma = \frac{1}{2} + \frac{I_1 - I_2}{2[(I_1 - I_2)^2 + (I_1 + I_2 - 2I_3)^2]^{1/2}} \tag{5.1}$$

$$\mathrm{sin}^2\chi = \frac{1}{I_B}[(I_1 - I_2)^2 + (I_1 + I_2 - 2I_3)^2]^{1/2} \tag{5.2}$$

Solving for γ and χ in above equations give the in-plane and out-of-plane orientations, respectively. The range of χ contracts and expands as I_B varies, but the relative difference in χ between particles remain consistent. In this work, I_B is set to 2. Since ptychography data at 4 EPU linear polarizations were collected, two sets of polarizations were used to calculate two PIC maps for each coral particle: first set used 0°, 45° and 90°, and second set used 0°, 135° and 90°.

4D-STEM and HAADF tomography

Scanning nano-diffraction (4D-STEM) data and high-angle annular dark-field (HAADF-STEM) tomography data were collected at the National Center for Electron Microscopy (NCEM), Molecular Foundry, Lawrence Berkeley National Laboratory, Berkeley, CA (USA). A Titan 60-300 equipped with an Orius 830 HAADF detector (Gatan, Pleasanton, CA) and four windowless silicon drift EDS detectors (FEI super-X) were used with a solid angle of 0.7 srad. The microscope operated in STEM mode at 200 kV with an electron beam current of ~16 pA for 4D-STEM datasets and ~40 pA for HAADF-STEM imaging. The 4D-STEM diffraction data were taken on Orius CCD with a camera length of 300 mm using a convergence angle ~0.51 mrad, with 64×64 square grid scan positions. Before clustering of 4D-STEM data, individual diffraction patterns were preprocessed by aligning the center of mass of the main beam to the image center to correct for horizontal and vertical shifts introduced by beam tilt.

A diffraction similarity map was generated using agglomerative hierarchical clustering [176] of 4D-STEM data. Agglomerative hierarchical clustering initializes all data points, or individual diffraction patterns, as independent clusters. The algorithm then computes the proximity between every pair of data points using a specified distance metric (e.g. Euclidean distance, cosine similarity, correlation). Next, pairs of data points can be linked to one another using a specified linkage metric (e.g. average distance, centroid distance, nearest neighbor distance) to form new grouped clusters, and this continue until all data points are linked together into a hierarchical tree. Finally, the consistency of the resulting clusters can be verified by evaluating the distances between each neighboring clusters in the tree. A distance that is greater than a predefined inconsistency score constitutes a natural partition between clusters, such that separate clusters are considered to be truly independent. This clustering was performed in MATLAB (MathWorks) environment with the linkage function, using correlation as the distance metric, nearest neighbor as the linkage metric, and an inconsistency score of 1.2.

HAADF tomography was performed using the GENeralized Fourier Iterative REconstruction (GENFIRE) [1], an algorithm that has been used to determine the 3D and 4D atomic structure in materials with unprecedented detail [62, 177, 178]. Before reconstruction, HAADF projections were aligned to a common tilt

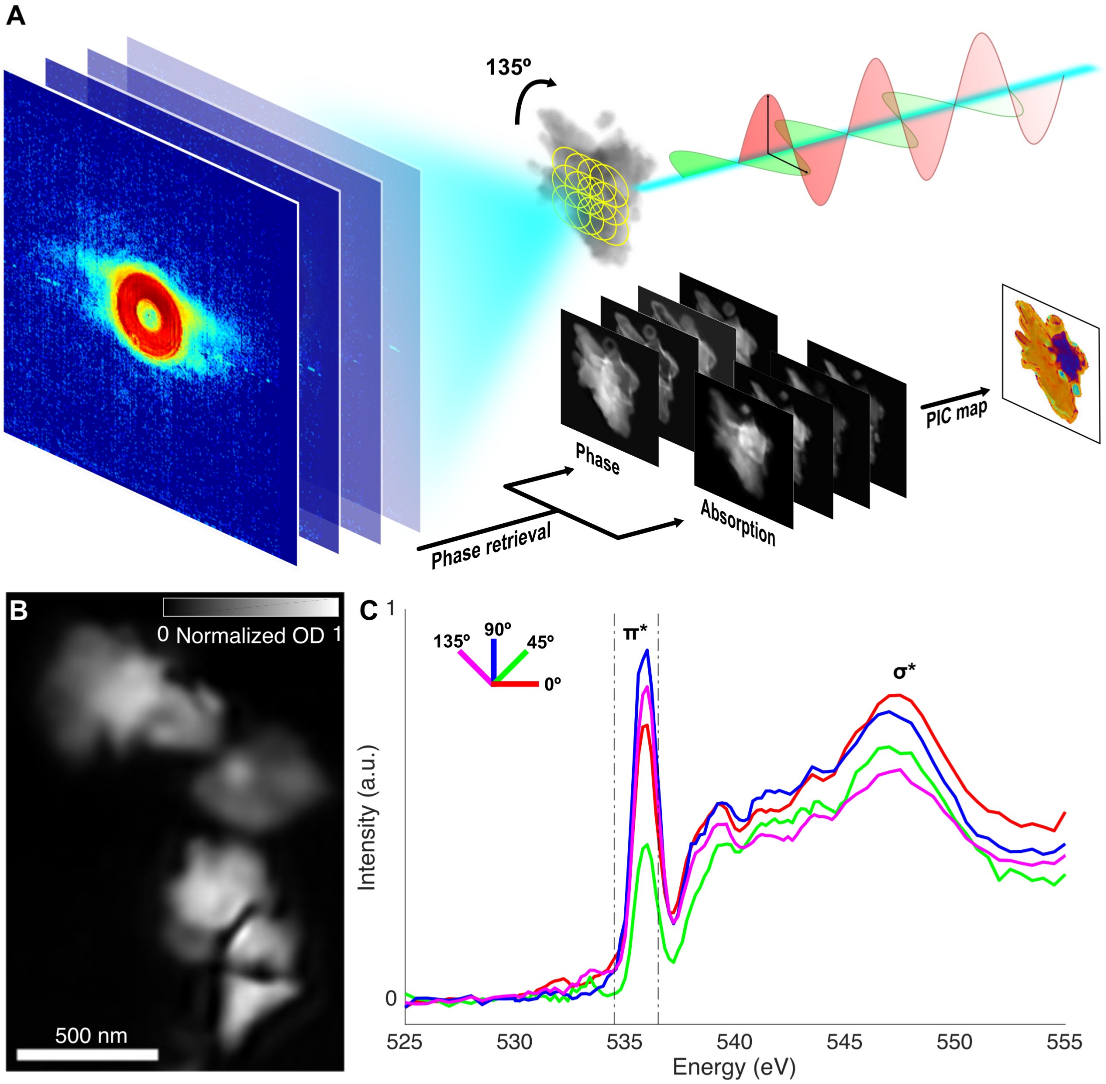
A
135º
Phase retrieval
Phase
Absorption
PIC map
B
0 Normalized OD 1
500 nm
C
1
0
135º
90º
45º
0º
π*
σ*
Intensity (a.u.)
Energy (eV)
525
530
535
540
545
550
555

axis using the center of mass and common line methods [70]. Next, a constant background – the average value in an empty region of the image – was subtracted from each projection, and the process was optimized by minimizing the differences between all common lines and a reference common line. the projections were then normalized to have the same total sum, since the integrated 3D density of the isolated coral particle should be consistent across all tilt angles. The preprocessed projections were used in GENFIRE reconstruction, which ran for 100 iterations, using oversampling ratio 2, 0.7-pixel interpolation distance, and with positivity and support constraints enforced.

5.3 Results

X-ray linear dichroic ptychography

Figure 5.1A shows the experimental schematic of linear dichroic X-ray ptychography experiment, in which coral particles deposited on TEM grid were imaged

---

Figure 5.1 *(preceding page)*: X-ray linear dichroic ptychography imaging setup. (**A**) Experimental schematic of the X-ray linear dichroic diffraction microscope. Horizontally and vertically polarized X-rays incident on the specimen as spatially overlapping diffraction patterns are acquired at below (534.5 eV) and on (536.5 eV) the O K-edge absorption edge to obtain 0° and 90° polarization data, then sample is rotated 135° and measured again to obtain the 45° and 135° data. The diffraction patterns are then directly phased to obtain high-resolution polarization-dependent ptychography images, from which the absorption images are used to compute the PIC maps. (**B**) Ptychography absorption image of a coral particle used to collect linear dichroic absorption spectrums. (**C**) Experimental XAS spectra of the coral fragment at 4 polarizations, showing a dependence of the $CaCO_3$'s π^* peak intensity on incident X-ray polarization angles. Scale bar: 500 nm.

with horizontally and vertically polarized X-rays to obtain 0° and 90° polarization images, then the grid was physically rotated in-plane by 135° to obtain 45° and 135° polarization images. Fig. 5.1C shows the O K-edge spectra obtained from STXM-XAS at each linear polarization, revealing a dependence of X-ray absorption intensity on the relative angle between crystal *c*-axis and X-ray polarization. The π^* peak absorption occurs around 536 eV and is maximum when X-ray polarization is parallel to the π orbitals of C and O in the trigonal planar carbonate group. The broad σ^* peak occurs around 547 eV and is anticorrelated with the π^* peak.

To study the effects of linear dichroism on the absorptive component of the coral's complex exit wave, we imaged 3 coral particles at 536.5 eV, an energy slightly above the π^* peak at 536 eV. Figure 5.2A shows on-edge ptychography absorption contrast images of 3 coral fragments at 0°, 45°, 90°, and 135° polarizations from top to bottom, and from left to right the particles are denoted as Particle #1, Particle #2 and Particle #3, respectively. Relative contrast in various subregions changes dramatically between polarizations, signifying the presence of differently oriented nanoscale domains in the coral. Moreover, diverse nanoscale morphologies are visible in the coral. Whereas Particle #1 displayed overall smooth features with little internal structures, Particle #2 and Particle #3 contained multiple facets with rich textures such as nanoscopic striations. While resonant imaging revealed rich polarization-dependent absorption contrast, imaging off resonance produced no absorption contrast changes at various polarizations due to the lack of linear dichroism effect (fig. S2A).

To examine the effects of linear dichroism on the phase component of the coral's complex exit wave, we also collected ptychography images at 534.5 eV (Fig. 5.2B), an energy slightly before the π^* peak. In general, the negative phase peak is at lower energy than both the positive phase peak and the absorption peak and provides the greatest contrast with respect to non-resonant material.

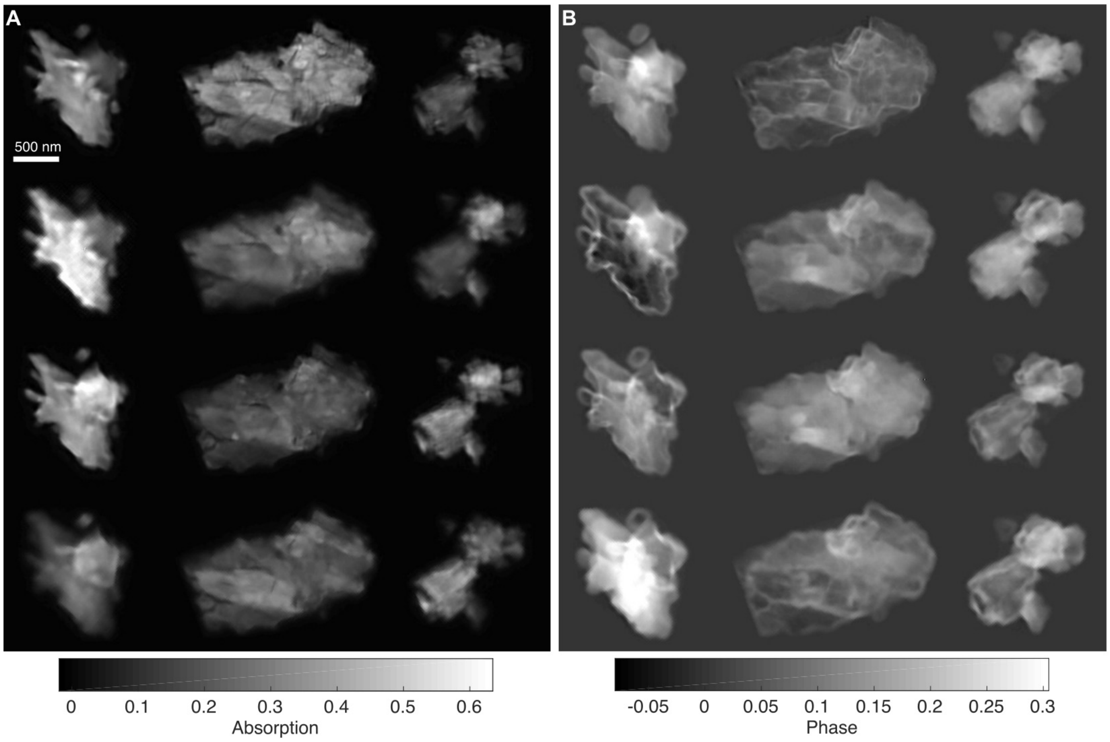

Figure 5.2: X-ray linear dichroic ptychography of coral skeleton fragments. (**A**) Ptychography absorption images of 3 aragonite particles recorded on the O K-edge absorption resonance at 536.5 eV, across 4 linear polarizations (top to bottom: 0°, 45°, 90° and 135°), showing strong polarization-dependent absorption contrast and revealing nanoscale morphologies ranging from smooth homogeneous fragments several hundred nm in size to sub-100-nm fine features. (**B**) Ptychography phase images of the same particles and polarizations recorded at an energy slightly before O K-edge absorption edge of 534.5 eV, showing strong polarization-dependent phase contrast and more edge-sensitive features in internal coral structures. Scale bar: 500 nm.

[179]. Phase contrast images reveal sharp boundaries and complex surface morphologies in the particles. On the other hand, on-edge phase images of the coral particles reveal polarization-dependent contrast that agree very well with on-edge absorption images (fig. S3B). According to the Kramers-Kronig relation, the effects of linear dichroism in crystal orientation manifests in both components of the complex refractive index. But as we observe in PIC images, while the effect on absorption is significant on resonance, the effect on phase is maximum off resonance. Resolution of the ptychography images is estimated to be 35 nm using the knife-edge method with 10-90% intensity cutoff (fig. S4). Given a mass attenuation coefficient (μ/ρ) of 2×10^4 cm^2/g for $CaCO_3$ on O K-edge and a roughly 50% overlap, each recorded projection absorbed an estimated dose of 1.44×10^8 Gy. At this dose and estimated resolution no noticeable deterioration was observed in the sample [112].

Polarization-induced contrast (PIC) map

PIC mapping revealed that the orientations of crystals are much more diverse at the nanoscale than previously appreciated. As is clear from Fig. 5.3, and in particular from the broad range of colors in all 3 particles in Fig. 5.3A, and the large width of the histograms in Fig. 5.3B, many crystallites are present in what was previously assumed to be a single crystal, e.g. Particle #2, or two crystals, e.g. Particle #1. These crystallites vary in orientation gradually, as displayed by color gradients across all larger domains, as in the mustard color domain of Particle #1, or the green-blue domain of Particle #2, or the red-blue domain of Particle #3. There are also unexpected, smaller (~100 nm) domains with orientation different from the larger domains, but not randomly oriented as in the previously observed sprinkles. These small domains are co-oriented with one another but separate from one another. See for example in Particle #1 the green string of crystallites at the bottom, or the two green crystallites on the right side, or in Particle #2 the

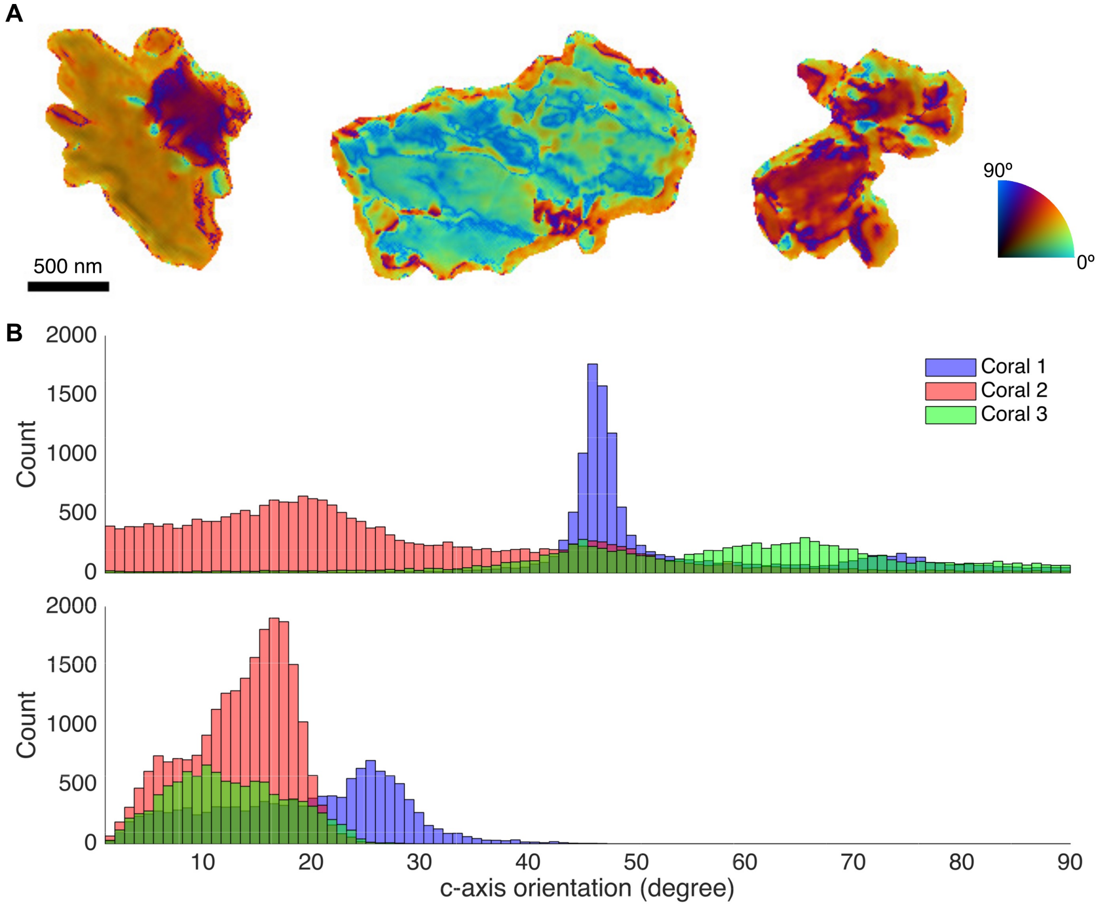

Figure 5.3: Polarization-dependent contrast (PIC) map of aragonite coral skeleton fragments. (**A**) Quantitative PIC maps of the 3 aragonite particles, calculated using 0°, 45° and 90° linear dichroic ptychography images. Hue denotes in-plane azimuthal crystal *c*-axis angle (γ) of the crystallite, while brightness denotes out-of-plane *c*-axis angle (χ), all ranging from 0° to 90°. Particle #1 consists of mostly homogeneous orientations, whereas Particle #2 and Particle #3 show much more orientational diversity. (**B**) Histograms of in-plane (γ, top) and out-of-plane (χ, bottom) angles for the 3 particles, showing a narrow angular spread for Particle #1 of less than 35°, and much broader spread for Particle #2 and Particle #3 of more than 35°, suggesting presence of both spherulitic and sprinkle-like crystallites at the nanoscopic scale. Scale bar: 500 nm.

red-dot crystallites along the top edge, and the dozen red dots across the entire particle. Particle #3 shows 8 very consistent small blue-green crystals interspersed with the rest of the particle, which is mostly red-yellow. These results are highly surprising, as previous methods failed to reveal them, such as those shown using X-PEEM in fig. S5.

We performed PIC mapping on the on-edge linear dichroic ptychography absorption images to quantitatively map c-axis angles in the coral particles and analyzed the in-plane (γ) and out-of-plane (χ) orientations. Since Eq. 1 and Eq. 2 only require 3 polarizations to compute the γ and χ, PIC maps in Fig. 5.3A were calculated using the 0°, 45° and 90° polarization images, and a second set of PIC maps were computed using 0°, 135° and 90° polarization images (fig. S6). In each PIC map, in-plane angles are color-coded according to the coral's crystal axes relative to the X-ray polarization, which is horizontal at 0°. Orientation ranges from 0° to 90°, since angles beyond that range are degenerate and cannot be distinguished from contrast alone. The out-of-plane angles between the c-axes and X-ray polarization are represented by brightness, such that axes that are parallel to the sample plane are displayed in high brightness, and axes that are perpendicular to the sample plane are shown in low brightness, and is lowest when the axes align directly with the X-ray beam.

Histograms of γ (top) and χ (bottom) in Fig. 5.3B present the c-axis angular distribution derived from the PIC maps. Particle #1 exhibits two distinct subdomains, where within each homogeneous region the angular spread is less than 20°, but between them there is a greater than 35° difference. In contrast, Particle #2 and Particle #3 show continuous sub-micrometer orientational fluctuations that spans greater than 35°, suggesting the particles are comprised of many differently oriented nanocrystals. To further examine the abrupt orientational change between subdomains in Particle #1, we performed STEM tomography on the particle, which reveals two separate fragments on top of each other (fig. S7).

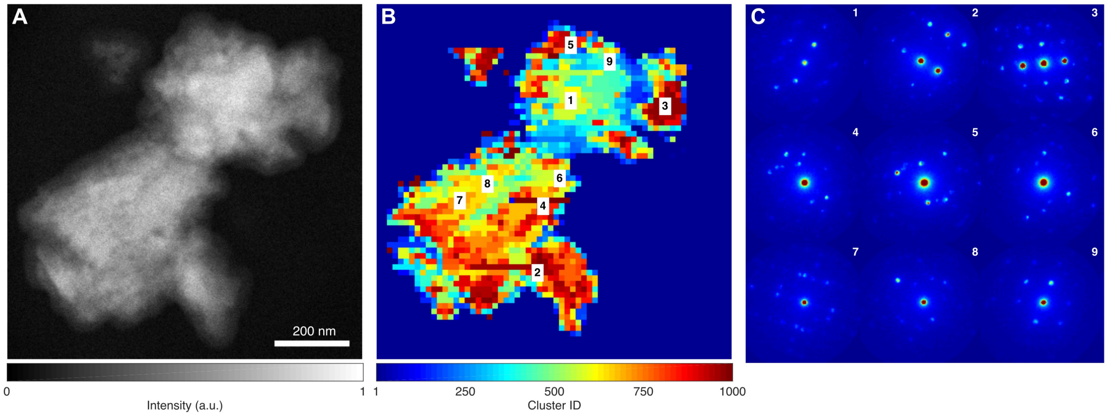

Figure 5.4: Diffraction similarity map from 4D-STEM with hierarchical clustering. (**A**) HAADF image of Particle #3, which was used to acquire scanning electron nano-diffraction patterns. (**B**) Crystal axis similarity map generated using hierarchical clustering of diffraction patterns. Areas with comparable color resemble subdomains with similar crystal orientations. The resulting map qualitatively agrees with the PIC map generated from ptychography. (**C**) Representative converging beam electron diffraction patterns from various regions of the coral fragment, co-labeled in (**B**) and (**C**), showing nanoscale orientational diversity. Scale bar: 200 nm.

4D-STEM and clustering analysis

In effort to further validate the localization of differently oriented crystallites in PIC maps, we collected scanning electron nano-diffraction 4D-STEM data on Particle #3 and assessed its nanoscale lattice changes over the entire particle. The converging beam electron diffraction (CBED) patterns were analyzed using unsupervised agglomerative hierarchical clustering [176] to sort the particle into different regions with similar crystal orientations. Fig. 5.4A shows a HAADF-STEM image of Particle #3, and Fig. 5.4B shows the resulting similarity ranking map generated by hierarchical clustering. The closer the regions are in color, the more similar their corresponding CBED patterns are. Representative CBED patterns from the coral are shown in Fig. 5.4C, with numbers corresponding to the labeled regions in Fig. 5.4B.

The CBED patterns reveal variations and similarity in diffraction – hence crystal orientations – across the particle. For instance, pattern #1 is similar to pattern #9, and both are in close proximity to another. In contrast, patterns #4 and #6, although within the same region, have dissimilar diffraction patterns. Moreover, the similarity ranking map divides the particle into subregions closely resembling those shown in ptychography PIC map in Fig. 5.3A. In particular, distinct subdomains in regions #2, #3, #4 and #7 of the similarity ranking map match well with the corresponding areas in the ptychographic PIC map. This result serves as further confirmation of the orientation heterogeneity within Particle #3.

5.4 Discussion

X-ray linear dichroic ptychography of coral particles shown in Fig. 5.2A,B unveil strong polarization-dependent absorption and phase contrast that is evident of differently oriented subdomains in the aggregate particle. Moreover, each particle exhibits diverse structural features and contains crystal subdomains that range in size from tens to hundreds of nanometers. While both on-edge absorption and pre-edge phase images reveal fine internal features in the coral, phase images seem to be more edge-sensitive and show surface morphologies and boundaries more clearly. The use of phase information to visualize weakly scattering fine features has previously been demonstrated with visible light phase ptychography to enhance cellular contrast in live cells [179, 180]. In the case of biominerals, the simultaneous phase and absorption contrast imaging provided by X-ray ptychography can be used to probe nanoscale boundary features beyond the surface, enabling structural study of inter-crystal topology that is critical in understanding biomineral nucleation and growth. To the best of our knowledge, this is the first demonstration of combined linear dichroic absorption and phase imaging of optically anisotropic materials.

PIC maps generated from the X-ray linear dichroic ptychography images (Fig. 5.2, fig. S3) provide quantitative crystal orientation information with high resolution, and at a depth beyond 5 nm, which is not available with the surface-sensitive X-PEEM (fig. S5). At a fine-grain level, PIC map of Particle #1 shows the presence of two overlaid homogeneous fragments, each having a *c*-axis angular spread less than 10° (Fig. 5.3). Such narrow angular spread has been suggested to be the result of nanoscale non-crystallographic branching, which is a type of spherulitic crystal growth that fills space isotropically with anisotropic crystals, and thus provides the coral skeleton with the needed structural support [181].

On the other hand, PIC maps of Particle #2 and Particle #3 show a multitude of subdomains with non-random crystal orientations, but distinct from the main crystal orientation (Fig. 5.3A,B), suggesting that these crystallites are neither sprinkles nor spherulitic crystals, but a type of crystallite not previously observed in coral skeletons. Note that these sub-micrometer crystal subdomains in corals have not been observed with such detail before, since previous studies did not have high enough photon penetration depth to visualize bulk subdomain morphology. Evidence of such co-oriented but disconnected corallites must be interpreted with new models for coral skeleton formation. Neither of the current models, with corals forming their skeletons by either precipitation from solution [182] or by attachment of amorphous precursor particles [183], predicts the nucleation and growth of co-oriented, disconnected crystals.

The crystal orientation diversity is unlikely to result from extraneous coral skeleton contaminants deposited on the surface of the three particles, as those would not be co-oriented with one another. It is also unlikely to be from nearby connected crystal fragments that separated after fracture, as such remnants would not be so consistent in size and be present in all three particles. Although additional evidence is needed to fully understand the source and formation mechanism of the observed co-oriented, disconnected crystallites, any model for coral skeleton formation must be consistent with their formation. By observing them, ptychographic PIC map has demonstrated its potential to be a useful tool in that endeavor.

To put ptychographic PIC map's fine-grain, nanoscale results into the larger perspective, we also used X-PEEM to acquire a wide-field of view, lower spatial resolution (60 nm) PIC map from another region of *S. aculeata* (fig. S5). X-PEEM PIC map reveals two main types of crystallites on a macroscopic level. One type consists of large, micrometer size spherulitic crystals with less than 35° angular spread, which resembles Particle #1 and its largely unidirectional crystal orientation. Another type consists of sub-micrometer size sprinkle-like crystals with randomly oriented c-axes, which agrees with Particle #2 and Particle #3 and their diverse angular spread. By correlating nanoscopic ptychography PIC map with its macroscopic X-PEEM analog, we get a multi-length scale picture of the coral skeleton architecture. The co-oriented, disconnected crystallites, however, are not detected by PEEM-PIC mapping, because its maximum probing depth is 5 nm at the O K-edge [184]. Thus, the co-oriented, disconnected crystallites must be interspersed with and within the volume of the larger aragonite crystals in each of the three particles analyzed here.

Ptychographic PIC mapping is qualitatively validated with 4D-STEM (Fig. 5.4B), in which hierarchical clustering sort the similarity of CBED patterns into a hierarchical tree. Regions with similar CBED patterns can be assumed to share the same crystal orientations. Comparison between ptychography PIC map of Particle #3 in Fig. 5.3A and similarity rank map in Fig. 5.4B show mostly consistent subdomains. While it is possible to simulate CBED patterns using a known aragonite model at various orientations and match them with experimental patterns to estimate *c*-axis orientation [185], the coral particle's arbitrary thickness near the center attenuated much of the beam, thereby making exact comparison difficult. In the future, more careful sample preparation using focused ion beam can produce coral specimen with desired thickness for optimal X-ray and electron transmission. Nonetheless, this work demonstrates a new attempt to correlate X-ray ptychography with 4D-STEM to understand nanoscale crystal orientations in biomaterials.

There are a few limitations in this work. First, since the aragonite particles studied here are randomly oriented polycrystals, X-ray linearly dichroic ptychography images actually measured the integrated sum of all *c*-axes along the beam direction, with contributions to the contrast from different nano-crystals. Therefore, PIC maps presented here represent only the average orientations in the coral particles. One strategy to overcome this limitation may be to use a ptychographic vector nanotomography approach similar to the ones used to study 3D magnetic vector field [186]. By doing such vector tomography reconstruction, one should be able to obtain true *c*-axis orientations of voxels in 3D. Second, since the coral specimens imaged here were ground by a pestle and thus produced uneven surface, the uncontrolled sample morphology makes quantitative interpretation of ptychographic phase images more complicated, as linear dichroic phase contrast then becomes a function of both specimen thickness and crystal orientation.

Also, the process of physically grinding the coral skeleton might fracture the particles and introduced extraneous structural artifacts. This can be alleviated by first fixing the specimen in epoxy resin then carefully polishing it into a suitable configuration for ptychography. Alternatively, the sample can be thinned by focused ion beam (FIB). Another limitation of the current work is that for simplicity we considered the refractive index of aragonite to be a scalar, not a tensor. For fully quantitative X-ray ptychography all calculations will have to be re-done considering the tensor refractive index of aragonite [187]. Although the observation of linear ptychographic phase dichroism is interesting, more careful sample preparation and measurements are needed in future studies to extract quantitative c-axis orientation information from phase.

X-ray linear dichroic ptychography results presented in this work implies an important possibility. Conventionally, enhanced polarization-dependent contrast is derived from absorption contrast when imaged on elemental absorption edges, with the trade-off that more energy is deposited into the sample per unit area and unit time, which inevitably exacerbates sample radiation damage. However, as this work has demonstrated, one major benefit of X-ray linear dichroic ptychography is that strong polarization-dependent phase contrast is also available when imaged off of resonant energy. This suggests that linear dichroic phase contrast imaging offers an alternative path to obtaining quantitative crystal orientation insights without having to subject the sample to the same radiation dose as absorption edge imaging. This potentially important finding can enable more sophisticated and data-intensive studies. Such dose-efficient technique will be especially advantageous when acquiring vector tomography datasets, since many tilt projections are needed to achieve high quality 3D reconstruction. So far most linear dichroism studies focused on absorption as linear phase dichroism is difficult to obtain experimentally. Therefore, if further explored, the X-ray linear dichroic phase ptychography technique presented here has the potential to become an important tool for studying dose-sensitive materials.

In the future, X-ray linear dichroic ptychography can be applied to image other materials such as tooth enamels, bone, seashells, sea urchin skeletons, polymers, and other classes of optically anisotropic materials with sophisticated nanoscale morphologies and crystallinity. It can also be used to study intricate mechanisms such as crystal nucleation, self-assembly, phase transitions and space-filling growth. In addition, given the ease with which X-ray linear polarization can be tuned at synchrotrons, such technique can be readily implemented in existing coherent diffractive imaging beamlines, and can be combined with X-ray absorption spectroscopy and X-ray fluorescence imaging to produce multidimensional images of heterogeneous samples. As coherent flux, data acquisition and big data technologies continue to advance in synchrotron radiation facilities, we envision this linear dichroic ptychography imaging technique to become part of a powerful suite of tools that offers both compositional and orientational information in real time.

In conclusion, in this work we present the first demonstration of X-ray linear dichroic ptychography. By imaging three *S. aculeata* coral skeleton particles at pre- and on-peak at the O K-edge, we observed strong polarization-dependent phase and absorption contrasts. Then we performed PIC mapping on the dichroic ptychography absorption images to quantitatively estimated *c*-axis orientations in the corals and discovered the presence of two types of previously known crystallites: one with narrow angular spread less than 35° and homogeneous morphology that is suggestive of spherulitic crystals, and another having sub-micrometer nanocrystal domains with orientational fluctuations greater than 35° that is indicative of a sprinkle-like architecture. A third, previously unknown type of crystallites, which are neither sprinkles nor spherulitic crystals, are co-oriented, disconnected crystallites, interspersed with and within larger crystals. We also validated the X-ray results with 4D-STEM and confirmed that regions of orientational diversity are largely consistent. The observation of strong linear phase dichroism off of absorption edge offers the potentially interesting possibility of using phase imaging rather than absorption imaging in future linear dichroism studies as a way to alleviate sample radiation damage. With further development, we expect X-ray linear dichroic ptychography will become a powerful non-destructive tool for probing general classes of optically anisotropic materials with sub-ten nanometer resolution over a wide field of view.

CHAPTER 6

In situ coherent diffractive imaging

6.1 Introduction

The first experimental demonstration of coherent diffractive imaging (CDI) in 1999 [10] has spawned a wealth of development in lensless imaging and computational microscopy methods with widespread scientific applications [45–50, 52, 54, 56, 95, 101,114,119,169,172,188–203]. With continuous rapid development of coherent X-ray sources [11, 204–206], high-speed detectors [207], and powerful algorithms [42, 43], CDI methods are expected to have a larger impact across different disciplines in the future [11]. As many natural phenomena of interest evolve in response to external stimuli, CDI can make important contributions to the understanding of these dynamic phenomena [11, 198, 202, 208, 209].

Recently, in situ and operando X-ray microscopy have advanced to study dynamic processes with elemental and chemical specificity [210, 211], but the spatial resolution is limited by the X-ray lens. While in situ electron microscopy can achieve much higher spatial resolution [16], the dynamic scattering effect limits the sample thickness and restricts the technique's applicability to a wider range of samples.

In this article, we demonstrate a general in situ CDI method to simultaneously reconstruct time-evolving complex exit waves of dynamic processes with spatial resolution only limited by diffraction signals. By introducing both static and dynamic regions in the experimental geometry, we apply the static region as a powerful time-invariant constraint to reconstruct dynamic processes with fast and robust convergence. Our numerical simulations indicate that with advanced synchrotron radiation, in situ CDI could potentially achieve 10 nm spatial resolution and 10 ms temporal resolution. Using an optical laser, we conduct proof-of-principle experiments of this method by capturing the growth of Pb dendrites on Pt electrodes immersed in an aqueous solution of $Pb(NO_3)_2$ and by reconstructing a time series of phase images of live glioblastoma cells in culture medium. Furthermore, by varying the incident X-ray flux between the static and dynamic regions, we demonstrate through numerical simulations that in situ CDI can potentially reduce the radiation dose to radiation sensitive samples by more than an order of magnitude relative to conventional CDI.

6.2 Methods

Numerical simulations of in situ CDI with coherent X-rays

To generate a time-evolving structure model for the simulation, we scaled an optical microscopy video of Pb dendrites in an electrochemical cell (fig. S5). The thickest part of the Pb dendrites is 500 nm and the thickness of the water layer is 1 µm. Using the complex atomic scattering factor of Pb and H_2O at 8 keV [131], we calculated the projected complex electron density of the structure model as a function of time, $O_t(\mathbf{r})$. Next, we created a dual-pinhole aperture consisting of two 1-µm-diameter holes spaced 1.25 µm apart center-to-center. The dual-pinhole illumination function $P(\mathbf{r})$ was calculated by propagating the aperture function to the sample plane with a distance of 10 µm. Small random fluctuation is added to $P(\mathbf{r})$ to introduce the effect of imperfect illumination function estimate. The diffraction pattern at frame t, $I_t(\mathbf{k})$, was collected by a 1024×1024 pixel detector,

$$I_t(\mathbf{k}) = I_0 \eta \Delta t \left(\frac{r_e \lambda}{a \sigma_1} \right)^2 | \Psi_{\mathrm{D},t}(\mathbf{k}) + \Psi_S(\mathbf{k}) |^2 \tag{6.1}$$

where $\Psi_{D,t}(\mathbf{k})$ and $\Psi_S(\mathbf{k})$ are the structure factors of the dynamic and static functions at frame t, respectively. $\Psi_{D,t}(\mathbf{k}) + \Psi_S(\mathbf{k})$ was calculated by using the FFT as $F[P(\mathbf{r}) \cdot O_t(\mathbf{r})]$, I_0 is the incident photon flux (10^{11} ph µm^{-2} s^{-1}), η is the detector efficiency (0.8), Δt is the acquisition time (10 ms), r_e is the classical electron radius, λ is the wavelength, α is the size of illuminated area (3 µm), and σ_1 is the linear oversampling ratio [29] (2). To simulate the dynamic process, we calculated each diffraction pattern by integrating 10 individual patterns, each generated from an image in fig. S5 with 1ms exposure. Poisson noise was added to the integrated diffraction patterns with a temporal resolution of 10 ms. This process introduces motion blurring that is more representative of experimental measurements (fig. S5).

Experiment setup with a HeNe laser

Our proof-of-principle experiments used a 543 nm HeNe laser (REO) with a power of 5 mW. A collimated beam with a diameter of 800 µm was directed onto a dual pinhole aperture, which consists of two 100 µm pinholes spaced 100 µm apart from edge to edge. The illumination was incident onto the sample 400 µm downstream of the aperture. A 35 mm objective lens was placed immediately downstream of the sample, and far-field diffraction patterns were measured by a 1340×1300 pixel CCD detector (16 bits, Princeton Instruments) at the lens' back focal plane. In order to increase the dynamic range of the diffraction intensity, three separate exposure times, 100, 1000, and 10,000 ms, were taken and the diffraction patterns were computationally stitched together without missing centers.

Electrochemical cell preparation

A sealed fluid cell was assembled to observe the dynamics of Pb dendrites. With the aid of an optical microscope, two platinum wires (diameter=50.8 µm, 99.95%

Alfa Aesar) were immersed in a thin layer of a saturated solution of $Pb(NO_3)_2$ (99.5%, SPI-Chem) in deionized water and were encapsulated between two glass microscope coverslips (22×22×0.13 mm^3). The two glass slides were epoxied together with the platinum wires exposed for making electrical contact.

Glioblastoma cell preparation

The glioblastoma cell line U-87 MG was purchased from ATCC (Manassas, Virginia). Cells were cultured in T75 cell culture flask (Thermo Fisher) in Dulbecco's Modified Eagle Medium (DMEM) (Thermo Fisher) with 10% fetal bovine serum (Corning Inc.) and 100 U/ml penicillinstreptomycin (Thermo Fisher) in 37°C and 5% CO_2 incubator. To seed the cells onto coverslips, the cells were treated with TrypLE (Thermo Fisher) for 5 min in a 37°C incubator. The reaction was stopped by adding an equal volume of the complete culture medium. Around 1 million cells were seeded in a 100 mm glass plate with four pieces of coverslips inside the plate to allow attachment.

Potential significant radiation dose reduction using in situ CDI

The dose reduction simulation used 530 eV X-rays to minimize water background and to ensure good cellular contrast. A dual-pinhole aperture with 3 µm diameter pinholes spaced 4 µm apart was used to illuminate the static structure and a biological sample covering 7×7 µm field of view. A 1100×1100 pixel detector with 10 µm detector pixel size and a 5×5 pixel missing center was placed 5 cm downstream of sample, with maximum resolution at detector edge of 21.2 nm and an oversampling ratio (σ_1) of 2 (σ_1 about 4 for single pinhole case). The simulated biological specimen consists of a 2 µm long organelle and various cytosolic components in a 3×3 μm^2 region of a 1 µm thick cell. The complex electron density of the biological specimen is calculated using the average composition of protein

($H_{50}C_{30}N_9O_{10}S_1$). Adjacent to the specimen is the static structure, composed of 20 nm thick Au pattern resembling a lacey carbon morphology. The recorded diffraction intensity $I(\mathbf{k})$ with 1 s exposure (Δt) was calculated as

$$I(\mathbf{k}) = \eta\Delta t \left(\frac{r_e\lambda}{a\sigma_1}\right)^2 \Big\{ I_D|\Psi_D(\mathbf{k})|^2 + I_S|\Psi_S(\mathbf{k})|^2 + \\ \sqrt{I_D I_S}\big(\Psi_D(\mathbf{k})\Psi_S^*(\mathbf{k}) + \Psi_D^*(\mathbf{k})\Psi_S(\mathbf{k})\big)\Big\} \quad (6.2)$$

Where $\mathit{\Psi}_D(\mathbf{k})$ and $\mathit{\Psi}_S(\mathbf{k})$ are the complex waves of the biological specimen and static structure, respectively, calculated using tabulated atomic scattering factors of their respective materials. I_S and I_D are photon fluxes on the static structure and biological specimen, respectively. Eq. (10) is an expansion of Eq. (9) to allow for differential flux through each structure. In the case that I_D equals I_S, Eq. (10) is reduced to Eq. (9). Phase retrieval on the simulated noisy diffraction intensity was performed using OSS [29] with 500 iterations. The reconstruction with the lowest Fourier R-factor in 10 independent runs was used as the final result. Resolution was quantified by the Fourier ring correlation (FRC),

$$\mathrm{FRC}(\mathbf{k}) = \frac{\mathit{\Sigma}\mathit{\Psi}_m(\mathbf{k}) \cdot \mathit{\Psi}_g(\mathbf{k})}{\sqrt{\mathit{\Sigma}|\,\mathit{\Psi}_m(\mathbf{k})|^2 \cdot \mathit{\Sigma}|\,\mathit{\Psi}_g(\mathbf{k})|^2}} \quad (6.3)$$

where $\mathit{\Psi}_m(\mathbf{k})$ and $\mathit{\Psi}_g(\mathbf{k})$ are the complex structure factors of the model and reconstruction, respectively.

Quantification of radiation dose in simulation

In the simulation, we estimated the radiation doses (D) imparted on the biological specimen as [112, 212],

$$D = \left(\frac{P_t}{A}\right)\left(\frac{\mu E}{\rho}\right) \quad (6.4)$$

where total incident X-ray photons (P_t) per unit area (A) through a 3 µm pinhole (P_t/A) varies from 3.5×10^4 to 3.5×10^7 photons µm^{-2}. The cell density (ρ) is 1.35 g cm^{-3}, and the linear absorption coefficient (μ) of average protein at 530 eV photon energy (E) is 1.25×10^4 cm^{-1}, which gives a mass absorption coefficient (μ/ρ) of 9.26×10^3 cm^2 g^{-1}. Thus, the total dose delivered to the biological specimen ranges from 2.75×10^3 to 2.75×10^6 Gy.

6.3 Results

In situ CDI principle. To achieve fast, reliable reconstruction of a time series of dynamic phenomena, in situ CDI takes advantage of two types of structures or regions. A dynamic region constantly changes over time or in response to external stimuli, while a static region remains stationary in time. A time series of far-field diffraction patterns are collected with interference between the static and dynamic regions. Since the static region remains unchanged during the data acquisition, this interference effectively creates a time-invariant overlapping region between the measured diffraction patterns, providing a powerful real-space constraint to simultaneously phase all diffraction patterns with fewer iterations and more robust convergence than conventional phase retrieval algorithms.

Figure 6.1A shows an experimental setup for in situ CDI. A dual pinhole aperture is placed upstream of the sample to create two separate regions on the sample plane. The dynamic specimen of interest is localized to the area of one pinhole, while the other pinhole illuminates a region without the sample. Note that the second, static region can be completely empty or a substrate containing some stationary structure. Experimentally, the sample holder can be prepared by using microfluidics so that there are regions where one pinhole occupies the dynamic specimen while the other one covers a static area (Fig. 6.1A).

Furthermore, this technique can be used to extend scanning CDI techniques such as ptychography, where a region of interest can first be obtained by scanning, and then the dynamic specimen can be magnified and perturbed to probe dynamic information. As a general method, in situ CDI requires only a static region or

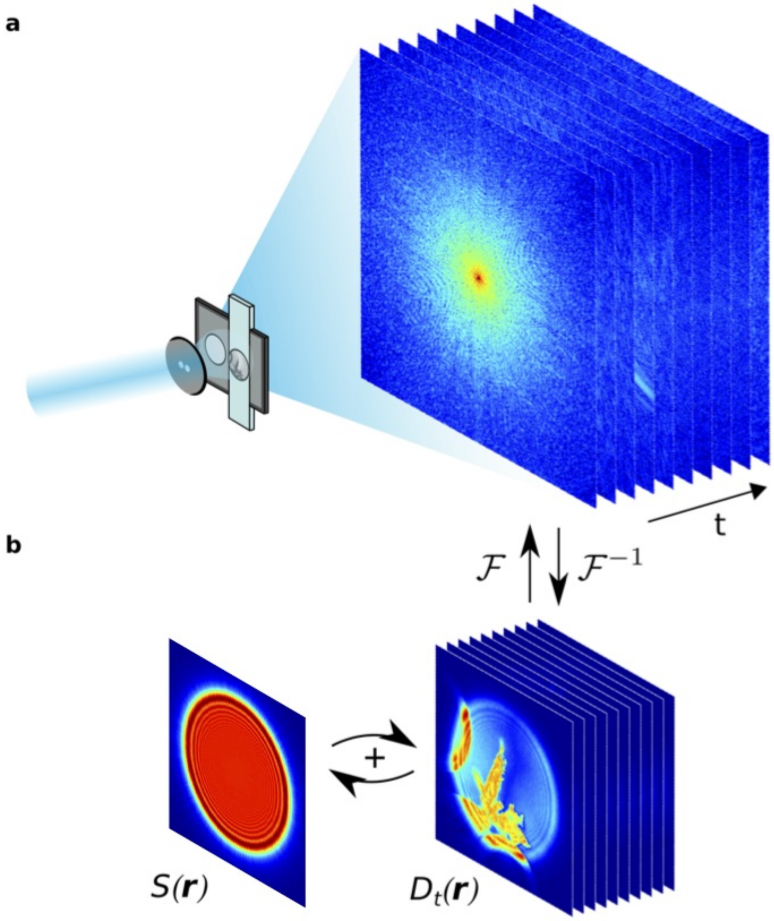

Figure 6.1: Schematic layout of the experimental geometry and the phase retrieval of in situ CDI. (**a**) A coherent wave illuminates a dual-pinhole aperture to create a static and a dynamic region, $S(\mathbf{r})$ and $D_t(\mathbf{r})$. A sample in the dynamic region changes its structure over time and a time series of diffraction patterns are collected by a detector. (**b**) By using the static region as a powerful time-invariant constraint in real space, the in situ CDI algorithm iterates between real and reciprocal space and simultaneously reconstructs a time series of complex exit waves of the dynamic processes in the sample with robust and fast convergence. F and F^{-1} represent the fast Fourier transform and its inverse, respectively. (*Figure reprinted from* [4])

structure between two consecutive time frames as the time-invariant constraint for phase retrieval, which can in principle be implemented with different experimental geometries.

In situ CDI phase retrieval algorithm

Figure 6.1B shows the schematic layout of the in situ CDI phase retrieval algorithm. Using random phases as an initial input, the algorithm iterates between real and reciprocal space with constraints incorporated in each space. The illumination function of the incident wave and a static function of the time-invariant overlapping region are enforced in real space, while the measured Fourier magnitudes are applied in reciprocal space. In each iteration, a weighted average static function is sequentially passed onto the reconstructions of the time series. Since the static function is shared and mutually reconstructed at different time frames, the solutions to the phase problem for the whole time series rapidly emerge without stagnation. The jth iteration of the algorithm consists of the following steps. Obtain a weighted average static function at time t,

$$S_{t,j'}(\mathbf{r}) = \gamma S_{t-1,j}(\mathbf{r}) + (1-\gamma) S_{t,j}(\mathbf{r}) \tag{6.5}$$

where $S_{t-1,j}(\mathbf{r})$ represents the static function at time $t1$ and the weighting factor γ is set to 0.8. Next, combine $S_{t,j'}(\mathbf{r})$ with a dynamic function, $D_{t,j}(\mathbf{r})$, to produce an object function,

$$O_{t,j}(\mathbf{r}) = S_{t,j'}(\mathbf{r}) + D_{t,j}(\mathbf{r}). \tag{6.6}$$

Multiply the object function by the illumination function, $P(\mathbf{r})$, to generate a complex exit wave function,

$$\psi_{t,j}(\mathbf{r}) = O_{t,j}(\mathbf{r}) P(\mathbf{r}). \tag{6.7}$$

In the current version of the algorithm, an accurate knowledge of $P(\mathbf{r})$ is necessary, and can be experimentally measured [30, 114, 191]. Next, apply the fast Fourier transform (FFT) F to the exit wave function to obtain its Fourier transform,

$$\Psi_{t,j}(\mathbf{k}) = F[\psi_{t,j}(\mathbf{r})]. \tag{6.8}$$

and replace the calculated Fourier magnitude with the measured one,

$$\Psi'_{t,j}(\mathbf{k}) = |\,\Psi_t^m(\mathbf{k})|\frac{\Psi_{t,j}(\mathbf{k})}{|\,\Psi_{t,j}(\mathbf{k})|}. \tag{6.9}$$

Apply the inverse FFT (F^{-1}) to obtain an updated exit wave function,

$$\psi_{t,j'}(\mathbf{r}) = F^{-1}[\,\Psi_{t,j'}(\mathbf{k})] \tag{6.10}$$

then remove $P(\mathbf{r})$ to get an updated object function,

$$O_{t,j'}(\mathbf{r}) = O_{t,j}(\mathbf{r}) + \frac{|P(\mathbf{r})|P^*(\mathbf{r})}{\alpha(|P(\mathbf{r})|^2 + \epsilon)}[\psi_{t,j'}(\mathbf{r}) - \psi_{t,j}(\mathbf{r})] \tag{6.11}$$

where $\alpha = max|P(\mathbf{r})|$ and ϵ is a small value to prevent division by 0 [30]. Next, separate $O_{t,j'}(\mathbf{r})$ into the updated static and dynamic functions, $S_{t+1,j}(\mathbf{r})$ and $D_{t,j+1}(\mathbf{r})$, respectively, and feed $S_{t+1,j}(\mathbf{r})$ back to beginning to reconstruct $D_{t+1,j}(\mathbf{r})$. After repeating above steps for the whole time series, R-factor is calculated for the jth iteration to monitor the convergence of the algorithm,

$$R_j = \frac{\Sigma_t \Sigma_k ||\,\Psi_t^m(\mathbf{k})| - |\,\Psi_{t,j}(\mathbf{k})||}{\Sigma_t \Sigma_k |\,\Psi_t^m(\mathbf{k})|} \tag{6.12}$$

Numerical simulations of in situ CDI using coherent X-rays

Batteries play an indispensable role in the development of modern technologies, but advances in high capacity batteries are hampered by dendritic growth, where microfibers of electrolyte materials sprout from the surface of electrodes during charge/ discharge cycles and short the circuit. In some serious cases, dendrites can cause rapid heating and explosion of the battery [213]. While in situ transmission electron microscopy (TEM) can observe dendritic growth at high spatial resolution [214], the sample thickness is limited by the dynamical electron scattering effect

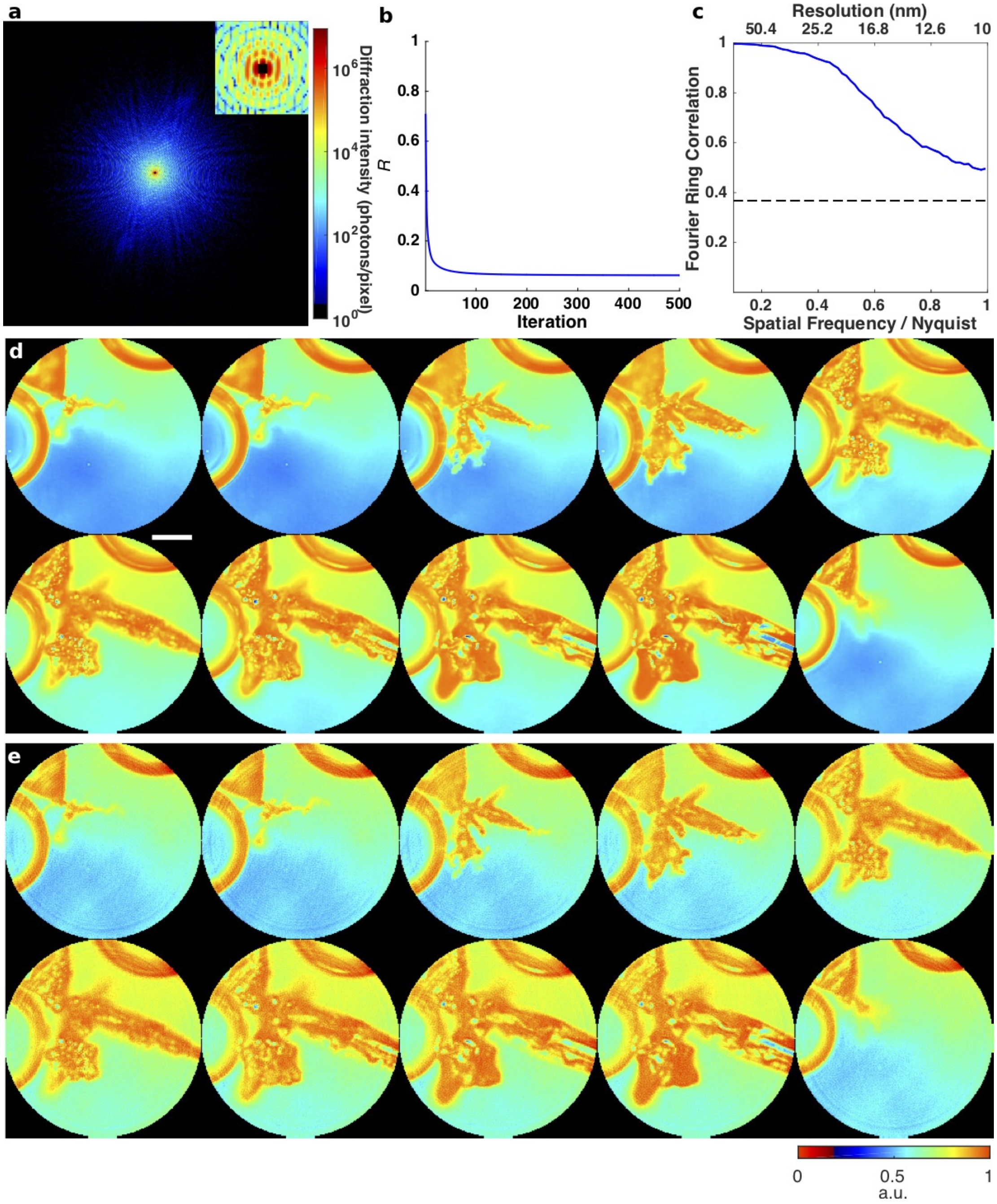
a
10^6
10^4
10^2
10^0
Diffraction intensity (photons/pixel)
b
1
0.8
0.6
0.4
0.2
0
R
100
200
300
400
500
Iteration
c
Resolution (nm)
50.4
25.2
16.8
12.6
10
1
0.8
0.6
0.4
0.2
Fourier Ring Correlation
0.2
0.4
0.6
0.8
1
Spatial Frequency / Nyquist
d
e
0
0.5
1
a.u.

and the temporal resolution is hampered by the electron flux [16]. Due to X-ray's larger penetration depth, in situ CDI is ideally suited to probe the dynamic phenomena of thick specimens with nanoscale spatial resolution and high temporal resolution.

To demonstrate in situ CDI's ability to reliably reconstruct dynamic structures, we performed numerical simulations on real time imaging of Pb dendrite growth in solution (Methods, Fig. 6.2). Coherent X-rays with 8 keV energy and a flux of 10^{11} photons m^{-2} s^{-1} were incident on a dual-pinhole aperture. The illumination function was generated by propagating an exit wave from the dual-pinhole aperture to the sample plane. One of the pinholes illuminated the growth process of Pb dendrites immersed in a 1-m-thick water layer (Methods), while the other pinhole was focused on a static region. A time series of diffraction patterns were collected by a 1024×1024 pixel detector with a frame rate of 100Hz and a linear oversampling ratio of $\sim$2 [214]. Poisson noise was added to each diffraction

---

Figure 6.2 *(preceding page)*: Numerical simulations of in situ CDI with coherent X-rays. (**A**) A representative diffraction pattern with Poisson noise and missing data, calculated from the Pb dendrite formation process in an electrochemical cell using 8 keV X-rays with a flux of 10^{11} photons µm^{-2} s. The insert indicates a 5×5 pixels missing data at the center. (**B**) *R*-factor used to monitor the iterative algorithm, showing the rapid convergence of the algorithm. (**C**) Average Fourier ring correlation between a time-evolving structure model and its corresponding reconstructions indicates a spatial resolution of 10 nm can be achieved, with a temporal resolution of 10 ms. (**D**) The time-evolving structure model of the dendrite formation process immersed in a 1-µm-thick water layer. Scale bar, 200 nm. (**E**) The corresponding reconstructions of the time-evolving complex exit waves (showing only the magnitude), which are in good agreement with the structure model. (*Figure reprinted from* [4]) pattern and the central 5×5 pixel data was removed to simulate the missing center problem (Fig. 6.2A).

By using random phase sets as an initial input, the in situ CDI algorithm quickly converged to the correct solution after several hundreds of iterations (Fig. 6.2B). Figure 6.2D shows a time series of the magnitudes of the reconstructed complex exit waves with a temporal resolution of 10 ms, which are in good agreement with the original structure model (Fig. 6.2C). Compared to conventional phase retrieval algorithms [26, 29, 42, 43, 215], the in situ CDI algorithm can produce very consistent final reconstructions with different random phase sets as the initial input. To quantify the reconstructions, we calculated the Fourier ring correlation (FRC, Methods) between the reconstructed images and the original structure models, indicating a spatial resolution of 10 nm was achieved in this case (Fig. 6.2B).

Optical laser experiment with battery material

As a proof-of-principle experiment, we demonstrated in situ CDI for materials science applications by capturing the growth of Pb dendrites on Pt electrodes immersed in an aqueous solution of $Pb(NO_3)_2$. A helium-neon (HeNe) laser was used as the coherent light source and illuminated a dual-pinhole aperture composed of two 100 µm holes spaced 100 µm apart edge-to-edge (Methods). An electrochemical cell was placed 400 µm downstream of the aperture. The cell was made from 50 µm diameter Pt wires immersed in 1.5 M $Pb(NO_3)_2$ solution and encased between two 100-µm-thick coverslips (Methods). The left pinhole was placed in front of the electrochemical cell, while the right pinhole was focused on the substrate devoid of any dendrite. Twelve DC voltages were applied to the electrochemical cell to generate Pb dendrite growth and dissolution. At each voltage, a diffraction pattern was measured by a liquid-nitrogen cooled CCD detector with 1340×1300 pixels and a pixel size of 20×20 µm. To validate the in situ CDI results, a 5×5

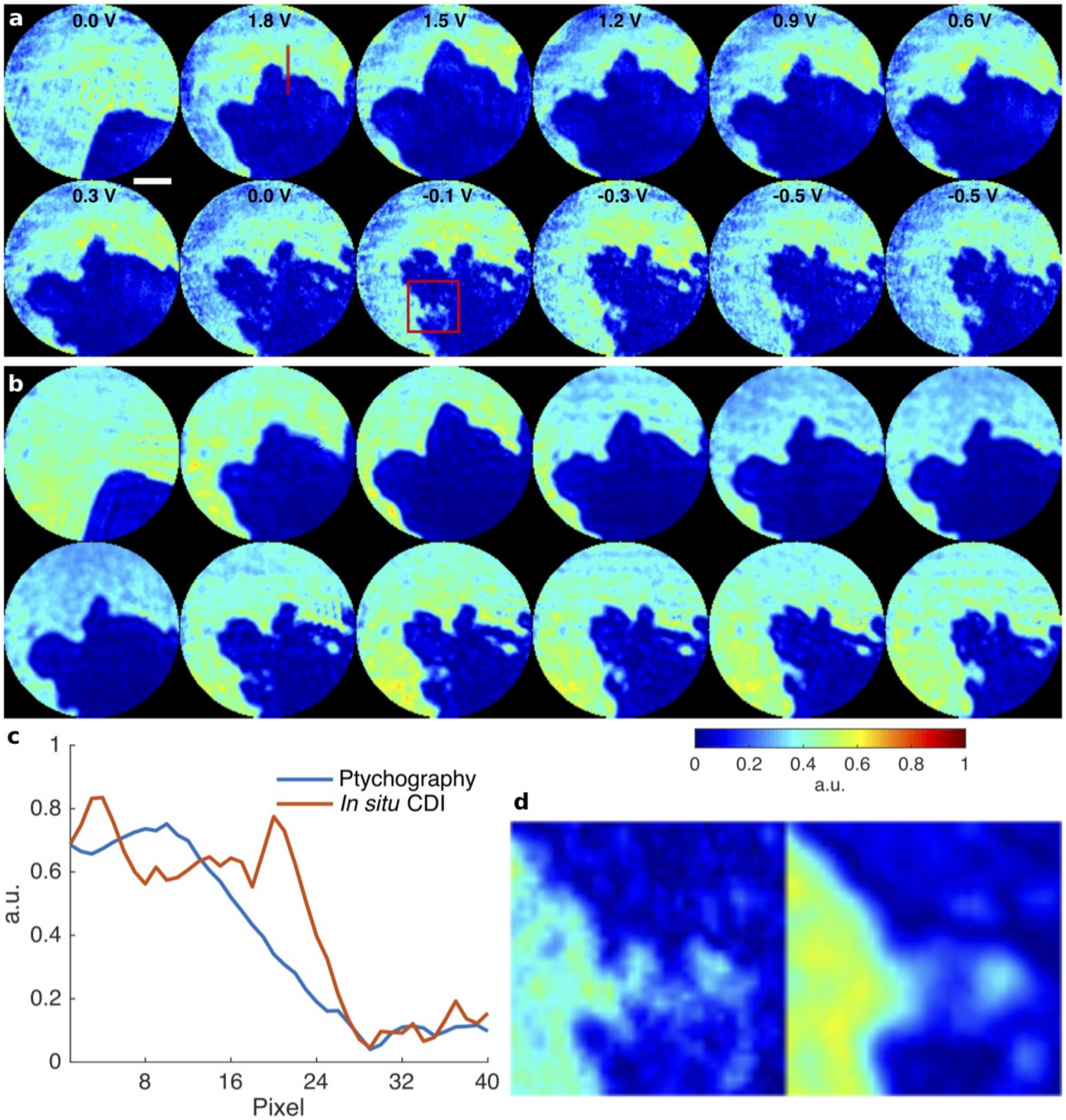
a
0.0 V
1.8 V
1.5 V
1.2 V
0.9 V
0.6 V
0.3 V
0.0 V
-0.1 V
-0.3 V
-0.5 V
-0.5 V
b
c
1
0.8
0.6
0.4
0.2
0
a.u.
8
16
24
32
40
Pixel
Ptychography
In situ CDI
0
0.2
0.4
0.6
0.8
1
a.u.
d

ptychographic scan was also collected at each voltage.

Figure 6.3 (A,B) and fig. S1 show the in situ CDI and ptychographic reconstructions of the same sample area at 12 different voltages. The overall structures are in good agreement between the two methods and the independent in situ CDI reconstructions are also very consistent (fig. S2). Figure 6.3 (C,D) show some fine features are resolved in in situ CDI, but blurred in the ptychographic reconstruction. This blurring is due to continuous dendrite dissolution as the aperture scans over the field of view, resulting in an average reconstruction within the ptychographic scan.

Our results show that, as the voltage was ramped up to 1.8 V, Pb was rapidly deposited on the tip of the Pt wire to form short and wide dendrites (Movie S1). Initially the growth continued as the voltage decreased to 1.5 V, but as the potential decreased further the dendrite began to dissolve from its tip down to the root. The dendrite did not fully dissolve from the tip during the measurement, even after the voltage was reversed. The presence of undissolved Pb dendrites increases the surface roughness of the electrode and can lead to enhanced dendrite growth

---

Figure 6.3 *(preceding page)*: Proof-of-principle experiment on in situ CDI with a materials science sample. (**A**) The magnitude of the complex exit waves reconstructed by in situ CDI, capturing the growth of Pb dendrites on Pt electrodes immersed in an aqueous solution of $Pb(NO_3)_2$ as a function of the applied voltage. Scale bar, 20 µm. (**B**) Ptychographic reconstructions of the same dynamic sample area. The overall structures agree well between the two methods. However, some fine features are resolved in in situ CDI, but blurred in the ptychographic reconstruction as indicated by a line-out (**C**) and a magnified view (**D**) of two areas. The blurring in ptychography is due to the continuous dendrite dissolution as the aperture scans over the field of view. Scale bar, 10 µm. (*Figure reprinted from* [4]) in subsequent charge/discharge cycles. This highlights dendrite growth as a significant problem in rechargeable batteries, where many repeated charge/discharge cycles occur over the lifespan of the battery [213].

Optical laser experiment with biological sample

Tumor cell interaction offers insights into cancer progression, including recognition, communication, and assembly among cell groups [216]. Tumor cell fusion, or fusogenic events, has also been suggested as a source of genetic instability, as well as mechanisms for metastasis and drug resistance [217]. The fate of fused cells could be either reproduction or apoptosis, with still unclear implications. To demonstrate in situ CDI in a biological context, we used a HeNe laser and collected a time series of 48 diffraction patterns from live glioblastoma cells sealed between two cover slips (Methods). To validate our method for imaging the biological specimen, a 5×5 ptychographic scan was also collected at each time point.

Figure 6.4 and fig. S3 show a good agreement between the unwrapped phase images of in situ CDI and ptychographic reconstructions. The phase images show a small cell, about 25 µm in length, slowly approaching and attaching to a larger cell, about 100 µm in length, over 2 hours (Movie S2). After 144 minutes, the large cell responded to the presence of the smaller cell and underwent a rapid morphological change. In the next three hours the large cell moved away from the small cell as the small cell's thin pseudopodium anchored and pulled on the large cell to keep it in place. In the subsequent 3 hours, the two cells fused together and formed a dense circular shape. Another time series of the cells taken after fusion showed no noticeable morphological change or cell motility, suggesting that apoptosis occurred after the cells merged.

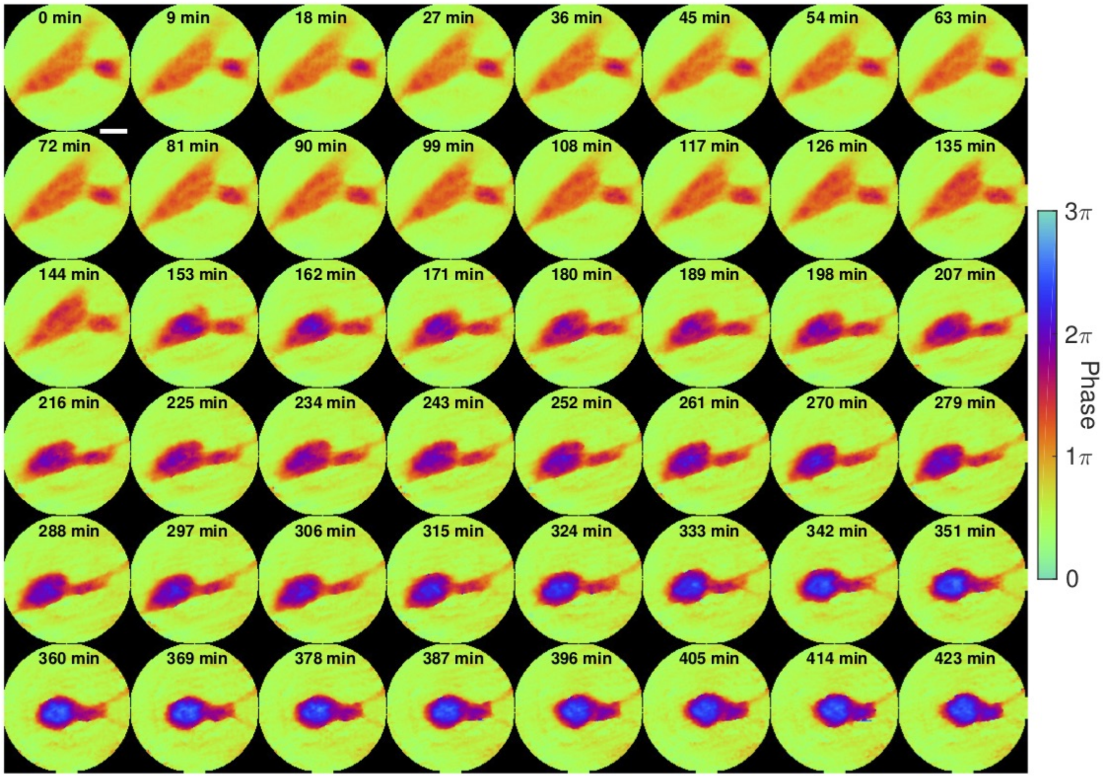

Figure 6.4: Proof-of-principle experiment on in situ CDI with a biological sample. Phase images of the fusion of glioblastoma cells reconstructed by in situ CDI. A smaller cell on the right approached a large cell and initiated cell attachment during the first 144 min. Upon attachment, the large cell underwent rapid morphology change and moved left, but the small cell anchored the large cell with thin pseudopodium on the right side of the field of view and began fusing until the 342nd min. The cells showed no motility post fusion, suggesting the occurrence of apoptosis following fusogenic event. Scale bar, 20 µm. (*Figure reprinted from* [4])

Simulation geometry	
Detector size	1100×1100 pixels
Detector quantum efficiency	80%
Detector pixel size	10 µm
X-ray energy	530 eV
Sample-to-detector distance	5 cm
Pinhole diameter	3 µm
Fluence on dynamic structure	3.5×10^{4}-3.5×10^{7} photons µm^{-2}
Fluence on static structure	1.4×10^{10} photons µm^{-2}
Simulated sample parameters	
Maximum dynamic structure ($H_{50}C_{30}N_{9}O_{10}S_{1}$) thickness	1 µm
Static structure (Au) thickness	20 nm
Protein density	1.35 g cm^{-3}

Table 6.1: Dose reduction simulation parameters.

Numerical simulations of potential radiation dose reduction

To image radiation-sensitive specimens with X-rays, the radiation damage process ultimately limits the achievable resolution [112, 212]. One area currently being explored is the addition of a known diffusive structure to the sample to enhance the scattered signal. Placing a high atomic number element structure in the field of view has demonstrated the possibility of reducing the dose required for obtaining minimum reconstructable diffraction signal [218–223]. Since photons incident on the static region in in situ CDI do not hit the sample, those photons can enhance the measurable signal without inducing extra radiation damage to the sample. Furthermore, a carefully constructed static structure may also be used as additional a priori information to aid phase retrieval. Exploring a combination of these dose reduction strategies can help advance in situ CDI toward dynamic imaging of radiation-sensitive samples.

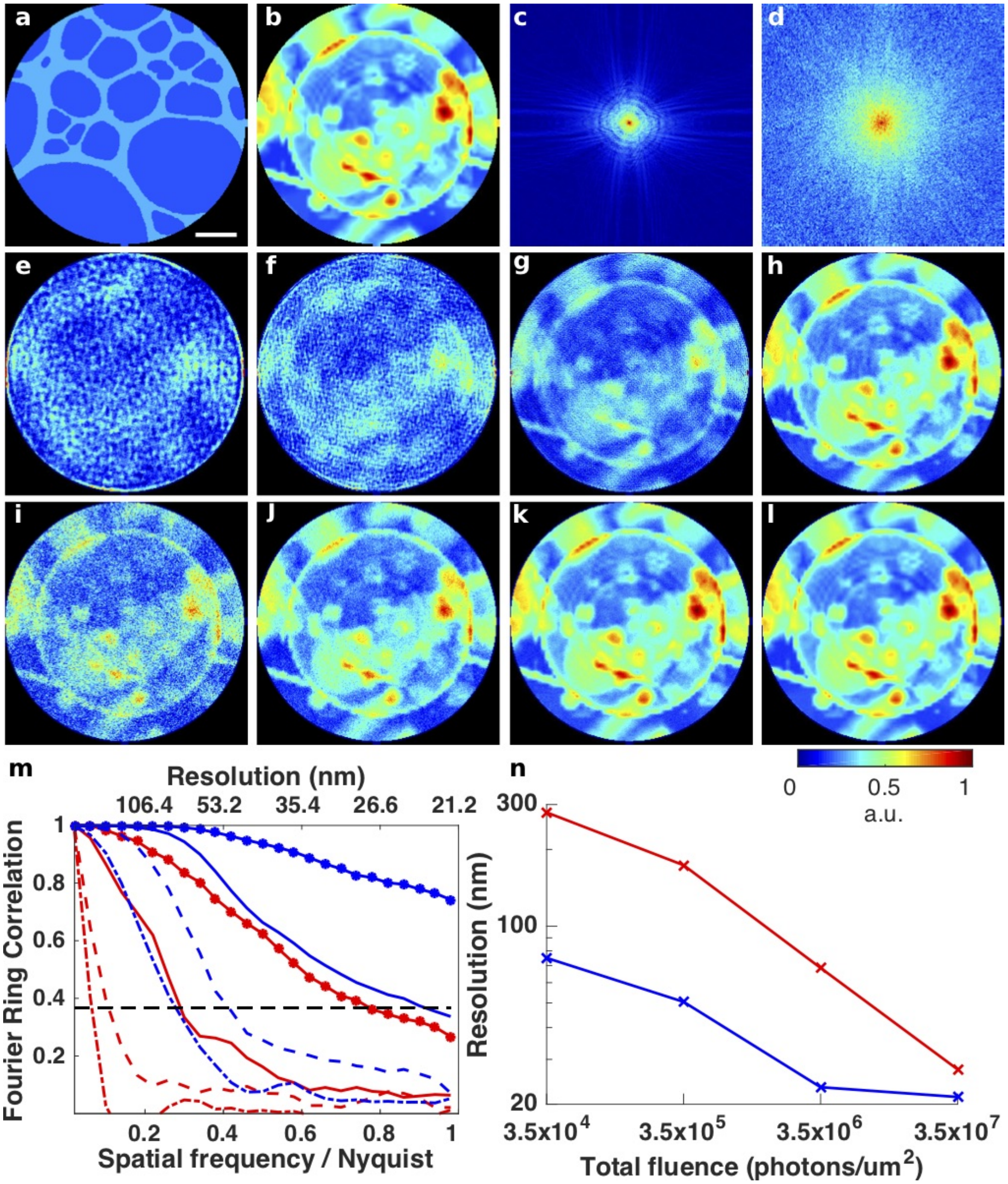
a
b
c
d
e
f
g
h
i
J
k
l
0
0.5
1
a.u.
m
Resolution (nm)
106.4
53.2
35.4
26.6
21.2
Fourier Ring Correlation
1
0.8
0.6
0.4
0.2
0.2
0.4
0.6
0.8
1
Spatial frequency / Nyquist
n
Resolution (nm)
300
100
20
3.5x10^4
3.5x10^5
3.5x10^6
3.5x10^7
Total fluence (photons/um^2)

To examine the feasibility of dose reduction using an auxiliary scattering enhancing structure, we simulated a static structure of a 20-nm-thick Au pattern (Fig. 6.5A) and a biological sample consisting of a vesicle and protein aggregates (Fig. 6.5B, Table 6.1, Methods). Both the static structure and biological sample are submerged in 1-µm-thick H_2O and masked by a 3 µm pinhole. Using coherent soft X-rays (E=530 eV), we first calculated the diffraction patterns only from the biological sample with a total fluence varying from 3.5×10^4 to 3.5×10^7 photons

---

Figure 6.5 *(preceding page)*: Numerical simulations of potential significant dose reduction using in situ CDI. (**A**) A simulated 20-nm-thick Au pattern in 1-µm-thick H_2O static structure. The diameter of the pinhole is 3 µm. (**B**) A simulated biological sample of a vesicle and protein aggregates in 1-µm-thick H_2O. (**C**) Soft X-ray diffraction pattern with a 5×5 missing center, calculated from the biological sample with a photon energy of 530 eV and a fluence of 3.5×10^7 photons μm^{-2}. Poisson noise was added to the diffraction intensity. (**D**) Soft X-ray diffraction pattern calculated from the biological sample with a fluence of 3.5×10^7 photons μm^{-2} and the static structure with a fluence of 1.4×10^{10} photons μm^{-2}. Poisson noise was added to the diffraction intensity. The center-to-center distance between the biological sample and static structure is 3.8 µm. (**E-H**) Image reconstructions of the biological sample without the static structure, with fluences 3.5×10^4, 3.5×10^5, 3.5×10^6, and 3.5×10^7 photons μm^{-2}, respectively. (**I-L**) Image reconstructions with the same fluences on the biological sample as (**E-H**), but with additional 1.4×10^{10} photons μm^{-2} on the static structure. (**M**) Fourier ring correlation of the reconstructions and the model. Red lines correspond to (**E-H**) (dash-dot, dashed, solid, solid-dotted lines, respectively), and blue lines to (**I-L**). (**N**) Achieved spatial resolution of each reconstruction determined by the $1/e$ threshold in the Fourier ring correlation. Scale bar, 400 nm. (*Figure reprinted from* [4]) µm^{-2}, corresponding to a radiation dose ranging from 2.75×10^{3} to 2.75×10^{6} Gy, respectively (Methods). The diffraction patterns were collected by a detector with quantum efficiency of 80% and Poisson noise was added to the diffraction intensity (Fig. 6.5C).

By using the oversampling smoothness (OSS) algorithm [29], we reconstructed the electron density of the biological sample from these noisy diffraction patterns (Fig. 6.5E-H). To quantify the spatial resolution, we calculated the Fourier ring correlation between the reconstructions and the model (Fig. 6.5M). Based on the $1/e$ criterion, we estimated the achieved resolution as a function of the total fluence.

Next, we calculated the diffraction patterns from a combination of the biological sample and the static structure. The total fluence on the biological sample varies from 3.5×10^{4} to 3.5×10^{7} photons µm^{-2}, while the total fluence on the static structure is fixed at 1.4×10^{10} photons µm^{-2}. Experimentally, this can be implemented by introducing an absorber to the pinhole in front of the biological sample. The center-to-center distance between the biological sample and the static structure is 3.8 µm. Figure 6.5D shows the noisy diffraction pattern with a fluence of 3.5×10^{7} photons µm^{-2} on the sample and 1.4×10^{10} photons µm^{-2} on the static structure, which exhibits much higher spatial frequency diffraction signals than that calculated from only the biological sample with the same fluence (Fig. 6.5C).

By using the static structure as a constraint, we reconstructed the electron density of the biological sample from the noisy diffraction patterns, showing significant improvement in image quality and spatial resolution (Fig. 6.5I-L). According to Fourier ring correction (Fig. 6.5M,N), the in situ CDI method can reduce the radiation dose incident on the sample by more than an order of magnitude, while maintaining the same spatial resolution. In some cases (for example, 3.5×10^{4} photons µm^{-2} in Figs. 5m, n), the total dose can be reduced by two orders of magnitude with the same achievable resolution.

Our numerical simulations suggest that the level of radiation dose reduction is related to the structure of the static pattern and the ratio of the coherent fluxes between the static and dynamic structure. Although template-based and phase diverse approachs have been introduced for radiation dose reduction in CDI [218, 219], with in situ CDI we have demonstrated the possibility of reducing the radiation dose by more than an order of magnitude, which we attribute mainly to the non-linearity of the phase retrieval process. If experimentally validated, this could be the most dose efficient X-ray imaging method to probe radiation sensitive systems.

6.4 Discussion

In situ CDI overcomes a major challenge associated with traditional phase retrieval algorithms. In the presence of incomplete data and noise, conventional phase retrieval algorithms can be trapped in local minima and require averaging multiple independent runs to improve the final reconstruction [26, 29, 42, 43, 215]. By enforcing a time-invariant overlapping region as a powerful real-space constraint, in situ CDI is robust to incomplete data and noise, and it can simultaneously reconstruct a time series of complex exit waves to reveal fine structural changes between frames without being trapped in local minima.

Furthermore, the experimental configuration of in situ CDI can be improved by using a dedicated sample chamber, such as microfluidics (Fig. 1a), where the specimen of interest is physically separated from the static region by a barrier. Such customized experimental configuration could simplify the data collection and optimize the quality of reconstructions.

Compared to Fourier holography [224–226], in situ CDI has three unique distinctions. First, in Fourier holography, the spatial resolution is determined by the size of the reference source. In the X-ray regime, it is not only a challenge to fabricate very small reference sources, but also a small reference source would throw away a large fraction of coherent X-ray flux. On the other hand, in situ CDI does not have these limitations as its spatial resolution is only determined by the spatial frequency of the diffraction intensity.

Second, Fourier holography calculates the autocorrelation function from the hologram using the inverse Fourier transform [224–226]. To extract the image of a sample from its autocorrelation function, the sample and the reference source must satisfy a geometry requirement. But in situ CDI uses an iterative algorithm for phase retrieval and has no geometry requirement between the static and dynamic structure.

Third, in Fourier holography, the magnitude of the reference wave has to be comparable to that of the object wave for obtaining good quality autocorrelation functions. With in situ CDI, our numerical simulations indicate the coherent flux incident on the static and dynamic structure can vary by almost six orders of magnitude (Fig. 6.5I). Furthermore, by adjusting the coherent flux between the static and dynamic structure, one can potentially reduce the radiation dose to biological samples by more than an order of magnitude relative to conventional CDI (Fig. 6.5M).

For a proof-of-the-principle purpose, we assumed in the dose reduction simulations that the Au static structure was known a priori, which explains why single frame reconstructions can still be reliable achieved even without time series data. This is in contrast with the Pb dendrite simulation, where the static structure was not known a priori, and was instead reconstructed simultaneously with the dynamic structure, with the aid of a rough mask. The in situ CDI method is unique in that the redundant information does not need to be known explicitly, but can instead be obtained iteratively. To highlight the importance of time series data for the in situ CDI reconstruction, we ran the same 8 keV Pb simulation without knowing or enforcing the static structure. fig. S4 shows that the reconstructions without enforcing the static structure constraint have much lower quality than those with the static structure constraint enforced.

In essence, we have developed a general in situ CDI method for simultaneously reconstructing a time series of complex exit waves of dynamic processes. We validate this method using both numerical simulations and experiments on materials science and biological samples. Our numerical results indicate that the combination of in situ CDI and advanced synchrotron radiation can be used to image dynamic processes in solution with a spatial resolution of 10 nm and a temporal resolution of 10 ms. Using an optical laser, we have performed proof-of-principle experiments of in situ CDI by capturing the growth of Pb dendrites on Pt electrodes immersed in an aqueous solution of $Pb(NO_3)_2$ and reconstructing a time series of the phase images of live glioblastoma cells in culture medium.

There are four unique features associated with in situ CDI. First, it can simultaneously reconstruct a time series of complex exit waves with robust and fast convergence. Because no averaging is required in the reconstruction, fine structure variation at different time frames can be reliably reconstructed. Second, compared to liquid cell TEM [16], this method can be used to study the dynamics of a wider range of specimens (either thick or thin) in an ambient environment by optimizing X-ray energy based on the sample thickness and the chemical composition and reducing the multiple scattering effect.

Third, while ptychography uses partially overlapping structure in the space domain as a constraint, in situ CDI uses partially overlapping structure in the time domain as a constraint. Furthermore, by avoiding the requirement of sample scanning, in situ CDI can achieve higher temporal resolution than ptychography. Finally, this in situ approach can be applicable to any type of radiation with flexible experimental geometry as long as a static structure can be used as a time-invariant constraint. The spatial and temporal resolution of the method is ultimately limited by the coherent flux and the read-out time of the detector.

As coherent X-ray sources such as XFELs, advanced synchrotron radiation and high harmonic generation [204–206] as well as high-speed detectors [207] are under rapid development worldwide, we expect that this general in situ CDI method can potentially open the door to imaging a wide range of dynamical phenomena with high spatiotemporal resolution.

CHAPTER 7

Conclusion

7.1 Summary of findings

Aim 1: To combine X-ray, electron and optical microscopy and collect multidimensional data for correlating different properties of a common sample

Study 1 reported the development of 3D correlative microscopy that used hard X-ray ptychography and X-ray fluorescence microscopy to simultaneously study intact, unlabeled, and cryogenically preserved cells. Ptychographic tomography provided detailed 3D ultrastructure of a 10 µm frozen-hydrated *C. reinhardtii* with 45 nm spatial resolution, and X-ray fluorescence tomography provided trace element distributions within the alga. Data from both methods are correlated to locate and verify the identities of major intracellular organelles such as contractile vacuoles and pyrenoids. Whereas conventional single modal microscopy methods can only rely on mass density thresholding to infer the identities of organelles, or on trace element distributions to localize organelles without seeing the surrounding structures, the correlative X-ray ptychography and fluorescence 3D microscopy demonstrated in this study was able to achieve both goals at the same time. Moreover, since both techniques captured different signals from a single measurement, this parallel data acquisition scheme was able to streamline data collection and post-processing, and also prevent unnecessary sample transfer. This ability to non-destructively map nanoscale cellular ultrastructure in 3D without chemical labeling highlighted the advantage of such intramodal correlative microscopy method for studying complex biological specimen.

To extend beyond intramodal X-ray microscopies by incorporating additional modalities that can provide multidimensional insights into complex samples, Study 2 examined the combined use of X-ray ptychography, STXM absorption spectromicroscopy, EDS and STEM tomography to probe a micrometer fragment from a heterogeneous Allende meteorite. This intermodal microscopy technique provided chemical and textural evidence of the meteorite's diverse nanoscopic phase assemblage with 15 nm spatial resolution and hinted at potential processes that occurred before or after accretion. EDS tomography provided 3D elemental mappings that revealed localized and highly heterogeneous compositions in the grain, and STXM spectromicroscopy provided unique absorption spectra that acted as fingerprints to elucidate different chemical states. Taken together, they revealed the presence of different phase assemblage that suggest various classifications of rock-forming silicates in the grain.

Furthermore, HAADF tomography revealed the presence of nanoscopic shock veins and pockets inside the grain, and spectroscopic ptychography further enhanced the finding by showing that the shock veins and pockets comprised Al, Fe and Cr, suggesting that the Allende parent body or the accreted components experienced impact-induced melting at some stage. This interesting finding showcased how potentially important intermodal X-ray and electron microscopy can be for understanding heterogeneous materials such as meteorites. The metallic shock veins revealed by spectroscopic ptychography was not observed in EDS due to differences in the underlying image formation principles (EDS measures secondary emission whereas CDI measures diffraction). Therefore, by leveraging observations from different imaging methods, we were able to synthesize diverse information to draw more complete conclusions from a sample.

Going beyond probing elemental, chemical and ensemble structural properties of materials using a multimodal imaging paradigm, Study 3 focused on leveraging linearly polarized X-ray ptychography and electron scanning nanobeam diffraction (4D-STEM) to study chemical bond orientations in optically anisotropic sample. Both techniques measured micrometer-sized *S. aculeata* coral fragments and mapped the distribution of crystal orientations with 35 nm spatial resolution. X-ray ptychography leveraged polarization-dependent absorption contrast to map crystal orientations in the dichroic biomineral, and it revealed nanoscale subdomains with both narrow ($< 20°$) and wide ($> 35°$) c-axis angular spread. Evidence of co-oriented but disconnected corallite subdomains indicated more diverse nanoscale crystalline architecture than previously appreciated, suggesting the need for a new model to elucidate coral skeleton formation. Moreover, the observation of strong linear phase dichroism suggested the possibility of using linearly polarized X-ray phase imaging as a dose-efficient alternative for mapping molecular bond orientations.

To validate ptychography results, we used electron scanning nanobeam diffraction to evaluate crystal orientation based on diffraction signals. The findings revealed similar regions of homogeneous crystal orientations that qualitatively agree with ptychography. In future studies, such correlative X-ray and electron methods could be used more effectively by studying dichroic materials at different length scales, with X-ray method probing the bulk specimen for ensemble orientational characteristics and medium-range order, and electron method examining boundary phase, orientation, strain mappings and local ordering.

Aim 2: To develop novel coherent diffractive imaging reconstruction algorithm for high spatiotemporal resolution in situ imaging

The previous three studies focused mostly on obtaining high resolution but static structural and chemical mappings of materials, so Study 4 extended the multidimensional hybrid imaging paradigm into the temporal domain. Study 4 focused on developing a new in situ CDI method for investigating ultrafast dynamics of non-crystalline materials in the nanometer regime. In situ CDI introduced a time-invariant overlapping region in real space and enforced it as a real-space constraint, much the same way spatial overlap in ptychography is applied as a redundancy constraint. The accompanying algorithm can simultaneously reconstruct a time series of complex exit wave of dynamic processes with robust and fast convergence.

We validated this method using optical laser experiments by capturing dynamic processes of dendritic growth in battery charge cycles, and of cell fusion events in glioblastoma community. The same principle behind the technique was applicable to other coherent light sources, as shown by numerical simulations with realistic X-ray CDI parameters. Furthermore, our numerical simulations suggested that in situ CDI can potentially reduce radiation dose by more than an order of magnitude relative to conventional single shot CDI when highly scattering structures were introduced into the time-invariant overlapping region. Taken together, in situ CDI introduced an additional temporal dimension that can add to the overall hybrid imaging paradigm demonstrated in previous studies.

7.2 Future directions and Implications

Beyond the efforts put forth in this dissertation to demonstrate hybrid X-ray and electron microscopy for functional, multidimensional imaging, much work remains to be done before a truly practical multimodal imaging paradigm can be realized. Specifically, more planning and experimentation is needed in three important areas: consolidated sample environment, streamlined data acquisition, and correlative data analysis. I will discuss each topic below.

Consolidated sample environment

The use of a standardized sample holder for different microscopes will be important for establishing a intermodal imaging paradigm. In Study 1, the cryogenic green algae is kept in a controlled cold stage unit from sample loading, sample transfer, all the way to data acquisition to avoid recrystallization of amorphous ice. In Study 2, the X-ray microscope used for ptychography is designed with a TEM-compatible specimen holder such that the meteorite grains deposited on a TEM grid can freely move between X-ray and electron microscopes without superfluous sample transfer overhead, and without unnecessarily perturbing the sample. Such sample holder compatibility should also extend to optical microscopy so that a truly multiscale microscopy can be achieved. Another improvement can be made by maintaining the sample in a controlled environment, which can enable multimodal in situ microscopy. Moreover, the repeated sample transfer to multiple imaging instruments also warrants the development of a customized sample substrate for easy localization of the same specimen in different microscopes. An ideal substrate should have clearly distinguishable built-in fiducials in the form of patterned structures that are easily recognized at the nano- to micrometer length scales.

Streamlined data acquisition

When considering horizontal integration across different imaging modalities, the reality of a single all-in-one microscope that combines synchrotron X-ray with electron and optical microscopes is unlikely due to inherently different stability requirements and instrument geometry (electron microscope beam path is vertical, X-ray microscope's is horizontal). A more realistic strategy will be to keep sample in a consolidated environment as mentioned previously and use a compatible sample holder to streamline transfers between microscopes.

Nonetheless, even within a single imaging mode, multiple advanced signals and techniques can still be incorporated into an instrument to streamline data acquisition. For instance, the correlative X-ray and electron microscopy of meteorite highlighted in Study 2 is open to other measurement channels, such as X-ray fluorescence microscopy from Study 1. Moreover, X-ray linear polarization shown in Study 3 is available at most synchrotron beamlines, therefore dichroic ptychography can be readily integrated into the experimental pipeline. Lastly, since in situ CDI employs a similar experimental geometry as ptychography, it can also readily integrate into any ptychography microscope to provide dynamic information. Similar integrations can help accelerate the experimental process by maximizing the information diversity of the measurements.

Even for intermodal imaging that involves multiple light sources and techniques, smart data collection processes can reduce required measurements and enhance data quality. One strategy would be to synergistically leverage redundant information acquired in different modalities to reduce the amount of data that needs to be collected for analysis. For instance, in ptychography, information redundancy in the form of spatial overlap is not as stringent when a good initial guess of the sample can be used as input to the phase retrieval algorithm. So with a carefully planned data acquisition workflow, it may be possible to collect fewer ptychographic diffraction patterns, but in post-processing feed low resolution STEM or STXM images as input into the ptychography algorithm and still get good quality ptychography results.

In the case where intermodal approach is needed to study a sample across a wide range of length scales, one strategy would be to first non-destructively probe the bulk structures using X-rays to understand its collective properties at the tens to hundreds of micrometer scale, then sequentially treat the specimen by ablation or sectioning to access finer structures for imaging. This process can iterate until internal near-atomic features are probed. A similar strategy that couples sequential sample preparation with imaging can ensure that the specimen maintains its integrity at each step of data acquisition, and will also greatly benefit subsequent data analysis.

Correlative data analysis

Extensive analysis and comparison of the multidimensional dataset obtained from different modalities is needed to fully take advantage of the hybrid imaging paradigm. A deeper understanding of each imaging technique's strengths and limitations is necessary to correlate information effectively and to unveil new insights. For instance, Study 2 demonstrates how differences in underlying image formation principles between EDS and spectroscopic ptychography manifest when investigating the small metallic melt veins in the meteoric fragment. Furthermore, although 4D-STEM is used in Study 3 mostly to validate linear dichroic X-ray ptychography results in the study of crystal ordering in corals, analysis of those types of data can be complementary by focusing on different hierarchies, perhaps with 4D-STEM used for higher resolution, near atomic characterization, and polarized X-ray imaging used for examining larger ensemble properties. Lastly, as in situ CDI gets implemented into synchrotron-based ptychography microscopes in the future, sample dynamics captured during in situ measurements can be coupled with large field of view ptychography images to correlate between structure and dynamics with high spatiotemporal resolution. Ideas for synthesizing new scientific insights through correlative data analysis, such as those mentioned above, can truly highlight the power of an adaptive X-ray and electron imaging platform.

Multi-modal correlative microscopy for the future

In the grand scheme of things, this dissertation leverages new sample preparation, fast detectors, advanced algorithms and big data manipulation to formulate a hybrid imaging technology that far exceeds the capabilities of single modal microscopy. It serves as an initial effort to encourage multidisciplinary thinking in X-ray and electron imaging sciences. The eventual goal of this research is to establish an imaging paradigm that can provide structural, chemical, electronic, magnetic and dynamic insights into complex functional materials and biological systems, with length scales spanning from single molecular machines to multiple cells. I believe such powerful and broadly-applicable microscopy tool can improve mesoscale detection and enable life and material science researchers to develop new treatment of diseases, assess the effectiveness of new biologics, materials, processes, devices, and procedures, and ultimately help to guide general scientific decision-making.

APPENDIX A

Chapters 3-6 supplementary materials

A.1 Chapter 3 supplementary materials

Please see next page

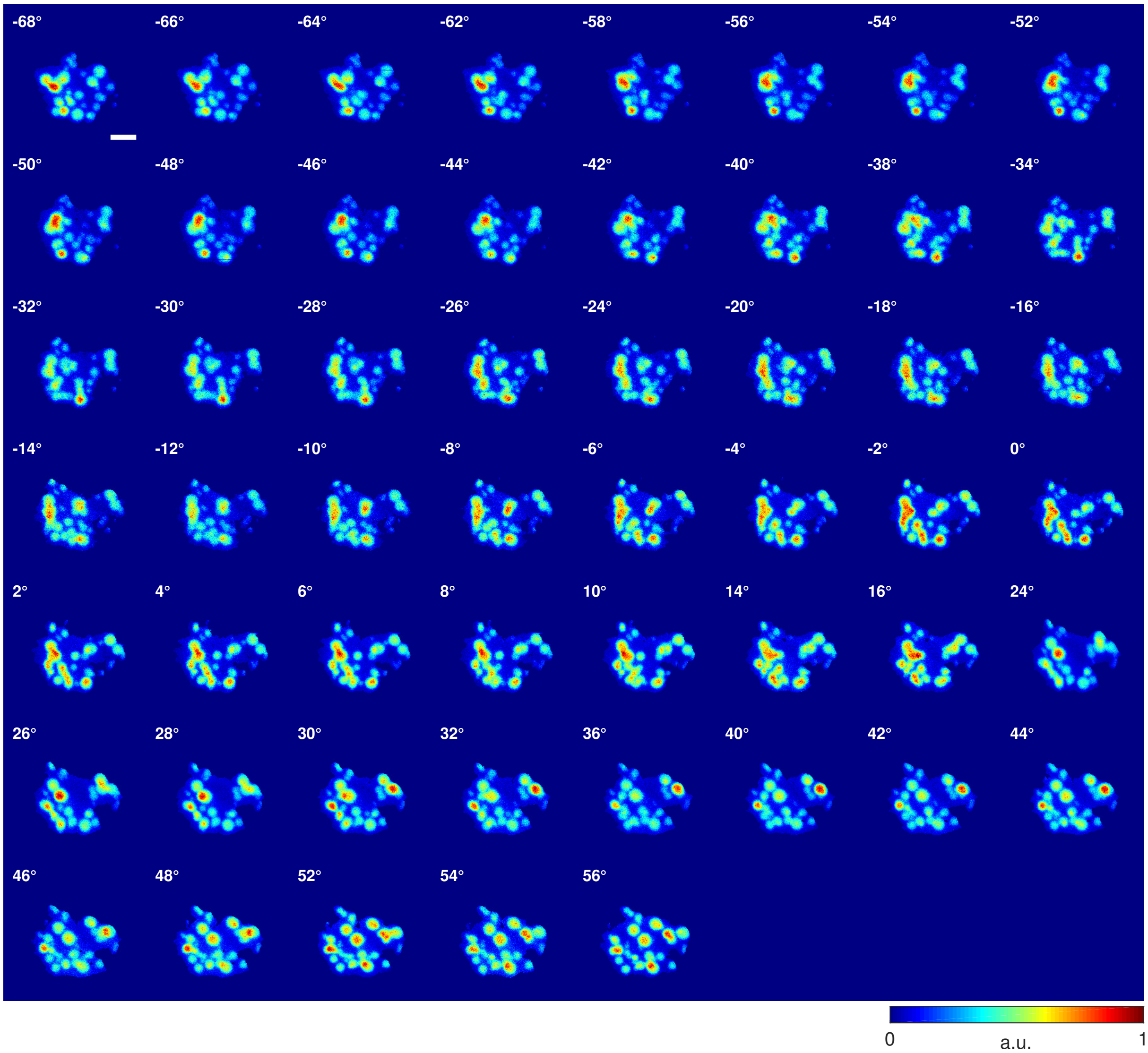

Figure S1. **Experimental phosphorus channel X-ray fluorescence projections.** All 53 background-subtracted and aligned phosphorus channel X-ray fluorescence microscopy projections used as input for GENFIRE reconstruction, with tilt range from -68° to 56°. Scale bar, 2 μm.

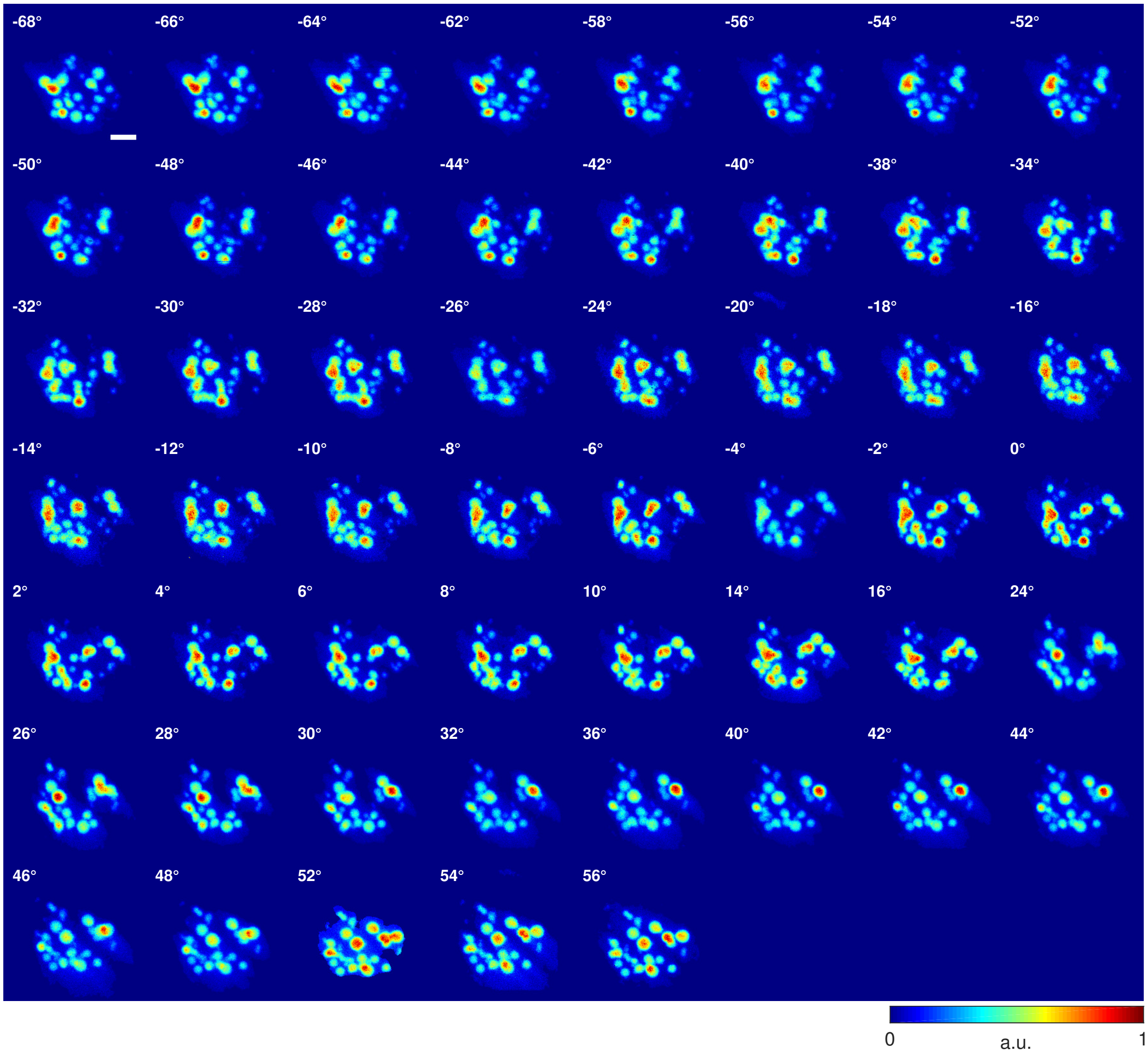

Figure S2. Experimental calcium channel X-ray fluorescence projections. All 53 background-subtracted and aligned calcium channel X-ray fluorescence microscopy projections used as input for GENFIRE reconstruction, with tilt range from -68° to 56°. Scale bar, 2 µm.

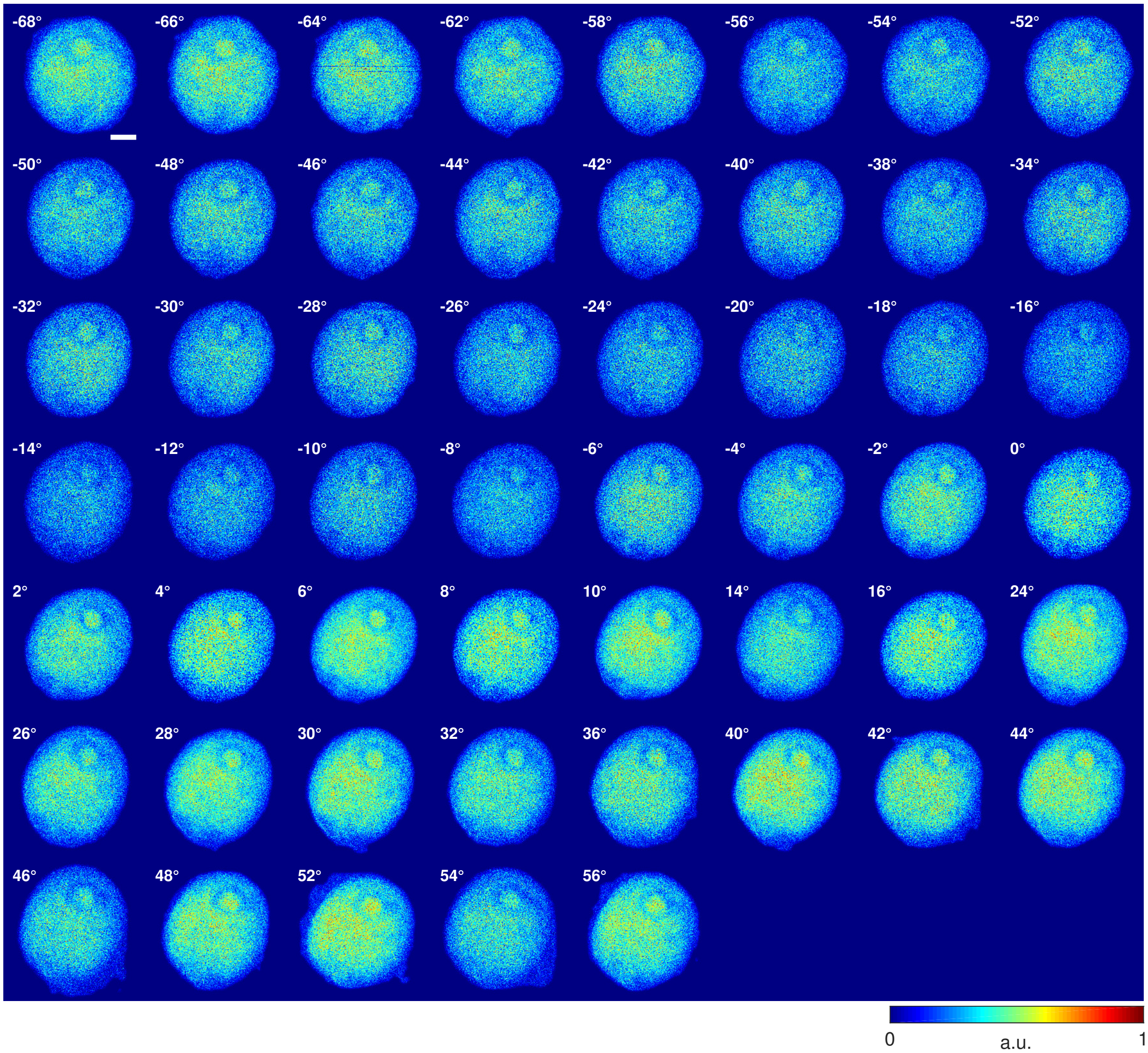

Figure S3. Experimental sulfur channel X-ray fluorescence projections. All 53 background-subtracted and aligned sulfur channel X-ray fluorescence microscopy projections used as input for GENFIRE reconstruction, with tilt range from -68° to 56°. Scale bar, 2 μm.

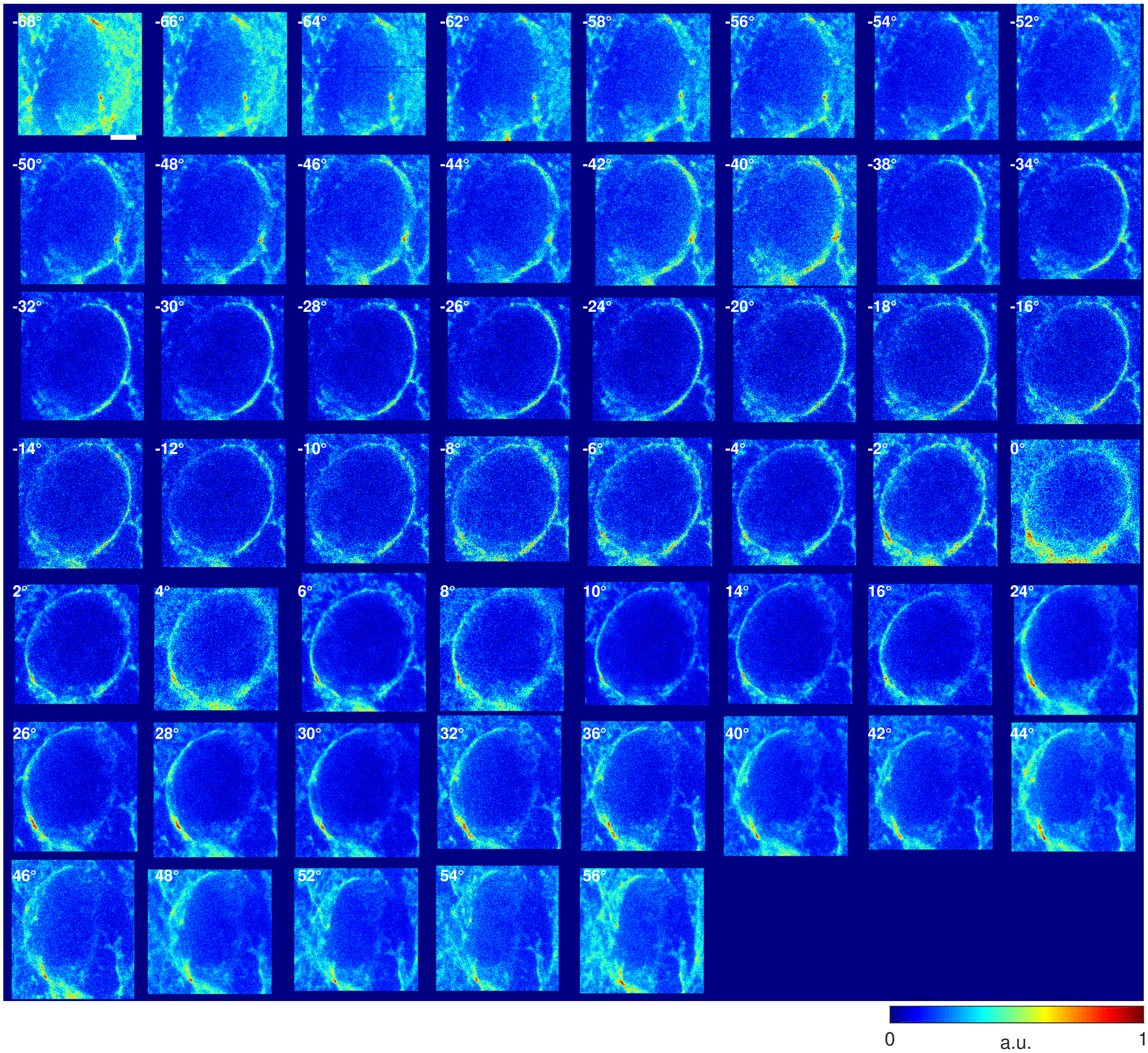

Figure S4. Experimental chlorine channel X-ray fluorescence projections. All 53 aligned chlorine channel X-ray fluorescence microscopy projections used as input for GENFIRE reconstruction, with tilt range from -68° to 56°. Scale bar, 2 μm.

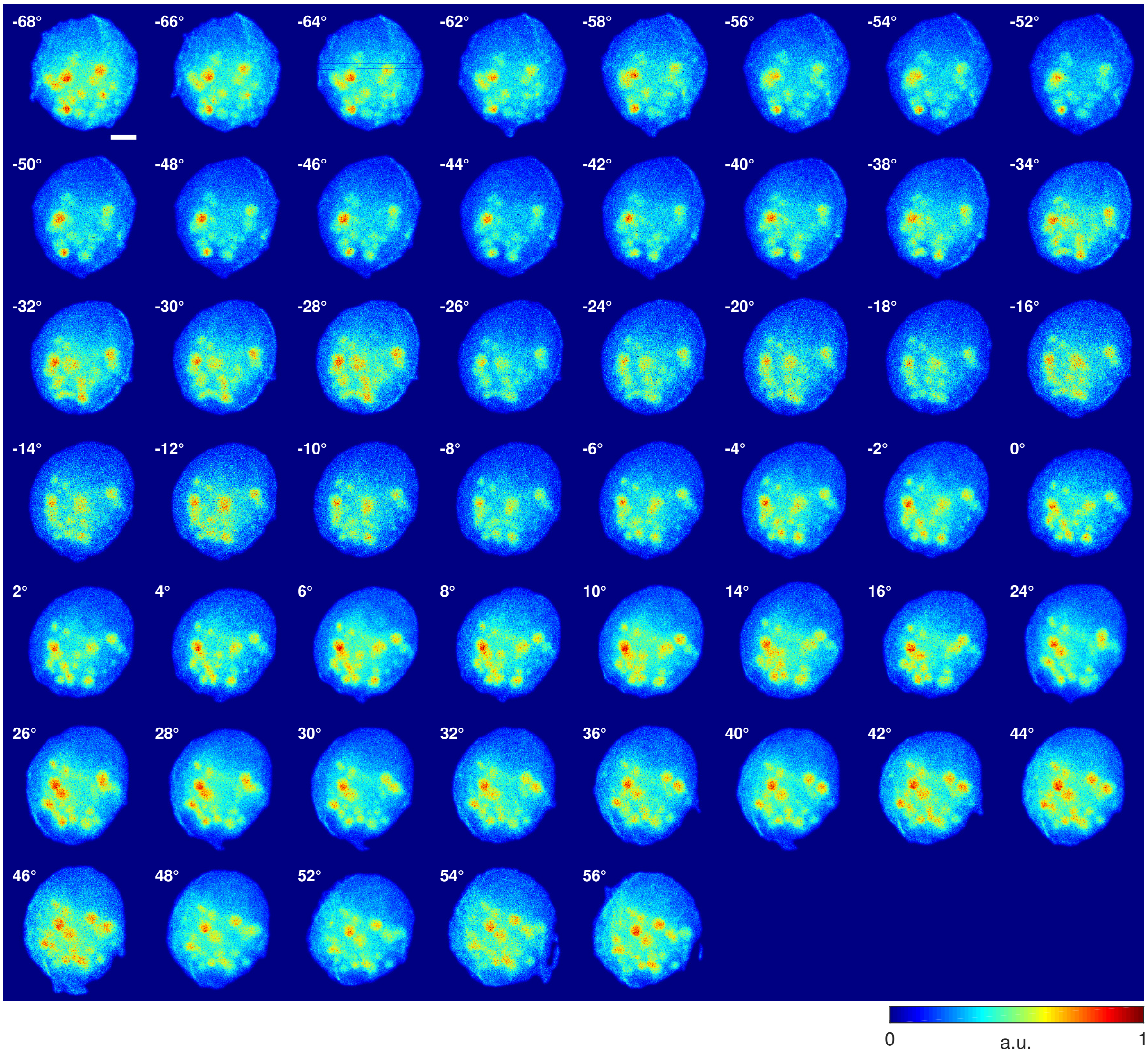

Figure S5. Experimental potassium channel X-ray fluorescence projections. All 53 background-subtracted and aligned potassium channel X-ray fluorescence microscopy projections used as input for GENFIRE reconstruction, with tilt range from -68° to 56°. Scale bar, 2 μm.

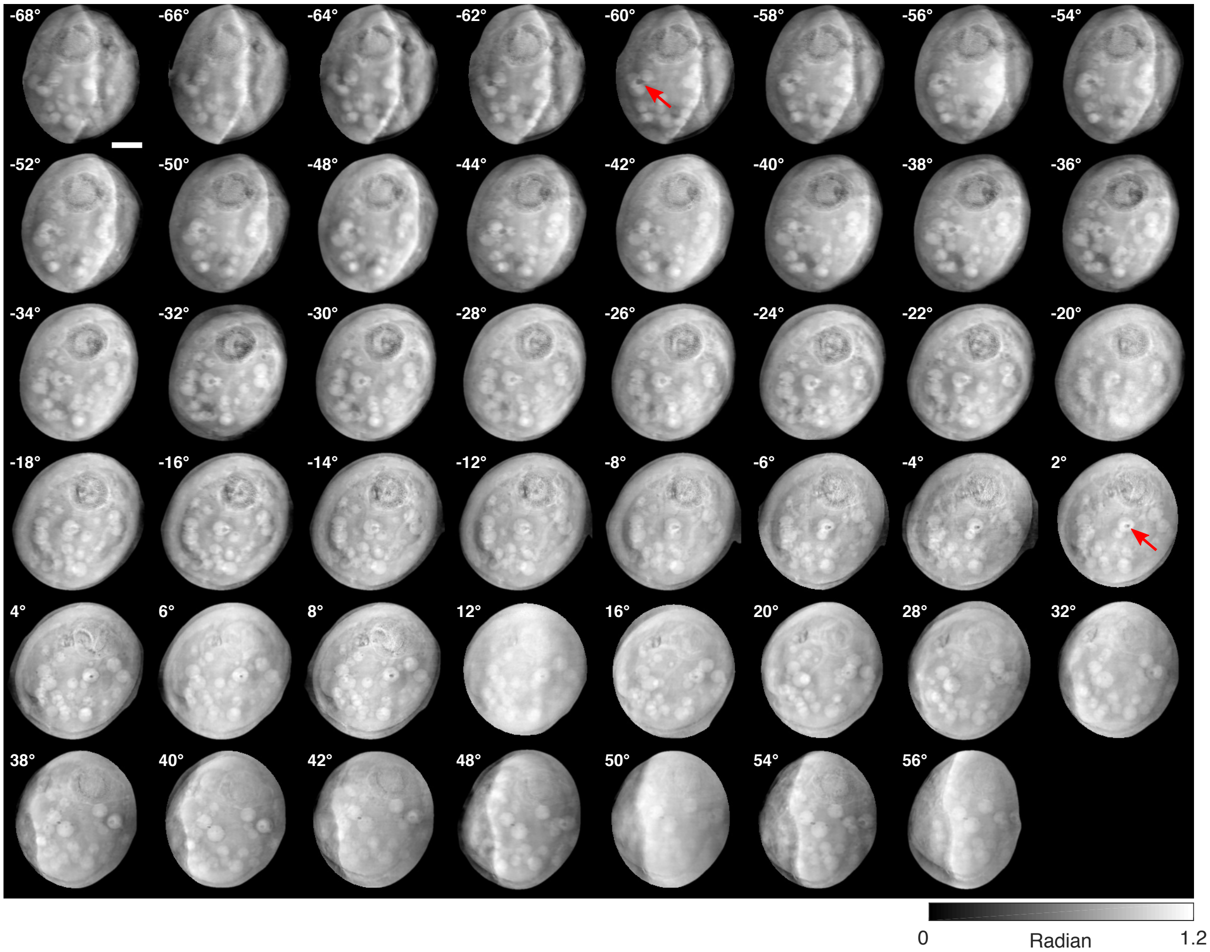

Figure S6. Experimental ptychography projections. All 47 background-subtracted and aligned ptychography phase projections used as input for GENFIRE reconstruction, with tilt range from -68° to 56°. The red arrows highlight the X-ray-induced damage from accidental over-exposure at 60° (correspond to same viewing angle as Fig. 2c) and 2° projections. Scale bar, 2 µm.

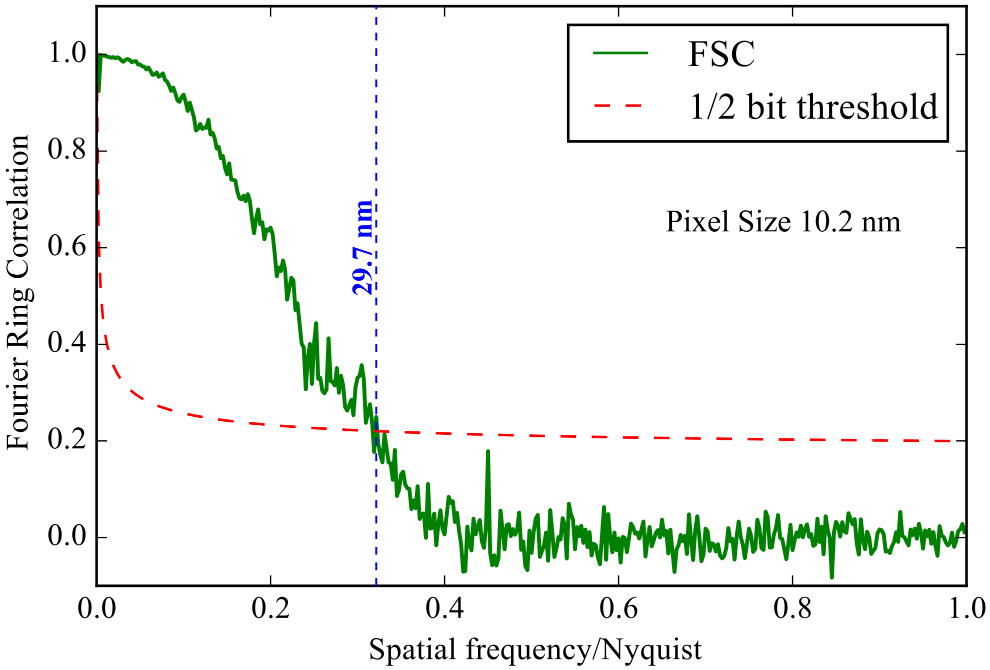

Figure S7. Resolution of 2D ptychography projections. Fourier ring correlation (FRC) of two identical ptychography projection measurements at zero degree, indicating a resolution of 29.7 nm using the half-bit criterion.

A.2 Chapter 4 supplementary materials

Please see next page

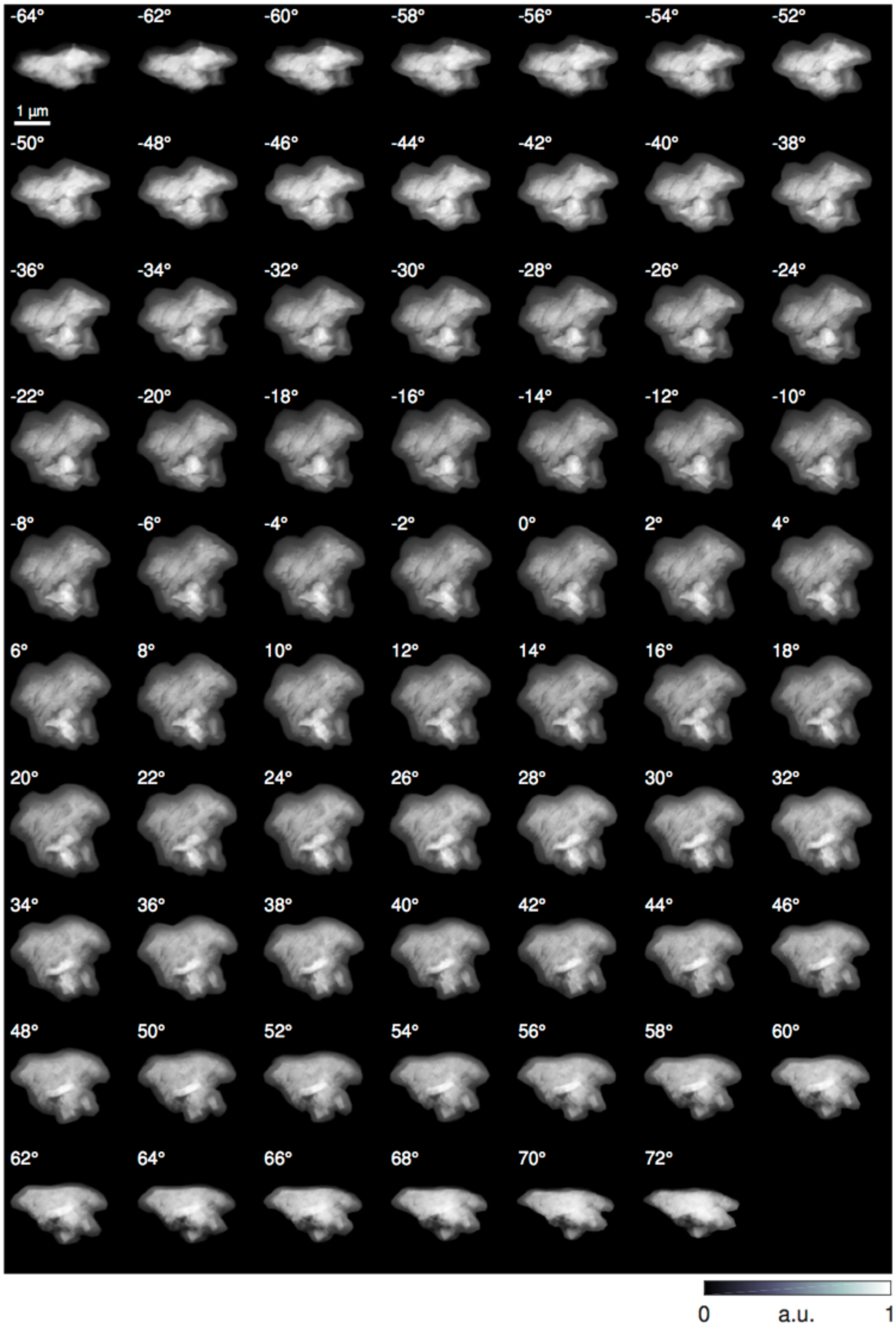

Fig. S1. Experimental HAADF tilt series. All 69 processed HAADF projections used as input for GENFIRE reconstruction. Each image was masked, normalized to reference projection, background subtracted, and aligned by center-of-mass and common line alignment. Background subtraction was iterated with alignment to minimize common line differences. Horizontal direction is the rotation axis.

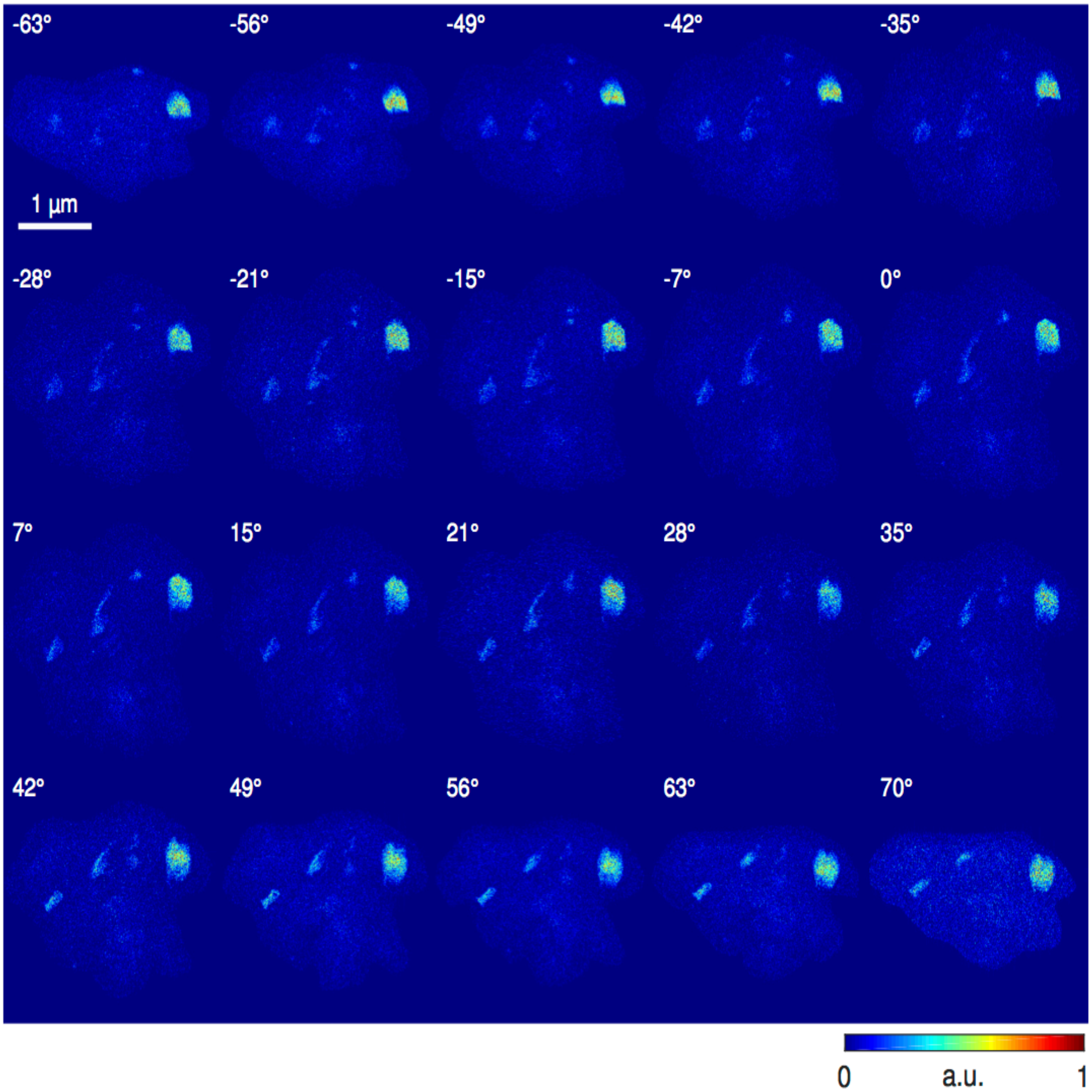

Fig. S2. Experimental Aluminum channel EDS tilt series. All 20 processed aluminum EDS projections used as input for GENFIRE reconstruction. Each image was masked, normalized to reference projection, background subtracted, and aligned by center-of-mass and common line alignment. Background subtraction was iterated with alignment to minimize common line differences.

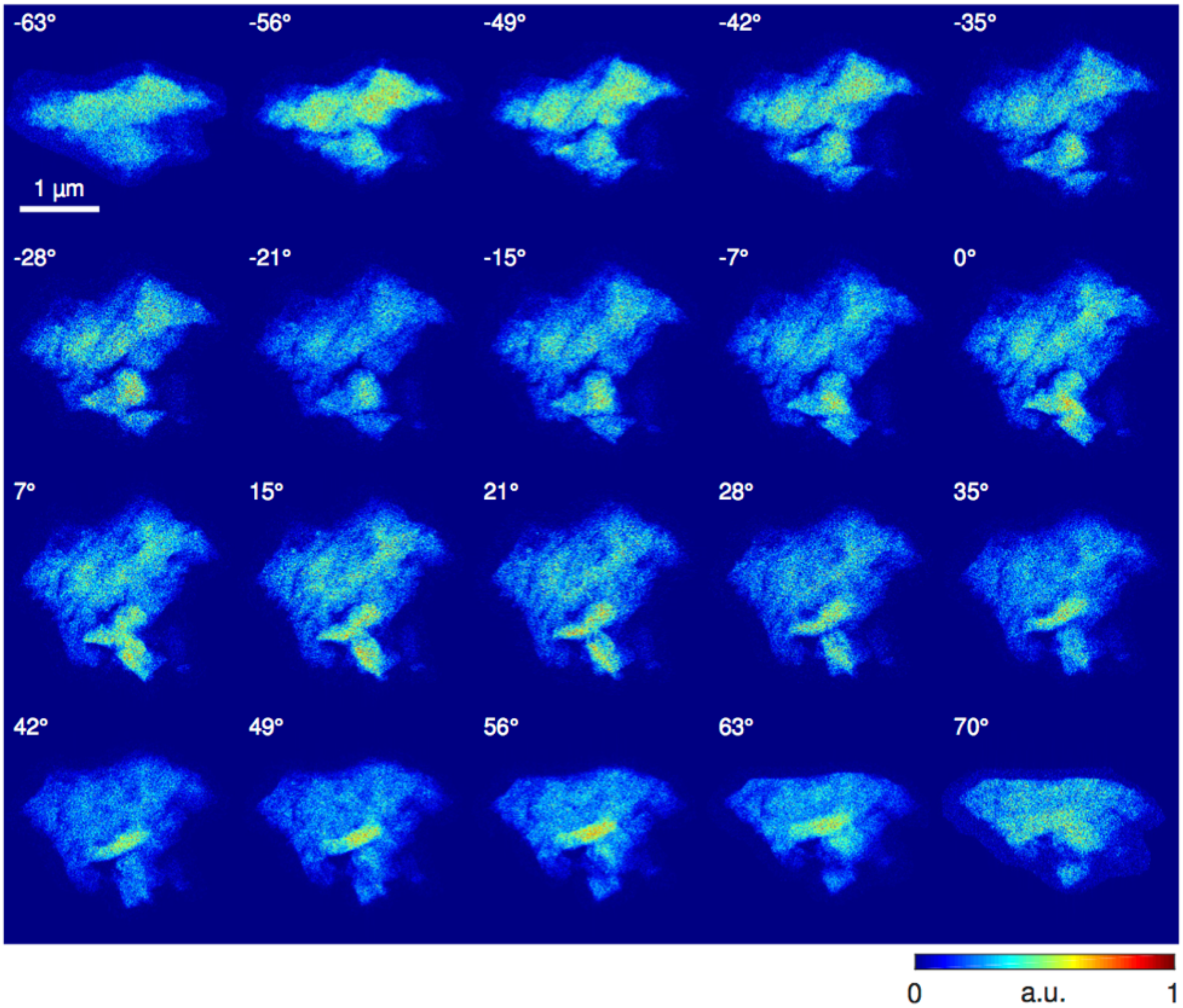

Fig. S3. Experimental Iron channel EDS tilt series. All 20 processed Iron EDS projections used as input for GENFIRE reconstruction. Each image was masked, normalized to reference projection, background subtracted, and aligned by center-of-mass and common line alignment. Background subtraction was iterated with alignment to minimize common line differences. Horizontal direction is the rotation axis.

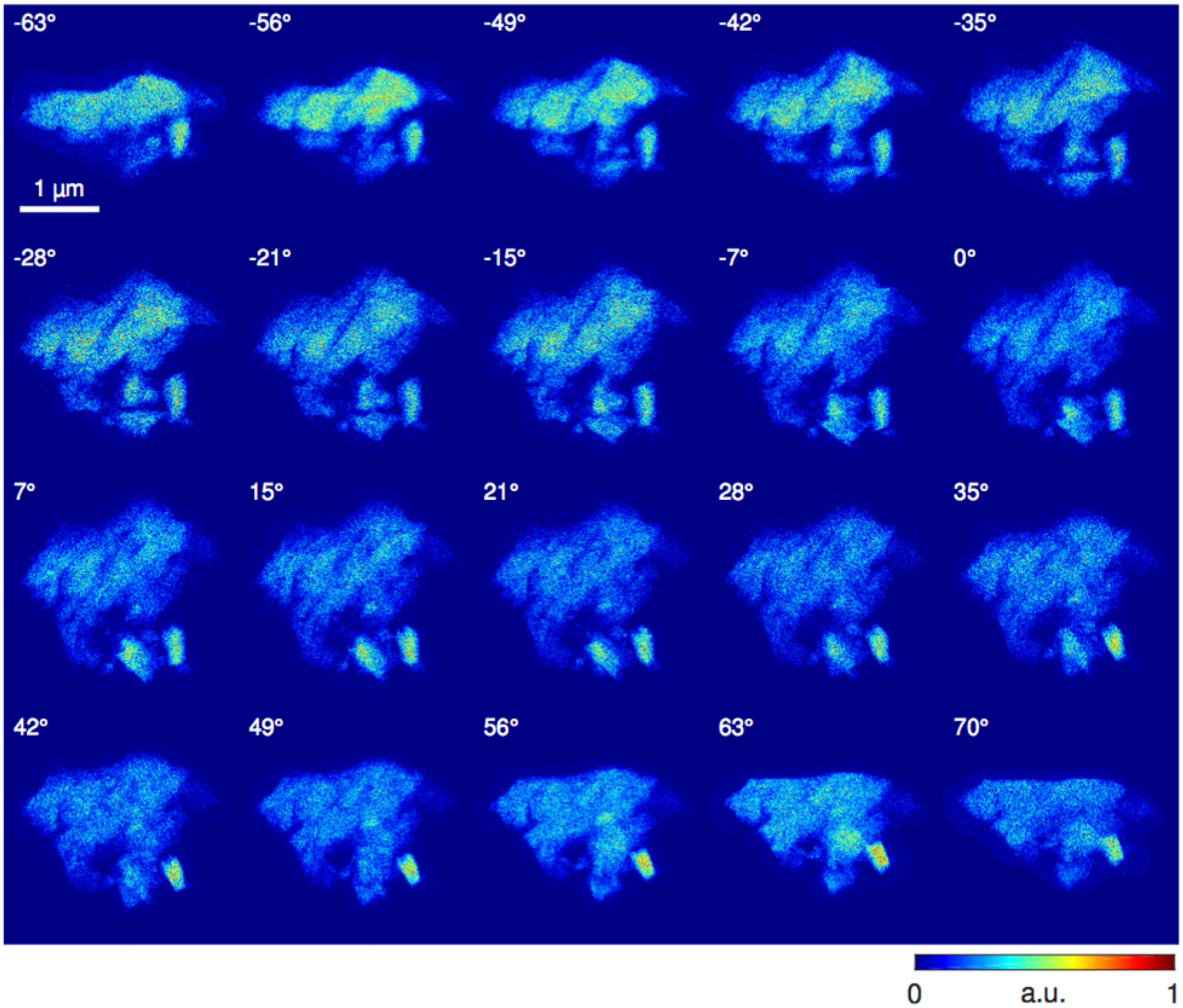

Fig. S4. Experimental Magnesium channel EDS tilt series. All 20 processed Magnesium EDS projections used as input for GENFIRE reconstruction. Each image was masked, normalized to reference projection, background subtracted, and aligned by center-of-mass and common line alignment. Background subtraction was iterated with alignment to minimize common line differences. Horizontal direction is the rotation axis.

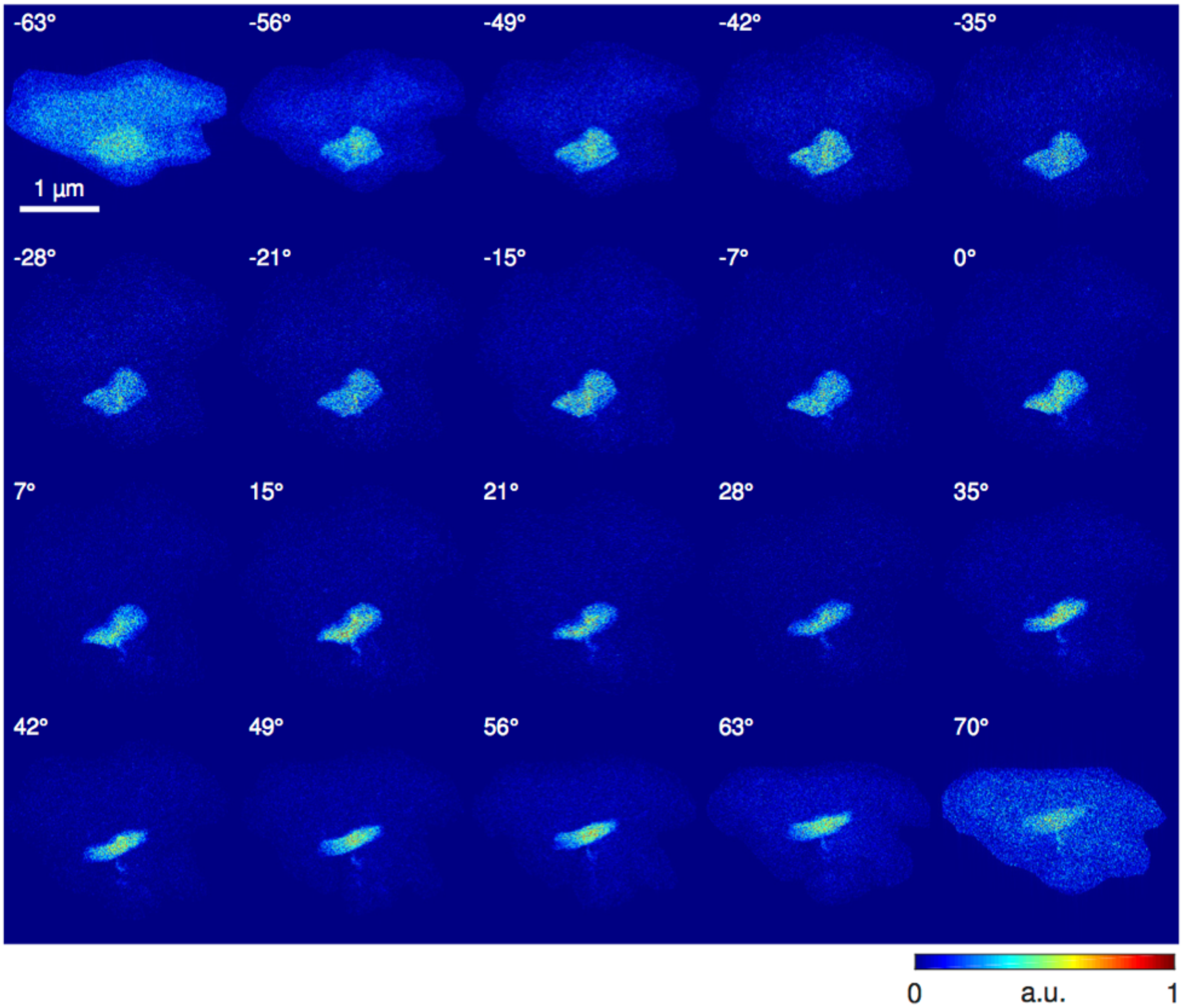

Fig. S5. Experimental Nickel channel EDS tilt series. All 20 processed Nickel EDS projections used as input for GENFIRE reconstruction. Each image was masked, normalized to reference projection, background subtracted, and aligned by center-of-mass and common line alignment. Background subtraction was iterated with alignment to minimize common line differences. Horizontal direction is the rotation axis.

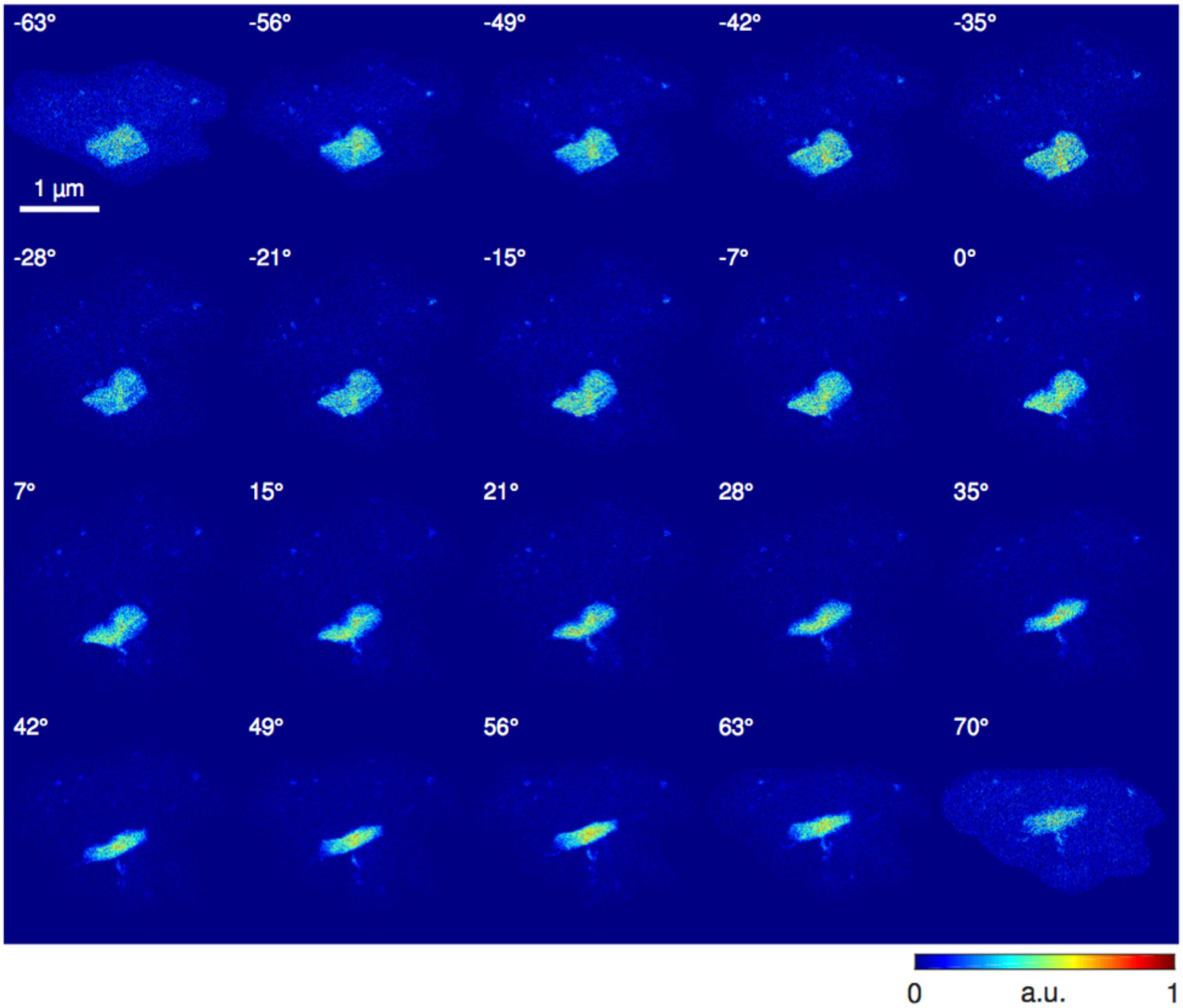

Fig. S6. Experimental Sulfur channel EDS tilt series. All 20 processed Sulfur EDS projections used as input for GENFIRE reconstruction. Each image was masked, normalized to reference projection, background subtracted, and aligned by center-of-mass and common line alignment. Background subtraction was iterated with alignment to minimize common line differences. Horizontal direction is the rotation axis.

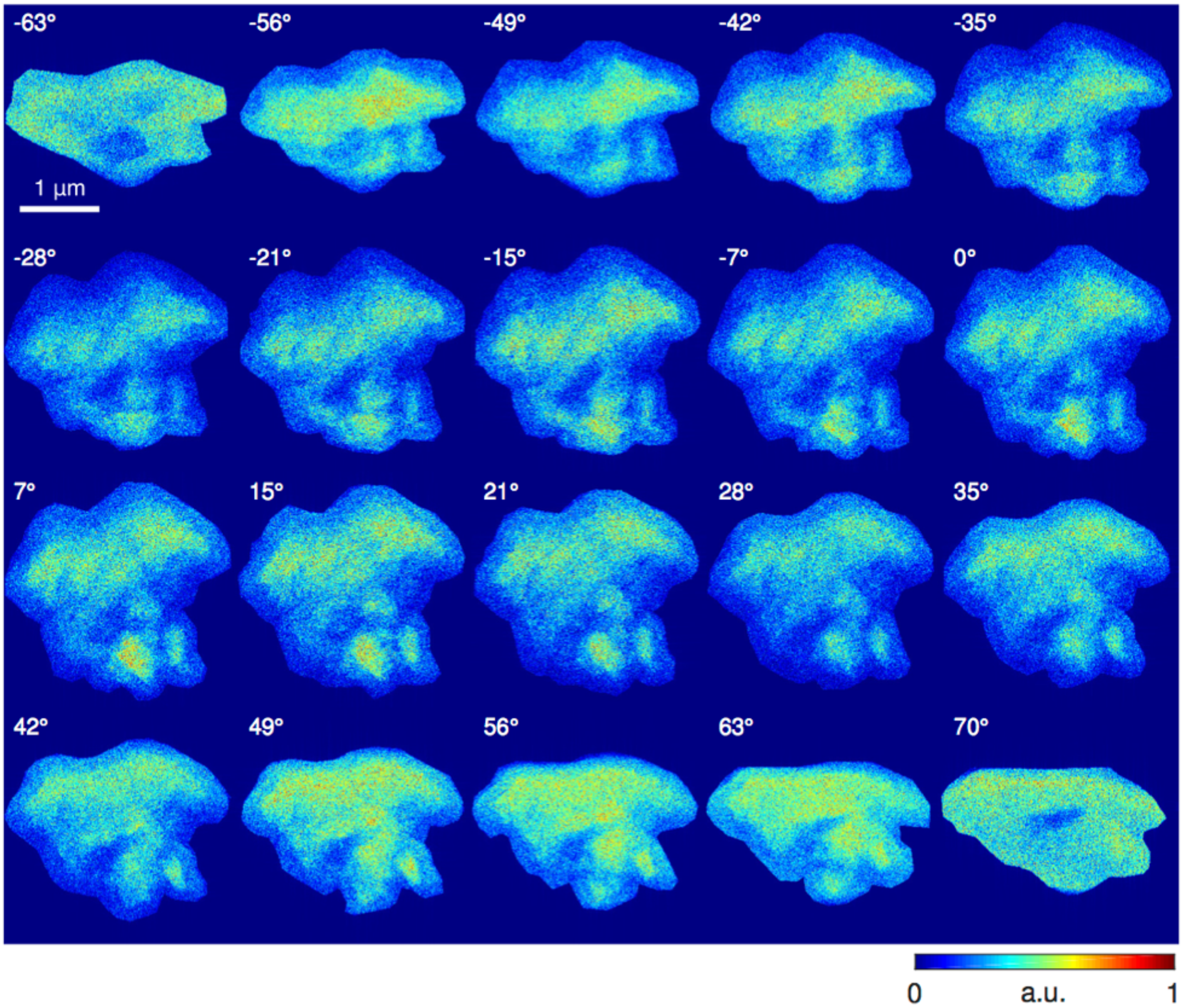

Fig. S7. Experimental oxygen channel EDS tilt series. All 20 processed oxygen EDS projections used as input for GENFIRE reconstruction. Each image was masked, normalized to reference projection, background subtracted, and aligned by center-of-mass and common line alignment. Background subtraction was iterated with alignment to minimize common line differences. Horizontal direction is the rotation axis.

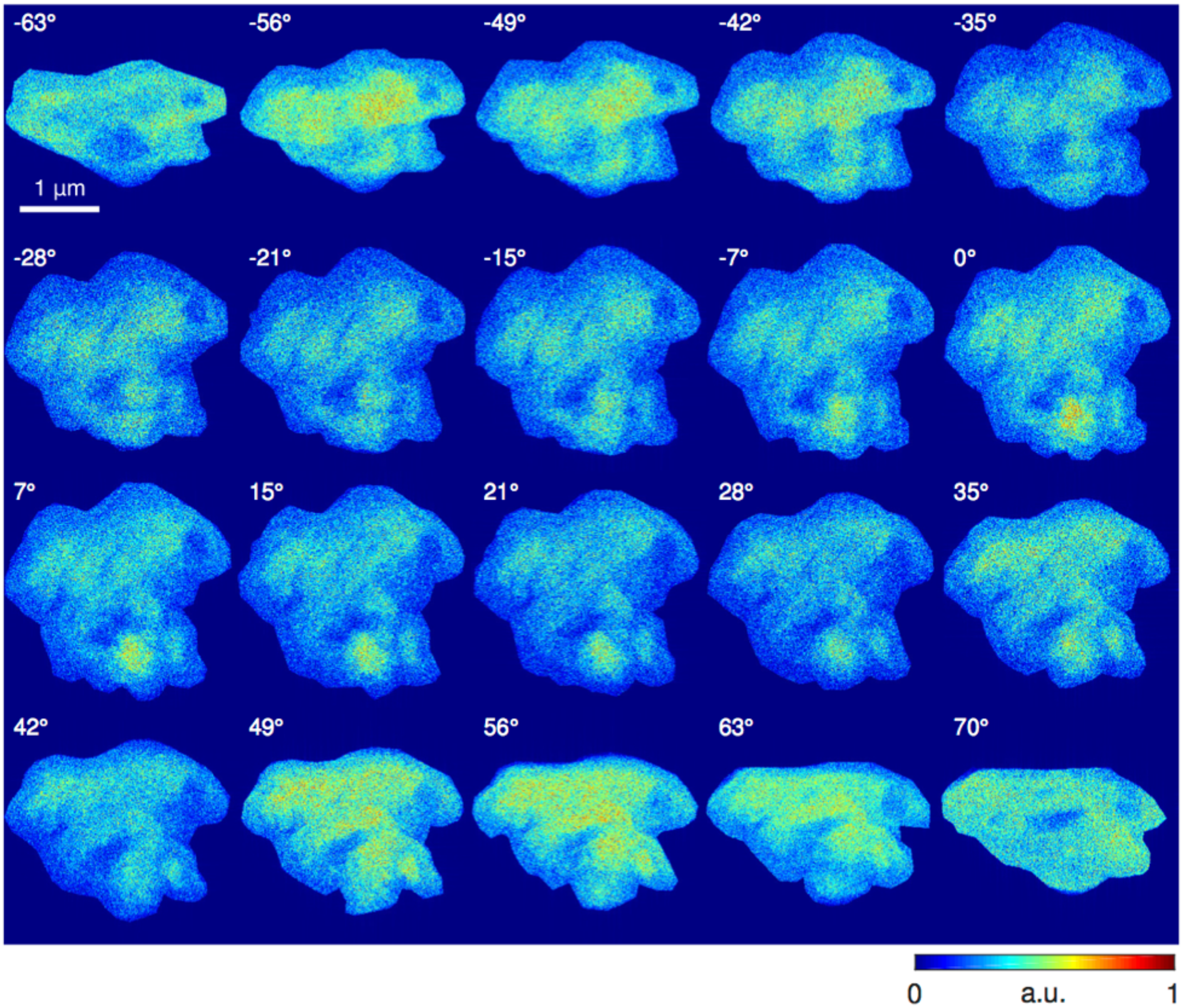

Fig. S8. Experimental silicon channel EDS tilt series. All 20 processed silicon EDS projections used as input for GENFIRE reconstruction. Each image was masked, normalized to reference projection, background subtracted, and aligned by center-of-mass and common line alignment. Background subtraction was iterated with alignment to minimize common line differences. Horizontal direction is the rotation axis.

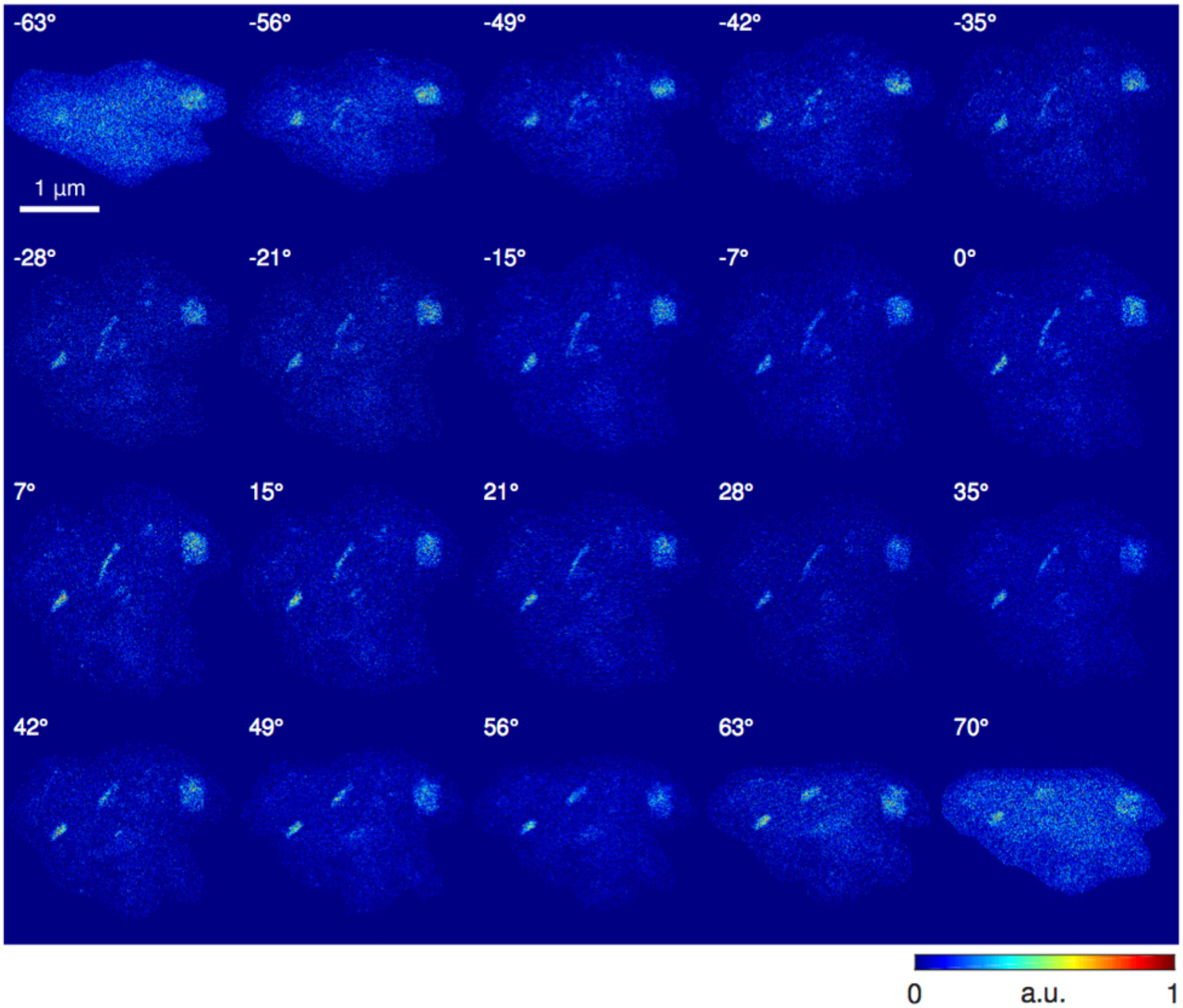

Fig. S9. Experimental chromium channel EDS tilt series. All 20 processed chromium EDS projections used as input for GENFIRE reconstruction. Each image was masked, normalized to reference projection, background subtracted, and aligned by center-of-mass and common line alignment. Background subtraction was iterated with alignment to minimize common line differences. Horizontal direction is the rotation axis.

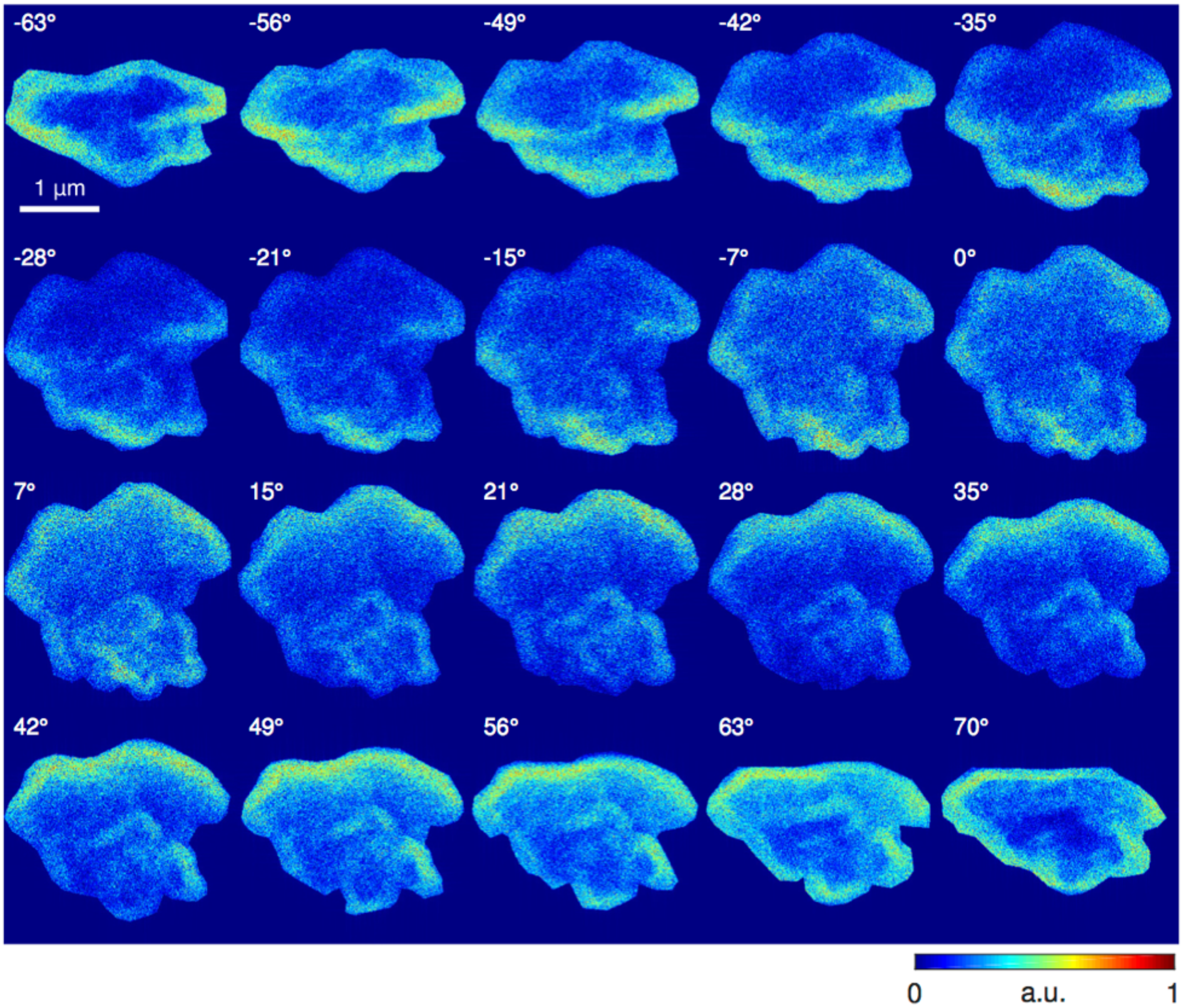

Fig. S10. Experimental carbon channel EDS tilt series. All 20 processed carbon EDS projections used as input for GENFIRE reconstruction. Each image was masked, normalized to reference projection, background subtracted, and aligned by center-of-mass and common line alignment. Background subtraction was iterated with alignment to minimize common line differences. Horizontal direction is the rotation axis.

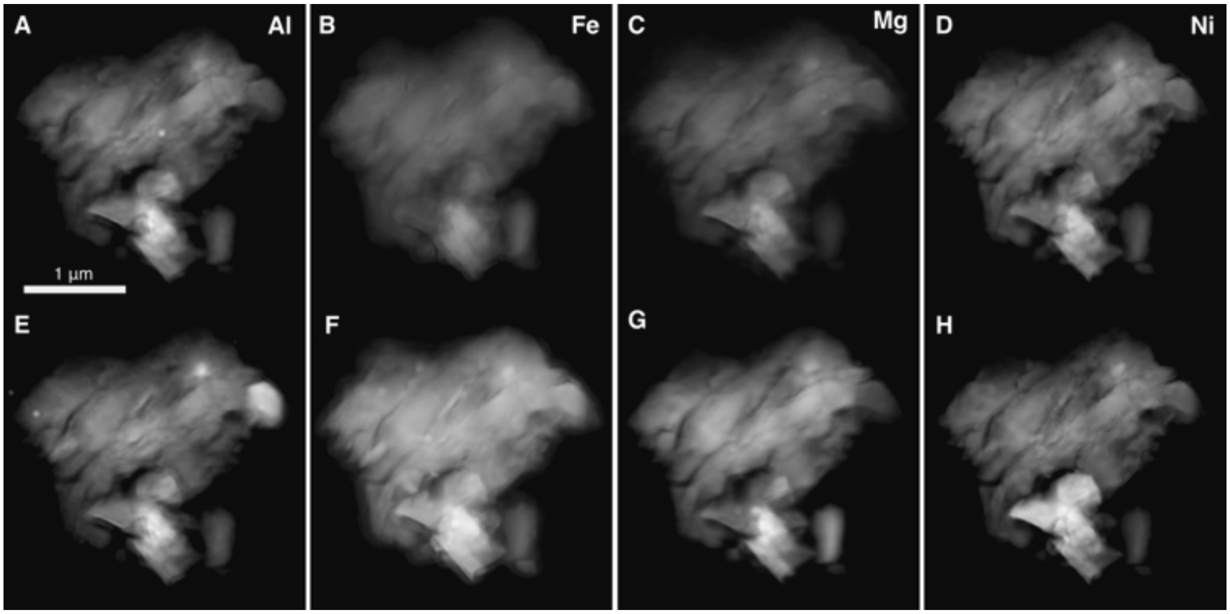

Fig. S11. Ptychography near Al, Fe, Mg, and Ni edges. Ptychographic images acquired near absorption edges for four major elements in the meteorite grain, Al, Fe, Mg and Ni. At pre-edge energies: 1,545.5 eV, 700 eV, 1,295 eV, and 842 eV (**A** to **D**), and at on-edge energies: 1,551 eV, 707 eV, 1,302 eV, and 848 eV (**E** to **H**). The elemental aggregations highlighted in Fig. 3A to D were obtained by dividing **E** to **F** by **A** to **D**.

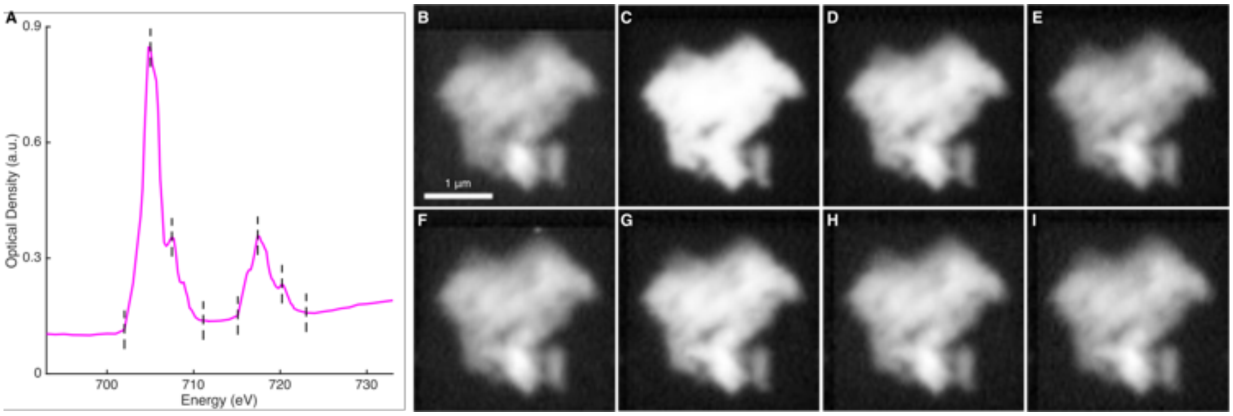

Fig. S12. STXM spectromicroscopy. Iron absorption spectrum generated from STXM energy scans across Fe L_3-edge (**A**), and the corresponding STXM images at various points on the spectrum (left to right dashed lines in **A**) to illustrate the change in absorption in different regions of the meteorite (**B** to **I**).

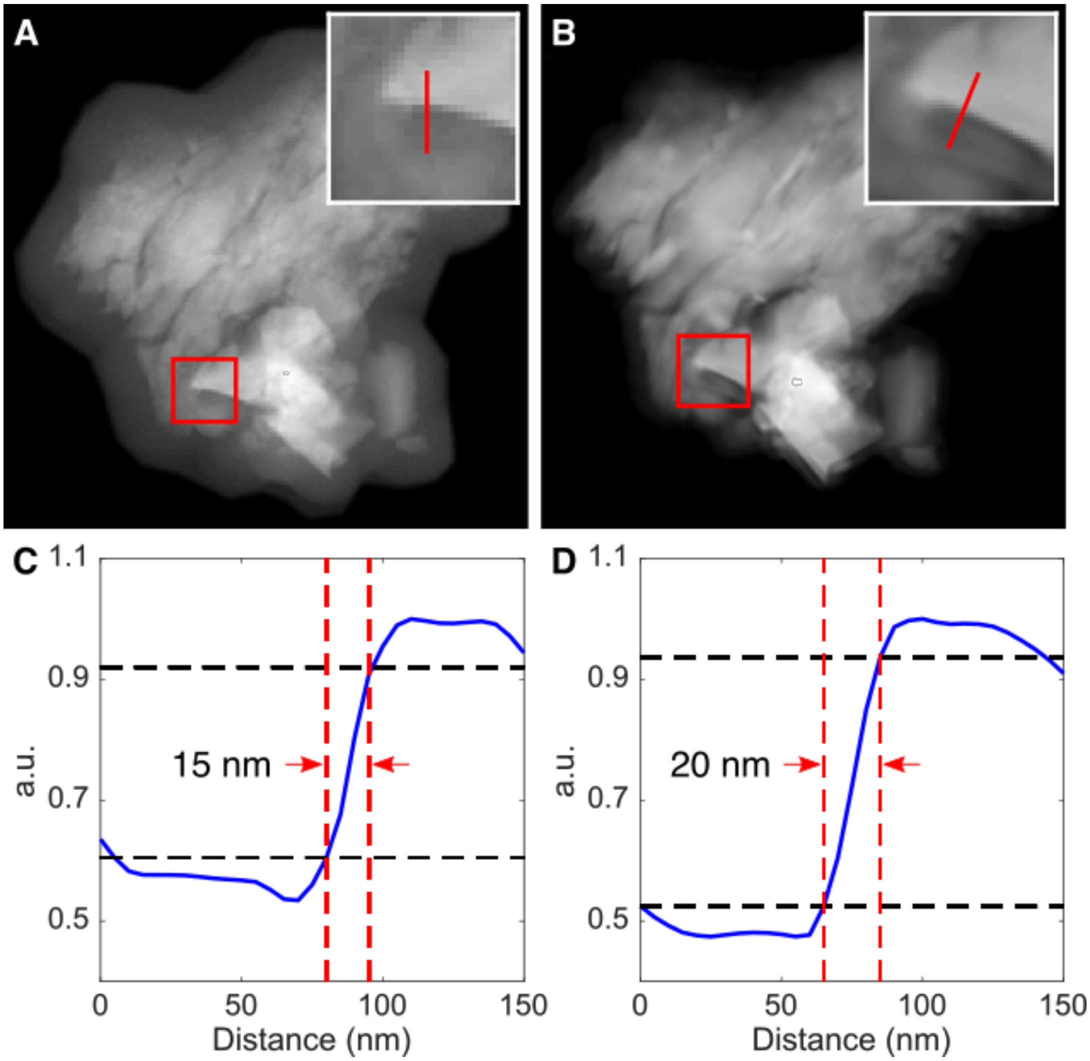

Fig. S13. Achieved spatial resolution for ptychography and HAADF microscopy. Knife-edge scans across the boundary between mineral phases, with spatial resolution quantified using the 10-90% criterion. The estimated resolutions are 15 nm for 0th degree HAADF projection (**A** and **C**), and 20 nm for ptychography on the Fe L3-edge (**B** and **D**).

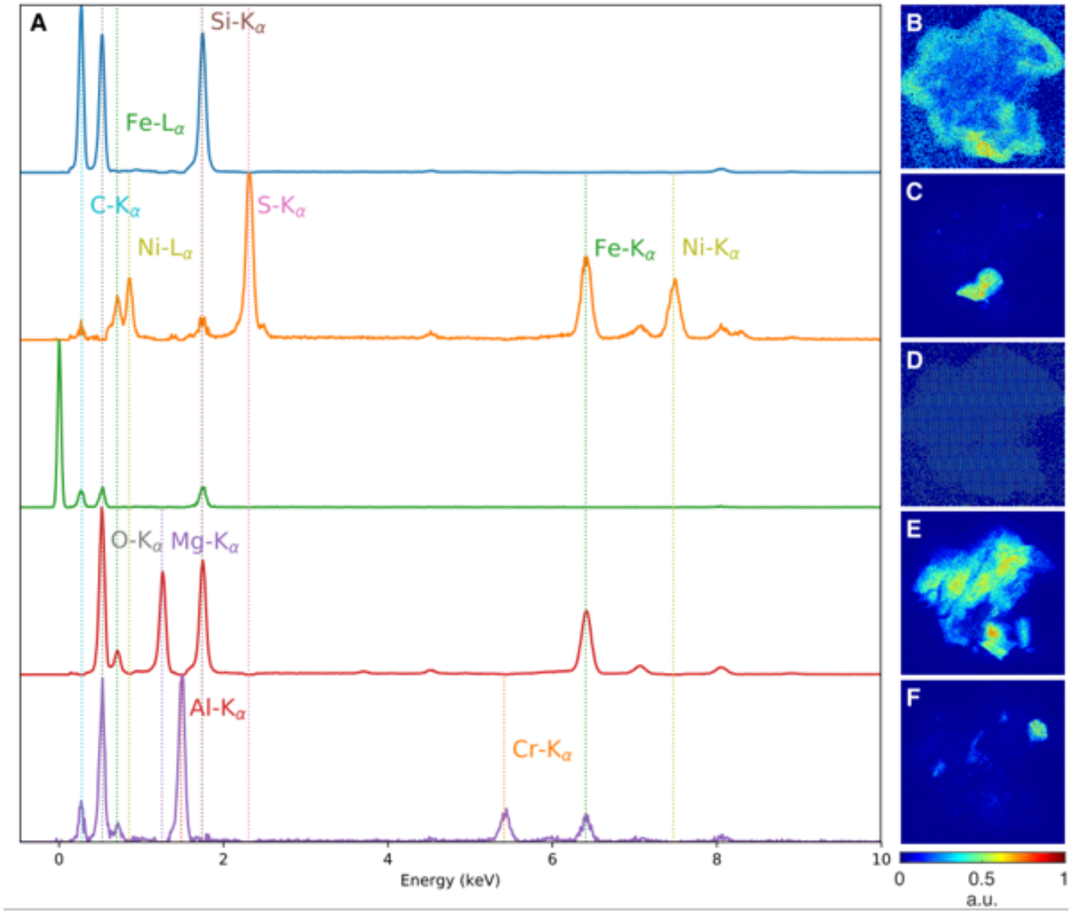

Fig. S14. EDS spectral decomposition. Spectral decomposition of the EDS data using non-negative matrix factorization in HyperSpy python package (**A**). The result reduces all EDS spectra into 5 major components with one component containing noise (**D**). The 4 major clustered spectra and their corresponding pixel locations highlight C, O, and Si contaminations on the grain surface (**B**), Iron-nickel sulfide (**C**), iron-magnesium silicate (**E**), and chromium-aluminum oxide (**F**). The integrated peak intensities from these decomposed spectra were used to quantify the elemental compositions in the three major mineral phases summarized in Fig. 4.

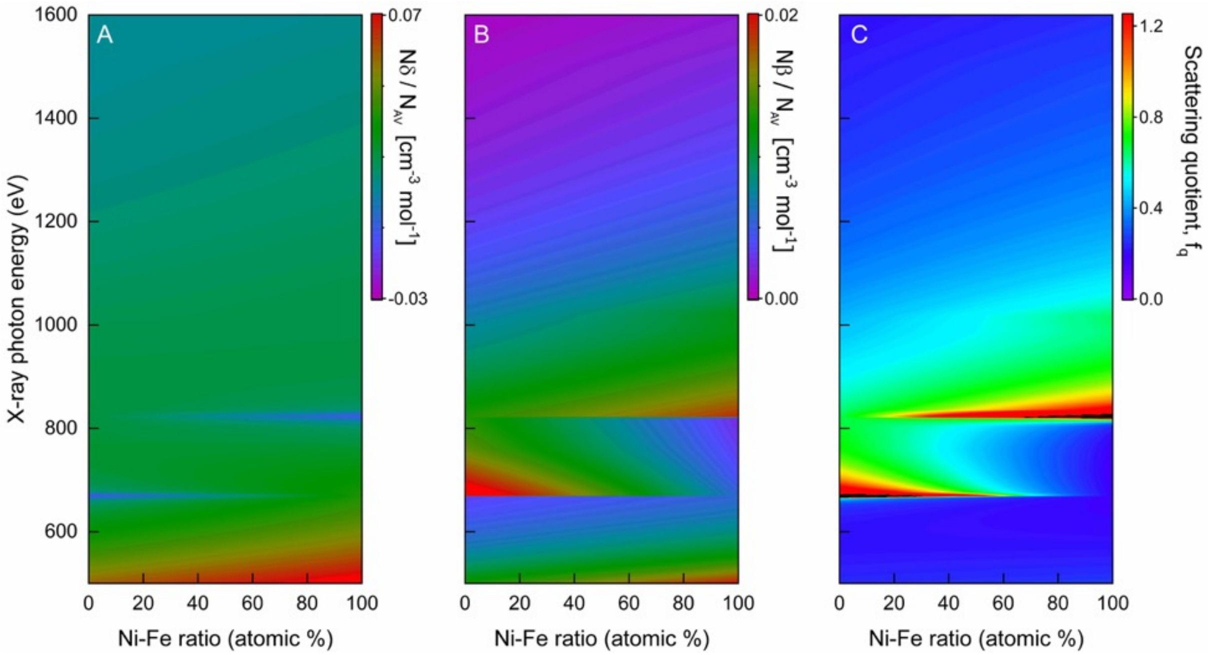

Fig. S15. Calculated conversion functions used in SQUARREL for iron-nickel sulfide. (**A**) The denominator of the scattering quotient ($\sum_i N_i\delta_i$), namely, the product of the atomic number density (N) and the real decrement part of the complex refractive index (δ). Similarly, (**B**) is the numerator of the scattering quotient ($\sum_i N_i\beta_i$), the product of N and the imaginary part of the complex refractive index (β). For simplicity, both (A) and (B) are normalized to Avogadro's constant (N_{AV}). (**C**) Scattering quotients of the iron-nickel sulfide mixture ($Fe_pNi_qS_{0.89}$), likely a pentlandite. The two-element ratio or q-to-p ratio here is the Ni-Fe ratio, where 100% implies a pure nickel sulfide without the presence of iron.

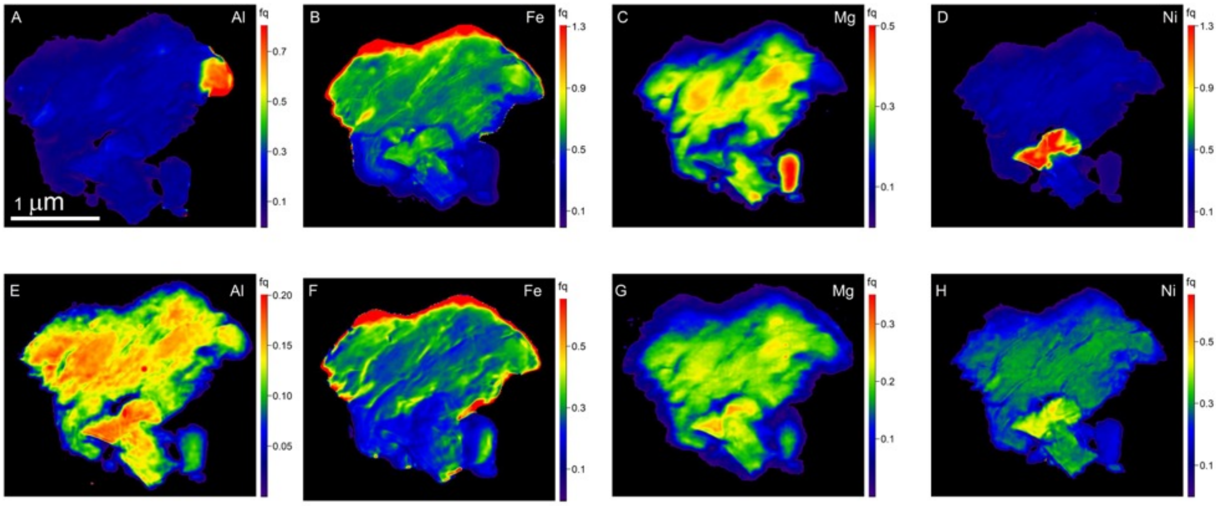

Fig. S16. Scattering quotient maps providing a novel contrast. These scattering quotient maps are derived from complex x-ray ptychographic images as in Fig. S11, including Al, Fe, Mg, and Ni on-edge images (A-D), and Al, Fe, Mg, and Ni pre-edge images (E-H). Note that Fig. 3E and 3F in the main text are the zoomed in of Fig. S16G and S16E shown here.

A.3 Chapter 5 supplementary materials

Please see next page

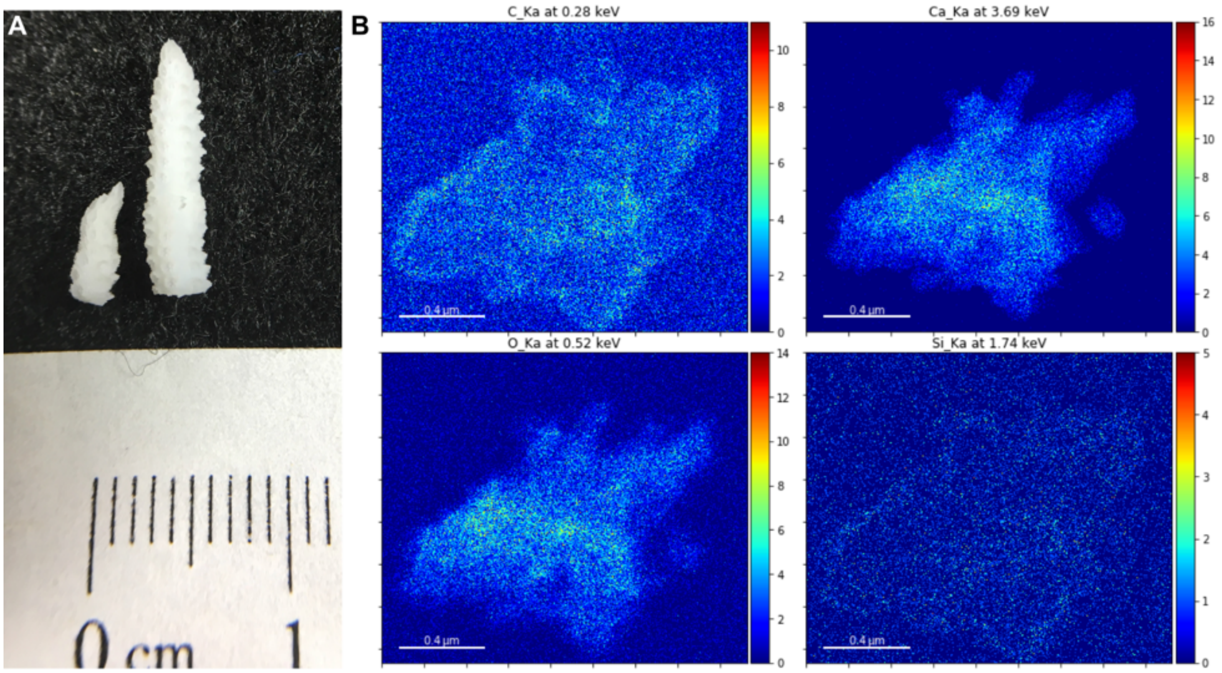

Fig S1. ***Seriatopora aculeata*** **coral skeleton.** (**A**) Bulk *S. aculeata* coral skeleton specimen from which micrometer-sized fragments were milled and extracted for x-ray and electron measurements. (**B**) Energy dispersive spectroscopy of a coral fragment, showing spectral images of 4 major elements in the particle and confirming aragonite's predominant composition of C, Ca and O, with some slight Si contamination.

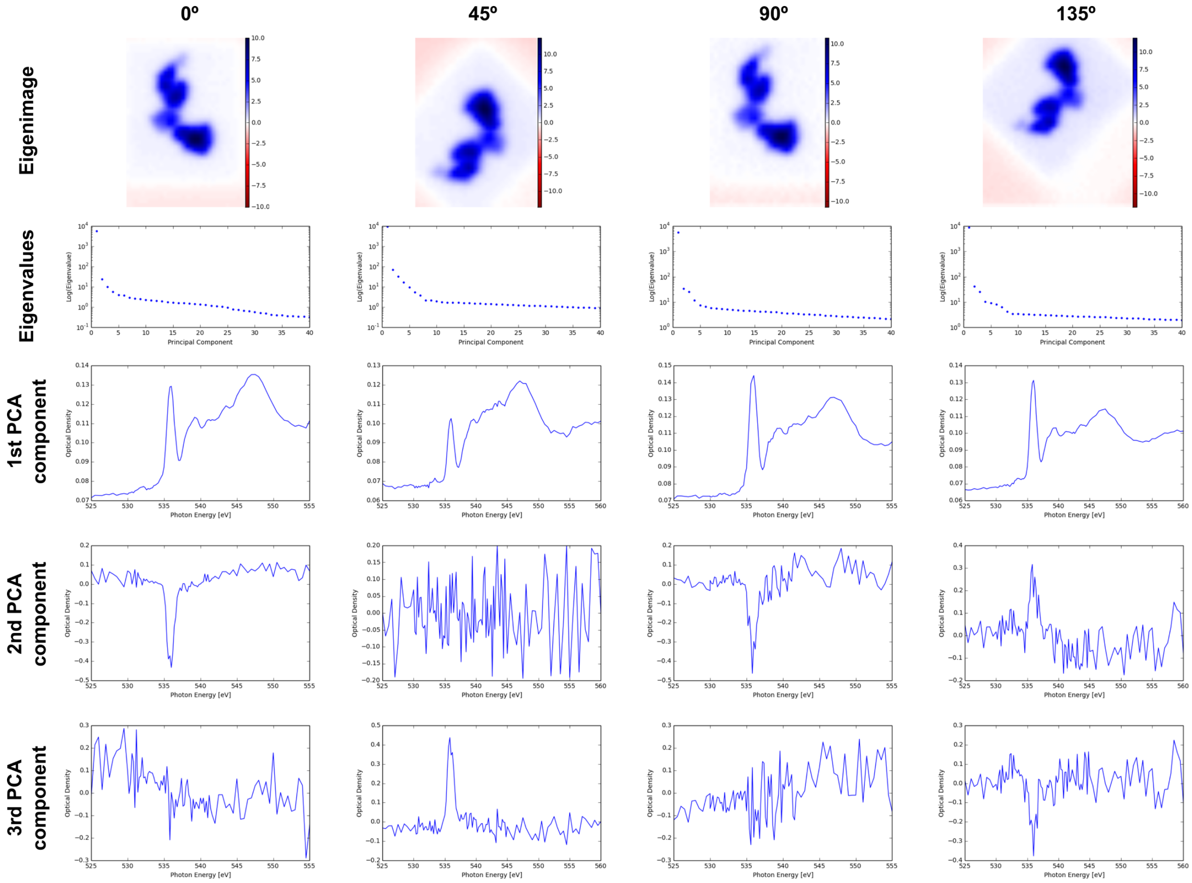

Fig. S2. STXM-XAS spectral decomposition. First row: First eigenimages of the coral skeleton at each linear polarization, representing the average thickness. Second row: Eigenvalues generated from PCA. Third row: First principal component spectral decomposition, representing the average absorption spectrum of the entire specimen. Fourth row: Second principal component spectral decomposition. Five row: Third principal component spectral decomposition.

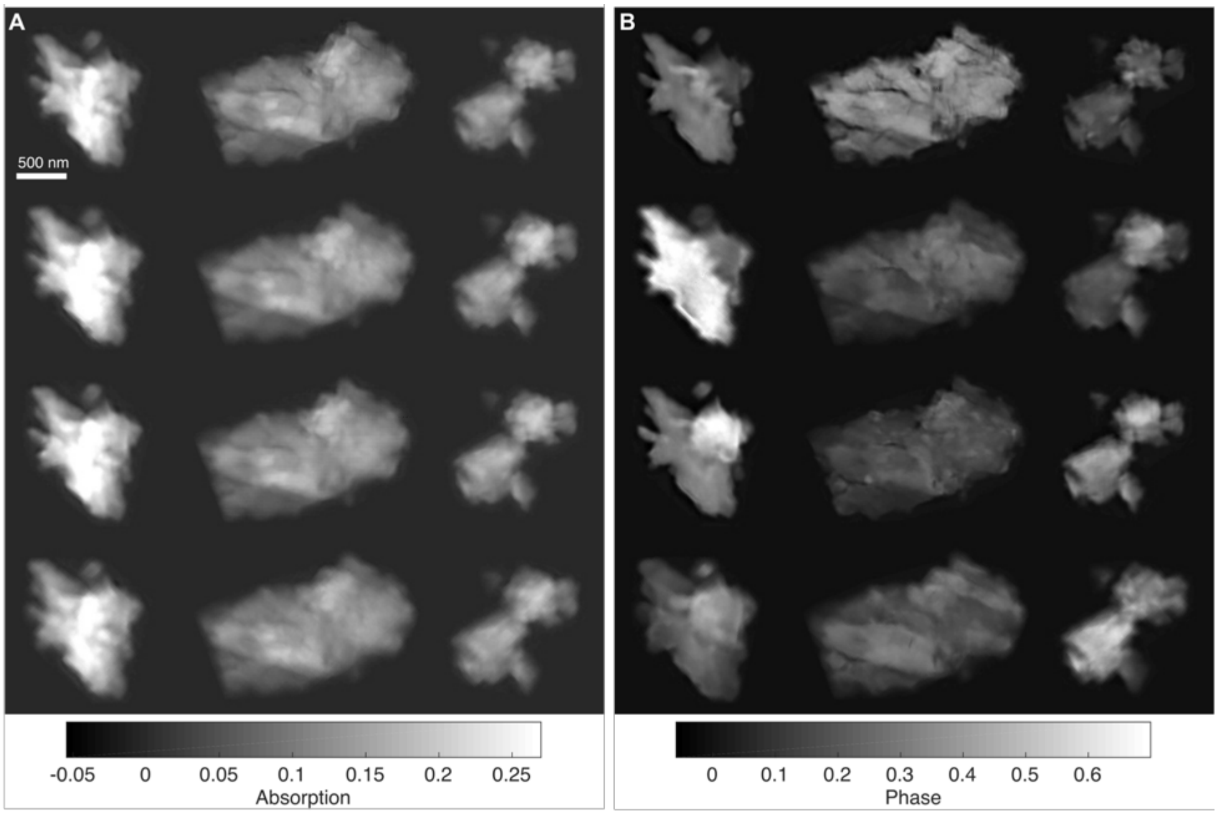

Fig. S3. X-ray linear dichroic ptychography of coral fragments at other energies. (**A**) Ptychography absorption images of 3 aragonite particles recorded at the O pre-edge energy of 534.5 eV across 4 linear polarizations, showing weak polarization-dependent absorption contrast and lower overall spatial resolution due to smaller scattering cross section. (**B**) Ptychography phase images of the same particles and polarizations recorded on O K-edge absorption resonance at 536.5 eV, showing strong polarization-dependent phase contrast that is analogous to on-edge absorption contrast. Scale bar: 500 nm.

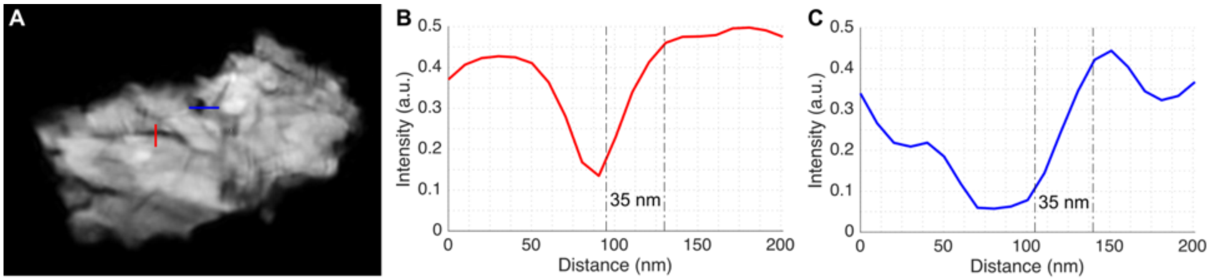

Fig. S4. Estimated ptychography resolution. (**A**) Two fine internal features used to estimate highest achieved spatial resolution. (**B**) (**C**) Line scans across the fine features. Colors correspond to line cut in (**A**). Highest resolution achieved by linear dichroic ptychography is estimated to be 35 nm using the knife-edge method with 10-90% intensity cutoff.

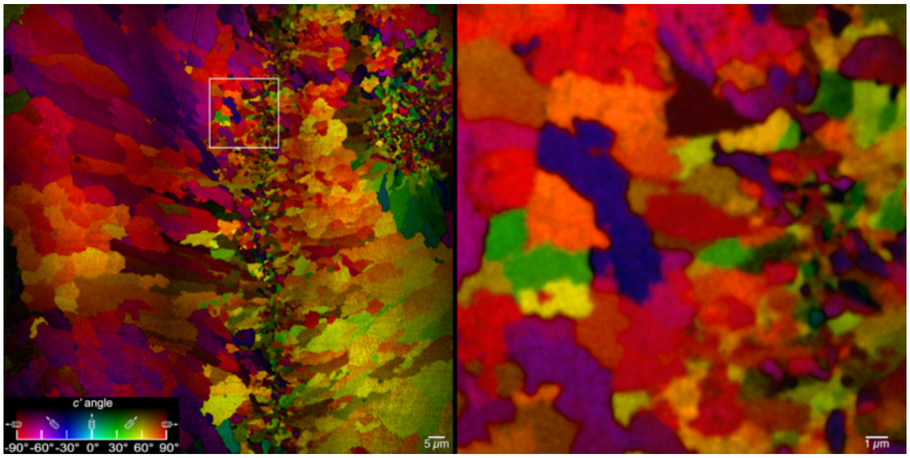

Fig. S5. Polarization-dependent contrast (PIC) map from PhotoEmission Electron spectroMicroscopy (PEEM). Large-area PIC map of another *S. aculeata* specimen. White box in the left panel indicates the area magnified in the right panel. (**A**) Left and right side of the image are filled with large, micrometer size spherulitic crystals that are slightly misoriented with respect to each other, always within 35°. The center vertical structure, termed center of calcification or CoC, contains smaller (200-2000 nm) randomly oriented crystals termed sprinkles[1]. (**B**) The magnified area contains a mix of spherulitic crystals (left region) and randomly oriented sub-micrometer crystallites (right region), termed sprinkles, Scale bars: 5 µm for the left panel, 1 µm for the right panel.

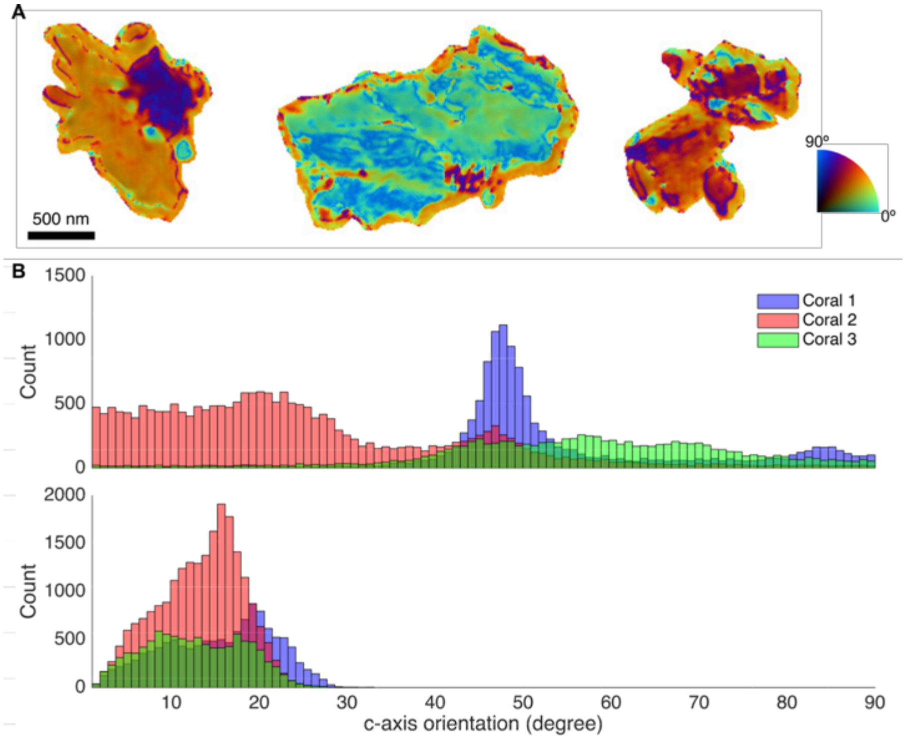

Fig. S6. Polarization-dependent contrast (PIC) map of aragonite fragments with second set of polarizations. (**A**) Quantitative PIC maps of the 3 aragonite particles, calculated using 0º, 135º and 90º linear dichroic ptychography images. Hue denotes in-plane azimuthal crystal *c*-axis angle (γ) of the crystallite, while brightness denotes out-of-plane *c*-axis angle (χ), all ranging from 0º to 90º. Relative angular spreads in the 3 particles agree well with PIC maps shown in Fig. 3. (**B**) Histograms of γ (top) and χ (bottom) for the 3 particles, again showing narrow γ angular spread for Particle #1 of less than 20º, and much broader spread for Particle #2 and Particle #3 of more than 35º. Scale bar: 500 nm.

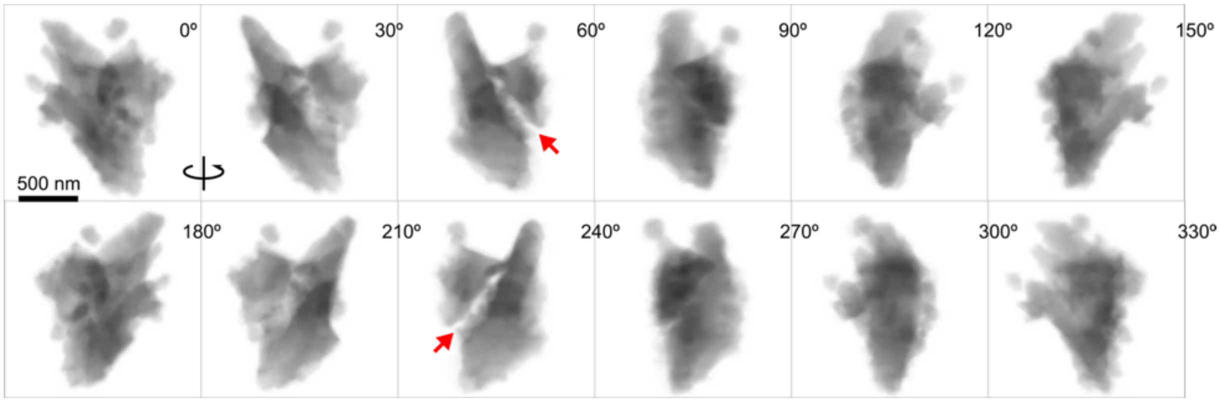

Fig. S7. HAADF tomography of Particle #1. Projected azimuthal views of 3D coral fragment, rotated to the right in 30º increments. Views along the 60º and 210º reveal the coral fragment consists of two joint particles overlapping on top of each other (red arrows). This explains the drastic orientational change across the two subdomains that is observed in Fig. 3's PIC map. Scale bar: 500 nm.

REFERENCES

1. C-Y Sun, L Gránásy, CA Stifler, JAY Zhang, T Zaquin, T Mass, S Goffredo, G Falini, MA Marcus, R Chopdekar, T Pusztai, JC Weaver, PUPA Gilbert. From sprinkles to spherulites: crystal coarsening in coral skeletons and beyond. Submitted.

A.4 Chapter 6 supplementary materials

Please see next page

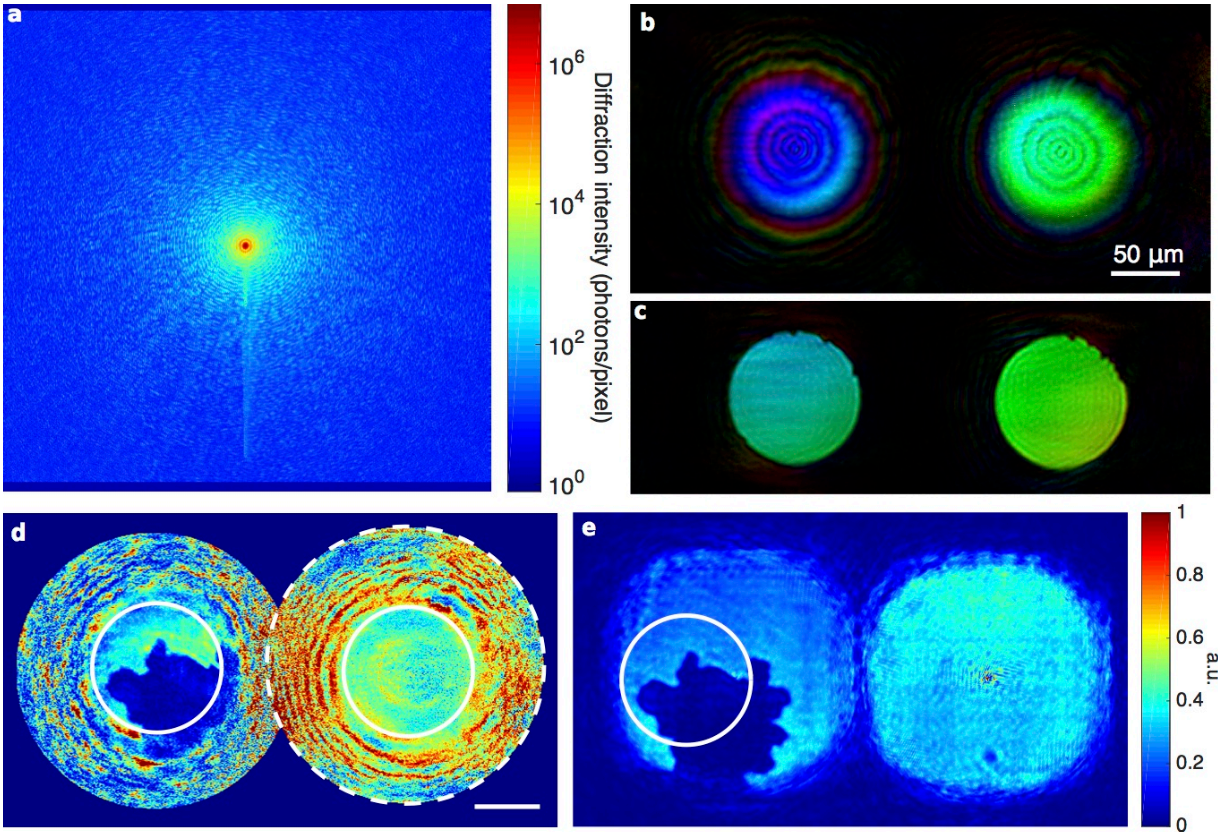

Figure S1. Optical laser data and reconstructions. (**a**) Representative diffraction pattern collected in the Pb dendrite growth experiment. (**b**) The complex illumination function on the sample plane, recovered from ptychography and used for the in situ CDI reconstruction. Brightness and hue represent magnitude and phase, respectively. (**c**) The illumination function propagated (460 µm) onto the aperture plane. (**d**) In situ CDI reconstruction of the 0.9 V frame in the Pb dendrite growth process, showing the fully reconstructed field of view. The two solid white circle represent the illumination field at the pinhole plane, the left solid white circle indicates the region used for Fig. 3a, and dashed white circle denotes the region masked for the static structure constraint. Note a loose support was used on the illumination function to bound the aperture area. Scale bar 50 µm. **e**, Ptychographic reconstruction of the same voltage frame as (**d**). Solid white circle indicates the region used for Fig. 3b.

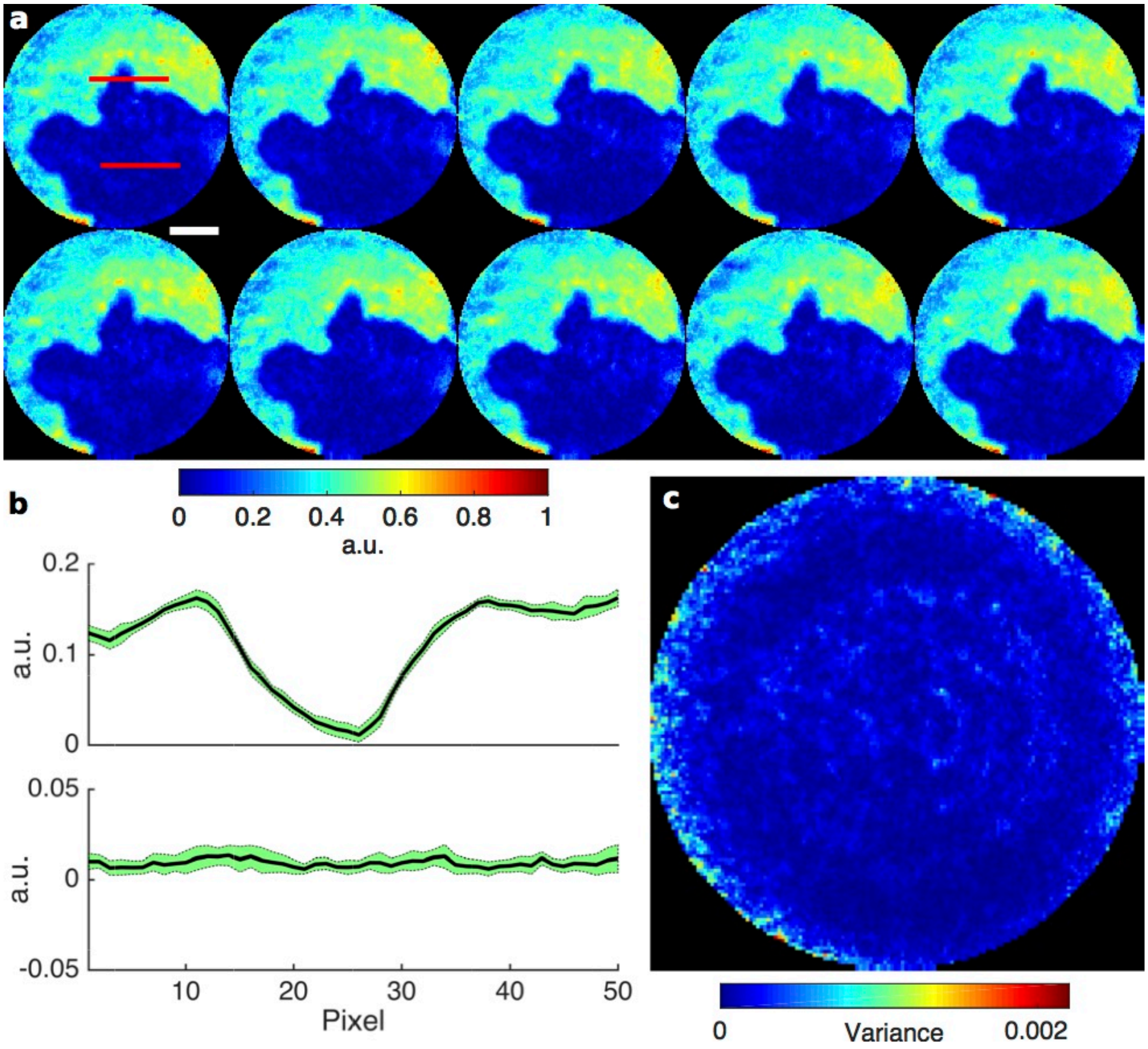

Figure S2. In situ CDI reconstruction consistency. (**a**) Ten independent runs of the in situ CDI reconstruction of the Pb dendrite growth process with the applied voltage of 0.9 V. Each run used a random dynamic and static function as an initial input. Scale bar, 20 µm. (**b**) Average line-scans across two regions of the reconstructions (red lines in (**a**)) with the standard deviation in green. (**c**) the variance map of the reconstructions, showing good consistency of the ten independent runs.

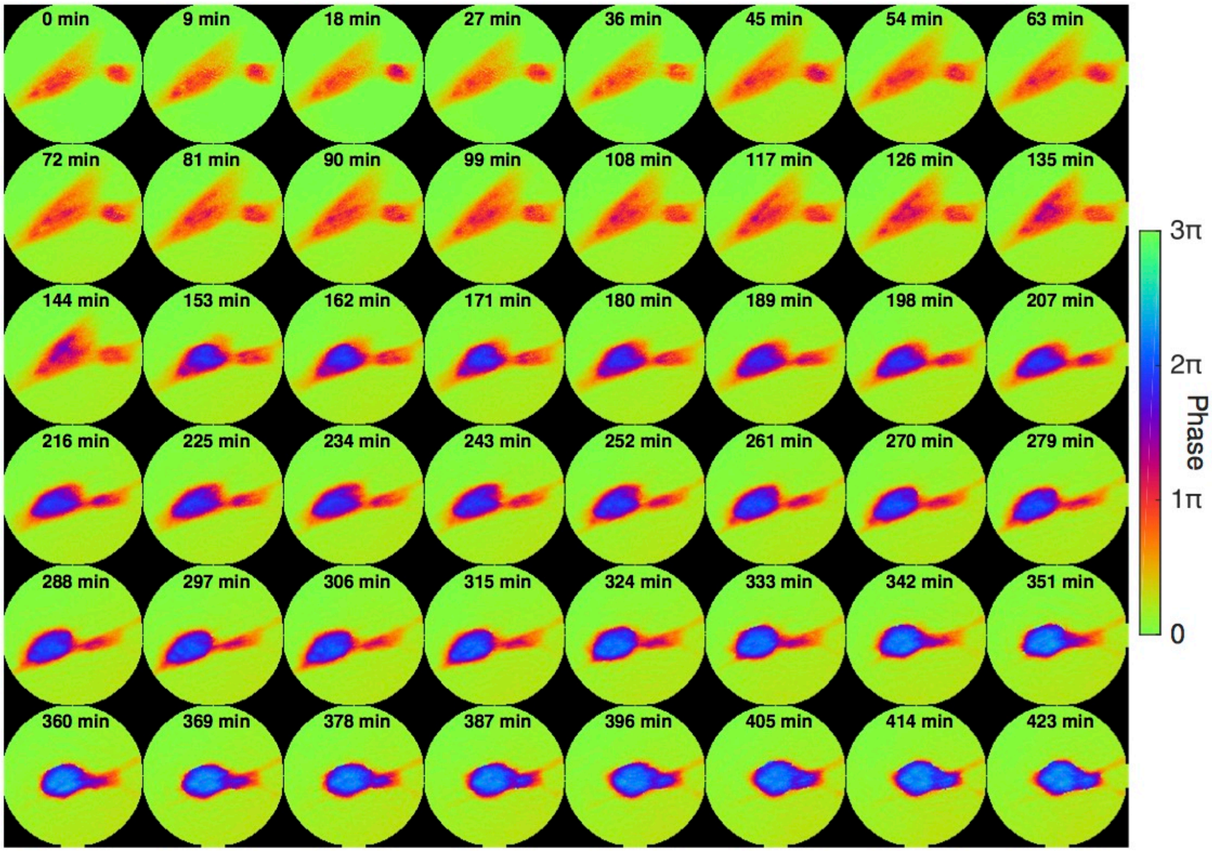

Figure S3. Cell fusion dynamics result from ptychography. Phase images of the fusion of glioblastoma cells reconstructed by ptychography. Each frame corresponds to the same region as the in situ CDI reconstruction in Fig. 4. Internal cellular structures reconstructed using both methods show good agreement, validating in situ CDI's ability to simultaneously reconstruct a time series of diffraction patterns.

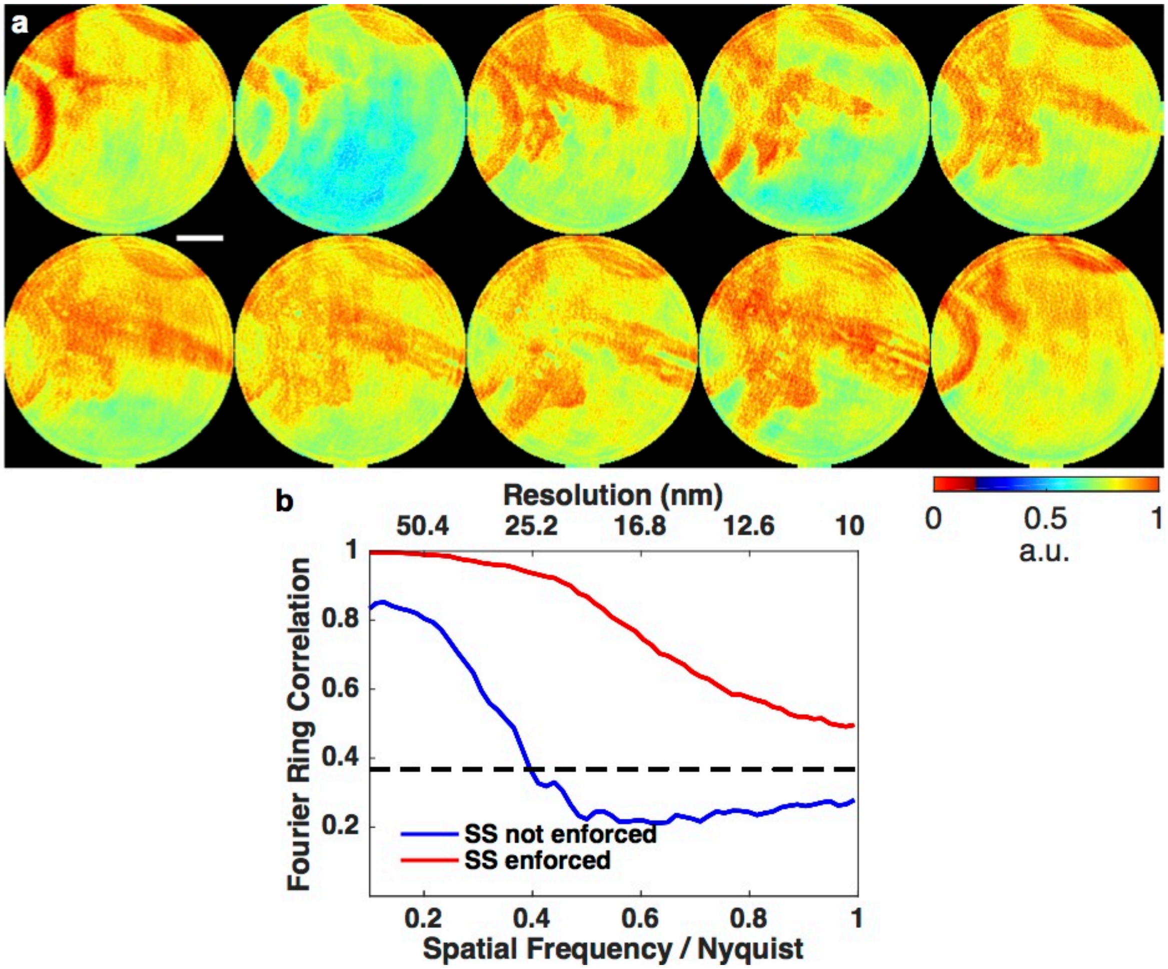

Figure S4. Results without static constraint enforcement. (**a**) In situ CDI reconstructions without enforcing the static structure (SS) constraint, exhibiting poor reconstruction quality than that with the SS constraint enforced. Scale bar, 200 nm. (**b**) Fourier ring correlation indicates that enforcing the SS constraint can improve the resolution of the reconstructions.

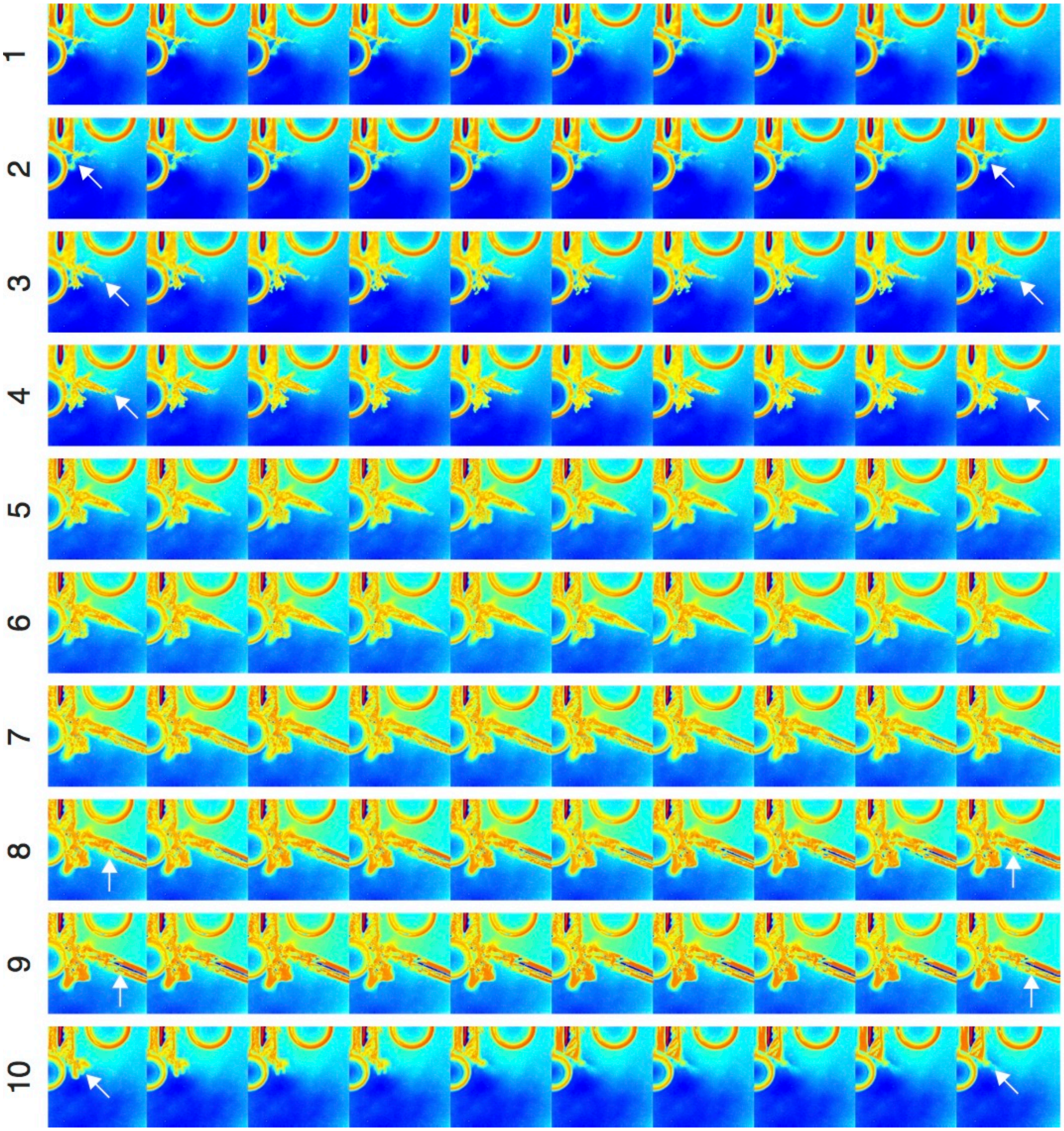

Figure S5. All frames used for constructing the Pb dendrite dynamic structure model. Each row represents 10 1-ms images used to calculate a diffraction pattern with a temporal resolution of 10 ms. The arrows indicate fine feature changes of the images.

APPENDIX B

Correlative cellular ptychography with functionalized nanoparticles at the Fe L-edge

B.1 Introduction

Functionalized nanoparticles are used in a broad array of nanomedicine applications for their utility as labels and drug delivery systems [227–230]. The ability to localize individual nanoparticles within cells is critical as it allows interactions between the nanoparticles and their target cells to be characterized, informing of the biological effects imparted by the nanoparticles. One method ideally suited to probe individual nanoparticles inside cells is coherent diffractive imaging (CDI) since it can image thick specimens with high resolution and contrast [6,10,11,44–48,52,192,195,231–240]. Since the first experimental demonstration in 1999 [10], various CDI methods have been developed [11] and a particularly powerful approach for imaging extended objects such as whole cells is ptychographic CDI (also known as ptychography) [30,49,54–57,59,114,118,127,191,241–246]. In ptychography, an extended sample is observed by illuminating with a coherent wave via a 2D raster scan. During such a 2D scan, diffraction patterns are recorded from overlapping fields of view with a predefined trajectory. The overlap between views can then be used as a strong constraint in phase retrieval algorithms30, leading to a unique, robust reconstruction of the complex exit wave of the object and the illumination function [49,54,55,57,59,114,118,127,242–246]. Furthermore, by measuring diffraction intensity with a numerical aperture significantly higher than that of X-ray lenses, ptychography can reach spatial resolution far beyond those of conventional X-ray microscopy. However, this powerful capability is hampered in the case of weakly scattering objects such as biological specimens, because the background scattering of the substrate and parasitic scattering from X-ray optics can dominate the weak signals from a biological specimen [54, 59, 118, 127, 247].

Here we demonstrate a correlative ptychographic approach for high-resolution imaging of functionalized nanoparticles internalized within an un-sectioned mammalian cell. To achieve high spatial resolution and image contrast, we first adapt transparent graphene-oxide substrates [248] to support cells during the X-ray imaging process. Graphene and graphene-oxide films have previously been shown to be an excellent support for high-resolution electron microscopy studies of cells and macromolecules, both frozen-hydrated [249] and in-situ [250–252]. Graphene-oxide in particular promotes cellular adhesion [253, 254] and growth [255, 256]. These substrates offer a significant reduction in background scattering for X-rays in the soft X-ray regime compared to conventional substrates. Next, we label HeLa cells with core-shell nanoparticles, functionalized by the addition of a fluorescent moiety and a super-paramagnetic core, and identify a region of interest using a fluorescence microscope. Finally, we combine 3D localization of nanolabels within the cell, using scanning transmission X-ray microscopy (STXM) tomography, with correlative high-resolution ptychographic imaging, with enhanced contrast for the nanoparticles by tuning the X-ray energy to the Fe L-edge. This correlative cellular imaging method allows us to localize individual nanoparticles in a cellular context at multiple length-scales, ranging from tens of microns to the ten-nanometer level.

B.2 Methods

Synthesis and characterization of $Fe_3O_4{-}SiO_2$ core-shell nanoparticles

The Nanoparticles (NPs) synthesis protocol was adapted from the literature [257, 258] to generate fluorescent $Fe_3O_4{-}SiO_2$ NPs as follows. A mixture of hydrated iron oxide (FeO(OH), 0.181 g), oleic acid (3.180 g) and docosane (5.016 g) was prepared in a round flask and stirred under vacuum for 1 h. This mixture was refluxed at 350 °C for 2 h in argon atmosphere. After cooling to room temperature, the resulting black solid was dissolved in pentane, mixed with an ether:ethanol solution (2:1) and centrifuged. The decomposed organic black solution was removed and the Fe_3O_4 nanoparticles were re-dispersed in pentane and washed with the ether:ethanol solution. After centrifugation, the NPs were stabilized with oleylamine (200 µL) and dispersed in chloroform. Then, 1.75 mL of 2 M NaOH solution was added into 200 mL of a CTAB solution (25 g L^{-1}) and this mixture was kept at room temperature for 1 h under constant stirring. This mixture was heated up to 75 °C and 7.5 mL of Fe_3O_4 NPs chloroform suspension was slowly added into the CTAB basic aqueous solution under vigorous stirring. The formation of an oil-in-water microemulsion resulted in a turbid brown solution. The resulting solution was vigorously stirred for 2 h at 75 °C resulting in a transparent black Fe_3O_4/CTAB suspension. Then, 5 mL of tetraethylorthosilicate (TEOS) and 5 mL of FTIC-APTES (10 mg of fluorescein isothiocynanate [FITC] was reacted with 250 µL of 3-aminopro-pyltriethoxysilane [APTES] in 10 mL of ethanol for 2 h) were added to the Fe_3O_4/CTAB suspension and stirred for 3 h at 75 °C to obtain the fluorescent $Fe_3O_4{-}SiO_2$ NPs. These nanoparticles were washed 3 times with ethanol to remove the unreacted species and then dispersed in 20 mL of ethanol. The remaining sample was refluxed twice with an alcoholic solution of ammonium nitrate (6 g.L^{-1}, NH_4NO_3) at 50 °C to remove CTAB from the NPs pores. After washing them twice with ethanol, the fluorescent $Fe_3O_4{-}SiO_2$ NPs were dried under airflow for a few hours. All chemicals used along this protocol were purchased from Sigma-Aldrich. The morphology of the nanoparticles was investigated on a JEM 2100 JEOL transmission electron microscope. The samples were evaluated by placing a highly diluted ethanolic nanoparticle suspension on regular TEM grids. The corresponding particle size distribution was obtained by measuring the core and the nanoparticle diameters of more than 400 particles.

Preparation of graphene-oxide coated lacey carbon TEM grids

All the biological assays were performed on a substrate composed of a Gold 400 Mesh TEM grid with lacey carbon. Additionally, a graphene layer was deposited on top of the lacey carbon to allow the culture of adherent cells on the TEM grid. The graphene layer was created by deposition of graphene oxide on the TEM grid by the 'drop-casting' method. A solution composed of 50% ethanol in double distilled water containing graphene oxide sheets is dropped on top of the TEM grid. After drying, TEM grids were annealed at 150 °C for 30 min creating a homogeneous surface. This process also guarantees sterilization of the TEM grid. The prepared TEM grid was submerged in Dulbeccos modified Eagles medium (DMEM) supplemented with 10% fetal calf serum and placed on the bottom of a cell culture dish. Next, suspended HeLa cells are dropped on the solution and maintained at 37 °C in a 5% CO_2 atmosphere for 24 h. This procedure allows the cells to adhere to and grow on the graphene.

Nanoparticle treatment

The HeLa cells that had adhered to the graphene TEM grid were treated with core-shell nanoparticles. The nanoparticles were suspended in distilled water (100 µg/ml), and three fifty micro- liter drops were added to five milliliters of solution and dispersed gently. Cells were exposed to nanoparticles for 30 min, the medium was removed and the cells were gently washed with medium. Finally, the cells were fixed with paraformaldehyde.

B.3 Results

Nano-labeling of HeLa cells with fluorescent nanoparticles on a graphene-oxide substrate

HeLa cells were first grown on a substrate specifically engineered for high-contrast imaging, consisting of a commercially available gold TEM grid coated with lacey carbon (Ted Pella) on top of which we deposited a few layers of graphene-oxide (www.graphenesupermarket.com) using the drop casting method [248]. Graphene-oxide is biocompatible and allows for the adherent growth of HeLa cells while being effectively invisible to the soft X-ray probe (Fig. B.1 and Materials and Methods). These grids provide significantly enhanced contrast when using the Nanosurveyor endstation in both STXM and ptychography modes. We attribute the improved stability and contrast to the atomically thin composition of the graphene layers and to the low density of graphene oxide relative to conventional silicon nitride-based supports. Graphene-oxide and silicon nitride have approximate densities of 1.9 g/cm^3 and 3.4 g/cm^3, respectively.

We imaged cells treated with fluorescent, core-shell mesoporous silica particles with an iron oxide core. Cells were treated with nanoparticles and suspended in growth media for 30minutes before gentle washing to remove excess nanoparticles, leaving mainly nanoparticles that had interacted with the cell surface or had been internalized. All samples were chemically fixed with paraformaldehyde, washed, and desiccated prior to imaging.

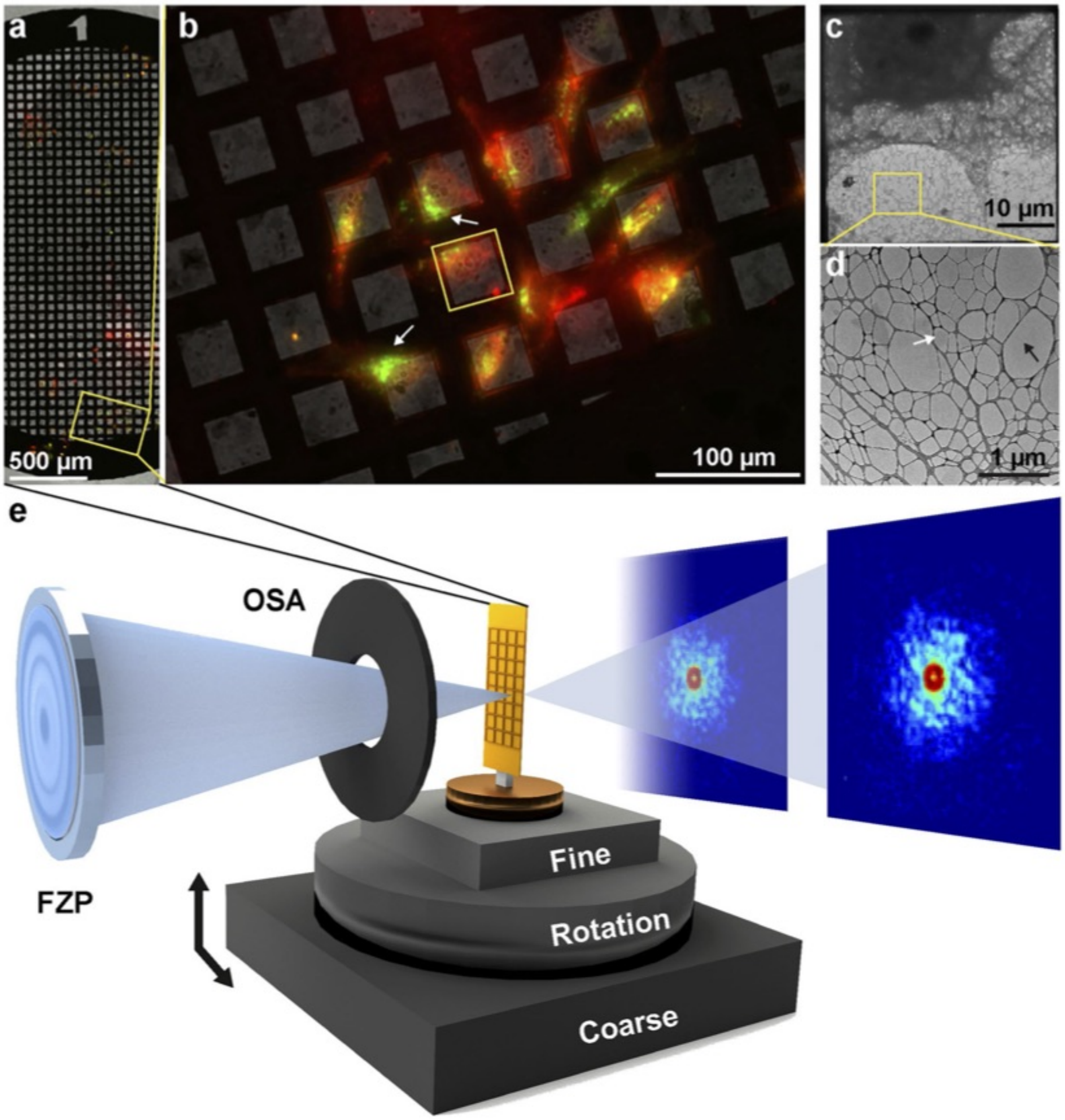
a
1
500 µm
b
100 µm
c
10 µm
d
1 µm
e
OSA
FZP
Fine
Rotation
Coarse

STXM and Ptychography experiments

X-rays were focused using a Fresnel zone plate with an outer diameter of 100 nm to give a total coherent flux of $\sim 5\times 10^5$ coherent photons s^{-1} at the sample position. An order-sorting aperture was placed slightly upstream of the focal spot to remove all but the first order of the focused beam.

To facilitate a full range of rotation without obstructing the order sorting aperture, grids containing adhered cells and nano-labels were cut into strips thinner than 1 mm using a zirconium nitride coated blade prior to transferring them to the Nanosurveyor instrument for X-ray experiments (Fig. B.1). Thin sample strips allowed a greater range of accessible tilt angles for tomography experiments, which

---

Figure B.1 *(preceding page)*: Experimental setup for correlative microscopy. (**A**) Composite fluorescent image of HeLa cells grown on graphene-oxide coated lacey carbon TEM grid. Cells were labeled with CMPTX (red) to facilitate tracking and treated with FITC labeled core-shell nanoparticles (green). (**B**) A magnified view of a region from this grid shows cells labeled with a tracking dye as well as fluorescent core-shell nanoparticles. White arrows point to cellular inclusions with clusters of fluorescent nanoparticles. (**C**) Electron micrograph of a portion of a HeLa cell covering an individual grid window, similar to the region highlighted in (**B**). (**D**) Magnified view of the lacey carbon grid. The black arrow points to empty regions of the grid whilst the white arrow indicates thin layers of grapheneoxide. (**E**) Experimental setup at BL 5.3.2.1 used for STXM/ptychographic imaging with key components labeled. The X-ray beam is focused using a Fresnel zone-plate (FZP) with all but the first order blocked by an order-sorting aperture (OSA). The focused beam is rastered across the sample using high-precision stages under interferometric feedback and diffraction patterns are captured by a fast-CCD at each scan point. (*Figure reprinted from* [5]) are normally restricted by the approximately 1 mm distance to the order-sorting aperture of the instrument (Fig. B.1).

We acquired a total of 58 STXM projections with a 3 ms exposure and 50 nm step, giving a full field of view of 10×5 µm, with tilt angles ranging between $-59°$ and $+40°$. Similarly, a total of 22 ptychography datasets, each consisting of 7,500 diffraction patterns, were collected using a compact Fast CCD [259]. Each ptychography pattern was measured with a dwell time of 200 ms and a step size of 60 nm, giving a full field of view of 9×3 µm with a pixel size of 5.5 nm.

3D reconstruction of a HeLa cells leading edge by STXM tomography

STXM projections were aligned preliminarily by cross correlation. Background was subtracted from each projection by removing the average value in an empty region of the sample. The projections were normalized to have the same total sum, as the integrated 3D density of the sample should be constant. This tilt series, acquired from a section of an extended object, imposes a unique challenge for the tomographic reconstruction, as the sample is not isolated. The field of view can drift from one acquisition to the next, but the projection-slice theorem, a fundamental assumption of tomographic reconstruction techniques, assumes that the projected density in each image results from the same 3D volume. Therefore, isolating the same density in each projection presents a challenge and was overcome in the following way: These preliminary angular alignments, translational centers, cropping, and intensity normalization parameters were used to make an initial set of projections for tomographic reconstruction.

The tomographic reconstruction was performed using a new generalized Fourier iterative reconstruction algorithm (GENFIRE) [1, 62], originally developed for atomic electron tomography [62, 99]. GENFIRE first pads zeros to each STXM projection and calculates an oversampled Fourier slice. The series of oversampled Fourier slices are interpolated to assemble a 3D Cartesian grid of the Fourier magnitudes and phases. The use of oversampling allows for accurate interpolation of grid points in the neighborhood of each Fourier slice [41], and the remaining Fourier grid points are set as undefined. The algorithm then iterates between reciprocal and real space using the fast Fourier transform (FFT) and its inversion. In reciprocal space, the measured grid points are enforced in each iteration, while undefined points are refined during the iterative process. In real space, the negative values and the electron density outside a predefined support are set to zero. An error metric, defined as the normalized difference between the measured and calculated Fourier grid points, is used to monitor the convergence of the algorithm. The iterative process is then terminated when the error metric cannot be further reduced. From this preliminary 3D reconstruction, the alignment and cropping of each projection was optimized with another iterative refinement loop. For each experimentally acquired projection, the reconstructed 3D volume was back projected to a range of Euler angles about the current guess and aligned to the experimental projection by normalized cross correlation. The alignment with the maximum cross correlation yields updated values for the orientation and center of the projection. Next, a mask was made by smoothing and thresholding the best-fitting back projection, and from this mask a new input projection was obtained from the corresponding raw STXM projections. The purpose of this remasking is to correct any inaccuracies in the initial cropping of the raw projections by utilizing the correlated information between the 3D reconstruction and each of its projections. After renormalization of the total intensity, an updated 3D reconstruction was computed from the new projections and orientation parameters. This loop was repeated until convergence of the alignment was obtained after 5 iterations. By using a Fourier based iterative process, GENFIRE produces better 3D reconstructions than other tomographic methods for a limited number of projections. A detailed comparison between GENFIRE and other 3D reconstruction methods is presented in a follow-up paper [1].

High-resolution ptychographic reconstruction

To obtain ptychographic reconstructions, 7,500 raw diffraction patterns were first corrected for differences in offset and gain among the 192 CCD readout channels using software at BL 5.3.2.1. The corrected patterns were padded with zeros to give an image pixel size that, based on the scan step, would produce an integer number of pixels between scan positions to eliminate rounding errors. The diffraction patterns were then reduced in size by binning to 128×128 pixels. To remove frames marred by readout errors, the patterns were sorted by integrated intensity and frames with excessively high or low intensity removed. Finally, an intensity-based threshold was applied to the remaining patterns and used to provide an estimate of the incoherent background scattering. This average background was subtracted from the diffraction patterns and spuriously bright pixels were set to zero.

Initial ptychographic reconstructions were performed during the experiment using the SHARP algorithm to monitor data quality [113]. Reconstructions were later refined using a strip wise probe relaxation to account for artifacts introduced in some scans by the interaction of the beam with the order sorting aperture during data acquisition. This relaxation was implemented within a reconstruction scheme based on the extended ptychographic iterative engine (ePIE) [30]. The probe reconstructed via SHARP was used as an initial guess. The probe was updated at each scan position and monitored during the course of the reconstruction. After each macro cycle of ePIE, individual probes were averaged along the axis parallel to the tilt axis. Then a weighted average was performed between strips using a 1D Gaussian kernel to promote communication between different strips and to avoid striping artifacts. For these reconstructions, a strip width of 5 pixels and Gaussian kernel of 1.5 times the strip width gave the best results.

Phase normalization of the reconstructed images is necessary before compari-

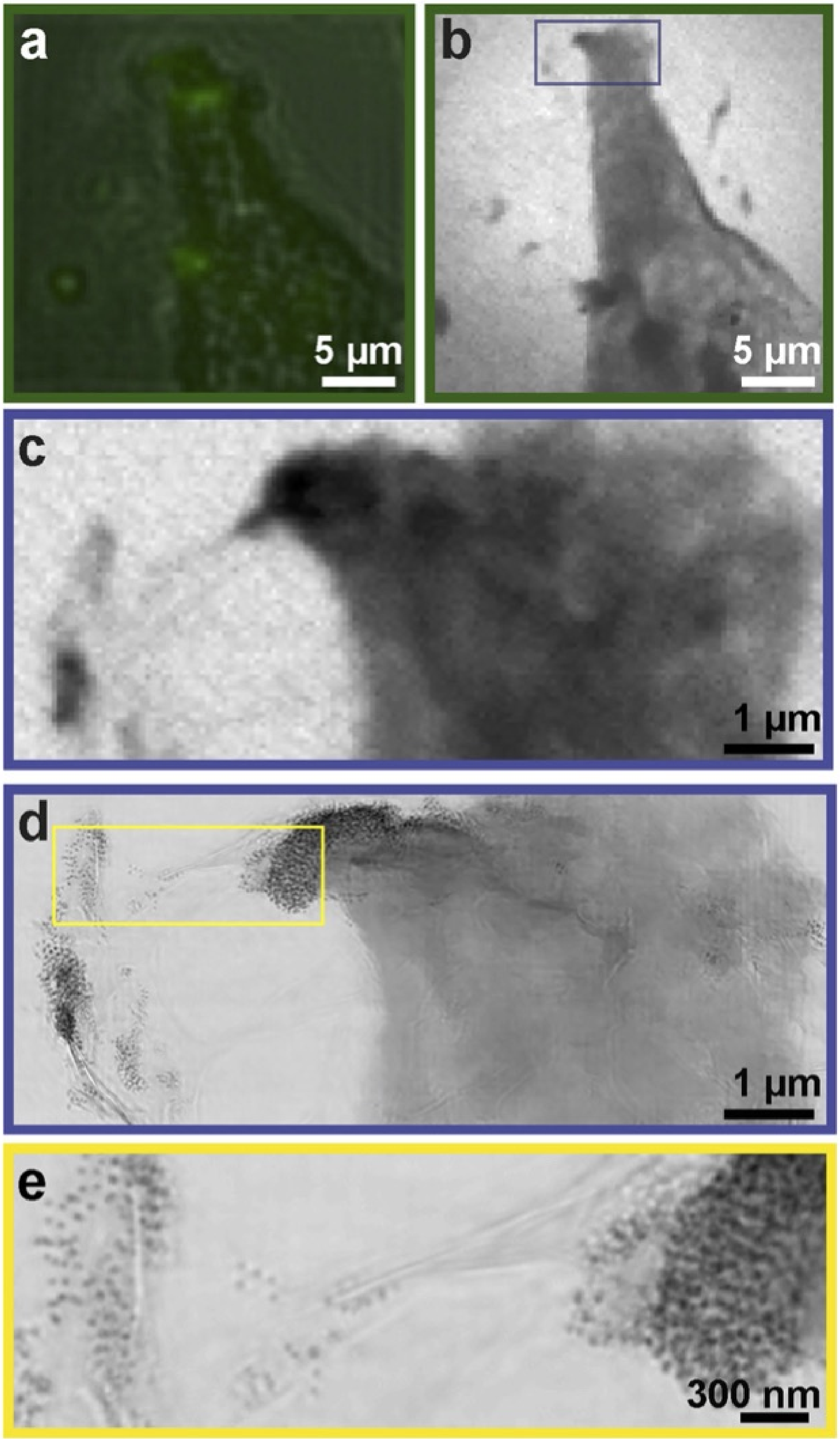
a
5 µm
b
5 µm
c
1 µm
d
1 µm
e
300 nm

son of neighboring ptychographic projections. A misalignment of the diffraction pattern relative to its true center translates to a phase gradient in the reconstruction of the object in real space [260]. Such a gradient can exist in both the horizontal and vertical directions, and an additional constant phase shift can exist without affecting the quality of fit of the reconstruction to the data. To perform this normalization, a pair of empty regions on either side of the sample was selected. A phase gradient in both the x- and y-axes was fit such that the standard deviation in the phase within these two regions was minimized. The constant phase term was then adjusted until the mean phase was zero within these regions.

Correlative cellular imaging using fluorescent microscopy, STXM tomography and ptychography

We achieved high-resolution imaging of the leading edge of a HeLa cell treated with fluorescent core-shell $Fe_3O_4-SiO_2$ nanoparticles by correlative microscopy. Figure B.2A shows part of an individual cell containing fluorescent nanoparticles. This same region was imaged using a coarse STXM scan to identify a smaller region of interest (Fig. B.2B). A fine STXM scan was then performed on the region of interest and a tilt series of 58 STXM projections were acquired from this region.

Figure B.2 *(preceding page)*: Localization of functionalized nanoparticles in a cellular context with correlative microscopy. (**A**) Part of a HeLa cell containing functionalized nanoparticles was first identified using fluorescent microscopy. (**B**) The same region was imaged using a coarse STXM scan. (**C**) A fine STXM scan was then performed on a smaller region of interest and a tomographic tilt series was acquired from this region. (**D**) Ptychographic imaging was performed on the same region as (**C**) to obtain higher resolution information. (**E**) Individual nanoparticles within and around the leading edge of the cell identified from the ptychographic reconstruction. (*Figure reprinted from* [5])

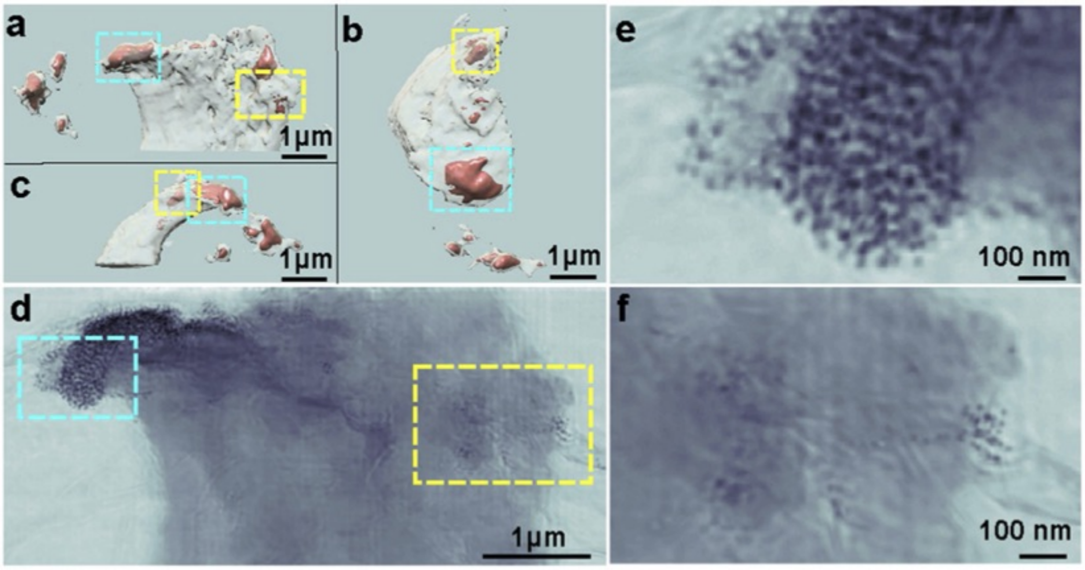

Figure B.3: STXM tomography reconstruction of the leading edge of a HeLa cell. (**A**-**C**) Iso-renderings of the 3D reconstruction showing several high-density regions (orange) within the cell, viewed along the z-, minus y- and x-axes, respectively. (**D**) High-resolution ptychographic image confirming that the internalized high-density regions correspond to nanoparticles uptaken by the cell. (**E**,**F**) Magnified views of two regions in (**D**) labeled with cyan and yellow rectangles, respectively. (*Figure reprinted from* [5])

These projections were reconstructed to produce a 3D volume using GENFIRE, shown in Fig. B.3A-C. A small section of the leading edge of the HeLa cell was reconstructed in its entirety. Several regions within the reconstructed 3D volume show high absorption. We attribute this high absorption to the concentrated uptake of nanoparticles into the cell.

The resolution of our 3D reconstruction is sufficient to observe membrane ruffles near the upper leading edge of the cell (Fig. B.3A). Due to obstruction of our sample by the TEM grid bars during rotation, our data suffers from a large missing wedge of more than 80°. Despite this, features in our STXM reconstruction of the sample along the missing wedge direction are still well defined, allowing for precise 3D localization of the nanoparticles. Traditional tomographic reconstruction techniques, such as filtered back projection [261], suffer greatly from elongation artifacts when viewed along angles corresponding to unmeasured projections due to the anisotropic resolution of reciprocal space along this direction. The clarity of our results is attributed to our reconstruction algorithm, GENFIRE, which produces quality tomographic reconstruction from a limited number of measured projections. In this particular example, views along the missing wedge provide extended context that is critical for drawing biologically relevant conclusions regarding particle internalization.

To reveal the local distribution of fluorescent $Fe_3O_4-SiO_2$ nanolabels in or near the HeLa cell, we performed 2D ptychographic CDI on regions of interest identified from the 3D reconstruction using STXM tomography (Fig. B.3A-C). Our ptychographic scans produced high-resolution images that allow visualization of individual nanolabels in a correlative manner (Fig. B.3D-F). The images also show, with high contrast, fine features such as membrane ruffles, filopodia, and the thin lacey carbon support (Fig. B.4). The enhanced contrast in these images is facilitated by the transparency of the graphene-oxide substrate and the presence of $Fe_3O_4-SiO_2$ nanolabels. The scattering signal produced by regions of cellular material containing these nanolabels is stronger than that produced by cellular material alone. The total scattered intensity in the presence of nanolabels increases by almost an order of magnitude compared to cellular material alone or the substrate. This increased image contrast and resolution facilitates localization of the nanolabels even when embedded within the cell.

Figure B.4 shows the phase and magnitude of the high-resolution ptychographic images. The phase images show fine cellular features such as membrane ruffles [262] and filopodia [263] (Fig. B.4A,B), while the magnitude images exhibit high contrast for the $Fe_3O_4{-}SiO_2$ nanolabels. Further cellular detail, such as cytoskeletal components, are however obscured due to the limited resolution and poor contrast of sub-cellular structures in a background of other cellular components in 2D projection. This combination of the phase and magnitude images allows us to determine the accurate localization of the nanolabels near the periphery of, and potentially within the HeLa cell. By imaging close to an absorption edge, we also made possible the distinction of multiple oxidation states based upon recovered phase and absorption contrast of the nanoparticles. Our magnitude images allow the precise localization of the core-shell nanoparticles (Fig. B.4C,D). The phases of our ptychographic reconstructions show the presence of nanoparticle cores in two possible states, indicating potential differences due to oxidation (Fig. B.4B). This remains consistent across projections and is not an artifact of reconstruction. Particles in the Fe3+ state, with an absorption resonance at 710 eV, will present zero phase shift relative to vacuum because of the value of the real part of the refractive index at the absorption resonance. Thus, those particles appear to have an annular structure in the phase images, which highlight the presence of the silica shell having non-zero phase shift. Although the initial step of the nanoparticle synthesis a single iron oxide is expected (Fe_3O_4). During the course of the storage at room temperature and in an aqueous medium, a subset of nanoparticles may naturally oxidize from Fe_3O_4 to γ-Fe_3O_4 [264]. The

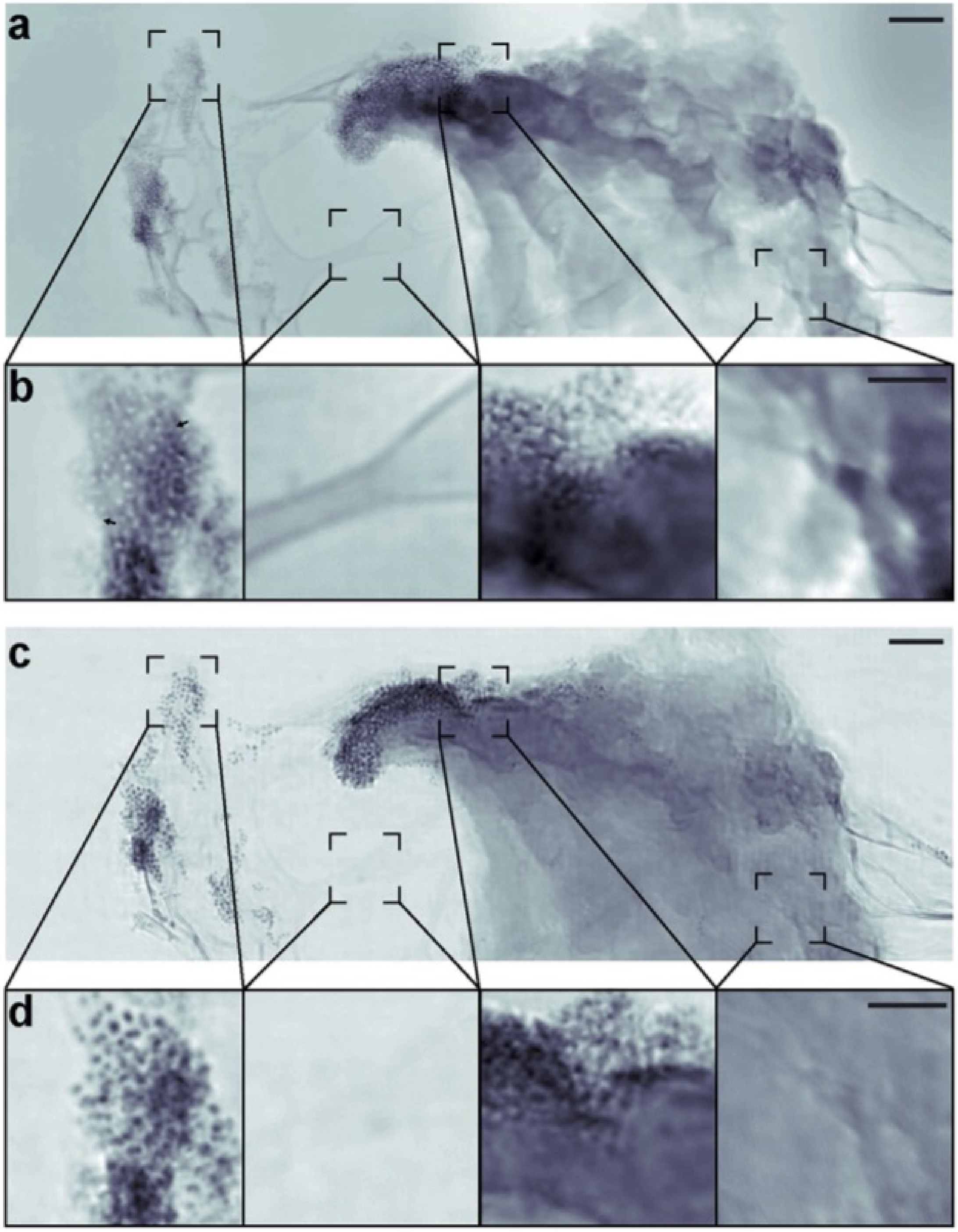
a
b
c
d

iron-oxide nanoparticles then exist as a mixture of these two oxides, each with distinct oxidative states and, consequently, distinct absorption coefficients at the X-ray energies used in this experiment. This difference in the scattering properties of our iron-oxide nanolabels is evident in the phase images (Fig. B.4B). While we did not focus on a spectroscopic analysis and did not image over a range of probe energies required to quantitatively measure the iron X-ray absorption coefficient of each species, our correlative technique is in principle capable of spectroscopic studies, allowing discernment of chemical species for a given nanoparticle in a cellular context.

Resolution estimation

To estimate the 3D resolution in our STXM tomogram, we compared independent reconstructions performed on two separate halves of the tilt-series. The

---

Figure B.4 *(preceding page)*: Phase and magnitude ptychographic images of cellular structure with functionalized nanoparticles. (**A**) Phase image of the ptychographic reconstruction of the leading edge of a HeLa cell labeled with core-shell nanoparticles showing high contrast for cellular features such as membrane ruffles and fillipodia. (**B**) Magnified views of the regions outlined by dashed boxes in (**A**), including (left to right) nanoparticles alone, grapheneoxide coated lacey carbon, cell and nanoparticles, and cell alone. The magnified view of the nanoparticles also demonstrates the phases ability to discern the silica shell (light gray halo around cores indicated by black arrows) as well as the two different oxidation states (light and dark cores). (**C**) Magnitude image of the ptychographic reconstruction showing high contrast for the Fe_3O_4 cores of the nanoparticles. (**D**) Magnified views of the same regions shown in (**B**), highlighting the different features that can be sharply resolved between the phase and magnitude images. Scale bars represent 500 nm (**A**,**C**) and 200 nm (**B**,**D**). (*Figure reprinted from* [5])

Fourier shell correlation (FSC) between the two reconstructions is an approach commonly used in single-particle cryo-electron microscopy to estimate the 3D resolution [265]. Based on the criterion of FSC = 0.143, we determined the 3D resolution of the STXM tomography reconstruction to be 157 nm. Next, we estimated the resolution of our ptychographic reconstructions in two ways. First, we calculated the average phase retrieval transfer function (PRTF) for all of the patterns in a particular scan [189]. This gave us an upper and lower bound of the resolution as being between 25 and 15.5 nm in the full period based on a threshold of 0.5. Second, we performed line scans across individual nanoparticles, which are well resolved and of known size (∼73 nm with ∼22 nm core). Line scans across the nanoparticle cores show that spacing of 3 pixels or greater can be easily distinguished, from which we estimate a resolution of ∼16.5 nm in the full period. Taking both of these into account, we estimated the overall resolution in our images to be approximately 16.5 nm in the full period.

Radiation dose and damage

Radiation dose is fundamentally limiting to high resolution imaging experiments. Our current experiment does not benefit from the advantage of cryo-protection and therefore directly suffers from the imparted X-ray dose at 710 eV. We limited the total dose on the sample by first obtaining low-dose STXM images of the sample. Each STXM projection imparts an estimated dose of only 25 Gy, with a full tomogram imparting a dose of 1.45×10^3 Gy; this is well within the tolerable limit for our desired resolution in 3D [112]. A single ptychography scan imparted a dose of 1.17×10^3 Gy per projection on the sample, similar to the total dose for the STXM tomography dataset. For this reason, while a full ptychographic tomography series was captured, we limited our analysis to a subset of measured projections suspecting that the high dose could lead to changes in sample morphology during the course of the tomography series. The zero degree projections taken before and after the ptychographic tomography series confirm these changes. In contrast, the appearance and localization of nanoparticles, which are more tolerant to dose, remains unchanged. Since the total dose imparted to this cell is within the tolerable limit for cryogenically frozen samples [112], we believe that cryo-preservation alone will facilitate similarly high-resolution results in 3D. Furthermore, cryo-preservation will alleviate some of the issues related to interpreting cellular ultrastructure as the cells will be preserved in a more natural state. The combination of higher-resolution and more faithful preservation of cellular material will significantly benefit this imaging method.

B.4 Discussion

The power of correlative microscopy lies in its potential to bridge the gap between complementary techniques, possibly expanding where a given method may be limited. Ptychographic CDI can provide high contrast images with a spatial resolution in the tens of nanometers from relatively thick, extended cells, particularly in the soft X-ray regime. As such, it is well suited to image in the regime between visible light and electron microscopy and its incorporation into correlative schemes is an area of active research [55, 127, 237, 240]. However, biological specimens are a challenge to image with high resolution due to their sensitivity to radiation. This sensitivity imposes strict limits on 3D imaging of cells, given the high dose required to obtain multiple projections of a single cell. STXM tomography complements ptychographic imaging, providing an opportunity to image a radiation sensitive sample in 3D with a lower dose than a single ptychography scan. In doing so, STXM tomography provides an overview of a large sample region or an entire cell in 3D prior to high-resolution ptychographic imaging. In the ideal correlative experiment, a labeled sample could be initially inspected by fluorescence microscopy to identify temporal and spatial regions of interest. Then, a STXM tilt series would provide an overview of the whole cell in 3D. Next, high-resolution ptychographic imaging would provide near molecular details that could be correlated with known cellular structures. Finally, electron microscopy could be used to provide true molecular detail. The present revolution in imaging methods across the length scales will continue to benefit such correlative approaches.

In summary, we demonstrate a proof-of-principle correlative imaging method across multiple length scales that facilitates the viewing of mammalian cells treated with functionalized fluorescent nanoparticles. Using a HeLa cell as a model system, we first identify cellular features of interest by fluorescent microscopy and correlate them in 3D via STXM tomography. We then image sub-regions of interest by ptychographic CDI with a resolution of $\sim$16.5 nm. We observe fine biological features such as membrane ruffles and filopodia, and accurately localize individual nanoparticles near the cell periphery and inside the cell. By choosing X-ray energies near the Fe L-edge, we enhance the image contrast of the core-shell $Fe_3O_4-SiO_2$ nanoparticles and identify them in two oxidation states. The ability to detect different oxidation states is important when the magnetic properties of the nanoparticles play a critical role in their function, such as magnetically induced heating of Fe_3O_4 nanoparticles in cancer therapy3. Although the nanoparticles were not targeted to specific biological structures in this study, incorporation of targeting moieties onto these nanoparticles is feasible and remains under investigation [266, 267]. By incorporating cryogenic techniques, the applicability and resolution of this method can be further improved by removing the need for extensive fixation protocols [112]. Higher resolution would allow the visualization of sub-cellular organelles with much greater detail, such that the interaction between nanoparticles and organelles can be better understood. The ability to perform correlative cellular imaging and localize individual nanoparticles inside intact, un-sectioned mammalian cells through a combination of fluorescent microscopy, STXM tomography and ptychography will not only yield a more comprehensive understanding of the cell as a complex biological system, but also find applications in quantifying cell-particle interactions in nanomedicine.

References

[1] A. Pryor, Y. Yang, A. Rana, M. Gallagher-Jones, J. Zhou, Y. H. Lo, G. Melinte, W. Chiu, J. A. Rodriguez, and J. Miao, "GENFIRE: A generalized Fourier iterative reconstruction algorithm for high-resolution 3D imaging," *Scientific Reports*, vol. 7, p. 10409, Sept. 2017.

[2] J. Deng, Y. H. Lo, M. Gallagher-Jones, S. Chen, A. Pryor, Q. Jin, Y. P. Hong, Y. S. G. Nashed, S. Vogt, J. Miao, and C. Jacobsen, "Correlative 3D x-ray fluorescence and ptychographic tomography of frozen-hydrated green algae," *Science Advances*, vol. 4, p. eaau4548, Nov. 2018.

[3] Y. H. Lo, C.-T. Liao, J. Zhou, A. Rana, C. S. Bevis, G. Gui, B. Enders, K. M. Cannon, Y.-S. Yu, R. Celestre, K. Nowrouzi, D. Shapiro, H. Kapteyn, R. Falcone, C. Bennett, M. Murnane, and J. Miao, "Multimodal x-ray and electron microscopy of the Allende meteorite," *Science Advances*, vol. 5, p. eaax3009, Sept. 2019.

[4] Y. H. Lo, L. Zhao, M. Gallagher-Jones, A. Rana, J. Lodico, W. Xiao, B. C. Regan, and J. Miao, "In situ coherent diffractive imaging," *Nature Communications*, vol. 9, p. 1826, May 2018.

[5] M. Gallagher-Jones, C. S. B. Dias, A. Pryor, K. Bouchmella, L. Zhao, Y. H. Lo, M. B. Cardoso, D. Shapiro, J. Rodriguez, and J. Miao, "Correlative cellular ptychography with functionalized nanoparticles at the Fe L-edge," *Scientific Reports*, vol. 7, p. 4757, July 2017.

[6] M. Gallagher-Jones, J. A. Rodriguez, and J. Miao, "Frontier methods in coherent X-ray diffraction for high-resolution structure determination," *Quarterly Reviews of Biophysics*, vol. 49, 2016/ed.

[7] A. A. Ekman, J.-H. Chen, J. Guo, G. McDermott, M. A. L. Gros, and C. A. Larabell, "Mesoscale imaging with cryo-light and X-rays: Larger than molecular machines, smaller than a cell," *Biology of the Cell*, vol. 109, no. 1, pp. 24–38, 2017.

[8] M. Holt, R. Harder, R. Winarski, and V. Rose, "Nanoscale Hard X-Ray Microscopy Methods for Materials Studies," *Annual Review of Materials Research*, vol. 43, no. 1, pp. 183–211, 2013.

[9] J. Kirz and C. Jacobsen, "The history and future of X-ray microscopy," *Journal of Physics: Conference Series*, vol. 186, p. 012001, Sept. 2009.

[10] J. Miao, P. Charalambous, J. Kirz, and D. Sayre, "Extending the methodology of X-ray crystallography to allow imaging of micrometre-sized non-crystalline specimens," *Nature*, vol. 400, pp. 342–344, July 1999.

[11] J. Miao, T. Ishikawa, I. K. Robinson, and M. M. Murnane, “Beyond crystallography: Diffractive imaging using coherent x-ray light sources,” *Science*, vol. 348, pp. 530–535, May 2015.

[12] F. Pfeiffer, “X-ray ptychography,” *Nature Photonics*, vol. 12, pp. 9–17, Jan. 2018.

[13] D. Shapiro, S. Roy, R. Celestre, W. Chao, D. Doering, M. Howells, S. Kevan, D. Kilcoyne, J. Kirz, S. Marchesini, K. A. Seu, A. Schirotzek, J. Spence, T. Tyliszczak, T. Warwick, D. Voronov, and H. A. Padmore, “Development of coherent scattering and diffractive imaging and the COSMIC facility at the Advanced Light Source,” *Journal of Physics: Conference Series*, vol. 425, p. 192011, Mar. 2013.

[14] P. Zhang, “Advances in cryo-electron tomography and subtomogram averaging and classification,” *Current Opinion in Structural Biology*, July 2019.

[15] L. F. Kourkoutis, J. M. Plitzko, and W. Baumeister, “Electron Microscopy of Biological Materials at the Nanometer Scale,” *Annual Review of Materials Research*, vol. 42, pp. 33–58, Aug. 2012.

[16] F. M. Ross, “Opportunities and challenges in liquid cell electron microscopy,” *Science*, vol. 350, pp. aaa9886–aaa9886, Dec. 2015.

[17] C. Y. J. Hémonnot and S. Köster, “Imaging of Biological Materials and Cells by X-ray Scattering and Diffraction,” *ACS Nano*, vol. 11, pp. 8542–8559, Sept. 2017.

[18] M. Holler, M. Odstrcil, M. Guizar-Sicairos, M. Lebugle, E. Müller, S. Finizio, G. Tinti, C. David, J. Zusman, W. Unglaub, O. Bunk, J. Raabe, A. F. J. Levi, and G. Aeppli, “Three-dimensional imaging of integrated circuits with macro- to nanoscale zoom,” *Nature Electronics*, pp. 1–7, Oct. 2019.

[19] B. Pichler, H. F. Wehrl, A. Kolb, and M. S. Judenhofer, “PET/MRI: THE NEXT GENERATION OF MULTI-MODALITY IMAGING?,” *Seminars in nuclear medicine*, vol. 38, pp. 199–208, May 2008.

[20] M. Wu and J. Shu, “Multimodal Molecular Imaging: Current Status and Future Directions,” *Contrast Media & Molecular Imaging*, vol. 2018, June 2018.

[21] J. Zhao, J. Chen, S. Ma, Q. Liu, L. Huang, X. Chen, K. Lou, and W. Wang, “Recent developments in multimodality fluorescence imaging probes,” *Acta Pharmaceutica Sinica B*, vol. 8, pp. 320–338, May 2018.

[22] A. Sartori, R. Gatz, F. Beck, A. Rigort, W. Baumeister, and J. M. Plitzko, "Correlative microscopy: Bridging the gap between fluorescence light microscopy and cryo-electron tomography," *Journal of Structural Biology*, vol. 160, pp. 135–145, Nov. 2007.

[23] L. F. van Driel, J. A. Valentijn, K. M. Valentijn, R. I. Koning, and A. J. Koster, "Tools for correlative cryo-fluorescence microscopy and cryo-electron tomography applied to whole mitochondria in human endothelial cells," *European Journal of Cell Biology*, vol. 88, pp. 669–684, Nov. 2009.

[24] G. McDermott, M. A. Le Gros, C. G. Knoechel, M. Uchida, and C. A. Larabell, "Soft X-ray Tomography and Cryogenic Light Microscopy: The Cool Combination in Cellular Imaging," *Trends in Cell Biology*, vol. 19, pp. 587–595, Nov. 2009.

[25] E. A. Smith, B. P. Cinquin, M. Do, G. McDermott, M. A. Le Gros, and C. A. Larabell, "Correlative cryogenic tomography of cells using light and soft x-rays," *Ultramicroscopy*, vol. 143, pp. 33–40, Aug. 2014.

[26] J. R. Fienup, "Phase retrieval algorithms: A comparison," *Applied Optics*, vol. 21, pp. 2758–2769, Aug. 1982.

[27] C.-C. Chen, J. Miao, C. W. Wang, and T. K. Lee, "Application of optimization technique to noncrystalline x-ray diffraction microscopy: Guided hybrid input-output method," *Physical Review B*, vol. 76, p. 064113, Aug. 2007.

[28] V. Elser, "Phase retrieval by iterated projections," *JOSA A*, vol. 20, no. 1, pp. 40–55, 2003.

[29] J. A. Rodriguez, R. Xu, C.-C. Chen, Y. Zou, and J. Miao, "Oversampling smoothness: An effective algorithm for phase retrieval of noisy diffraction intensities," *Journal of Applied Crystallography*, vol. 46, pp. 312–318, Apr. 2013.

[30] A. M. Maiden and J. M. Rodenburg, "An improved ptychographical phase retrieval algorithm for diffractive imaging," *Ultramicroscopy*, vol. 109, pp. 1256–1262, Sept. 2009.

[31] S. J. Sahl, S. W. Hell, and S. Jakobs, "Fluorescence nanoscopy in cell biology," *Nature Reviews Molecular Cell Biology*, vol. 18, pp. 685–701, Nov. 2017.

[32] V. Lučić, A. Rigort, and W. Baumeister, "Cryo-electron tomography: The challenge of doing structural biology in situ," *The Journal of Cell Biology*, vol. 202, pp. 407–419, Aug. 2013.

[33] B. D. Engel, M. Schaffer, L. K. Cuellar, E. Villa, J. M. Plitzko, and W. Baumeister, “Native architecture of the Chlamydomonas chloroplast revealed by in situ cryo-electron tomography,” *eLife*, vol. 4, p. e04889, Jan. 2015.

[34] D. Weiß, G. Schneider, B. Niemann, P. Guttmann, D. Rudolph, and G. Schmahl, “Computed tomography of cryogenic biological specimens based on X-ray microscopic images,” *Ultramicroscopy*, vol. 84, pp. 185–197, Aug. 2000.

[35] C. A. Larabell and M. A. Le Gros, “X-ray Tomography Generates 3-D Reconstructions of the Yeast, Saccharomyces cerevisiae, at 60-nm Resolution,” *Molecular Biology of the Cell*, vol. 15, pp. 957–962, Mar. 2004.

[36] T. Paunesku, S. Vogt, J. Maser, B. Lai, and G. Woloschak, “X-ray fluorescence microprobe imaging in biology and medicine,” *Journal of Cellular Biochemistry*, vol. 99, pp. 1489–1502, Dec. 2006.

[37] C. J. Fahrni, “Biological applications of X-ray fluorescence microscopy: Exploring the subcellular topography and speciation of transition metals,” *Current Opinion in Chemical Biology*, vol. 11, pp. 121–127, Apr. 2007.

[38] S. Majumdar, J. R. Peralta-Videa, H. Castillo-Michel, J. Hong, C. M. Rico, and J. L. Gardea-Torresdey, “Applications of synchrotron μ-XRF to study the distribution of biologically important elements in different environmental matrices: A review,” *Analytica Chimica Acta*, vol. 755, pp. 1–16, Nov. 2012.

[39] M. D. de Jonge, C. Holzner, S. B. Baines, B. S. Twining, K. Ignatyev, J. Diaz, D. L. Howard, D. Legnini, A. Miceli, I. McNulty, C. J. Jacobsen, and S. Vogt, “Quantitative 3D elemental microtomography of Cyclotella meneghiniana at 400-nm resolution,” *Proceedings of the National Academy of Sciences of the United States of America*, vol. 107, pp. 15676–15680, Sept. 2010.

[40] G. Schneider, “Cryo X-ray microscopy with high spatial resolution in amplitude and phase contrast,” *Ultramicroscopy*, vol. 75, pp. 85–104, Nov. 1998.

[41] J. Miao, D. Sayre, and H. N. Chapman, “Phase retrieval from the magnitude of the Fourier transforms of nonperiodic objects,” *JOSA A*, vol. 15, no. 6, pp. 1662–1669, 1998.

[42] Y. Shechtman, Y. C. Eldar, O. Cohen, H. N. Chapman, J. Miao, and M. Segev, “Phase Retrieval with Application to Optical Imaging: A contemporary overview,” *IEEE Signal Processing Magazine*, vol. 32, pp. 87–109, May 2015.

[43] S. Marchesini, “Invited article: A unified evaluation of iterative projection algorithms for phase retrieval,” *Review of scientific instruments*, vol. 78, no. 1, p. 011301, 2007.

[44] J. Miao, K. O. Hodgson, T. Ishikawa, C. A. Larabell, M. A. LeGros, and Y. Nishino, “Imaging whole Escherichia coli bacteria by using single-particle x-ray diffraction,” *Proceedings of the National Academy of Sciences*, vol. 100, pp. 110–112, Jan. 2003.

[45] D. Shapiro, P. Thibault, T. Beetz, V. Elser, M. Howells, C. Jacobsen, J. Kirz, E. Lima, H. Miao, A. M. Neiman, *et al.*, “Biological imaging by soft x-ray diffraction microscopy,” *Proceedings of the National Academy of Sciences*, vol. 102, no. 43, pp. 15343–15346, 2005.

[46] Y. Nishino, Y. Takahashi, N. Imamoto, T. Ishikawa, and K. Maeshima, “Three-dimensional visualization of a human chromosome using coherent X-ray diffraction,” *Physical Review Letters*, vol. 102, p. 018101, Jan. 2009.

[47] H. Jiang, C. Song, C.-C. Chen, R. Xu, K. S. Raines, B. P. Fahimian, C.-H. Lu, T.-K. Lee, A. Nakashima, J. Urano, *et al.*, “Quantitative 3D imaging of whole, unstained cells by using X-ray diffraction microscopy,” *Proceedings of the National Academy of Sciences*, vol. 107, no. 25, pp. 11234–11239, 2010.

[48] C. Song, H. Jiang, A. Mancuso, B. Amirbekian, L. Peng, R. Sun, S. S. Shah, Z. H. Zhou, T. Ishikawa, and J. Miao, “Quantitative Imaging of Single, Unstained Viruses with Coherent X Rays,” *Physical Review Letters*, vol. 101, Oct. 2008.

[49] T. Kimura, Y. Joti, A. Shibuya, C. Song, S. Kim, K. Tono, M. Yabashi, M. Tamakoshi, T. Moriya, T. Oshima, T. Ishikawa, Y. Bessho, and Y. Nishino, “Imaging live cell in micro-liquid enclosure by X-ray laser diffraction,” *Nature Communications*, vol. 5, Jan. 2014.

[50] M. Gallagher-Jones, Y. Bessho, S. Kim, J. Park, S. Kim, D. Nam, C. Kim, Y. Kim, D. Y. Noh, O. Miyashita, F. Tama, Y. Joti, T. Kameshima, T. Hatsui, K. Tono, Y. Kohmura, M. Yabashi, S. S. Hasnain, T. Ishikawa, and C. Song, “Macromolecular structures probed by combining single-shot free-electron laser diffraction with synchrotron coherent X-ray imaging,” *Nature Communications*, vol. 5, May 2014.

[51] M. Bergh, G. Huldt, N. Tîmneanu, F. R. N. C. Maia, and J. Hajdu, “Feasibility of imaging living cells at subnanometer resolutions by ultrafast X-ray diffraction,” *Quarterly Reviews of Biophysics*, vol. 41, p. 181, Nov. 2008.

[52] M. M. Seibert, T. Ekeberg, F. R. N. C. Maia, M. Svenda, J. Andreasson, O. Jönsson, D. Odić, B. Iwan, A. Rocker, D. Westphal, M. Hantke, D. P. DePonte, A. Barty, J. Schulz, L. Gumprecht, N. Coppola, A. Aquila, M. Liang,

T. A. White, A. Martin, C. Caleman, S. Stern, C. Abergel, V. Seltzer, J.-M. Claverie, C. Bostedt, J. D. Bozek, S. Boutet, A. A. Miahnahri, M. Messerschmidt, J. Krzywinski, G. Williams, K. O. Hodgson, M. J. Bogan, C. Y. Hampton, R. G. Sierra, D. Starodub, I. Andersson, S. Bajt, M. Barthelmess, J. C. H. Spence, P. Fromme, U. Weierstall, R. Kirian, M. Hunter, R. B. Doak, S. Marchesini, S. P. Hau-Riege, M. Frank, R. L. Shoeman, L. Lomb, S. W. Epp, R. Hartmann, D. Rolles, A. Rudenko, C. Schmidt, L. Foucar, N. Kimmel, P. Holl, B. Rudek, B. Erk, A. Hömke, C. Reich, D. Pietschner, G. Weidenspointner, L. Strüder, G. Hauser, H. Gorke, J. Ullrich, I. Schlichting, S. Herrmann, G. Schaller, F. Schopper, H. Soltau, K.-U. Kühnel, R. Andritschke, C.-D. Schröter, F. Krasniqi, M. Bott, S. Schorb, D. Rupp, M. Adolph, T. Gorkhover, H. Hirsemann, G. Potdevin, H. Graafsma, B. Nilsson, H. N. Chapman, and J. Hajdu, "Single mimivirus particles intercepted and imaged with an X-ray laser," *Nature*, vol. 470, pp. 78–81, Feb. 2011.

[53] I. Schlichting and J. Miao, "Emerging opportunities in structural biology with X-ray free-electron lasers," *Current Opinion in Structural Biology*, vol. 22, pp. 613–626, Oct. 2012.

[54] K. Giewekemeyer, P. Thibault, S. Kalbfleisch, A. Beerlink, C. M. Kewish, M. Dierolf, F. Pfeiffer, and T. Salditt, "Quantitative biological imaging by ptychographic x-ray diffraction microscopy," *Proceedings of the National Academy of Sciences*, vol. 107, pp. 529–534, Jan. 2010.

[55] J. Deng, D. J. Vine, S. Chen, Y. S. G. Nashed, Q. Jin, N. W. Phillips, T. Peterka, R. Ross, S. Vogt, and C. J. Jacobsen, "Simultaneous cryo X-ray ptychographic and fluorescence microscopy of green algae," *Proceedings of the National Academy of Sciences*, vol. 112, pp. 2314–2319, Feb. 2015.

[56] M. Dierolf, A. Menzel, P. Thibault, P. Schneider, C. M. Kewish, R. Wepf, O. Bunk, and F. Pfeiffer, "Ptychographic X-ray computed tomography at the nanoscale," *Nature*, vol. 467, pp. 436–439, Sept. 2010.

[57] I. Zanette, B. Enders, M. Dierolf, P. Thibault, R. Gradl, A. Diaz, M. Guizar-Sicairos, A. Menzel, F. Pfeiffer, and P. Zaslansky, "Ptychographic X-ray nanotomography quantifies mineral distributions in human dentine," *Scientific Reports*, vol. 5, p. 9210, Mar. 2015.

[58] E. Hummel, P. Guttmann, S. Werner, B. Tarek, G. Schneider, M. Kunz, A. S. Frangakis, and B. Westermann, "3D Ultrastructural Organization of Whole Chlamydomonas reinhardtii Cells Studied by Nanoscale Soft X-Ray Tomography," *PLOS ONE*, vol. 7, p. e53293, Dec. 2012.

[59] A. Diaz, B. Malkova, M. Holler, M. Guizar-Sicairos, E. Lima, V. Panneels, G. Pigino, A. G. Bittermann, L. Wettstein, T. Tomizaki, O. Bunk,

G. Schertler, T. Ishikawa, R. Wepf, and A. Menzel, “Three-dimensional mass density mapping of cellular ultrastructure by ptychographic X-ray nanotomography,” *Journal of Structural Biology*, vol. 192, pp. 461–469, Dec. 2015.

[60] D. J. Vine, D. Pelliccia, C. Holzner, S. B. Baines, A. Berry, I. McNulty, S. Vogt, A. G. Peele, and K. A. Nugent, “Simultaneous X-ray fluorescence and ptychographic microscopy of Cyclotella meneghiniana,” *Optics Express*, vol. 20, pp. 18287–18296, July 2012.

[61] J. Deng, D. J. Vine, S. Chen, Q. Jin, Y. S. G. Nashed, T. Peterka, S. Vogt, and C. Jacobsen, “X-ray ptychographic and fluorescence microscopy of frozen-hydrated cells using continuous scanning,” *Scientific Reports*, vol. 7, p. 445, Mar. 2017.

[62] Y. Yang, C.-C. Chen, M. C. Scott, C. Ophus, R. Xu, A. Pryor, L. Wu, F. Sun, W. Theis, J. Zhou, M. Eisenbach, P. R. C. Kent, R. F. Sabirianov, H. Zeng, P. Ercius, and J. Miao, “Deciphering chemical order/disorder and material properties at the single-atom level,” *Nature*, vol. 542, p. 75, Feb. 2017.

[63] S. Chen, J. Deng, Y. Yuan, C. Flachenecker, R. Mak, B. Hornberger, Q. Jin, D. Shu, B. Lai, J. Maser, C. Roehrig, T. Paunesku, S. C. Gleber, D. J. Vine, L. Finney, J. VonOsinski, M. Bolbat, I. Spink, Z. Chen, J. Steele, D. Trapp, J. Irwin, M. Feser, E. Snyder, K. Brister, C. Jacobsen, G. Woloschak, and S. Vogt, “The Bionanoprobe: Hard X-ray fluorescence nanoprobe with cryogenic capabilities,” *Journal of Synchrotron Radiation*, vol. 21, pp. 66–75, Jan. 2014.

[64] J. Deng, Y. S. G. Nashed, S. Chen, N. W. Phillips, T. Peterka, R. Ross, S. Vogt, C. Jacobsen, and D. J. Vine, “Continuous motion scan ptychography: Characterization for increased speed in coherent x-ray imaging,” *Optics Express*, vol. 23, pp. 5438–5451, Feb. 2015.

[65] P. M. Pelz, M. Guizar-Sicairos, P. Thibault, I. Johnson, M. Holler, and A. Menzel, “On-the-fly scans for X-ray ptychography,” *Applied Physics Letters*, vol. 105, p. 251101, Dec. 2014.

[66] X. Huang, K. Lauer, J. N. Clark, W. Xu, E. Nazaretski, R. Harder, I. K. Robinson, and Y. S. Chu, “Fly-scan ptychography,” *Scientific Reports*, vol. 5, p. 9074, Mar. 2015.

[67] R. D. Leapman, “Detecting single atoms of calcium and iron in biological structures by electron energy-loss spectrum-imaging,” *Journal of Microscopy*, vol. 210, pp. 5–15, Apr. 2003.

[68] T. Beetz and C. Jacobsen, "Soft X-ray radiation-damage studies in PMMA using a cryo-STXM," *Journal of Synchrotron Radiation*, vol. 10, pp. 280–283, May 2003.

[69] S. Vogt, "MAPS : A set of software tools for analysis and visualization of 3D X-ray fluorescence data sets," *Journal de Physique IV*, vol. 104, pp. 635–638, Mar. 2003.

[70] M. C. Scott, C.-C. Chen, M. Mecklenburg, C. Zhu, R. Xu, P. Ercius, U. Dahmen, B. C. Regan, and J. Miao, "Electron tomography at 2.4-ångström resolution," *Nature*, vol. 483, p. 444, Mar. 2012.

[71] Y. S. G. Nashed, D. J. Vine, T. Peterka, J. Deng, R. Ross, and C. Jacobsen, "Parallel ptychographic reconstruction," *Optics Express*, vol. 22, pp. 32082–32097, Dec. 2014.

[72] F. A. Ruiz, N. Marchesini, M. Seufferheld, Govindjee, and R. Docampo, "The Polyphosphate Bodies of Chlamydomonas reinhardtii Possess a Proton-pumping Pyrophosphatase and Are Similar to Acidocalcisomes," *Journal of Biological Chemistry*, vol. 276, pp. 46196–46203, July 2001.

[73] R. Docampo and S. N. J. Moreno, "Acidocalcisomes," *Cell Calcium*, vol. 50, pp. 113–119, Aug. 2011.

[74] N. Lander, C. Cordeiro, G. Huang, and R. Docampo, "Polyphosphate and acidocalcisomes," *Biochemical Society Transactions*, vol. 44, pp. 1–6, Feb. 2016.

[75] O. Stehling and R. Lill, "The Role of Mitochondria in Cellular Iron–Sulfur Protein Biogenesis: Mechanisms, Connected Processes, and Diseases," *Cold Spring Harbor Perspectives in Biology*, vol. 5, Aug. 2013.

[76] J. Miao, F. Förster, and O. Levi, "Equally sloped tomography with oversampling reconstruction," *Physical Review B*, vol. 72, p. 052103, Aug. 2005.

[77] Y. Komine, L. L. Eggink, H. Park, and J. K. Hoober, "Vacuolar granules in Chlamydomonas reinhardtii: Polyphosphate and a 70-kDa polypeptide as major components," *Planta*, vol. 210, pp. 897–905, May 2000.

[78] D. G. Robinson, M. Hoppenrath, K. Oberbeck, P. Luykx, and R. Ratajczak, "Localization of Pyrophosphatase and V-ATPase in Chlamydomonas reinhardtii," *Botanica Acta*, vol. 111, no. 2, pp. 108–122, 1998.

[79] Z. T. Wang, N. Ullrich, S. Joo, S. Waffenschmidt, and U. Goodenough, "Algal Lipid Bodies: Stress Induction, Purification, and Biochemical Characterization in Wild-Type and Starchless Chlamydomonas reinhardtii," *Eukaryotic Cell*, vol. 8, pp. 1856–1868, Jan. 2009.

[80] M. Uchida, Y. Sun, G. McDermott, C. Knoechel, M. A. Le Gros, D. Parkinson, D. G. Drubin, and C. A. Larabell, "Quantitative analysis of yeast internal architecture using soft X-ray tomography," *Yeast (Chichester, England)*, vol. 28, pp. 227–236, Mar. 2011.

[81] M. Uchida, G. McDermott, M. Wetzler, M. A. L. Gros, M. Myllys, C. Knoechel, A. E. Barron, and C. A. Larabell, "Soft X-ray tomography of phenotypic switching and the cellular response to antifungal peptoids in Candida albicans," *Proceedings of the National Academy of Sciences*, vol. 106, pp. 19375–19380, Nov. 2009.

[82] M. Odstrčil, M. Holler, and M. Guizar-Sicairos, "Arbitrary-path fly-scan ptychography," *Optics Express*, vol. 26, pp. 12585–12593, May 2018.

[83] M. D. de Jonge, A. M. Kingston, N. Afshar, J. Garrevoet, R. Kirkham, G. Ruben, G. R. Myers, S. J. Latham, D. L. Howard, D. J. Paterson, C. G. Ryan, and G. McColl, "Spiral scanning X-ray fluorescence computed tomography," *Optics Express*, vol. 25, pp. 23424–23436, Sept. 2017.

[84] R. Hegerl and W. Hoppe, "Influence of Electron Noise on Three-dimensional Image Reconstruction," *Zeitschrift für Naturforschung A*, vol. 31, no. 12, pp. 1717–1721, 1976.

[85] H. Öztürk, H. Yan, Y. He, M. Ge, Z. Dong, M. Lin, E. Nazaretski, I. K. Robinson, Y. S. Chu, and X. Huang, "Multi-slice ptychography with large numerical aperture multilayer Laue lenses," *Optica*, vol. 5, pp. 601–607, May 2018.

[86] E. H. R. Tsai, I. Usov, A. Diaz, A. Menzel, and M. Guizar-Sicairos, "X-ray ptychography with extended depth of field," *Optics Express*, vol. 24, pp. 29089–29108, Dec. 2016.

[87] P. Li and A. Maiden, "Multi-slice ptychographic tomography," *Scientific Reports*, vol. 8, p. 2049, Feb. 2018.

[88] A. M. Maiden, M. J. Humphry, and J. M. Rodenburg, "Ptychographic transmission microscopy in three dimensions using a multi-slice approach," *JOSA A*, vol. 29, pp. 1606–1614, Aug. 2012.

[89] M. Du and C. Jacobsen, "Relative merits and limiting factors for x-ray and electron microscopy of thick, hydrated organic materials," *Ultramicroscopy*, vol. 184, pp. 293–309, Jan. 2018.

[90] R. Falcone, C. Jacobsen, J. Kirz, S. Marchesini, D. Shapiro, and J. Spence, "New directions in X-ray microscopy," *Contemporary Physics*, vol. 52, pp. 293–318, July 2011.

[91] A. P. Hitchcock, “Soft X-ray spectromicroscopy and ptychography,” *Journal of Electron Spectroscopy and Related Phenomena*, vol. 200, pp. 49–63, Apr. 2015.

[92] R. Celestre, K. Nowrouzi, D. A. Shapiro, P. Denes, J. M. Joseph, A. Schmid, and H. A. Padmore, “Nanosurveyor 2: A Compact Instrument for Nano-Tomography at the Advanced Light Source,” *Journal of Physics: Conference Series*, vol. 849, no. 1, p. 012047, 2017.

[93] D. A. Shapiro, R. Celestre, P. Denes, M. Farmand, J. Joseph, A. L. D. Kilcoyne, Stefano Marchesini, H. Padmore, S. V. Venkatakrishnan, T. Warwick, and Y.-S. Yu, “Ptychographic Imaging of Nano-Materials at the Advanced Light Source with the Nanosurveyor Instrument,” *Journal of Physics: Conference Series*, vol. 849, no. 1, p. 012028, 2017.

[94] J. Deng, Y. P. Hong, S. Chen, Y. S. G. Nashed, T. Peterka, A. J. F. Levi, J. Damoulakis, S. Saha, T. Eiles, and C. Jacobsen, “Nanoscale x-ray imaging of circuit features without wafer etching,” *Physical Review B*, vol. 95, p. 104111, Mar. 2017.

[95] M. Holler, M. Guizar-Sicairos, E. H. R. Tsai, R. Dinapoli, E. Müller, O. Bunk, J. Raabe, and G. Aeppli, “High-resolution non-destructive three-dimensional imaging of integrated circuits,” *Nature*, vol. 543, pp. 402–406, Mar. 2017.

[96] J. Thieme, I. McNult, S. Vogt, and a. D. Paterson, “X-Ray Spectromicroscopy—A Tool for Environmental Sciences,” *Environmental Science & Technology*, vol. 41, pp. 6885–6889, Oct. 2007.

[97] X.-c. Bai, G. McMullan, and S. H. W. Scheres, “How cryo-EM is revolutionizing structural biology,” *Trends in Biochemical Sciences*, vol. 40, pp. 49–57, Jan. 2015.

[98] R. Fernandez-Leiro and S. H. W. Scheres, “Unravelling biological macromolecules with cryo-electron microscopy,” *Nature*, vol. 537, pp. 339–346, Sept. 2016.

[99] J. Miao, P. Ercius, and S. J. L. Billinge, “Atomic electron tomography: 3D structures without crystals,” *Science*, vol. 353, p. aaf2157, Sept. 2016.

[100] R. Xu, C.-C. Chen, L. Wu, M. C. Scott, W. Theis, C. Ophus, M. Bartels, Y. Yang, H. Ramezani-Dakhel, M. R. Sawaya, H. Heinz, L. D. Marks, P. Ercius, and J. Miao, “Three-dimensional coordinates of individual atoms in materials revealed by electron tomography,” *Nature Materials*, vol. 14, pp. 1099–1103, Nov. 2015.

[101] I. Robinson and R. Harder, “Coherent X-ray diffraction imaging of strain at the nanoscale,” *Nature Materials*, vol. 8, pp. 291–298, Apr. 2009.

[102] Y. Zhao, B. W. Graf, E. J. Chaney, Z. Mahmassani, E. Antoniadou, R. DeVolder, H. Kong, M. D. Boppart, and S. A. Boppart, “Integrated multimodal optical microscopy for structural and functional imaging of engineered and natural skin,” *Journal of biophotonics*, vol. 5, pp. 437–448, May 2012.

[103] S. Yue, M. N. Slipchenko, and J.-X. Cheng, “Multimodal Nonlinear Optical Microscopy,” *Laser & photonics reviews*, vol. 5, July 2011.

[104] D. W. Townsend, “Multimodality imaging of structure and function,” *Physics in Medicine and Biology*, vol. 53, pp. R1–R39, Feb. 2008.

[105] R. Schafer, H. M. Leung, and A. F. Gmitro, “Multi-modality imaging of a murine mammary window chamber for breast cancer research,” *BioTechniques*, vol. 57, pp. 45–50, July 2014.

[106] S. R. Cherry, “Multimodality Imaging: Beyond PET/CT and SPECT/CT,” *Seminars in Nuclear Medicine*, vol. 39, pp. 348–353, Sept. 2009.

[107] D. A. Muller, “Structure and bonding at the atomic scale by scanning transmission electron microscopy,” *Nature Materials*, vol. 8, pp. 263–270, Apr. 2009.

[108] Y. Liu, F. Meirer, C. M. Krest, S. Webb, and B. M. Weckhuysen, “Relating structure and composition with accessibility of a single catalyst particle using correlative 3-dimensional micro-spectroscopy,” *Nature Communications*, vol. 7, p. 12634, Aug. 2016.

[109] D. C. Hezel, P. Elangovan, S. Viehmann, L. Howard, R. L. Abel, and R. Armstrong, “Visualisation and quantification of CV chondrite petrography using micro-tomography,” *Geochimica et Cosmochimica Acta*, vol. 116, pp. 33–40, Sept. 2013.

[110] A. W. Tait, K. R. Fisher, P. Srinivasan, and J. I. Simon, “Evidence for impact induced pressure gradients on the Allende CV3 parent body: Consequences for fluid and volatile transport,” *Earth and Planetary Science Letters*, vol. 454, pp. 213–224, Nov. 2016.

[111] R. D. Hanna and R. A. Ketcham, “X-ray computed tomography of planetary materials: A primer and review of recent studies,” *Geochemistry*, vol. 77, pp. 547–572, Dec. 2017.

[112] M. Howells, T. Beetz, H. Chapman, C. Cui, J. Holton, C. Jacobsen, J. Kirz, E. Lima, S. Marchesini, H. Miao, D. Sayre, D. Shapiro, J. Spence, and

D. Starodub, “An assessment of the resolution limitation due to radiation-damage in X-ray diffraction microscopy,” *Journal of Electron Spectroscopy and Related Phenomena*, vol. 170, pp. 4–12, Mar. 2009.

[113] S. Marchesini, H. Krishnan, B. J. Daurer, D. A. Shapiro, T. Perciano, J. A. Sethian, and F. R. N. C. Maia, “SHARP: A Distributed GPU-Based Ptychographic Solver,” *Journal of Applied Crystallography*, vol. 49, pp. 1245–1252, Aug. 2016.

[114] P. Thibault, M. Dierolf, A. Menzel, O. Bunk, C. David, and F. Pfeiffer, “High-resolution scanning x-ray diffraction microscopy,” *Science*, vol. 321, no. 5887, pp. 379–382, 2008.

[115] P. Thibault, M. Dierolf, O. Bunk, A. Menzel, and F. Pfeiffer, “Probe retrieval in ptychographic coherent diffractive imaging,” *Ultramicroscopy*, vol. 109, pp. 338–343, Mar. 2009.

[116] H. H. Bauschke, P. L. Combettes, and D. R. Luke, “Hybrid projection–reflection method for phase retrieval,” *JOSA A*, vol. 20, pp. 1025–1034, June 2003.

[117] E. R. Shanblatt, C. L. Porter, D. F. Gardner, G. F. Mancini, R. M. Karl, M. D. Tanksalvala, C. S. Bevis, V. H. Vartanian, H. C. Kapteyn, D. E. Adams, and M. M. Murnane, “Quantitative Chemically Specific Coherent Diffractive Imaging of Reactions at Buried Interfaces with Few Nanometer Precision,” *Nano Letters*, vol. 16, pp. 5444–5450, Sept. 2016.

[118] B. Zhang, D. F. Gardner, M. D. Seaberg, E. R. Shanblatt, H. C. Kapteyn, M. M. Murnane, and D. E. Adams, “High contrast 3D imaging of surfaces near the wavelength limit using tabletop EUV ptychography,” *Ultramicroscopy*, vol. 158, pp. 98–104, Nov. 2015.

[119] D. F. Gardner, M. Tanksalvala, E. R. Shanblatt, X. Zhang, B. R. Galloway, C. L. Porter, R. Karl Jr, C. Bevis, D. E. Adams, H. C. Kapteyn, M. M. Murnane, and G. F. Mancini, “Subwavelength coherent imaging of periodic samples using a 13.5 nm tabletop high-harmonic light source,” *Nature Photonics*, vol. 11, pp. 259–263, Apr. 2017.

[120] Francisco de la Peña, pburdet, M. Sarahan, magnunor, T. Ostasevicius, J. Taillon, A. Eljarrat, S. Mazzucco, vidartf, Gaël, L. F. Zagonel, M. Walls, and iygr, “Hyperspy: HyperSpy 0.8.” Zenodo, Apr. 2015.

[121] G. Cliff and G. W. Lorimer, “The quantitative analysis of thin specimens,” *Journal of Microscopy*, vol. 103, pp. 203–207, Mar. 1975.

[122] G. W. Lorimer, “Quantitative X-ray microanalysis of thin specimens in the transmission electron microscope; a review,” *Mineralogical Magazine*, vol. 51, pp. 49–60, Mar. 1987.

[123] M. Lerotic, R. Mak, S. Wirick, F. Meirer, and C. Jacobsen, "MANTiS: A program for the analysis of X-ray spectromicroscopy data," *Journal of Synchrotron Radiation*, vol. 21, pp. 1206–1212, Sept. 2014.

[124] J. N. Clark, C. T. Putkunz, M. A. Pfeifer, A. G. Peele, G. J. Williams, B. Chen, K. A. Nugent, C. Hall, W. Fullagar, S. Kim, and I. McNulty, "Use of a complex constraint in coherent diffractive imaging," *Optics Express*, vol. 18, pp. 1981–1993, Feb. 2010.

[125] M. W. M. Jones, A. G. Peele, and G. A. van Riessen, "Application of a complex constraint for biological samples in coherent diffractive imaging," *Optics Express*, vol. 21, pp. 30275–30281, Dec. 2013.

[126] M. W. M. Jones, K. Elgass, M. D. Junker, M. B. Luu, M. T. Ryan, A. G. Peele, and G. A. van Riessen, "Mapping biological composition through quantitative phase and absorption X-ray ptychography," *Scientific Reports*, vol. 4, p. 6796, Oct. 2014.

[127] M. W. M. Jones, K. D. Elgass, M. D. Junker, M. D. de Jonge, and G. A. van Riessen, "Molar concentration from sequential 2-D water-window X-ray ptychography and X-ray fluorescence in hydrated cells," *Scientific Reports*, vol. 6, p. 24280, Apr. 2016.

[128] J. C. da Silva, P. Trtik, A. Diaz, M. Holler, M. Guizar-Sicairos, J. Raabe, O. Bunk, and A. Menzel, "Mass Density and Water Content of Saturated Never-Dried Calcium Silicate Hydrates," *Langmuir*, vol. 31, pp. 3779–3783, Apr. 2015.

[129] H. Yan, E. Nazaretski, K. Lauer, X. Huang, U. Wagner, C. Rau, M. Yusuf, I. Robinson, S. Kalbfleisch, L. Li, N. Bouet, J. Zhou, R. Conley, and Y. S. Chu, "Multimodality hard-x-ray imaging of a chromosome with nanoscale spatial resolution," *Scientific Reports*, vol. 6, p. 20112, Feb. 2016.

[130] H. Yan, Y. S. Chu, J. Maser, E. Nazaretski, J. Kim, H. C. Kang, J. J. Lombardo, and W. K. S. Chiu, "Quantitative x-ray phase imaging at the nanoscale by multilayer Laue lenses," *Scientific Reports*, vol. 3, Feb. 2013.

[131] B. Henke, E. Gullikson, and J. Davis, "X-Ray Interactions: Photoabsorption, Scattering, Transmission, and Reflection at E = 50-30,000 eV, Z = 1-92," *Atomic Data and Nuclear Data Tables*, vol. 54, pp. 181–342, July 1993.

[132] K. Lodders, "Solar System Abundances and Condensation Temperatures of the Elements," *The Astrophysical Journal*, vol. 591, no. 2, p. 1220, 2003.

[133] A. J. Brearley, "Origin of Graphitic Carbon and Pentlandite in Matrix Olivines in the Allende Meteorite," *Science*, vol. 285, pp. 1380–1382, Aug. 1999.

[134] J. C. Sánchez-López, A. Caballero, and A. Fernández, "Characterisation of passivated aluminium nanopowders: An XPS and TEM/EELS study," *Journal of the European Ceramic Society*, vol. 18, pp. 1195–1200, Jan. 1998.

[135] Y. K. Chang, K. P. Lin, W. F. Pong, M.-H. Tsai, H. H. Hseih, J. Y. Pieh, P. K. Tseng, J. F. Lee, and L. S. Hsu, "Charge transfer and hybridization effects in Ni3Al and Ni3Ga studies by x-ray-absorption spectroscopy and theoretical calculations," *Journal of Applied Physics*, vol. 87, pp. 1312–1317, Jan. 2000.

[136] B. He, M. Zhou, Z. Hou, G. Li, and Y. Kuang, "Facile synthesis of Ni3S2/rGO nanosheets composite on nickel foam as efficient electrocatalyst for hydrogen evolution reaction in alkaline media," *Journal of Materials Research*, vol. 33, pp. 519–527, Mar. 2018.

[137] T. Yoshimura, Y. Tamenori, N. Iwasaki, H. Hasegawa, A. Suzuki, and H. Kawahata, "Magnesium K-edge XANES spectroscopy of geological standards," *Journal of Synchrotron Radiation*, vol. 20, pp. 734–740, Sept. 2013.

[138] A. J. Westphal, A. L. Butterworth, J. A. Tomsick, and Z. Gainsforth, "Measurement of the Oxidation State of Fe in the ISM Using X-Ray Absorption Spectroscopy," *The Astrophysical Journal*, vol. 872, p. 66, Feb. 2019.

[139] F. Bourdelle, K. Benzerara, O. Beyssac, J. Cosmidis, D. R. Neuville, G. E. Brown, and E. Paineau, "Quantification of the ferric/ferrous iron ratio in silicates by scanning transmission X-ray microscopy at the Fe L2,3 edges," *Contributions to Mineralogy and Petrology*, vol. 166, pp. 423–434, Aug. 2013.

[140] M. Miyahara, A. El Goresy, E. Ohtani, M. Kimura, S. Ozawa, T. Nagase, and M. Nishijima, "Fractional crystallization of olivine melt inclusion in shock-induced chondritic melt vein," *Physics of the Earth and Planetary Interiors*, vol. 177, pp. 116–121, Dec. 2009.

[141] L. Bonal, E. Quirico, M. Bourot-Denise, and G. Montagnac, "Determination of the petrologic type of CV3 chondrites by Raman spectroscopy of included organic matter," *Geochimica et Cosmochimica Acta*, vol. 70, pp. 1849–1863, Apr. 2006.

[142] C. T. Chantler, "Theoretical Form Factor, Attenuation, and Scattering Tabulation for Z=1–92 from E=1–10 eV to E=0.4–1.0 MeV," *Journal of Physical and Chemical Reference Data*, vol. 24, pp. 71–643, Jan. 1995.

[143] C. T. Chantler, "Detailed Tabulation of Atomic Form Factors, Photoelectric Absorption and Scattering Cross Section, and Mass Attenuation Coefficients in the Vicinity of Absorption Edges in the Soft X-Ray (Z=30–36, Z=60–89,

E=0.1 keV–10 keV), Addressing Convergence Issues of Earlier Work," *Journal of Physical and Chemical Reference Data*, vol. 29, pp. 597–1056, July 2000.

[144] R. W. Shewman and L. A. Clark, "Pentlandite phase relations in the Fe–Ni–S system and notes on the monosulfide solid solution," *Canadian Journal of Earth Sciences*, vol. 7, pp. 67–85, Feb. 1970.

[145] V. Raghavan, "Fe-Ni-S (iron-nickel-sulfur)," *Journal of Phase Equilibria and Diffusion*, vol. 25, Oct. 2004.

[146] C.-T. Liao, Y. H. Lo, J. Zhou, A. Rana, C. S. Bevis, G. Gui, B. Enders, K. Cannon, D. Shapiro, C. Bennett, H. Kapteyn, R. Falcone, J. Miao, and M. Murnane, "SQUARREL: Scattering Quotient Analysis to Retrieve the Ratio of Elements in X-ray Ptychography," *Microscopy Microanalysis*, vol. 25 (Suppl 2), 2019. (in press).

[147] M. Chen, T. G. Sharp, A. E. Goresy, B. Wopenka, and X. Xie, "The Majorite-Pyrope + Magnesiowüstite Assemblage: Constraints on the History of Shock Veins in Chondrites," *Science*, vol. 271, pp. 1570–1573, Mar. 1996.

[148] T. G. Sharp and P. S. de Carli, "Shock Effects in Meteorites," in *Meteorites and the Early Solar System II*, pp. 653–677, 2006.

[149] D. Stöffler, K. Keil, and S. Edward R.D, "Shock metamorphism of ordinary chondrites," *Geochimica et Cosmochimica Acta*, vol. 55, pp. 3845–3867, Dec. 1991.

[150] J. I. Goldstein, E. R. D. Scott, and N. L. Chabot, "Iron meteorites: Crystallization, thermal history, parent bodies, and origin," *Chemie der Erde - Geochemistry*, vol. 69, pp. 293–325, Nov. 2009.

[151] U. B. Marvin, J. A. Wood, and J. S. Dickey, "Ca-Al rich phases in the allende meteorite," *Earth and Planetary Science Letters*, vol. 7, pp. 346–350, Jan. 1970.

[152] L. Grossman, "Petrography and mineral chemistry of Ca-rich inclusions in the Allende meteorite," *Geochimica et Cosmochimica Acta*, vol. 39, pp. 433–454, Apr. 1975.

[153] F. J. Ciesla, "Outward Transport of High-Temperature Materials Around the Midplane of the Solar Nebula," *Science*, vol. 318, pp. 613–615, Oct. 2007.

[154] H. A. Lowenstam, P. E. D. o. G. a. P. S. H. a Lowenstam, and S. Weiner, *On Biomineralization.* Oxford University Press, 1989.

[155] U. G. K. Wegst, H. Bai, E. Saiz, A. P. Tomsia, and R. O. Ritchie, "Bioinspired structural materials," *Nature Materials*, vol. 14, pp. 23–36, Jan. 2015.

[156] Z. Yin, F. Hannard, and F. Barthelat, "Impact-resistant nacre-like transparent materials," *Science*, vol. 364, pp. 1260–1263, June 2019.

[157] N. K. Dhami, M. S. Reddy, and A. Mukherjee, "Biomineralization of calcium carbonates and their engineered applications: A review," *Frontiers in Microbiology*, vol. 4, Oct. 2013.

[158] J. Stöhr, K. Baberschke, R. Jaeger, R. Treichler, and S. Brennan, "Orientation of Chemisorbed Molecules from Surface-Absorption Fine-Structure Measurements: CO and NO on Ni(100)," *Physical Review Letters*, vol. 47, pp. 381–384, Aug. 1981.

[159] M. J. Olszta, D. J. Odom, E. P. Douglas, and L. B. Gower, "A New Paradigm for Biomineral Formation: Mineralization via an Amorphous Liquid-Phase Precursor," *Connective Tissue Research*, vol. 44, pp. 326–334, Jan. 2003.

[160] I. M. Weiss, N. Tuross, L. Addadi, and S. Weiner, "Mollusc larval shell formation: Amorphous calcium carbonate is a precursor phase for aragonite," *Journal of Experimental Zoology*, vol. 293, no. 5, pp. 478–491, 2002.

[161] R. A. Metzler, J. A. Jones, A. J. D'Addario, and E. J. Galvez, "Polarimetry of Pinctada fucata nacre indicates myostracal layer interrupts nacre structure," *Royal Society Open Science*, vol. 4, Feb. 2017.

[162] R. A. Metzler, C. Burgess, B. Regan, S. Spano, and E. J. Galvez, "Polarimetry of nacre in iridescent shells," in *The Nature of Light: Light in Nature V*, vol. 9187, p. 918704, International Society for Optics and Photonics, Sept. 2014.

[163] R. A. Metzler, M. Abrecht, R. M. Olabisi, D. Ariosa, C. J. Johnson, B. H. Frazer, S. N. Coppersmith, and P. U. P. A. Gilbert, "Architecture of Columnar Nacre, and Implications for Its Formation Mechanism," *Physical Review Letters*, vol. 98, p. 268102, June 2007.

[164] R. T. DeVol, R. A. Metzler, L. Kabalah-Amitai, B. Pokroy, Y. Politi, A. Gal, L. Addadi, S. Weiner, A. Fernandez-Martinez, R. Demichelis, J. D. Gale, J. Ihli, F. C. Meldrum, A. Z. Blonsky, C. E. Killian, C. B. Salling, A. T. Young, M. A. Marcus, A. Scholl, A. Doran, C. Jenkins, H. A. Bechtel, and P. U. P. A. Gilbert, "Oxygen Spectroscopy and Polarization-Dependent Imaging Contrast (PIC)-Mapping of Calcium Carbonate Minerals and Biominerals," *The Journal of Physical Chemistry B*, vol. 118, pp. 8449–8457, July 2014.

[165] P. U. P. A. Gilbert, A. Young, and S. N. Coppersmith, "Measurement of c-axis angular orientation in calcite (CaCO3) nanocrystals using X-ray absorption spectroscopy," *Proceedings of the National Academy of Sciences*, vol. 108, pp. 11350–11355, July 2011.

[166] R. A. Metzler, D. Zhou, M. Abrecht, J.-W. Chiou, J. Guo, D. Ariosa, S. N. Coppersmith, and P. U. P. A. Gilbert, "Polarization-dependent imaging contrast in abalone shells," *Physical Review B*, vol. 77, p. 064110, Feb. 2008.

[167] H. Ade and B. Hsiao, "X-ray Linear Dichroism Microscopy," *Science*, vol. 262, pp. 1427–1429, Nov. 1993.

[168] J. M. Rodenburg and H. M. Faulkner, "A Phase Retrieval Algorithm for Shifting Illumination," *Applied physics letters*, vol. 85, no. 20, pp. 4795–4797, 2004.

[169] D. A. Shapiro, Y.-S. Yu, T. Tyliszczak, J. Cabana, R. Celestre, W. Chao, K. Kaznatcheev, A. L. D. Kilcoyne, F. Maia, S. Marchesini, Y. S. Meng, T. Warwick, L. L. Yang, and H. A. Padmore, "Chemical composition mapping with nanometre resolution by soft X-ray microscopy," *Nature Photonics*, vol. 8, pp. 765–769, Oct. 2014.

[170] M. E. Birkbak, M. Guizar-Sicairos, M. Holler, and H. Birkedal, "Internal structure of sponge glass fiber revealed by ptychographic nanotomography," *Journal of Structural Biology*, vol. 194, pp. 124–128, Apr. 2016.

[171] P. Ferrand, A. Baroni, M. Allain, and V. Chamard, "Quantitative imaging of anisotropic material properties with vectorial ptychography," *Optics Letters*, vol. 43, pp. 763–766, Feb. 2018.

[172] A. Tripathi, J. Mohanty, S. H. Dietze, O. G. Shpyrko, E. Shipton, E. E. Fullerton, S. S. Kim, and I. McNulty, "Dichroic coherent diffractive imaging," *Proceedings of the National Academy of Sciences*, vol. 108, pp. 13393–13398, Aug. 2011.

[173] C. Ophus, "Four-Dimensional Scanning Transmission Electron Microscopy (4D-STEM): From Scanning Nanodiffraction to Ptychography and Beyond," *Microscopy and Microanalysis*, vol. 25, pp. 563–582, June 2019.

[174] D. Doering, N. C. Andresen, D. Contarato, P. Denes, J. M. Joseph, P. McVittie, J. Walder, J. T. Weizeorick, and B. Zheng, "High speed, direct detection 1k Frame-Store CCD sensor for synchrotron radiation," *2011 IEEE Nuclear Science Symposium Conference Record*, pp. 1840–1845, 2011.

[175] A. Maiden, D. Johnson, and P. Li, "Further improvements to the ptychographical iterative engine," *Optica*, vol. 4, pp. 736–745, July 2017.

[176] L. Rokach and O. Maimon, "Clustering Methods," in *Data Mining and Knowledge Discovery Handbook* (O. Maimon and L. Rokach, eds.), pp. 321–352, Boston, MA: Springer US, 2005.

[177] J. Zhou, Y. Yang, Y. Yang, D. S. Kim, A. Yuan, X. Tian, C. Ophus, F. Sun, A. K. Schmid, M. Nathanson, H. Heinz, Q. An, H. Zeng, P. Ercius, and J. Miao, "Observing crystal nucleation in four dimensions using atomic electron tomography," *Nature*, vol. 570, pp. 500–503, June 2019.

[178] X. Tian, D. S. Kim, S. Yang, C. J. Ciccarino, Y. Gong, Y. Yang, Y. Yang, B. Duschatko, Y. Yuan, P. M. Ajayan, J.-C. Idrobo, P. Narang, and J. Miao, "Correlating 3D atomic defects and electronic properties of 2D materials with picometer precision," *arXiv:1901.00633 [cond-mat]*, Jan. 2019.

[179] M. Farmand, R. Celestre, P. Denes, A. L. D. Kilcoyne, S. Marchesini, H. Padmore, T. Tyliszczak, T. Warwick, X. Shi, J. Lee, Y.-S. Yu, J. Cabana, J. Joseph, H. Krishnan, T. Perciano, F. R. N. C. Maia, and D. A. Shapiro, "Near-edge X-ray refraction fine structure microscopy," *Applied Physics Letters*, vol. 110, p. 063101, Feb. 2017.

[180] J. Marrison, L. Räty, P. Marriott, and P. O'Toole, "Ptychography – a label free, high-contrast imaging technique for live cells using quantitative phase information," *Scientific Reports*, vol. 3, Aug. 2013.

[181] C.-Y. Sun, M. A. Marcus, M. J. Frazier, A. J. Giuffre, T. Mass, and P. U. P. A. Gilbert, "Spherulitic Growth of Coral Skeletons and Synthetic Aragonite: Nature's Three-Dimensional Printing," *ACS Nano*, vol. 11, pp. 6612–6622, July 2017.

[182] L. C. Nielsen, D. J. DePaolo, and J. J. De Yoreo, "Self-consistent ion-by-ion growth model for kinetic isotopic fractionation during calcite precipitation," *Geochimica et Cosmochimica Acta*, vol. 86, pp. 166–181, June 2012.

[183] T. Mass, A. J. Giuffre, C.-Y. Sun, C. A. Stifler, M. J. Frazier, M. Neder, N. Tamura, C. V. Stan, M. A. Marcus, and P. U. P. A. Gilbert, "Amorphous calcium carbonate particles form coral skeletons," *Proceedings of the National Academy of Sciences*, vol. 114, pp. E7670–E7678, Sept. 2017.

[184] B. H. Frazer, B. Gilbert, B. R. Sonderegger, and G. De Stasio, "The probing depth of total electron yield in the sub-keV range: TEY-XAS and X-PEEM," *Surface Science*, vol. 537, pp. 161–167, July 2003.

[185] M. Gallagher-Jones, C. Ophus, K. C. Bustillo, D. R. Boyer, O. Panova, C. Glynn, C.-T. Zee, J. Ciston, K. C. Mancia, A. M. Minor, and J. A. Rodriguez, "Nanoscale mosaicity revealed in peptide microcrystals by scanning electron nanodiffraction," *Communications Biology*, vol. 2, p. 26, Jan. 2019.

[186] C. Donnelly, M. Guizar-Sicairos, V. Scagnoli, S. Gliga, M. Holler, J. Raabe, and L. J. Heyderman, "Three-dimensional magnetization structures revealed with X-ray vector nanotomography," *Nature*, vol. 547, pp. 328–331, July 2017.

[187] P. Ferrand, M. Allain, and V. Chamard, "Ptychography in anisotropic media," *Optics Letters*, vol. 40, pp. 5144–5147, Nov. 2015.

[188] M. A. Pfeifer, G. J. Williams, I. A. Vartanyants, R. Harder, and I. K. Robinson, "Three-dimensional mapping of a deformation field inside a nanocrystal," *Nature*, vol. 442, pp. 63–66, July 2006.

[189] H. N. Chapman, A. Barty, S. Marchesini, A. Noy, S. P. Hau-Riege, C. Cui, M. R. Howells, R. Rosen, H. He, J. C. Spence, *et al.*, "High-resolution ab initio three-dimensional x-ray diffraction microscopy," *JOSA A*, vol. 23, no. 5, pp. 1179–1200, 2006.

[190] H. N. Chapman, A. Barty, M. J. Bogan, S. Boutet, M. Frank, S. P. Hau-Riege, S. Marchesini, B. W. Woods, S. Bajt, W. H. Benner, R. A. London, E. Plönjes, M. Kuhlmann, R. Treusch, S. Düsterer, T. Tschentscher, J. R. Schneider, E. Spiller, T. Möller, C. Bostedt, M. Hoener, D. A. Shapiro, K. O. Hodgson, D. van der Spoel, F. Burmeister, M. Bergh, C. Caleman, G. Huldt, M. M. Seibert, F. R. N. C. Maia, R. W. Lee, A. Szöke, N. Timneanu, and J. Hajdu, "Femtosecond diffractive imaging with a soft-X-ray free-electron laser," *Nature Physics*, vol. 2, pp. 839–843, Dec. 2006.

[191] J. M. Rodenburg, A. C. Hurst, A. G. Cullis, B. R. Dobson, F. Pfeiffer, O. Bunk, C. David, K. Jefimovs, and I. Johnson, "Hard-X-Ray Lensless Imaging of Extended Objects," *Physical Review Letters*, vol. 98, Jan. 2007.

[192] R. L. Sandberg, A. Paul, D. A. Raymondson, S. Hädrich, D. M. Gaudiosi, J. Holtsnider, R. I. Tobey, O. Cohen, M. M. Murnane, H. C. Kapteyn, C. Song, J. Miao, Y. Liu, and F. Salmassi, "Lensless Diffractive Imaging Using Tabletop Coherent High-Harmonic Soft-X-Ray Beams," *Physical Review Letters*, vol. 99, p. 098103, Aug. 2007.

[193] B. Abbey, K. A. Nugent, G. J. Williams, J. N. Clark, A. G. Peele, M. A. Pfeifer, M. de Jonge, and I. McNulty, "Keyhole coherent diffractive imaging," *Nature Physics*, vol. 4, pp. 394–398, May 2008.

[194] C. Song, R. Bergstrom, D. Ramunno-Johnson, H. Jiang, D. Paterson, M. D. de Jonge, I. McNulty, J. Lee, K. L. Wang, and J. Miao, "Nanoscale Imaging of Buried Structures with Elemental Specificity Using Resonant X-Ray Diffraction Microscopy," *Physical Review Letters*, vol. 100, p. 025504, Jan. 2008.

[195] J. Nelson, X. Huang, J. Steinbrener, D. Shapiro, J. Kirz, S. Marchesini, A. M. Neiman, J. J. Turner, and C. Jacobsen, "High-resolution x-ray diffraction microscopy of specifically labeled yeast cells," *Proceedings of the National Academy of Sciences*, vol. 107, pp. 7235–7239, Apr. 2010.

[196] A. Greenbaum, W. Luo, T.-W. Su, Z. Göröcs, L. Xue, S. O. Isikman, A. F. Coskun, O. Mudanyali, and A. Ozcan, "Imaging without lenses: Achievements and remaining challenges of wide-field on-chip microscopy," *Nature Methods*, vol. 9, pp. 889–895, Sept. 2012.

[197] A. Szameit, Y. Shechtman, E. Osherovich, E. Bullkich, P. Sidorenko, H. Dana, S. Steiner, E. B. Kley, S. Gazit, T. Cohen-Hyams, S. Shoham, M. Zibulevsky, I. Yavneh, Y. C. Eldar, O. Cohen, and M. Segev, "Sparsity-based single-shot subwavelength coherent diffractive imaging," *Nature Materials*, vol. 11, pp. 455–459, Apr. 2012.

[198] J. N. Clark, L. Beitra, G. Xiong, A. Higginbotham, D. M. Fritz, H. T. Lemke, D. Zhu, M. Chollet, G. J. Williams, M. Messerschmidt, B. Abbey, R. J. Harder, A. M. Korsunsky, J. S. Wark, and I. K. Robinson, "Ultrafast Three-Dimensional Imaging of Lattice Dynamics in Individual Gold Nanocrystals," *Science*, vol. 341, pp. 56–59, July 2013.

[199] G. Zheng, R. Horstmeyer, and C. Yang, "Wide-field, high-resolution Fourier ptychographic microscopy," *Nature Photonics*, vol. 7, pp. 739–745, July 2013.

[200] H. Jiang, R. Xu, C.-C. Chen, W. Yang, J. Fan, X. Tao, C. Song, Y. Kohmura, T. Xiao, Y. Wang, Y. Fei, T. Ishikawa, W. L. Mao, and J. Miao, "Three-Dimensional Coherent X-Ray Diffraction Imaging of Molten Iron in Mantle Olivine at Nanoscale Resolution," *Physical Review Letters*, vol. 110, p. 205501, May 2013.

[201] R. Xu, H. Jiang, C. Song, J. A. Rodriguez, Z. Huang, C.-C. Chen, D. Nam, J. Park, M. Gallagher-Jones, S. Kim, S. Kim, A. Suzuki, Y. Takayama, T. Oroguchi, Y. Takahashi, J. Fan, Y. Zou, T. Hatsui, Y. Inubushi, T. Kameshima, K. Yonekura, K. Tono, T. Togashi, T. Sato, M. Yamamoto, M. Nakasako, M. Yabashi, T. Ishikawa, and J. Miao, "Single-shot three-dimensional structure determination of nanocrystals with femtosecond X-ray free-electron laser pulses," *Nature Communications*, vol. 5, p. 4061, June 2014.

[202] A. Ulvestad, M. J. Welland, S. S. E. Collins, R. Harder, E. Maxey, J. Wingert, A. Singer, S. Hy, P. Mulvaney, P. Zapol, and O. G. Shpyrko, "Avalanching strain dynamics during the hydriding phase transformation in individual palladium nanoparticles," *Nature Communications*, vol. 6, p. 10092, Dec. 2015.

[203] M. Hirose, K. Shimomura, A. Suzuki, N. Burdet, and Y. Takahashi, "Multiple defocused coherent diffraction imaging: Method for simultaneously reconstructing objects and probe using X-ray free-electron lasers," *Optics Express*, vol. 24, p. 11917, May 2016.

[204] P. Emma, R. Akre, J. Arthur, R. Bionta, C. Bostedt, J. Bozek, A. Brachmann, P. Bucksbaum, R. Coffee, F.-J. Decker, Y. Ding, D. Dowell, S. Edstrom, A. Fisher, J. Frisch, S. Gilevich, J. Hastings, G. Hays, P. Hering, Z. Huang, R. Iverson, H. Loos, M. Messerschmidt, A. Miahnahri, S. Moeller, H.-D. Nuhn, G. Pile, D. Ratner, J. Rzepiela, D. Schultz, T. Smith, P. Stefan, H. Tompkins, J. Turner, J. Welch, W. White, J. Wu, G. Yocky, and J. Galayda, "First lasing and operation of an ångstrom-wavelength free-electron laser," *Nature Photonics*, vol. 4, pp. 641–647, Sept. 2010.

[205] T. Ishikawa, H. Aoyagi, T. Asaka, Y. Asano, N. Azumi, T. Bizen, H. Ego, K. Fukami, T. Fukui, Y. Furukawa, S. Goto, H. Hanaki, T. Hara, T. Hasegawa, T. Hatsui, A. Higashiya, T. Hirono, N. Hosoda, M. Ishii, T. Inagaki, Y. Inubushi, T. Itoga, Y. Joti, M. Kago, T. Kameshima, H. Kimura, Y. Kirihara, A. Kiyomichi, T. Kobayashi, C. Kondo, T. Kudo, H. Maesaka, X. M. Maréchal, T. Masuda, S. Matsubara, T. Matsumoto, T. Matsushita, S. Matsui, M. Nagasono, N. Nariyama, H. Ohashi, T. Ohata, T. Ohshima, S. Ono, Y. Otake, C. Saji, T. Sakurai, T. Sato, K. Sawada, T. Seike, K. Shirasawa, T. Sugimoto, S. Suzuki, S. Takahashi, H. Takebe, K. Takeshita, K. Tamasaku, H. Tanaka, R. Tanaka, T. Tanaka, T. Togashi, K. Togawa, A. Tokuhisa, H. Tomizawa, K. Tono, S. Wu, M. Yabashi, M. Yamaga, A. Yamashita, K. Yanagida, C. Zhang, T. Shintake, H. Kitamura, and N. Kumagai, "A compact X-ray free-electron laser emitting in the sub-ångström region," *Nature Photonics*, vol. 6, pp. 540–544, Aug. 2012.

[206] T. Popmintchev, M.-C. Chen, D. Popmintchev, P. Arpin, S. Brown, S. Ališauskas, G. Andriukaitis, T. Balčiunas, O. D. Mücke, A. Pugzlys, A. Baltuška, B. Shim, S. E. Schrauth, A. Gaeta, C. Hernández-García, L. Plaja, A. Becker, A. Jaron-Becker, M. M. Murnane, and H. C. Kapteyn, "Bright Coherent Ultrahigh Harmonics in the keV X-ray Regime from Mid-Infrared Femtosecond Lasers," *Science*, vol. 336, pp. 1287–1291, June 2012.

[207] T. Hatsui and H. Graafsma, "X-ray imaging detectors for synchrotron and XFEL sources," *IUCrJ*, vol. 2, pp. 371–383, May 2015.

[208] M. C. Newton, A. Parsons, U. Wagner, and C. Rau, "Coherent x-ray diffraction imaging of photo-induced structural changes in BiFeO3nanocrystals," *New Journal of Physics*, vol. 18, p. 093003, Sept. 2016.

[209] X. Liu, M. A. G. Aranda, B. Chen, P. Wang, R. Harder, and I. Robinson, "In Situ Bragg Coherent Diffraction Imaging Study of a Cement Phase Micro-

crystal during Hydration," *Crystal Growth & Design*, vol. 15, pp. 3087–3091, July 2015.

[210] E. de Smit, I. Swart, J. F. Creemer, G. H. Hoveling, M. K. Gilles, T. Tyliszczak, P. J. Kooyman, H. W. Zandbergen, C. Morin, B. M. Weckhuysen, and F. M. F. de Groot, "Nanoscale chemical imaging of a working catalyst by scanning transmission X-ray microscopy," *Nature*, vol. 456, pp. 222–225, Nov. 2008.

[211] J. Nelson, S. Misra, Y. Yang, A. Jackson, Y. Liu, H. Wang, H. Dai, J. C. Andrews, Y. Cui, and M. F. Toney, "In Operando X-ray Diffraction and Transmission X-ray Microscopy of Lithium Sulfur Batteries," *Journal of the American Chemical Society*, vol. 134, pp. 6337–6343, Apr. 2012.

[212] J. Kirz, C. Jacobsen, and M. Howells, "Soft X-ray microscopes and their biological applications," *Quarterly Reviews of Biophysics*, vol. 28, p. 33, Feb. 1995.

[213] P. G. Bruce, S. A. Freunberger, L. J. Hardwick, and J.-M. Tarascon, "Li-O2 and Li-S batteries with high energy storage," *Nature Materials*, vol. 11, pp. 19–29, Jan. 2012.

[214] E. R. White, S. B. Singer, V. Augustyn, W. A. Hubbard, M. Mecklenburg, B. Dunn, and B. C. Regan, "In Situ Transmission Electron Microscopy of Lead Dendrites and Lead Ions in Aqueous Solution," *ACS Nano*, vol. 6, pp. 6308–6317, July 2012.

[215] D. R. Luke, "Relaxed averaged alternating reflections for diffraction imaging," *Inverse Problems*, vol. 21, pp. 37–50, Nov. 2004.

[216] N. A. Charles, E. C. Holland, R. Gilbertson, R. Glass, and H. Kettenmann, "The brain tumor microenvironment," *Glia*, vol. 59, pp. 1169–1180, Aug. 2011.

[217] M. Zhang, J. Chen, L. Wang, X. Ji, L. Yang, Y. Sheng, H. Liu, H. Wang, A. Wang, X. Dai, *et al.*, "Preliminary analysis of cellular sociology of co-cultured glioma initiating cells and macrophages in vitro," *Translational Neuroscience and Clinics*, vol. 2, no. 2, pp. 77–86, 2016.

[218] T.-Y. Lan, P.-N. Li, and T.-K. Lee, "Method to enhance the resolution of x-ray coherent diffraction imaging for non-crystalline bio-samples," *New Journal of Physics*, vol. 16, p. 033016, Mar. 2014.

[219] C. T. Putkunz, J. N. Clark, D. J. Vine, G. J. Williams, M. A. Pfeifer, E. Balaur, I. McNulty, K. A. Nugent, and A. G. Peele, "Phase-Diverse Coherent Diffractive Imaging: High Sensitivity with Low Dose," *Physical Review Letters*, vol. 106, p. 013903, Jan. 2011.

[220] C. Kim, Y. Kim, C. Song, S. S. Kim, S. Kim, H. C. Kang, Y. Hwu, K.-D. Tsuei, K. S. Liang, and D. Y. Noh, "Resolution enhancement in coherent x-ray diffraction imaging by overcoming instrumental noise," *Optics Express*, vol. 22, p. 29161, Nov. 2014.

[221] Y. Takayama, S. Maki-Yonekura, T. Oroguchi, M. Nakasako, and K. Yonekura, "Signal enhancement and Patterson-search phasing for high-spatial-resolution coherent X-ray diffraction imaging of biological objects," *Scientific Reports*, vol. 5, p. 8074, Jan. 2015.

[222] S. Boutet, M. J. Bogan, A. Barty, M. Frank, W. H. Benner, S. Marchesini, M. M. Seibert, J. Hajdu, and H. N. Chapman, "Ultrafast soft X-ray scattering and reference-enhanced diffractive imaging of weakly scattering nanoparticles," *Journal of Electron Spectroscopy and Related Phenomena*, vol. 166-167, pp. 65–73, Nov. 2008.

[223] D. Y. Noh, C. Kim, Y. Kim, and C. Song, "Enhancing resolution in coherent x-ray diffraction imaging," *Journal of Physics: Condensed Matter*, vol. 28, no. 49, p. 493001, 2016.

[224] I. McNulty, J. Kirz, C. Jacobsen, E. H. Anderson, M. R. Howells, and D. P. Kern, "High-Resolution Imaging by Fourier Transform X-ray Holography," *Science*, vol. 256, pp. 1009–1012, May 1992.

[225] S. Eisebitt, J. Lüning, W. F. Schlotter, M. Lörgen, O. Hellwig, W. Eberhardt, and J. Stöhr, "Lensless imaging of magnetic nanostructures by X-ray spectro-holography," *Nature*, vol. 432, pp. 885–888, Dec. 2004.

[226] S. Marchesini, S. Boutet, A. E. Sakdinawat, M. J. Bogan, S. Bajt, A. Barty, H. N. Chapman, M. Frank, S. P. Hau-Riege, A. Szöke, C. Cui, D. A. Shapiro, M. R. Howells, J. C. H. Spence, J. W. Shaevitz, J. Y. Lee, J. Hajdu, and M. M. Seibert, "Massively parallel X-ray holography," *Nature Photonics*, vol. 2, pp. 560–563, Sept. 2008.

[227] W. H. De Jong and P. J. Borm, "Drug delivery and nanoparticles: Applications and hazards," *International Journal of Nanomedicine*, vol. 3, pp. 133–149, June 2008.

[228] A. Z. Wang, R. Langer, and O. C. Farokhzad, "Nanoparticle Delivery of Cancer Drugs," *Annual Review of Medicine*, vol. 63, no. 1, pp. 185–198, 2012.

[229] T. R. Pisanic, J. D. Blackwell, V. I. Shubayev, R. R. Fiñones, and S. Jin, "Nanotoxicity of iron oxide nanoparticle internalization in growing neurons," *Biomaterials*, vol. 28, pp. 2572–2581, June 2007.

[230] J. J. Conesa, J. Otón, M. Chiappi, J. M. Carazo, E. Pereiro, F. J. Chichón, and J. L. Carrascosa, "Intracellular nanoparticles mass quantification by near-edge absorption soft X-ray nanotomography," *Scientific Reports*, vol. 6, p. 22354, Mar. 2016.

[231] I. K. Robinson, I. A. Vartanyants, G. J. Williams, M. A. Pfeifer, and J. A. Pitney, "Reconstruction of the Shapes of Gold Nanocrystals Using Coherent X-Ray Diffraction," *Physical Review Letters*, vol. 87, p. 195505, Oct. 2001.

[232] J. Miao, H. N. Chapman, J. Kirz, D. Sayre, and K. O. Hodgson, "Taking X-Ray Diffraction to the Limit: Macromolecular Structures from Femtosecond X-Ray Pulses and Diffraction Microscopy of Cells with Synchrotron Radiation," *Annual Review of Biophysics and Biomolecular Structure*, vol. 33, no. 1, pp. 157–176, 2004.

[233] R. L. Sandberg, C. Song, P. W. Wachulak, D. A. Raymondson, A. Paul, B. Amirbekian, E. Lee, A. E. Sakdinawat, C. La-O-Vorakiat, M. C. Marconi, C. S. Menoni, M. M. Murnane, J. J. Rocca, H. C. Kapteyn, and J. Miao, "High numerical aperture tabletop soft x-ray diffraction microscopy with 70-nm resolution," *Proceedings of the National Academy of Sciences*, vol. 105, pp. 24–27, Aug. 2008.

[234] X. Huang, J. Nelson, J. Kirz, E. Lima, S. Marchesini, H. Miao, A. M. Neiman, D. Shapiro, J. Steinbrener, A. Stewart, J. J. Turner, and C. Jacobsen, "Soft X-Ray Diffraction Microscopy of a Frozen Hydrated Yeast Cell," *Physical Review Letters*, vol. 103, p. 198101, Nov. 2009.

[235] E. Lima, L. Wiegart, P. Pernot, M. Howells, J. Timmins, F. Zontone, and A. Madsen, "Cryogenic X-Ray Diffraction Microscopy for Biological Samples," *Physical Review Letters*, vol. 103, p. 198102, Nov. 2009.

[236] D. Nam, J. Park, M. Gallagher-Jones, S. Kim, S. Kim, Y. Kohmura, H. Naitow, N. Kunishima, T. Yoshida, T. Ishikawa, and C. Song, "Imaging Fully Hydrated Whole Cells by Coherent X-Ray Diffraction Microscopy," *Physical Review Letters*, vol. 110, p. 098103, Feb. 2013.

[237] C. Song, M. Takagi, J. Park, R. Xu, M. Gallagher-Jones, N. Imamoto, and T. Ishikawa, "Analytic 3D Imaging of Mammalian Nucleus at Nanoscale Using Coherent X-Rays and Optical Fluorescence Microscopy," *Biophysical Journal*, vol. 107, pp. 1074–1081, Sept. 2014.

[238] M. F. Hantke, D. Hasse, F. R. N. C. Maia, T. Ekeberg, K. John, M. Svenda, N. D. Loh, A. V. Martin, N. Timneanu, D. S. D. Larsson, G. van der Schot, G. H. Carlsson, M. Ingelman, J. Andreasson, D. Westphal, M. Liang, F. Stellato, D. P. DePonte, R. Hartmann, N. Kimmel, R. A. Kirian, M. M. Seibert, K. Mühlig, S. Schorb, K. Ferguson, C. Bostedt, S. Carron, J. D. Bozek,

D. Rolles, A. Rudenko, S. Epp, H. N. Chapman, A. Barty, J. Hajdu, and I. Andersson, "High-throughput imaging of heterogeneous cell organelles with an X-ray laser," *Nature Photonics*, vol. 8, pp. 943–949, Dec. 2014.

[239] J. A. Rodriguez, R. Xu, C.-C. Chen, Z. Huang, H. Jiang, A. L. Chen, K. S. Raines, A. Pryor Jr, D. Nam, L. Wiegart, C. Song, A. Madsen, Y. Chushkin, F. Zontone, P. J. Bradley, and J. Miao, "Three-dimensional coherent X-ray diffractive imaging of whole frozen-hydrated cells," *IUCrJ*, vol. 2, pp. 575–583, Sept. 2015.

[240] Y. Takayama and K. Yonekura, "Cryogenic coherent X-ray diffraction imaging of biological samples at SACLA: A correlative approach with cryo-electron and light microscopy," *Acta Crystallographica Section A: Foundations and Advances*, vol. 72, pp. 179–189, Mar. 2016.

[241] F. B. de la Cuesta, M. P. E. Wenger, R. J. Bean, L. Bozec, M. A. Horton, and I. K. Robinson, "Coherent X-ray diffraction from collagenous soft tissues," *Proceedings of the National Academy of Sciences*, vol. 106, pp. 15297–15301, Sept. 2009.

[242] R. N. Wilke, M. Priebe, M. Bartels, K. Giewekemeyer, A. Diaz, P. Karvinen, and T. Salditt, "Hard X-ray imaging of bacterial cells: Nano-diffraction and ptychographic reconstruction," *Optics Express*, vol. 20, pp. 19232–19254, Aug. 2012.

[243] Y. Takahashi, A. Suzuki, S. Furutaku, K. Yamauchi, Y. Kohmura, and T. Ishikawa, "High-resolution and high-sensitivity phase-contrast imaging by focused hard x-ray ptychography with a spatial filter," *Applied Physics Letters*, vol. 102, p. 094102, Mar. 2013.

[244] A. Maiden, G. Morrison, B. Kaulich, A. Gianoncelli, and J. Rodenburg, "Soft X-ray spectromicroscopy using ptychography with randomly phased illumination," *Nature Communications*, vol. 4, p. 1669, Apr. 2013.

[245] M. D. Seaberg, B. Zhang, D. F. Gardner, E. R. Shanblatt, M. M. Murnane, H. C. Kapteyn, and D. E. Adams, "Tabletop nanometer extreme ultraviolet imaging in an extended reflection mode using coherent Fresnel ptychography," *Optica*, vol. 1, pp. 39–44, July 2014.

[246] K. Giewekemeyer, C. Hackenberg, A. Aquila, R. N. Wilke, M. R. Groves, R. Jordanova, V. S. Lamzin, G. Borchers, K. Saksl, A. V. Zozulya, M. Sprung, and A. P. Mancuso, "Tomography of a Cryo-immobilized Yeast Cell Using Ptychographic Coherent X-Ray Diffractive Imaging," *Biophysical Journal*, vol. 109, pp. 1986–1995, Nov. 2015.

[247] M. Dierolf, P. Thibault, A. Menzel, C. M. Kewish, K. Jefimovs, Ilme Schlichting, K. von König, O. Bunk, and F. Pfeiffer, "Ptychographic coherent diffractive imaging of weakly scattering specimens," *New Journal of Physics*, vol. 12, no. 3, p. 035017, 2010.

[248] Y. Zhu, W. Cai, R. D. Piner, A. Velamakanni, and R. S. Ruoff, "Transparent self-assembled films of reduced graphene oxide platelets," *Applied Physics Letters*, vol. 95, p. 103104, Sept. 2009.

[249] R. S. Pantelic, J. C. Meyer, U. Kaiser, W. Baumeister, and J. M. Plitzko, "Graphene oxide: A substrate for optimizing preparations of frozen-hydrated samples," *Journal of Structural Biology*, vol. 170, pp. 152–156, Apr. 2010.

[250] J. Park, H. Park, P. Ercius, A. F. Pegoraro, C. Xu, J. W. Kim, S. H. Han, and D. A. Weitz, "Direct Observation of Wet Biological Samples by Graphene Liquid Cell Transmission Electron Microscopy," *Nano Letters*, vol. 15, pp. 4737–4744, July 2015.

[251] M. Wojcik, M. Hauser, W. Li, S. Moon, and K. Xu, "Graphene-enabled electron microscopy and correlated super-resolution microscopy of wet cells," *Nature Communications*, vol. 6, p. 7384, June 2015.

[252] N. Mohanty, M. Fahrenholtz, A. Nagaraja, D. Boyle, and V. Berry, "Impermeable Graphenic Encasement of Bacteria," *Nano Letters*, vol. 11, pp. 1270–1275, Mar. 2011.

[253] J.-T. Jeong, M.-K. Choi, Y. Sim, J.-T. Lim, G.-S. Kim, M.-J. Seong, J.-H. Hyung, K. S. Kim, A. Umar, and S.-K. Lee, "Effect of graphene oxide ratio on the cell adhesion and growth behavior on a graphene oxide-coated silicon substrate," *Scientific Reports*, vol. 6, pp. 1–10, Sept. 2016.

[254] M. Kalbacova, A. Broz, J. Kong, and M. Kalbac, "Graphene substrates promote adherence of human osteoblasts and mesenchymal stromal cells," *Carbon*, vol. 48, pp. 4323–4329, Dec. 2010.

[255] W. C. Lee, C. H. Y. X. Lim, H. Shi, L. A. L. Tang, Y. Wang, C. T. Lim, and K. P. Loh, "Origin of Enhanced Stem Cell Growth and Differentiation on Graphene and Graphene Oxide," *ACS Nano*, vol. 5, pp. 7334–7341, Sept. 2011.

[256] E. Garcia-Alegria, M. Iliut, M. Stefanska, C. Silva, S. Heeg, S. J. Kimber, V. Kouskoff, G. Lacaud, A. Vijayaraghavan, and K. Batta, "Graphene Oxide promotes embryonic stem cell differentiation to haematopoietic lineage," *Scientific Reports*, vol. 6, pp. 1–13, May 2016.

[257] W. W. Yu, J. C. Falkner, C. T. Yavuz, and V. L. Colvin, "Synthesis of monodisperse iron oxide nanocrystals by thermal decomposition of iron carboxylate salts," *Chemical Communications*, pp. 2306–2307, Oct. 2004.

[258] J. Kim, H. S. Kim, N. Lee, T. Kim, H. Kim, T. Yu, I. C. Song, W. K. Moon, and T. Hyeon, "Multifunctional Uniform Nanoparticles Composed of a Magnetite Nanocrystal Core and a Mesoporous Silica Shell for Magnetic Resonance and Fluorescence Imaging and for Drug Delivery," *Angewandte Chemie*, vol. 120, no. 44, pp. 8566–8569, 2008.

[259] P. Denes, D. Doering, H. A. Padmore, J.-P. Walder, and J. Weizeorick, "A fast, direct x-ray detection charge-coupled device," *Review of Scientific Instruments*, vol. 80, p. 083302, Aug. 2009.

[260] M. Guizar-Sicairos, A. Diaz, M. Holler, M. S. Lucas, A. Menzel, R. A. Wepf, and O. Bunk, "Phase tomography from x-ray coherent diffractive imaging projections," *Optics Express*, vol. 19, pp. 21345–21357, Oct. 2011.

[261] M. Radermacher, "Weighted Back-projection Methods," in *Electron Tomography: Methods for Three-Dimensional Visualization of Structures in the Cell* (J. Frank, ed.), pp. 245–273, New York, NY: Springer New York, 2006.

[262] B. Borm, R. P. Requardt, V. Herzog, and G. Kirfel, "Membrane ruffles in cell migration: Indicators of inefficient lamellipodia adhesion and compartments of actin filament reorganization," *Experimental Cell Research*, vol. 302, pp. 83–95, Jan. 2005.

[263] J. Albuschies and V. Vogel, "The role of filopodia in the recognition of nanotopographies," *Scientific Reports*, vol. 3, p. 1658, Apr. 2013.

[264] R. M. Cornell and U. Schwertmann, *The Iron Oxides: Structure, Properties, Reactions, Occurrences and Uses.* John Wiley & Sons, Dec. 2006.

[265] J. Frank, *Three-Dimensional Electron Microscopy of Macromolecular Assemblies: Visualization of Biological Molecules in Their Native State.* Oxford University Press, Feb. 2006.

[266] S. K. Natarajan and S. Selvaraj, "Mesoporous silica nanoparticles: Importance of surface modifications and its role in drug delivery," *RSC Advances*, vol. 4, pp. 14328–14334, Mar. 2014.

[267] A. A. Hwang, J. Lu, F. Tamanoi, and J. I. Zink, "Functional Nanovalves on Protein-Coated Nanoparticles for In vitro and In vivo Controlled Drug Delivery," *Small*, vol. 11, no. 3, pp. 319–328, 2015.